

# **Fracture Mechanisms in Resistance Spot Weld of Magnesium Alloys**

by

Seyedtirdad Niknejad

A thesis  
presented to the University of Waterloo  
in fulfillment of the  
thesis requirement for the degree of  
Doctor of Philosophy  
in  
Mechanical Engineering

Waterloo, Ontario, Canada, 2015

©Seyedtirdad Niknejad 2015

## **AUTHOR'S DECLARATION**

I hereby declare that I am the sole author of this thesis. This is a true copy of the thesis, including any required final revisions, as accepted by my examiners.

I understand that my thesis may be made electronically available to the public.

Seyedtirdad Niknejad

## Abstract

The automotive industry is adopting the application of magnesium and magnesium alloys in order to produce light-weight auto-body structures. Therefore, it is essential to evaluate the load bearing capability of these metals in spot welded applications, since spot welding is widely used to assemble the body components.

Failure of spot welds is one of the major durability issues of auto-body structures in monotonic, cyclic and impact loading conditions. Spot weld performance is a special concern because of the operation of a localized stress field at the edge of each weld nugget. The load-bearing capability of a spot weld depends strongly on the toughness of the microstructure existing at the edge of the nugget including fusion zone and heat affected zone. Therefore, any microstructural feature which deteriorates the toughness properties is considered to be detrimental to the structural integrity of a spot weld. This study attempts to assess the effects of microstructure on failure characteristics and mechanical performance of magnesium spot-welded structures in monotonic loading.

Microstructural evolution in resistance spot welding of AZ31, AZ61 and AZ80 magnesium alloys has been studied. The results indicated formation of  $\beta$ - $\text{Mg}_{17}(\text{Al,Zn})_{12}$  divorced eutectic phase at the grain boundaries of both fusion zone and heat affected zone. As the Al content of the magnesium base alloy increased from 3 wt.% (AZ31) to 6 wt.% (AZ61) and 8 wt.% (AZ80), the volume fraction of  $\beta$  phase increased both in heat affected zone and fusion zone. It was found that with increase in volume fraction of the  $\beta$  phase, tensile shear properties of spot welds were adversely affected. Microstructural examinations identified the  $\beta$  intermetallics as preferred sites for micro-crack initiation in monotonic loading of spot welds. It was found that as the Al content of base metal increased from 3 wt.% (AZ31) to 6 wt.% (AZ61) and 8 wt.% (AZ80), the load-to-failure and elongation-to-failure of spot welds (with almost identical nugget diameter) decreased. At the same time, the failure mode changed from interfacial (in AZ31) to nugget pull-out (in AZ61 and AZ80). Removal of the  $\beta$  phase particles via post-weld solutionizing treatment was found to increase the weld strength and ductility of high Al-bearing magnesium spot welds (i.e. AZ61 and AZ80). Failure mode also changed from nugget pull-out to through-thickness.

With the absence of  $\beta$  intermetallics in the microstructure of post-weld heat treated welds, plasticity occurred near the edge of nuggets under load, which introduced resistance against crack initiation. The plastic zones could be identified by observation of heavily twinned microstructure near the crack region. Inspection of misorientation boundaries between the parent and twinned segments revealed the role of  $\{10\bar{1}1\}$ - $\{10\bar{1}2\}$  double twinning, which essentially involved rotation of  $\langle 1\bar{2}10 \rangle/37.5^\circ$  relative to parent, on formation of transgranular micro-cracks. This twinning mode intensified the shear stresses resolved onto the basal slip

systems, leading to early shear localization and transgranular void/crack initiation. It was argued that the susceptibility of an individual grain to transgranular cracking depended strongly on its orientation relative to the stress condition. Those grains in which the stress field created a high shear stresses onto their  $\{1\ 0\ \bar{1}\ 1\}$  twinning systems were more susceptible to transgranular fracture. The primary  $\{1\ 0\ \bar{1}\ 1\}$  twinning mode was found to follow a Schmid-type behavior in most of the studied grains.

For AZ61 and AZ80 magnesium sheets with sharp basal texture, the stress condition under loading at the coarse-grained microstructure of the heat affected zone resulted in high activity of  $\{1\ 0\ \bar{1}\ 1\}$  twinning. Therefore, the heat affected zones of these AZ alloys were susceptible to transgranular fracture. The heat affected zone in ZEK100 sheet, demonstrated higher toughness. Due to its fine-grained microstructure along with more randomized texture, heat affected zone of ZEK100 exhibited lower twinning activity. Therefore, in tensile shear loading of AZ80/ZEK100 dissimilar spot weld (in post-weld heat treated condition), fracture occurred preferentially in the heat affected zone of AZ80, while the heat affected zone of ZEK100 demonstrated high resistance against fracture initiation.

From the experimental-numerical work on fracture study in tensile shear loading of magnesium spot welds, it was concluded that the toughness of the material was associated with combined effect of stress condition and microstructure. This combined effect was further investigated by mechanical testing of magnesium sheet metals using double-edged notched tensile (DENT) specimens. In order to evaluate the effect of texture on the notch sensitivity, DENT specimens were made with notches whose tip was pointing to the sheet's normal direction (for ND specimens) and transverse direction (for TD specimens). The mechanical test results for AZ alloys indicated that the strength and ductility of specimens with notches along the normal direction were lower compared to those with notches along the transverse direction. Schmid law numerical calculations were conducted based on the notch stress condition and crystallographic texture of the alloys to predict the activity of different deformation mechanisms (i.e basal slip, prismatic slip,  $\{1\ 0\ \bar{1}\ 2\}$  twinning and  $\{1\ 0\ \bar{1}\ 1\}$  twinning) at the notch root. The difference in notch sensitivity in ND and TD specimens was associated with an activity competition between prismatic slip and  $\{1\ 0\ \bar{1}\ 1\}$  twinning. The numerical results predicted higher activity for  $\{1\ 0\ \bar{1}\ 1\}$  contraction twinning at the notch root of ND specimens than that in TD specimens. The easy activation of  $\{1\ 0\ \bar{1}\ 1\}$  twins in ND specimens, led to transgranular shear localization and early fracture; however in case of TD specimens, prismatic slip was more active at the notch root which led to more homogeneous deformation and delay in shear localization. Owing to its more randomized texture, ZEK100 alloy appeared to be less sensitive to the notch orientation.

## **Acknowledgements**

I would like to express my sincere gratitude to my supervisors, Profs. Norman Zhou and Shahrzad Esmaeili.

I am thankful to my friends and colleagues in Centre for Advanced Materials Joining (CAMJ) including Ali Nasiri, Ray Liu, Paola Russo, Boyd Panton, Ehsan Marzbanrad and Sashank Nayak who supported me throughout these years. I am also grateful for the help and guidance of the people in Canadian Centre for Electron Microscopy (CCEM), including Chris Butcher, Carmen Andrei, Brian Langelier and Mohsen Danaei.

I greatly appreciate Prof. Sean Agnew for sharing invaluable thoughts and discussions.

This work has been supported by Magnesium Network of Canada (NSERC-MagNET), Automotive Partnership Canada (APC) and NSERC-Discovery.

*TO MY LOVING FAMILY*

# Table of Contents

List of Figures .....	x
List of Tables .....	xix
<b>Chapter 1 Introduction .....</b>	<b>1</b>
1.1 Motivation.....	1
1.2 Objectives .....	2
<b>Chapter 2 Background and Literature Review.....</b>	<b>5</b>
2.1 Magnesium and Magnesium Alloys .....	5
2.1.1 Deformation and Ductility of Magnesium Alloys .....	5
2.1.2 Microstructural Aspects of Fracture in Magnesium Alloys .....	7
2.2 Resistance Spot Welding.....	14
2.2.1 Heat Generation and Welding .....	14
2.2.2 Mechanical Testing and Failure Modes in RSW .....	16
2.2.3 Stress and Strain Analysis at the Edge of Nugget.....	18
2.3 Microstructure-Property Relationship in Welding of Magnesium Alloys .....	21
2.3.1 Heterogeneous Nucleation and Mechanical Properties of Magnesium Spot Weld.....	21
2.3.2 Liquation and Grain Growth in HAZ.....	23
2.4 Summary .....	24
<b>Chapter 3 Materials and Methods .....</b>	<b>25</b>
3.1 Materials.....	25
3.2 Resistance Spot Welding and Heat Treatment .....	25
3.3 Microstructural Examinations and Mechanical Testing.....	26
3.4 Advanced Microscopic Analysis .....	27
3.4.1 Electron Backscattered Diffraction .....	27
3.4.2 Transmission Electron Microscopy .....	30
<b>Chapter 4 Microstructure and Mechanical Properties of Resistance Spot Weld of AZ Alloys.....</b>	<b>31</b>
4.1 Introduction.....	31
4.2 Experiments .....	31
4.3 Results.....	31
4.3.1 Microstructural Observations.....	32

4.3.2 Mechanical Properties and Fracture Analysis.....	54
4.4 Discussion on Microstructure-Property Relationships.....	62
4.5 Summary .....	64
<b>Chapter 5 The Role of Double Twinning on Transgranular Fracture in Magnesium AZ61 in the Localized</b>	
<b>Stress Field of Spot Weld .....</b>	<b>66</b>
5.1 Introduction.....	66
5.2 Background on Double Twinning.....	66
5.3 Experiments .....	68
5.4 Schmid Law Model Description .....	71
5.5 Results.....	73
5.5.1 Observation of Transgranular Cracks and Twin Variants.....	73
5.5.2 Prediction of Deformation Mechanisms at the Vicinity of Notch .....	78
5.5.3 TEM Observations of Slip Activity in Matrix and Double Twin .....	84
5.6 Discussion .....	87
5.6.1 Schmid-type Behavior of $\{1\ 0\ 1\ 1\}$ Twinning .....	87
5.6.2 Strain Accommodation and Cracking .....	89
5.6.3 Grain Size Effects .....	90
5.7 Summary .....	90
<b>Chapter 6 Microstructural Effects on Mechanical Properties and Failure of AZ80/ZEK100 Spot Weld.....</b>	<b>92</b>
6.1 Introduction.....	92
6.2 Experiments .....	92
6.3 Calculation of Energy-to-Failure for a Unit of Spot Weld .....	93
6.4 Results.....	94
6.4.1 Microstructural Observations.....	94
6.4.2 Mechanical Characteristics and Failure mode .....	98
6.4.3 Fracture Mechanisms and Microstructural Effects .....	102
6.5 Discussion .....	106
6.6 Summary .....	109
<b>Chapter 7 Microstructural Effects on Notch Strength and Ductility of Magnesium Alloys.....</b>	<b>111</b>
7.1 Introduction.....	111
7.2 Experiments .....	112



7.3 Results.....	115
7.3.1 Tensile Notch Response.....	115
7.3.2 Fracture Characteristics.....	118
7.3.3 Micro-texture Analysis .....	120
7.4 Prediction of Deformation Mechanisms at Notch Root.....	123
7.4.1 Stress Analysis at Notch Root.....	123
7.4.2 Calculation of Resolved Shear Stresses for Deformation Mechanisms .....	126
7.5 Discussion .....	129
7.6 Summary .....	132
<b>Chapter 8 Conclusions and Outlook .....</b>	<b>133</b>
8.1 Conclusions.....	133
8.2 Outlook .....	135
<b>Appendix A Tensile Test Data for Magnesium Alloys in Different Heat Treatmen Conditions.....</b>	<b>138</b>
<b>Appendix B Tensile Shear Test Results for the Spot Welds of AZ Alloys .....</b>	<b>139</b>
<b>Appendix C Flowchart for numerical calculation of resolved shear stress for deformation systems .....</b>	<b>141</b>
<b>Appendix D Determination of Schmid-type behavior of 1 0 1 1 twinning.....</b>	<b>142</b>
<b>Bibliography.....</b>	<b>163</b>

## List of Figures

Figure 2-1 Plastic deformation systems in magnesium single crystal .....	6
Figure 2-2 Al-Mg binary phase diagram [49].....	8
Figure 2-3 The crystal structures of the two phases (a) Mg and (b) $\beta$ -Mg <sub>17</sub> Al <sub>12</sub> and (c) Schematic diagram showing the lattice correspondence between hcp and bcc structures described as Pitsch-Schrader OR [50] .....	9
Figure 2-4 SEM micro-graph near a crack tip of (a) AZ51 and (b) AZ51+3wt. %Sn [57]....	10
Figure 2-5 (a) 2D model for crack and twin nucleation at the region of stress concentration; (b) basal crack blunting by two symmetrical twins; (c) accommodation of slip/crack ahead of twin tip [59].....	11
Figure 2-6 (a) SEM images of voids in ZK60 at failure with the EBSD map showing 1 0 1 1 and 1 0 1 1 – {1 0 1 2} twin boundaries [19]; (b) TEM analysis of the 1 0 1 1 – {1 0 1 2} near the fracture surface of AZ31 [31] .....	12
Figure 2-7 Schematic illustration of crack propagation and dimple formation in (a) pre-crack parallel and (b) pre-crack normal to the basal plane, d is the inclusion size, $\lambda$ is the spacing from pre-crack to inclusion and D is the dimple size [60].....	13
Figure 2-8 Schematic drawing of stress state in a bi-crystal: (a) before deformation; (b) deformed grains without any bonding; (c) resultant stress state in order to maintain the grain boundary bonding [61].....	14
Figure 2-9 Schematic drawing of resistance spot welding in a sheet stack-up [66] .....	14
Figure 2-10 Schematic presentation of the spot weld under tensile-shear force F .....	16
Figure 2-11 Schematic drawing of a spot weld and possible failure modes during TS loading and their reasons (as reported in [8], [9], [73]).....	17
Figure 2-12 TS coupon (a) in high cycle regime and (b) in low cycle regime [75] .....	18
Figure 2-13 Typical fatigue failure mode of spot weld [79].....	19
Figure 2-14 Stress distribution in spot weld along longitudinal direction for upper and lower plates; (b) Stress distribution in plate thickness direction, both in plane of symmetry [83]...	20
Figure 2-15 Maximum principal strain contour for a spot weld of steel subjected to shear load of 1446 N .....	20

Figure 2-16 (a) Schematic diagram of shear necking in spot weld; (b) Contour plot of plastic strains at the edge of spot weld [9] .....	20
Figure 2-17 Microstructure variation across RSW of AZ31 (a) Alloy 1 with sub-micron Al-Mn particles, (b) Alloy 2 with micron-sized Al-Mn particles [90].....	22
Figure 2-18 Twinning in the fatigued spot weld of AZ31, incident beam // [0 1 1 0] [86]....	23
Figure 2-19 EBSD inverse pole figure map across the laser weld of AZ31[93] .....	23
Figure 3-1 a) Schematic diagram of RSW specimens b) Schematic plot of the tensile shear test for assessment of the crack location.....	26
Figure 3-2 Assembly of specimen on mount for surface preparation for EBSD.....	28
Figure 3-3 Electro-polishing module .....	29
Figure 3-4 Polished surface appearance (a) viewed under polarized light; (b) viewed by electron backscattered image (the particles which cause shadowing effect are highlighted by black arrows).....	30
Figure 4-1 SEM micrographs taken from microstructures of as-received AZ base alloys (a,b) AZ31, (c,d) AZ61, (e,f) AZ80. the EDS analysis results for highlighted particles are shown in Table 4-1 .....	33
Figure 4-2 Microstructures across the RSW (a) AZ31, (b) AZ61 and (c) AZ80.....	34
Figure 4-3 Optical micrographs taken from center of the FZ in the center of nugget in (a) AZ31; (b) AZ61; (c) AZ80 .....	36
Figure 4-4 SEM micro-graphs taken from FZ in AZ31 (a,b); AZ61 (c,d); AZ80 (e,f). The EDS analysis results for the highlighted particles are shown in Table 4-2 .....	37
Figure 4-5 Mg-Al phase diagram predicted by thermodynamic calculations (Zn: 1wt. % and Mn: 0.33wt. %) .....	38
Figure 4-6 Microstructure at the fusion boundary of AZ80 .....	39
Figure 4-7 Solidification model for AZ80 alloy (Scheil cooling calculations) (a) Overall solidification behavior (b) Formation of $Al_8Mn_5$ .....	39
Figure 4-8 TEM image of the sub-micron Al-Mn and $Mg_{17}Al_{12}$ particle. The Al-Mn particles are shown by white arrows .....	41

Figure 4-9 Schematic diagram of supercooling for solidification of imaginary alloys 1, 2 ( $C_2 > C_1$ ).....	41
Figure 4-10 SEM micrograph taken from microstructures of the HAZ in AZ31 (a,b); AZ61 (c,d); AZ80 (e,f), the EDS analysis results for highlighted particles are shown in Table 4-3	43
Figure 4-11 (a) TEM micro-graphs from the inter-granular and intra-granular $\beta$ particles in FZ of AZ80, (b) HRTEM image for the area marked by white circle in (a), the incident beam was along $[1\ 1\ 1]_\beta$ direction .....	44
Figure 4-12 TEM micrographs from $\beta$ particle in the FZ of AZ80 (a) TEM image of inter-granular particle; (b) HRTEM image for the area marked by a white circle in (a) the incident beam was along the $[2\ 1\ 1\ 0]_\alpha/[1\ 1\ 1]_\beta$ directions .....	46
Figure 4-13 Area in which the FIB specimen was extracted .....	47
Figure 4-14 (a) TEM image from $\beta$ particle in the HAZ of AZ80; (b) SAED of Mg matrix in area 1 (Incident beam // $[5\ 1\ 4\ 3]$ ); (c) SAED of $\beta$ particle in area 2 (Incident beam // $[1\ 1\ 1]$ ); (d) SAED of $\alpha/\beta$ interface in area 3 and (e) its schematic representation in $[5\ 1\ 4\ 3]_\alpha/[111]_\beta$ directions .....	48
Figure 4-15 (a) Atomic arrangement on $(3\ 3\ 0)$ plane of $\beta$ unit cell. The $\{3\ 3\ 0\}$ planes are not flat, but “corrugated”, i.e. some of the Al atoms (as indicated by Al_R) have the centers which are not exactly located on the plane. The maximum displacement of the centers of such atoms normal to plane normal is 1.32 Å. Atomic arrangement based on (b) OR.1 and (c) OR.2 .....	50
Figure 4-16 SEM micrographs taken from microstructures of the post weld heat-treated FZ and HAZ for AZ31 (a,b), AZ61 (c,d) and AZ80 (e,f) .....	52
Figure 4-17 Grain size in BM, HAZ and heat-treated HAZ for AZ31, AZ61 and AZ80.....	53
Figure 4-18 XRD spectra from a) FZ b) HAZ of AZ80 .....	54
Figure 4-19 (a) Micro-hardness values of the BM, HAZ and FZ of RSW in as-welded and heat-treated conditions (b) Load-to-failure and displacement at failure load for the spot welded specimens (5 specimens for each joint/condition) in as-welded and heat treated conditions .....	56

Figure 4-20 Illustration of fracture modes: (a) Interfacial (b) Nugget pull-out (c) Through-thickness.....	57
Figure 4-21 Typical crack pathway for RSW in the as-welded condition (a) AZ61; (b) AZ80 .....	57
Figure 4-22 (a) Microstructure near the primary crack in the AZ80 spot weld in as-welded condition (b) Area A at higher magnification (c) Area B at higher magnification.....	57
Figure 4-23 Typical crack propagation path of the RSW in the heat-treated condition (a) AZ61; (b) AZ80 .....	58
Figure 4-24 Microstructure near the crack for the AZ80 RSW in the heat-treated condition	59
Figure 4-25 Fracture surface of AZ80 RSW in as-welded condition: (a) Scheme of the fracture location showing three sections; (b) Fracture surface in section 1 and 2; (c) Fracture surface in section 2 and 3; (d) Magnified image of fracture surface in section 1; (e) Magnified image of fracture surface in section 2 .....	60
Figure 4-26 Fracture surface of the spot weld in the heat-treated condition: a) Scheme of the fracture location b) Fracture surface in section 1, 2, 3 c) Magnified image of fracture surface in section 1 d) Magnified image of fracture surface in section 2 e) Fracture surface in AZ80 BM in heat-treated condition .....	61
Figure 5-1 Schematic diagram of hcp lattice rotation via variant 1 and 4 double twinning and their diffraction patterns (taken from Ref. [34]) .....	67
Figure 5-2 Stereographic projection of $\{0\ 0\ 0\ 1\}$ poles of the six $\{1\ 0\ 1\ 1\}$ primary twins and 36 double twin variants. The symbols representing the orientations are as per Table 5-1 .....	68
Figure 5-3 (a) Typical microstructure near the spot weld notch as encircled in the schematic drawing of spot weld; the projection direction of inverse pole-figure map is parallel to sheet normal direction (ND); (b) Grain size distribution in HAZ of AZ61 (heat treated at 420 °C for 60 minutes); the area from which the grains were picked for the measurements, is highlighted in the schematic drawing .....	69
Figure 5-4 Schematic drawing of welding assembly and accommodation of extensometer..	70
Figure 5-5 Tensile shear response of AZ61 spot weld in as-welded and heat treated conditions .....	70

Figure 5-6 Finite element half-model model presentation of spot weld and cross section near the notch.....	72
Figure 5-7 x-y location of EBSD area relative to the notch .....	72
Figure 5-8 (a) Typical microstructure near the notch after crack initiation during tensile shear test. Plastic zones are encircled; (b) EBSD Kikuchi band contrast map presenting microstructure near the notch before crack initiation in tensile shear test (applied load: 5.2 kN). The twin boundaries are identified as per Table 1-1 .....	74
Figure 5-9 Typical microstructures near the edge of spot weld after tensile shear test as shown in the schematic drawings. The EBSD Kikuchi band contrast maps presents the microstructure within the grains suffered from transgranular fracture as shown in the optical micrographs. The twin boundaries are identified as per Table 1-1. In the accompanying pole-figures, dark square represents the orientation of the parent grain, rhombic represents the orientation of primary $\{1\ 0\ 1\ 1\}$ twins and triangle represents the orientation of the double twins. The $1\ 2\ 1\ 0$ rotation axes are circled in the corresponding pole-figures.....	76
Figure 5-10 Typical optical micrograph and the EBSD map near the fracture edge from ND view.....	78
Figure 5-11 Predicted plastic zone created ahead of the notch.....	79
Figure 5-12 Principal stresses near the notch during tensile shear loading .....	79
Figure 5-13 Prediction of maximum resolved shear stress applied on basal slip systems for the EBSD data shown in Figure 5-9a (a), Figure 5-10b (b), Figure 5-10c (c) and Figure 5-10 (d). The black arrows show those double twins variants which did not demonstrate high activity for basal slip.....	81
Figure 5-14 Maximum Schmid factor predictions of basal slip (a), $1\ 0\ 1\ 2$ twinning (b) and $\{1\ 0\ 1\ 1\}$ twinning (c). The inverse pole-figures reflect the orientation of tensile stress axis in reference frame of parent crystal. The spots were obtained from the transformation of the directions corresponding to maximum principal stress from the specimen reference frame to the crystallographic frame of the parent grains in which the cracks were observed. ....	83

Figure 5-15 (a) FIB surface image of a fractured grain (twin boundaries are visible in BS mode); (b) TEM image from the double twins; (c) diffraction pattern showing a misorientation of $1210/38^\circ$ at the twin boundary as encircled in (b) .....	85
Figure 5-16 (a) STEM image from a double twin and matrix; (b) two beam diffraction condition from a double twin: the diffraction vector (g) is shown by black arrow; (c) microstructure within a double twin showing dislocation arrays forming a low angle grain boundary .....	86
Figure 5-17 (a) Cumulative frequency of primary $\{1011\}$ twinning incidences in terms of their $\tau_{RSS}$ value; (b) frequency of $\{1011\}$ twinning incidences in terms of their $\tau_{RSS}$ rank for all grains and (c) for cases with one twin per grain .....	88
Figure 6-1 Schematic of load (F) vs. extension (x) in TS test of a spot weld; the area for calculation of energy-to-failure is highlighted.....	93
Figure 6-2 SEM micrographs taken from microstructure of the as-received ZEK100 alloy, the chemical composition of the particles shown by arrows are illustrated in Table 6-1 .....	94
Figure 6-3 (a) Overview of the nugget produced in ZEK100/AZ80 joint; (b) Nugget diameter vs. welding current for AZ80/AZ80 and ZEK100/ZEK100 spot welds.....	95
Figure 6-4 Mg-rich area of binary phase diagrams (a) Mg-Nd (Zn:1.25wt.%, Zr:0.35wt.%) and (b) Mg-Al (Mn:0.2wt% , Zn:0.7wt.%). The dashed lines show the chemical composition in ZEK100 (a) and AZ80 (b) .....	96
Figure 6-5 SEM micrographs taken from FZ close to the edge of ZEK100/AZ80 nugget at (a) ZEK100 side; (b) near the boundary of the two sheets and (c) AZ80 side.....	96
Figure 6-6 SEM micrographs taken from FZ of ZEK100/AZ80 (the chemical compositions of the highlighted particles are shown in Table 6-2 .....	98
Figure 6-7 SEM micrograph at the edge of the nugget as highlighted in Figure 6-3a .....	98
Figure 6-8 Tensile shear response of the spot welds for (a) ZEK100/AZ80 (nugget diameter in ZEK side: 9.51 mm); (b) ZEK100/ZEK100 (nugget diameter: 9.67 mm) and (c) AZ80/AZ80 (nugget diameter:9.38 mm) joint combinations in the as welded and heat treated conditions; The arrows (solid for as welded and dashed for the heat treated) on the schematics demonstrate the fracture mode/location. ....	100

Figure 6-9 Tensile shear test results for three RSW coupons (for each joint/condition) for ZEK100/AZ80, ZEK100/ZEK100 and AZ80/AZ80 .....	101
Figure 6-10 Overview of AZ80/ZEK100 nugget after the tensile shear test (stopped at load-to-failure): (a) As welded and (b) heat treated conditions .....	102
Figure 6-11 Failure in ZEK100/ZEK100 weld in as welded condition.....	102
Figure 6-12 Microstructure near crack in ZEK100/AZ80 weld .....	103
Figure 6-13 Microstructure at the edge of AZ80/ZEK100 nugget in heat treated condition after TS test (stopped at peak load); (a) AZ80 side i.e. fracture process zone and (b) ZEK100 side (the side which experienced tensile stresses) .....	104
Figure 6-14 (a) EBSD Kikuchi band contrast maps from the area highlighted in Figure 6-13a: The twin boundaries were highlighted as yellow ( $1\ 2\ 1\ 0/56.2 \pm 5^0$ ) accounting for the primary $1\ 0\ 1\ 1$ twinning and as blue ( $1\ 2\ 1\ 0/37.5^0$ ) accounting for $1\ 0\ 1\ 1-1\ 0\ 1\ 2$ double twinning; (b) Corresponding pole-figures showing the crystallographic orientations within the matrix and the twinned segments.....	104
Figure 6-15 Microstructure at the edge of nugget in heat treated condition.....	105
Figure 6-16 EBSD inverse pole-figure maps from the microstructures corresponding to (a) area A and (b) area B as highlighted in the schematic drawing The pole-figures in (b) demonstrate the texture only in HAZ of ZEK100 .....	106
Figure 6-17 (a) Schematic drawing of stress condition in HAZ at the edge of spot nugget and (b) effect of crystallographic orientation on the activity of deformation micro-mechanisms based on stress condition in HAZ of AZ80 and ZEK100.....	109
Figure 7-1 Tensile properties (along rolling direction) in different heat treatment conditions as explained in; Table 7-1 (a) Yield strength ( $\sigma_0$ ); (b) True tensile strength ( $\sigma_u$ ); Elongation (EL) and (d) grain size (from ND view) .....	113
Figure 7-2(a) Schematic drawing of the DENT specimens (ND and TD) and the corresponding dimensions; The sheet (RD-TD-ND) and specimen (L-W-B) coordinate systems are defined. Note that in ND specimens: $L  RD, W  ND, B  TD$ and in TD specimens: $L  RD, B  ND, W  TD$ . (b) Typical DENT (ND and TD) specimens; (c) Notch appearance from cross sectional view (notch depth: 0.5 mm).....	114



Figure 7-3 Instron 5548 Micro-tensile tester .....	115
Figure 7-4 Tensile notch response for the Mg alloys in (a) AR; (b) 1h, (c) 6h and (d) 10h conditions. Specimens have a notch depth of 0.3 mm .....	116
Figure 7-5 Tensile notch response for the Mg alloys in (a) AR; (b) 1h, (c) 6h and (d) 10h conditions. Specimens have a notch depth of 0.5 mm .....	117
Figure 7-6 Notch yield ratio vs. tensile yield strength for magnesium alloys (a) Notch depth: 0.3 mm; (b) Notch depth: 0.5 mm.....	118
Figure 7-7 (a) Notch appearance in AZ80-AR after fracture, notch depth: 0.3 mm; (b) Mg/Mg <sub>17</sub> Al <sub>12</sub> de-cohesion; (c) Brittle fracture of Mg <sub>17</sub> Al <sub>12</sub> .....	119
Figure 7-8 Cross section of the notched specimens after fracture for (a) AZ61-10h and (b) ZEK100-10h; Notch depth:0.3mm .....	119
Figure 7-9 Typical microstructures near the notch of fractured specimens (AZ61-6h, ND); notch depth: 0.3 mm .....	120
Figure 7-10 EBSD IPF maps (relative to sheet's ND) of the microstructures 10h condition corresponding to (a) AZ31; (b) AZ61; AZ80 and (d) ZEK100. The associated pole-figures demonstrate the general texture relative to the sheet's ND .....	121
Figure 7-11 Three dimensional half-model used for the notch stress analysis.....	124
Figure 7-12 Stress and strain analysis at the notch root for AZ31-10h when $\sigma_{nss} = \sigma_0$ . (a) Plastic zone at the notch root for mid-thickness (B=1) section; (b) Principal stress directions along the thickness at 50 $\mu$ m away from notch root;.....	125
Figure 7-13 Stress distribution (according to specimen coordinate system) along the thickness at 50 $\mu$ m away from notch root for (a) AZ31; (b) AZ61; (c) AZ80 and (d) ZEK100 all in 10h condition .....	126
Figure 7-14 Contour plot of maximum resolved shear stress (MPa) on the deformation systems for microstructures subjected to notch stresses in ND and TD specimens (a) AZ31-10h, (b) AZ61-10h, (c) AZ80-10h, (d) ZEK100-10h .....	127
Figure 7-16 Averaged resolved shear stress values on different deformation systems calculated as shown in Figure 7-14.....	129

Figure 7-17 (a) Schematic drawing of stress condition at notch root using Mohr's circle; (b) heavily stressed deformation systems in crystal near the notch in ND and TD specimens in case of AZ alloys; (c) general crystallographic orientation relative to the stress condition in ZEK100..... 131

Figure 8-1 Schematic diagram showing the probability of crack initiation vs. imposed strain based on the type of micro-mechanisms to be activated in a localized stress field ..... 135

## List of Tables

Table 2-1 Estimated CRSS values (MPa) of deformation mechanisms i.e. basal slip, prismatic slip, extension twinning (E-twin) and contraction twinning (C-twin), reported in the literature for magnesium alloys .....	7
Table 3-1 Chemical composition (wt. %) of the three AZ alloys and ZEK100 and tensile properties (along sheet's rolling direction) for the magnesium alloys used in this study in as-received condition .....	25
Table 4-1 EDS analysis results for the highlighted particles shown in Figure 4-1.....	35
Table 4-2 EDS analysis results for the highlighted particles shown in Figure 4-4.....	39
Table 4-3 EDS analysis results for the highlighted particles shown in Figure 4-10.....	44
Table 4-4 Atom position in $\beta$ unit cell (the values were taken from Ref. [44]).....	49
Table 4-5 EDS analysis results for the particles shown in Figure 4-25e .....	61
Table 5-1 Rotation axis/angle pair for $\{1\ 0\ 1\ 1\}$ twinning and $1\ 0\ 1\ 1\text{-}\{1\ 0\ 1\ 2\}$ double twinning variants and the symbols used in this study for presentation of different twin variants .....	67
Table 5-2 Definition of stress tensors corresponding to the EBSD areas shown in Figure 5-9 and Figure 5-10 with their measured x-y locations relative to notch .....	80
Table 6-1 Chemical composition (weight percent) of the particles shown in Figure 6-2.....	94
Table 6-2 Chemical composition of the particles shown in Figure 6-6.....	97
Table 7-1 Heat treatment procedures for different conditions of the alloys .....	112
Table 7-2 Stress tensors (MPa) obtained from FE model for the alloys in 10h condition in ND and TD specimens ( $\sigma_{nss} = \sigma_0$ ) .....	125

# Chapter 1

## Introduction

With the growing demand for increasing the fuel efficiency and reducing of pollutant emissions, production of light-weight structures has attracted much interest in the automotive industry. Magnesium alloys owing to their low density combined with high specific tensile strength, are potentially good candidates to replace the steel and aluminum alloys in structural components of automobiles. Magnesium is the sixth most abundant element in the earth's crust. Its density is approximately 75% less than that of steel and 33% less than the density of aluminum [1]. According to U.S. Automotive Materials Partnership (including Chrysler, Ford and General Motors), Magnesium-based components should contribute to 15% weight reduction per vehicle by 2020 [2]. Recently, magnesium alloys in the form of rolled sheet metal is being considered for use in the auto-body components [3]. The sheet metals are assembled by resistance spot welding for manufacturing of automotive body components. A modern car typically contains 2000-5000 spot welds [4]. Therefore, having the science and technology for production of magnesium spot welds with high load-bearing and energy-absorbing capabilities is essential to expand the application of magnesium materials in the automotive industry.

### 1.1 Motivation

Over the past decades leading automobile makers have used magnesium-based materials in their automotive parts such as gearbox housing, steering wheel, fuel tank cover, air bag housing and suspension systems [1], [5], [6]; however its role as a major material for auto-body manufacturing is still challenged. Therefore, it is essential to examine the mechanical performance of spot welded magnesium sheet metal components under static and cyclic loads.

Failure in resistance spot welds has been identified as one of the major durability concerns in auto-body components [7]. Due to presence of a sharp notch at the circumference of every spot weld, the material is subjected to complex multiaxial loads during service. Due to the restrictive nature of spot welding assembly, the design process is not able to do much to alleviate the stress condition. Therefore, strength and integrity of a spot weld depends strongly on the quality of the material at the vicinity of the spot weld notch. The failure location and mode can significantly affect the load-bearing capability of spot welds as well as their energy-absorbing capacity in a car crash. For a spot weld under service, with low ratio of nugget diameter to sheet thickness, interfacial failure is the

dominant mechanism of failure [4], [8]. In case of a spot weld with high ratio of nugget diameter to sheet thickness, the materials in the fusion zone, heat affected zone and base metal experience high stresses. Therefore, fracture can occur in any of these regions [8], [9]. The local notch toughness of materials determines the failure mode and mechanical properties in the large spot welds [10]. Notch toughness is an indication of capacity of materials to absorb strain energy before fracture and depends strongly on the material's strength and ductility [11], [12]. Therefore, any microstructural features which affect the strength and ductility of material, substantially contribute to failure mode and load-bearing capability of a spot weld.

Ductility of magnesium alloys depends strongly on the microstructural features such as secondary phase(s), grain size and crystallographic texture. When magnesium material is subjected to a tensile stress, brittle fracture of intermetallic compounds may lead to early fracture [13]–[16]. Elongation-to-failure is significantly affected by grain size [17], [18]. Wrought Mg alloys normally take up a strong basal texture during mechanical processing [19], [20]. Due to lack of active slip systems in the hcp lattice at ambient temperatures, these alloys demonstrate anisotropic behavior during plastic deformation. The conventional magnesium sheet metals lack the ductility for energy absorption and shear easily [2].

## **1.2 Objectives**

The major aim of the current research is to understand the microstructural effects on fracture characteristics of magnesium alloys, subjected to a localized stress field, operating due to presence of a stress raiser. The major objectives in this work are as follows:

➤ **Characterization of microstructural evolution during resistance spot welding**

Since both heat affected zone and fusion zone are present at the edge of a nugget, they are both subjected to intensified stresses when a spot weld is in service. The significant effects of welding thermal cycle on the microstructure of fusion zone and heat affected zone must be studied in order to predict the mechanical strength and energy-absorbing capacity of a spot weld.

➤ **Microstructure-property relationships in spot weld**

In the majority of previously published works, the mechanical performance and fracture mode of spot welds (in static and cyclic loading conditions) were investigated using solid mechanics approaches and microstructural factors (such as intermetallics, micro-texture and grain size) were

mostly neglected. This study aims to understand the contribution of such microstructural features to mechanical performance and failure mode of spot welds.

➤ **Characterization of failure micro-mechanisms**

Before general fracture, microstructure is damaged locally by certain types of mechanisms during loading. A major part of the current work is to characterize such micro-mechanisms and find a correlation between their activity and microstructural fractures. Reduction of the activity of such micro-mechanisms (by microstructural modification) leads to delay in fracture and consequent improvement in mechanical properties.

➤ **Modeling the combined effect of micro-texture and stress condition**

There has been a lack of data on how magnesium alloys respond to a complex stress field, operating ahead of a stress raiser. It is of great importance to understand how the localized strain energy is released in the microstructure. A model has been developed in the current research, accounting for both micro-texture and stress condition, in order to predict the activity of deformation mechanisms. Having the fundamental knowledge of the effects of stress condition on deformation activity in microstructure, enables the design engineers to alleviate (or change) the stress state in order to exploit the desired mechanical performance from weld-fabricated magnesium alloy structures.

## **Organization of the Thesis**

The current work is subdivided into eight chapters. Chapter 2 provides background information regarding fracture in magnesium and microstructural effects on its fracture strength and fracture characteristics. This chapter also presents background information regarding stress and strain conditions in spot welds subjected to external loading. Moreover, the impacts of microstructure (including fusion zone and heat affected zone) on the failure mode and load-bearing capacity of spot weld are discussed.

In chapter 3, the materials, conditions, experimental methods and test equipment used in the current work are explained in detail.

Chapter 4 discussed in detail the effects of alloying elements (in chemical composition of Mg-Al-Zn alloys) on the mechanical properties of spot welds. The effects of welding thermal cycle on microstructure in fusion zone and heat affected zone are presented. The weld microstructure has been characterized by optical microscopy (OM), scanning electron microscopy (SEM), X-ray diffraction

(XRD) and transmission electron microscopy (TEM). This chapter demonstrates that ductility of magnesium is adversely affected by the formation intermetallic compounds during welding. Fracture micro-mechanisms are also characterized in microstructures with high volume fraction of the intermetallic compounds. The capability of post weld heat treatment for improvement of microstructure and mechanical properties of the weld is discussed.

In Chapter 5 attempts are made to find a correlation between fracture initiation and twinning activity in magnesium subjected to intensified stresses at the vicinity of spot weld notch. This was achieved by experimental investigation of micro-texture, along with numerical modeling using Schmid law combined with finite element analysis. In order to characterize the twins, micro-texture in the fracture zone was studied by electron backscattered diffraction (EBSD). The dislocation activity within the matrix and twins were investigated by TEM. It was demonstrated that local ductility of magnesium material depends strongly on the micro-texture and grain size.

Chapter 6 presents experimental approaches to confirm the claims made in chapter 5. It was demonstrated that the spot weld toughness and ductility were significantly affected by grain size and crystallographic texture at the vicinity of notch. This is due to the fact that a magnesium polycrystalline material, with finer grain size and more randomized texture, is able to accommodate the localized inelastic strains more effectively.

Chapter 7 discusses the effect of micro-texture on the notch strength and notch sensitivity of the magnesium materials. The justification for the notch sensitivity has been calculated using a Schmid-based numerical analysis combined with finite element analysis at the notch root.

Finally chapter 8 lists the major conclusions and contributions made in this work and provides recommendations for future research.

## Chapter 2

### Background and Literature Review

In this chapter, background information regarding the materials and processes used in this study are presented. Firstly, magnesium and magnesium alloys are introduced with focus on their fracture characteristics and the effects of microstructural features on fracture strength and ductility. Such information has been utilized in the current work to understand the micro-mechanisms leading to failure in resistance spot weld of magnesium alloys. In the second section, resistance spot welding is presented with focus on failure mode and mechanisms, when spot welds are subjected to a mechanical loading. Background information associated with stress and strain conditions in spot weld under mechanical loading is presented as well. Having a good understanding of stress and strain fields in spot welds is necessary to understand the failure micro-mechanisms. At the end of this chapter, the literature associated with process-structure-property relationships in welding of magnesium alloys are presented.

#### 2.1 Magnesium and Magnesium Alloys

##### 2.1.1 Deformation and Ductility of Magnesium Alloys

Despite their industrially desired properties such as high specific strength (strength to weight ratio), good castability and machining behavior, the wrought magnesium alloys have demonstrated poor formability and ductility at room temperature, which has significantly limited their applications in auto-body production. The theory proposed by Tylor [21], following von Mises [22] suggested that five independent slips systems are necessary to be activated in a polycrystalline material in order to have a homogeneous deformation. Those crystal structures lacking five independent slip systems are more prone to premature fracture and thus considered to have poor ductility.

Magnesium has a hexagonal close packed (hcp) crystal structure with the lattice parameters of  $a=3.21 \text{ \AA}$  and  $c/a$  ratio of 1.624 [23]. Basal and prismatic slip systems with  $\langle a \rangle$  Burgers vectors, offer only four independent modes for deformation. Slip on the close packed (0 0 0 1) planes of Mg-hcp lattice is energetically more favored than the other slip systems. Although the non-close packed prismatic planes possess greater Interplanar spacing than the basal planes, prismatic slip is more difficult to be activated due to production of stacking fault[24]. The four pyramidal slip modes with  $\langle a \rangle$  burgers vector cannot be considered as independent modes as they are the product of the cross-slip between



the basal and prismatic slip modes [25]. It has been argued that the pyramidal slip with  $\langle c + a \rangle$  Burgers vector also provides further five independent slip modes [26], [27]. Therefore the Taylor criteria would apparently be fulfilled; however activation of  $\langle c + a \rangle$  pyramidal slip modes at room temperature is of argument in the previous researches, since the critical resolved shear stress (CRSS) for the pyramidal slip is at least two orders of magnitude larger than that for basal slip [28] in magnesium single crystal.

It was proposed by Kocks and Westlake that ductility of polycrystalline hcp materials can be improved by localized deformation produced by the twins which are nucleated at the highly stressed grain boundaries [29]. Twinning takes place via small atomic translation (known as shuffling) for accommodation of deformation [30]. While slip deformation is a reversible process, the twinning possesses a one-directional character. Therefore, twinning is considered as only 0.5 independent deformation mode; however study of twinning behavior is of great importance. Two different twinning systems have been identified in magnesium. A twinning system leading to accommodation of tensile strain along the c-axis is known as extension twinning which has shown to be activated and propagated easily when a crystal is favorably oriented. The twinning which accommodates the compressive strain along c-axis is known as contraction twinning which is of great important in fracture studies [19], [31]–[34]. Figure 2-1 schematically presents the possible slip/twinning systems in magnesium. Table 2-1 lists the reported CRSS values for the slip and twinning systems. Twinning and crystallographic reorientation by twinning is discussed in more detail in chapter 5.

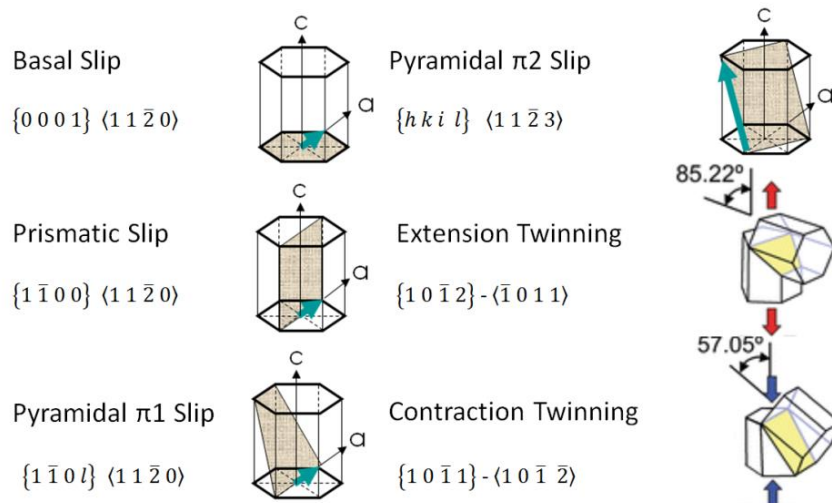


**Figure 2-1 Plastic deformation systems in magnesium single crystal**

**Table 2-1 Estimated CRSS values (MPa) of deformation mechanisms i.e. basal slip, prismatic slip, extension twinning (E-twin) and contraction twinning (C-twin), reported in the literature for magnesium alloys**

Material	Method	CRSS <sub>basal</sub>	CRSS <sub>prism</sub>	CRSS <sub>E-twin</sub>	CRSS <sub>C-twin</sub>
Mg	SC <sup>1</sup>	0.81[35]; 0.76[36]	39.2[37]		
		0.45[38]; 0.65[39]			
		0.52			
AZ31	SC				
AZ31	PC <sup>2</sup> , VPSC <sup>3</sup> , XRD <sup>4</sup>	45[40]	110[40]	15[40]	
AZ31	PC, EBSD <sup>5</sup> , ND <sup>6</sup>	10[20]	55[20]	30[20]	
AZ31	PC,SF <sup>7</sup> ,EBSD				100[32]
AZ31	Numerical				
AZ31	PC, ND, SF			25- 35[41]	
AZ61	PC, XRD				
Mg 7.7 at.% Al				65- 75[42]	

### 2.1.2 Microstructural Aspects of Fracture in Magnesium Alloys

A cleavage fracture normally occurs in a brittle or poorly ductile material due to significant increase in the elastic stresses. A ductile material is capable of relieving the stresses by the generation and motion of dislocations. Fracture in a ductile material is associated with shear localization and

<sup>1</sup> single crystal

<sup>2</sup> poly crystal

<sup>3</sup> visco-plastic self-consistent model

<sup>4</sup> X-ray diffraction

<sup>5</sup> Electron backscattered diffraction

<sup>6</sup> Neutron diffraction

<sup>7</sup> Schmid factor

subsequent void nucleation [43]. Therefore, any metallurgical factor which limits plastic deformation or promotes early shear localization is considered to be detrimental to fracture strength and ductility of Mg alloys. Such factors can be divided into three categories as follows:

### 2.1.2.1 Intermetallics

Aluminum is the major element added to enhance the strength of the magnesium alloys. Aluminum is also added in order to improve the corrosion resistance in Chloride media [44]. Figure 2-2 shows the Mg-Al binary phase diagram. The room temperature microstructure of the magnesium alloys is composed of the  $\alpha$ -Mg and  $\beta$ -Mg<sub>17</sub>Al<sub>12</sub> with the Strukturbericht A12 lattice structure (space group  $I\bar{4}3m$  and  $a \sim 1.06$  nm [45]). The strength of alloys based on the Mg-Al system comes from both Al solid solution hardening and Mg<sub>17</sub>Al<sub>12</sub> precipitation hardening mechanisms [46]–[48]. Figure 2-3 shows a low-energy orientation relationship (OR) normally established between  $\alpha$ -Mg and  $\beta$ -Mg<sub>17</sub>Al<sub>12</sub> during isothermal aging process. The aging response of the magnesium alloys based on the Mg-Al system is small compared to the other age hardenable alloys such as Al-Cu and Cu-Be. The problem is associated with the nature of the precipitation process which is based on formation of only equilibrium  $\beta$  phase. Due to higher energy barrier of the equilibrium phase(s) compared to the transition phase(s), the nucleation rate of the equilibrium phase(s) is lower during isothermal age treatment. Thus, resultant inter-plate spacing of the particles is not small enough to require the dislocations to shear [49].

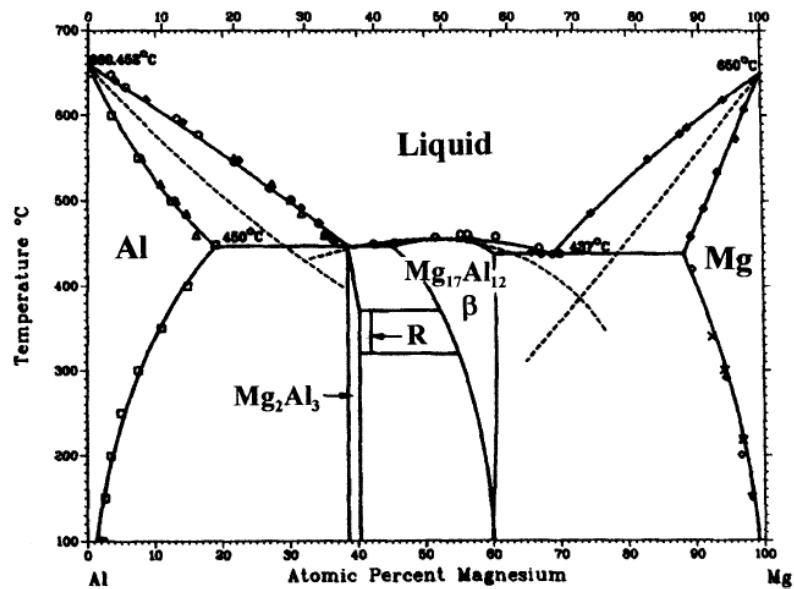
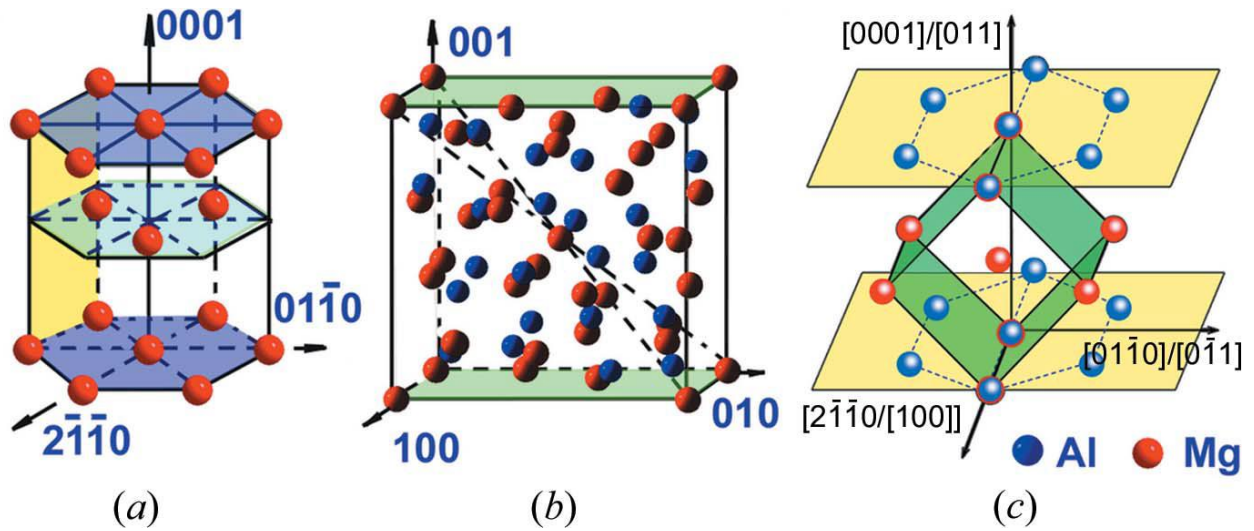


Figure 2-2 Al-Mg binary phase diagram [50]



**Figure 2-3** The crystal structures of the two phases (a) Mg and (b)  $\beta$ -Mg<sub>17</sub>Al<sub>12</sub> and (c) Schematic diagram showing the lattice correspondence between hcp and bcc structures described as Pitsch-Schrader OR [51]

The as-cast structure of the magnesium alloys demonstrates poor mechanical properties in tensile loading. In non-equilibrium solidification of a Mg-Al-Zn system solid solution  $\alpha$ -Mg is formed depleted in Al pushing the remaining Al to the inter-dendritic regions. The solidification is completed by the formation of eutectic phase i.e.  $\alpha$ -Mg +  $\beta$ -Mg<sub>17</sub>(Al,Zn)<sub>12</sub>. The morphology of  $\beta$  phase in solidified microstructure depends strongly on the Al content of the alloy and cooling conditions. The phase shape changes from scattered fine particles to dense large particles as Al content increases. In low and moderate solidification rates (such as in casting processes), lamellar  $\alpha$ + $\beta$  eutectic is formed, whereas at higher solidification rates, the divorced eutectic phase has been mostly observed [14], [52]–[54]. This is due the fact that insufficient time has been provided for diffusion through both liquid and solid and thus, the condition for intimate contact between the two eutectic forming phases is not provided [55].

The presence of divorced eutectic  $\beta$  phase has been shown to deteriorate the ductility and fracture toughness of as cast magnesium alloys [56]. The fracture mode in the as cast microstructure of Mg-Al-Zn alloys was intergranular [13]–[15], [57]. Micro-cracks have been observed at the cell boundaries of  $\beta$  phase near the primary crack during the SEM in-situ fracture test of the as cast AZ51 alloy [58] as shown in Figure 2-4a. Addition of alloying elements such as Sn was demonstrated to improve the mechanical performance since mechanical twinning was activated ahead of propagating crack-tips as shown in Figure 2-4b.

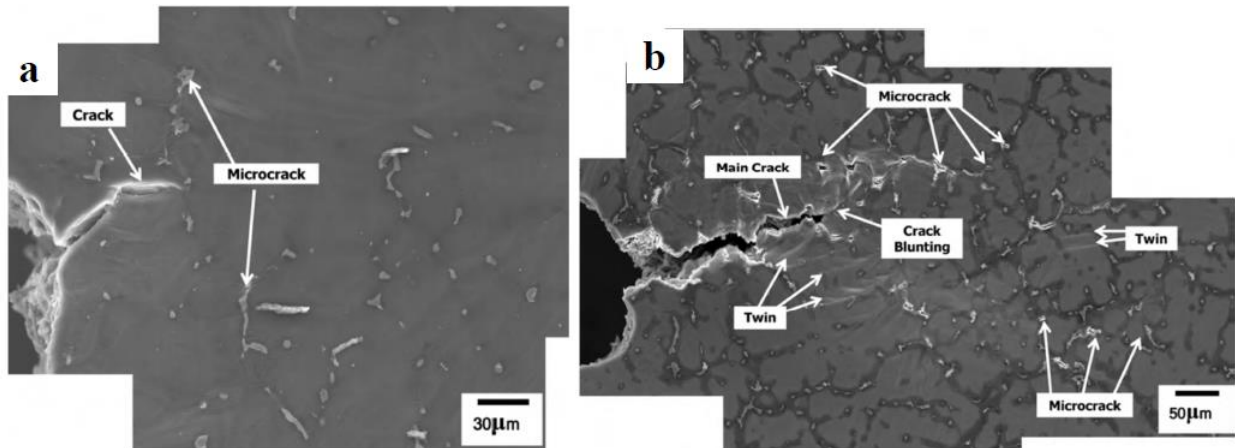


**Figure 2-4 SEM micro-graph near a crack tip of (a) AZ51 and (b) AZ51+3wt. %Sn [58]**

### 1.1.1.1 Crystallographic Texture

Magnesium alloys generally take up a strong basal texture during thermo-mechanical processes (such as rolling and extrusion). The mechanical properties of a magnesium alloy are significantly affected by a sharp texture. Failure in wrought magnesium alloys occurs in shear mode with very small reduction in the cross-sectional area when contraction along the c-axis of crystal is needed to accommodate the imposed strains [20] (i.e. tension perpendicular to c-axis or compression along the c-axis).

Several previous researchers have claimed that there is a correlation between twinning activity and cracking in magnesium alloys. It was first proposed by Tuer [59] that both twinning and fracture possess a cataclysmic nature in releasing the elastic strains. Thus a condition suitable for the formation of the former might be ideal for the formation of the latter. Yoo [60] developed a model to evaluate a critical stress state for the crack extension or twin extension as shown in Figure 2-5. He argued that as long as the parameters involved in equilibrium equations are provided, such as surface energy, twin boundary energy and lattice resistance to twinning dislocations, it is possible to predict whether the elastic strains are to be released via twinning deformation or cracking. A simple expression was defined based on the ratio of critical stresses:

$$\frac{\sigma_t}{\sigma_c} = k \sqrt{\frac{\Gamma_t}{\Gamma_c}} \quad \text{eq.1.1}$$

where  $\sigma_c$  and  $\sigma_t$  are the critical stresses for activation of cracking and twinning respectively,  $\Gamma_c$  is the surface energy and  $\Gamma_t$  is the twin boundary energy.  $k$  is a function of axial ratio and elastic constants of the material. When a propagating twin intersects a boundary, crack initiation is possible due to production of stress concentration (Figure 2-5a). On the other hand, when a crack intersects a twin boundary, its path might change either based on the twin's equivalent habit plane or along the twin boundary (Figure 2-5b).

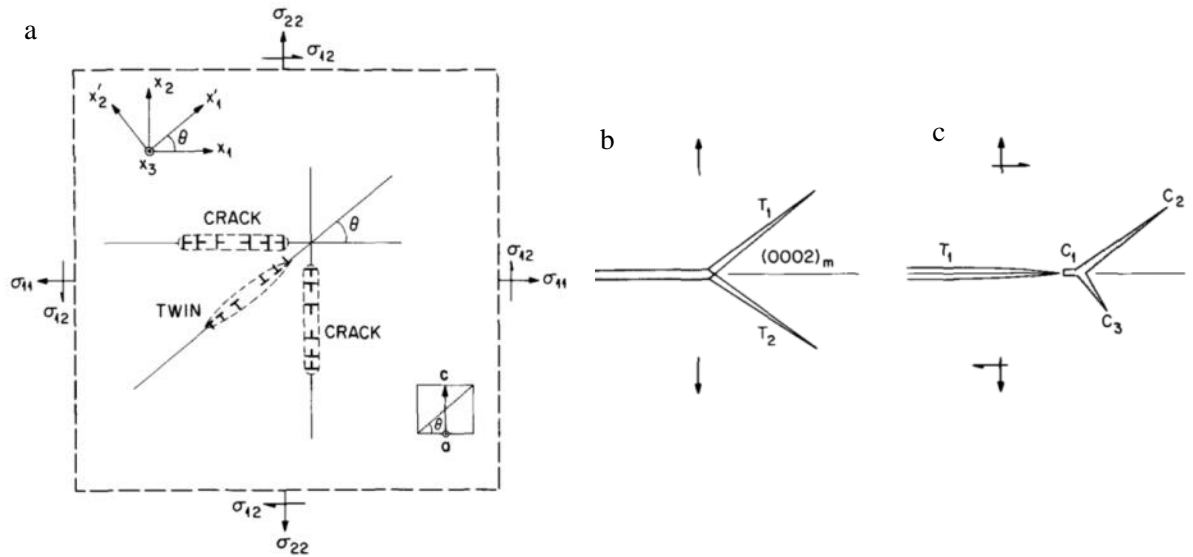


**Figure 2-5 (a) 2D model for crack and twin nucleation at the region of stress concentration; (b) basal crack blunting by two symmetrical twins; (c) accommodation of slip/crack ahead of twin tip [60]**

Microstructural evidence concerning twin-induced fracture in magnesium was first presented by Reed-Hill. He demonstrated various twin traces on  $\{3\ 0\ \bar{3}\ 4\}$ ,  $\{1\ 1\ \bar{2}\ 4\}$ ,  $\{1\ 0\ \bar{1}\ 4\}$  and  $\{1\ 0\ \bar{1}\ 5\}$  crystallographic planes near fracture location [37]. Barnett for the first time [19] found a strong evidence correlating the fracture during in-plane tension to the activity of  $\{1\ 0\ \bar{1}\ 1\}$  contraction twinning (Figure 2-6a). He argued that these twinned segments are unstable and immediately transform to double twins via a secondary  $\{1\ 0\ \bar{1}\ 2\}$  twinning. He further demonstrated traces of different variants of double twins within the vicinity of fracture surface of AZ31, subjected to tensile loading perpendicular to the  $c$ -axes of the grains [31] (Figure 2-6b). Ando et al. found large surface steps near the fracture area caused by double twinning activity [34]. These surface steps were further shown to be able to act as crack nucleation sites in fatigue failure [33].

Somekawa et al. performed an extensive research on the effects of texture on the fracture toughness of magnesium alloys [61]. They argued that having a sample with a pre-crack normal to the basal plane resulted in higher value of plane strain fracture toughness than having a sample with a pre-crack parallel to the basal plane. They correlated such difference in the fracture characteristic to the surface energy of different crystallographic planes: Due to lower surface energy, free surfaces of  $\{0001\}$  were created easily. Thus, the stretched zone ahead of a crack front is small and cracks remain sharp during propagation (Figure 2-7a). When new surfaces of the non-basal planes were to be formed, a propagating crack faced more resistance and thus the stretch zone ahead of crack front was larger (Figure 2-7b)

Somekawa et al. showed high activity of  $\{10\bar{1}2\}$  twinning ahead of the propagating crack [62] during a fracture toughness test of conventionally extruded AZ31. They found significant improvement in fracture toughness for the same material when it was subjected to the equal channel angular processing (ECAP). They found reduced twinning activity due to rotation of the basal planes to an orientation favorable for slip.

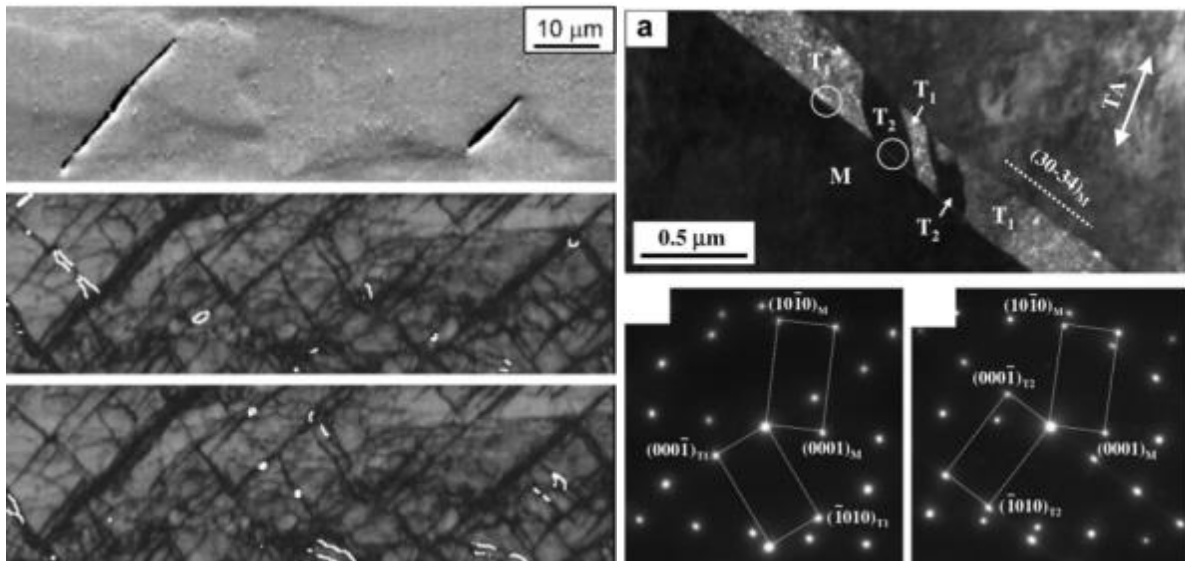
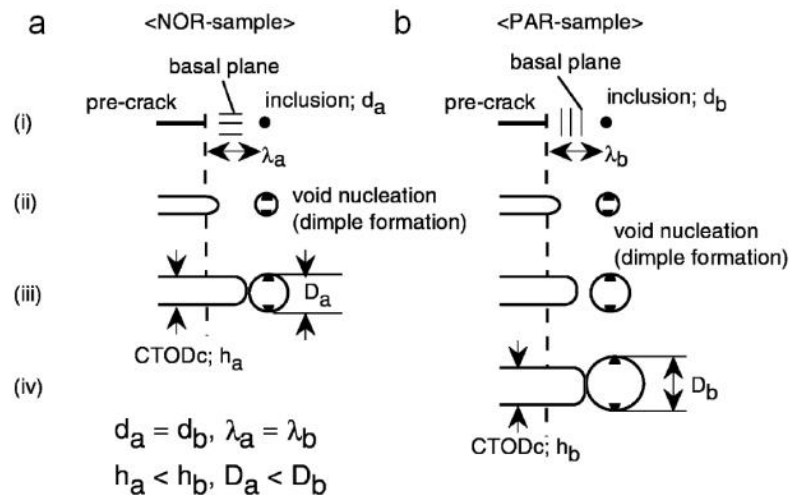


Figure 2-6 (a) SEM images of voids in ZK60 at failure with the EBSD map showing  $\{10\bar{1}1\}$  and  $\{10\bar{1}1\} - \{10\bar{1}2\}$  twin boundaries [19]; (b) TEM analysis of the  $\{10\bar{1}1\} - \{10\bar{1}2\}$  near the fracture surface of AZ31 [31]

### 1.1.1.2 Grain size

Grain refinement in magnesium was reported to increase the fracture strength in monotonic and cyclic loading [62]–[64]. The effect of grain size was associated with a reduced twinning activity at the stress concentrated zone due to activation of non-basal slip. Koike [65] showed that the yield anisotropy decreased in magnesium via grain refinement [62]. Yield anisotropy is defined as  $\frac{\tau_{NBS}}{\tau_{BS}}$ , where  $\tau_{BS}$  and  $\tau_{NBS}$  are the CRSS values for basal and non-basal slip respectively. The room temperature activation of non-basal slip systems was reported in fine grained AZ31 alloy [65]. The reason was attributed to the increased operation of the compatibility stress at the grain boundaries (GBs) as shown schematically in Figure 2-8.

Other than non-basal slip systems, GB sliding was reported to occur in a fine-grained magnesium due to the increased diffusion rate and also pile-up of lattice dislocations [66]. The critical grain size for the change of dominant deformation from twinning to slip was estimated to be 20  $\mu\text{m}$ . The mechanical asymmetry was reported to disappear for grain sizes of less than 4  $\mu\text{m}$  [47].



**Figure 2-7 Schematic illustration of crack propagation and dimple formation in (a) pre-crack parallel and (b) pre-crack normal to the basal plane, d is the inclusion size,  $\lambda$  is the spacing from pre-crack to inclusion and D is the dimple size [61]**



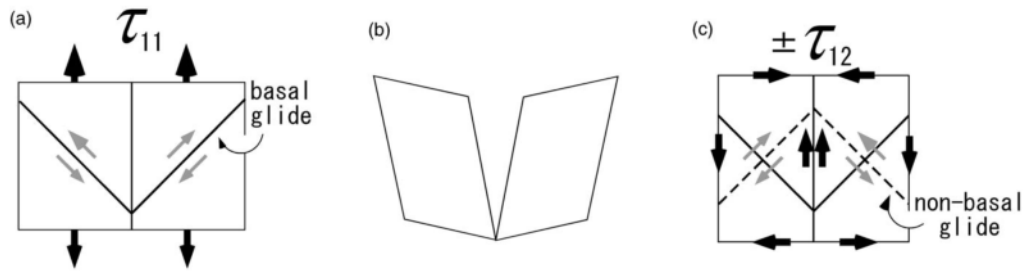


Figure 2-8 Schematic drawing of stress state in a bi-crystal: (a) before deformation; (b) deformed grains without any bonding; (c) resultant stress state in order to maintain the grain boundary bonding [62]

## 2.2 Resistance Spot Welding

### 2.2.1 Heat Generation and Welding

In the resistance spot welding (RSW) process, the heat ( $Q$ ) required for melting of the two metal sheets clamped together, is generated based on the principals of Joule heating, by the application of an AC or DC electric current through the two electrodes on the either sides of the two sheets as shown in Figure 2-9 [67]:

$$Q = I^2 R t \quad \text{eq.2.2}$$

Where  $I$  is the welding current,  $R$  is the electrical resistance of the circuit which is comprised of the contact resistance at electrode/sheet interfaces ( $R_1$ ,  $R_3$ ), the bulk resistance of materials ( $R_2$ ,  $R_4$ ) and the contact resistance at the sheet contact interface ( $R_3$ ), and  $t$  is the time the current is flowing.

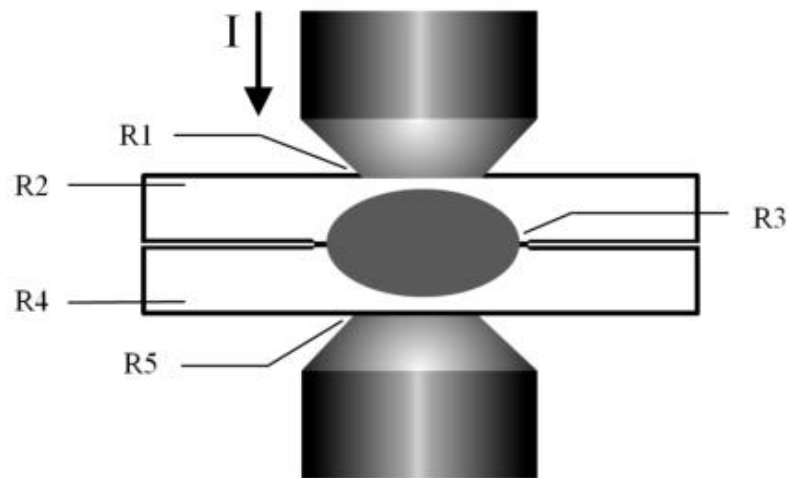


Figure 2-9 Schematic drawing of resistance spot welding in a sheet stack-up [67]

The contact resistance and heat generation at the interface are determined by the surface roughness, hardness and cleanliness of the sheets. The actual contact between the two strongly smoothed surfaces slightly pressed together is a small fraction of the apparent contact area. The contact area is developed in the form of a number of clusters of micro-contacts [68]. When the electrical current is applied and the temperature rises in the contact area, the sheet surfaces become softened and the actual contact area increases due to increase in the plasticity. Consequently the resistance decreases.

The surface properties affect both the quality and shape of the weld nugget. The contact area is reduced by excess contaminants, mainly oxides, which results in excessive heat generation and expulsion of liquid metal. Due to metal loss in the weld pool, solidification shrinkage intensifies tensile stresses leading to pore/crack formation in the center of the weld nugget [69], [70]. Chemical cleaning of the surfaces reduces the chance for metal expulsion and increases the weld soundness [71].

RSW has been mostly performed by the application of AC current; however, due to demand for energy conservation, the new technology of DC spot welding known as mid-frequency DC (MFDC) has been recently developed [72]. Welding current, welding cycle (time) and electrode force are the three major parameters in RSW to be adjusted appropriately based on the material and thickness of the sheets.

According to eq.2.2, the generated heat is proportional to the square of the electrical current. Consequently, changes in the electrical current results in more significant changes in the heat input than the other two parameters i.e. resistance and welding time.

The RSW welding time is generally defined by cycles ( $=1/60$  sec.) and determined by the electrical constants of the system. In case of materials such as aluminum and magnesium with high thermal conductivities, the nugget diameter initially increases with welding time, but levels off with further increase [10], [71]. Generally, higher welding currents and shorter welding time are needed for welding of magnesium and aluminum alloys than for steels.

The functions of the electrode force are: (1) to bring the interface(s) into intimate contact; (2) to reduce the initial contact resistance at the interface; (3) to suppress the expulsion of the molten metal from the joint and (4) consolidate the weld nugget. Large expulsion and cracking can be prevented when more constraints are applied against the escape of liquid from the nugget [10].

## 2.2.2 Mechanical Testing and Failure Modes in RSW

Due to geometric characteristics of spot welds, mechanical loading results in creation of a non-uniform stress field. The weldment is usually considered a unit and its mechanical response is often expressed in terms of load vs. displacement instead of stress vs. strain. To evaluate the mechanical performance of the joint under the static and cyclic loadings three types of tests are generally used:

- a. Tensile shear testing
- b. Cross tension testing
- c. Coach-peel testing

Tensile shear (TS) testing is most commonly used to evaluate the load-bearing capability of the weld due to its simplicity in specimen fabrication and testing. The most important monitored variable in TS testing is the load-to-failure; however the elongation at the load-to-failure also helps in determining the energy-absorbing capacity of a weld [10]. The schematic drawings of the specimens and the direction of loading in the TS test are illustrated in Figure 2-10.

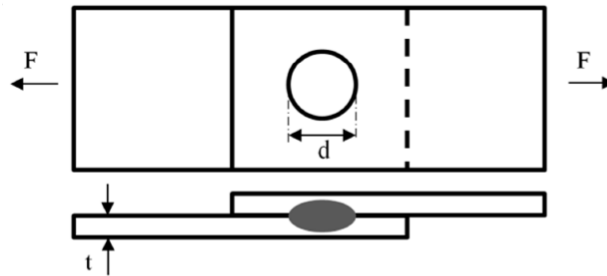


**Figure 2-10 Schematic presentation of the spot weld under tensile-shear force F**

Since the mechanical performance of RSW is not solely determined by its fusion zone (FZ) but by its surroundings i.e. heat affected zone (HAZ) and base material (BM), understanding the properties of these regions leads to better interpretation of testing results. Failure mode in TS testing is a strong function of the nugget size, sheet thickness and fracture toughness of material existing at the circumference of the nugget [10]. Such dependence has not explicitly been formulated mainly due to the complicated relationship between the weld size ( $d$ ) and specimen thickness ( $t$ ). Chao claimed that there is a competition between two failure modes for the TS specimens i.e, interfacial and through-thickness and defined a term “critical weld nugget diameter” ( $d_{cr}$ ) [4]:

$$d_{cr} = 0.86 \left( \frac{\tau_f}{K_C} \right)^{2/3} t^{4/3} \quad \text{eq.2.3}$$

where  $t$  is thickness,  $\tau_f$  is the shear strength of HAZ and  $K_C$  is the fracture toughness of FZ. Specimens with small welds tend to fail in interfacial mode in which the crack propagates through the joint area and hence separated the two sheets after final fracture. In large nuggets, the stress state is changed and normally crack will propagate along the thickness of the sheets. Based on eq.2.3, as thickness of the sheet(s) increases, the fracture toughness of FZ, required to avoid the interfacial failure, must increase. The low value of the hardness ratio of FZ to pull-out failure location (i.e. HAZ or BM) and the high tendency to shrinkage void formation are the two main factors contributing to high susceptibility of a large nugget to interfacial failure [8], [73]. Figure 2-11 schematically illustrates the possible failure modes in TS testing of spot welds.

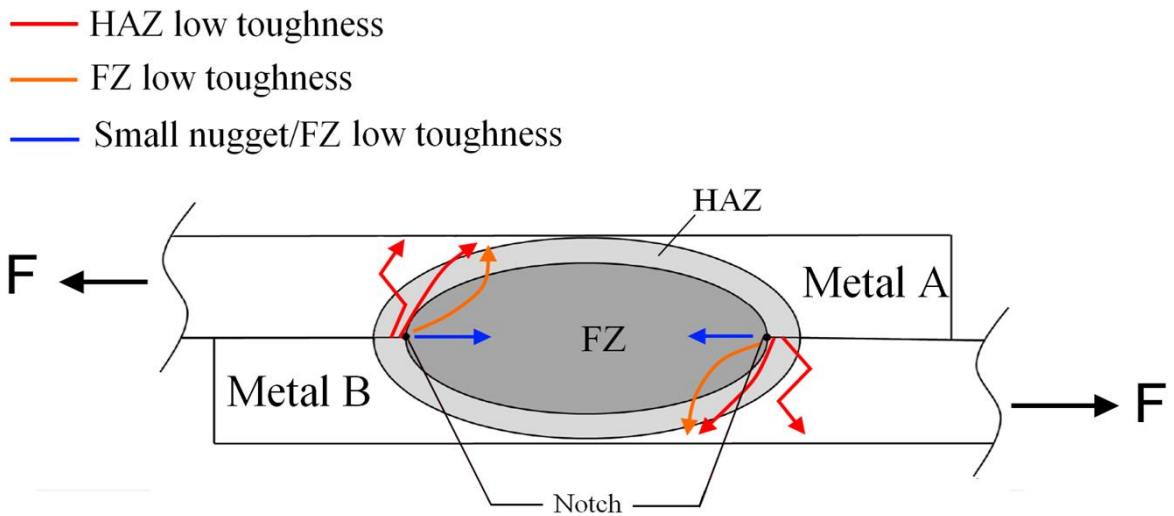


**Figure 2-11 Schematic drawing of a spot weld and possible failure modes during TS loading and their reasons (as reported in [8], [9], [74])**

Under cyclic load applications, mode I stress intensity factor controls the crack growth rate in the tensile-shear spot welds [75]. Failure has been shown to occur through the thickness of magnesium sheets when TS coupons were subjected to a high cycle fatigue (HCF) condition; however interfacial failure occurred in low cycle fatigue (LCF) condition [76]. In the HCF condition, since small load was applied, the joint area was bent slightly, hence the components of the load on the “n-plane” ( $P_n$  as shown schematically in Figure 2-12a) dominated and crack propagated faster on the n-plane compared to the t-plane. In the LCF condition where the applied load was large, bending occurred more and the load component on the t-plane ( $P_t$ ) became comparable to that on the n-plane ( $P_n$ ) (Figure 2-12b). Therefore, stress intensity factors for the two planes were similar and the crack grew

with the same speed in both directions. As the applied load increased, the stress intensity factor on the “t” plane became larger and fracture mode changed to interfacial.

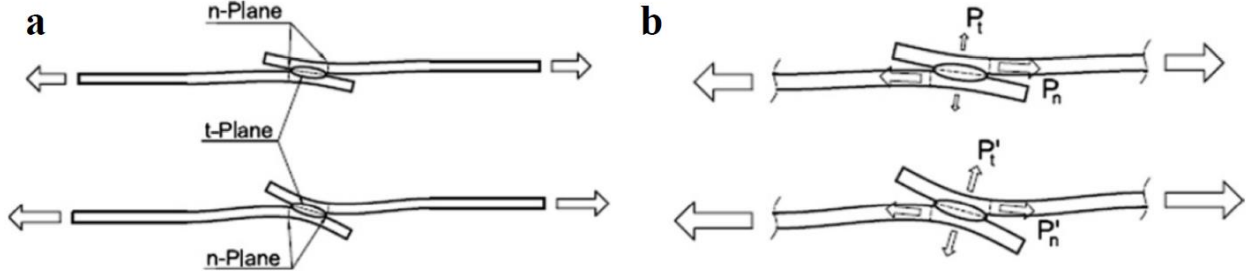


Figure 2-12 TS coupon (a) in high cycle regime and (b) in low cycle regime [76]

### 2.2.3 Stress and Strain Analysis at the Edge of Nugget

The unique shape and geometry of the FZ relative to the BM has made the resistance spot weld an interesting subject for study in the field of fracture mechanics. The sharp slit between the two overlapping BM plates joined by the spot weld nugget can be considered an intrinsic three dimensional crack or notch. Pook [75] considered the circumference of the spot nugget as a crack-like flaw and proposed maximum global stress intensity solutions in lap shear specimens based on fracture modes I and II ( $K_I$  and  $K_{II}$ ).

$$K_I = \frac{F}{d\sqrt{d}} \left[ 0.964 \left( \frac{d}{t} \right)^{0.397} \right] \quad \text{eq.2.4}$$

$$K_{II} = \frac{F}{d\sqrt{d}} \left[ 0.798 + 0.458 \left( \frac{d}{t} \right)^{0.71} \right] \quad \text{eq.2.5}$$

where  $d$  is the nugget diameter and  $t$  is the sheet thickness.

Zhang [77], [78] utilized the J-integral method to determine the maximum intensity factors at the nugget edge of TS coupons in order to predict the life of spot welds subjected to cyclic loading:

$$K_I = \frac{\sqrt{3}F}{2\pi d\sqrt{t}}, K_{II} = \frac{2F}{\pi d\sqrt{t}}, K_{III} = \frac{\sqrt{2}F}{\pi d\sqrt{t}} \quad \text{eq.2.6}$$

The equivalent stress intensity factor ( $K_{eq}$ ) was derived for different spot weld specimens:

$$K_{eq} = \sqrt{K_I + \alpha K_{II} + \beta K_{III}} \quad \text{eq.2.7}$$

where  $\alpha$  and  $\beta$  are the constants depending on the observed fracture mode and materials properties. Zhang's stress intensity solutions were further validated using finite element (FE) analysis [79]. In

most cases, the circumference of the nugget was assumed to be an initial crack in the publications on fatigue-life prediction of spot welds; however microstructural observations from cross-sections of spot welds after TS test revealed notch blunting as shown in Figure 2-13a. It has also been found that the through-thickness crack did not initiate exactly from the edge but at a distance away from it (Figure 2-13b). Pan [80] utilized such observations and calculated the stress intensity factor based on a pre-existing through-thickness crack in order to predict the fatigue life.

Stress and strain analysis confirmed that local yielding occurred near the nugget circumference which affected the stress intensity and therefore fatigue life [80]–[82]. Based on Neuber’s rule [83] when yielding occurs ahead of a stress raiser, the stress concentration factor ( $K_\sigma$ ) and strain concentration factor ( $K_\epsilon$ ) no longer stay constant and equal to each other. The maximum stress ahead of a notch is reduced by local plastic deformation. Unfortunately, an analytical elastic-plastic solution to estimate the strains and stresses at the edge of a nugget is difficult to obtain [9]. Therefore, numerical methods are the most widely used approaches. Elastic-plastic analysis showed that the strains within the nugget at the plane of symmetry were small and maximum plastic strain occurred in the HAZ under low-cycle fatigue condition [9], [74].

The FE analysis results indicated that during loading of TS coupons, the maximum principal stress was introduced exactly at the edge of the nugget in the plane of symmetry and its direction was close to the direction of the applied load (Figure 2-14) [84], [85]. Pan et al. investigated the mechanisms for the through-thickness failure of spot nuggets when the ratio of nugget diameter to the sheet thickness was high [9], [86]. Using FE stress-strain analysis, they demonstrated that the maximum strain location is not at the notch root but up to the root during TS loading as shown in Figure 2-15. Their elastic-plastic FE model indicated that necking failure occurred at the base metal at a distance in order of the thickness away from the notch root (i.e. nugget edge). Necking occurred due to localized shear bands as shown in Figure 2-16.

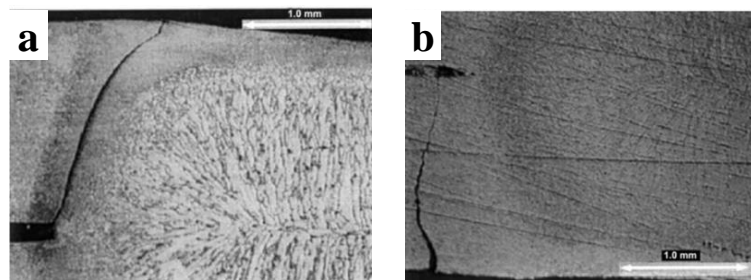


**Figure 2-13 Typical fatigue failure mode of spot weld [80]**

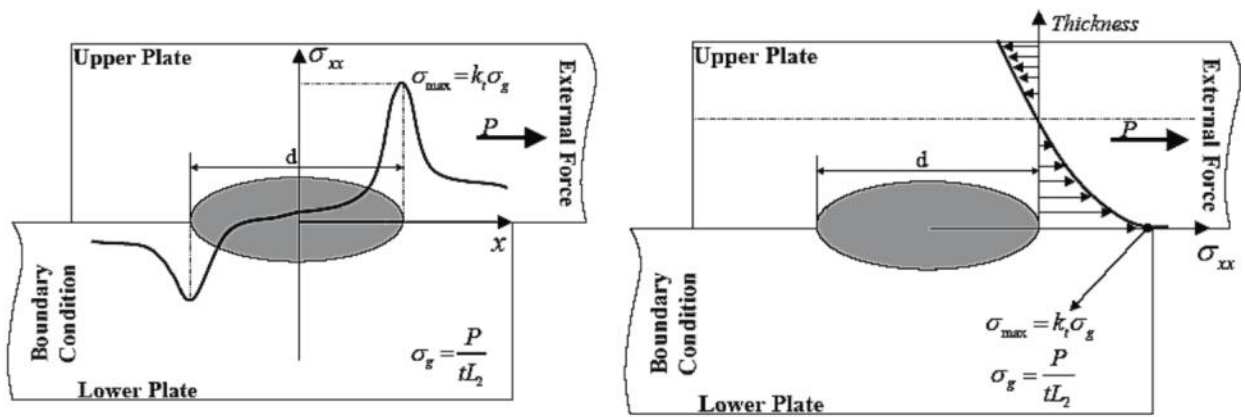


Figure 2-14 Stress distribution in spot weld along longitudinal direction for upper and lower plates; (b) Stress distribution in plate thickness direction, both in plane of symmetry [84]

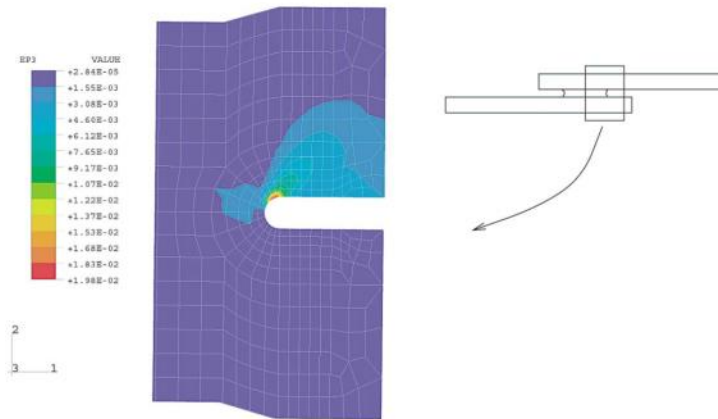


Figure 2-15 Maximum principal strain contour for a spot weld of steel subjected to shear load of 1446 N

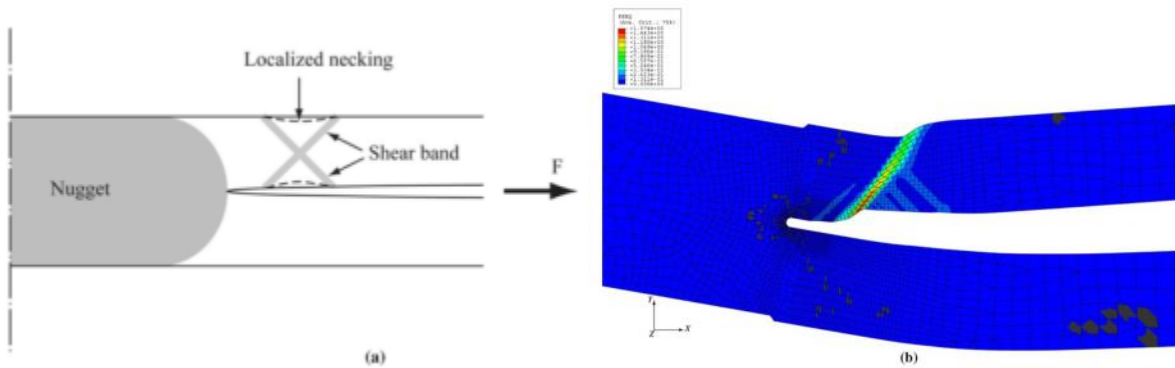


Figure 2-16 (a) Schematic diagram of shear necking in spot weld; (b) Contour plot of plastic strains at the edge of spot weld [9]

## **2.3 Microstructure-Property Relationship in Welding of Magnesium Alloys**

There have been numerous publications regarding weldability of the magnesium alloys in fusion welding processes. In this section, a brief summary of the reports [54], [56], [87]–[91] concerning the fundamental understanding of the microstructure-property relationships in weld of magnesium alloys is presented.

### **2.3.1 Heterogeneous Nucleation and Mechanical Properties of Magnesium Spot Weld**

Interfacial cracking is the most prevalent fracture mode during the monotonic loading of AZ31 spot weld with a high ratio of nugget diameter to sheet thickness [87], [90], [92]. The morphology and grain size of solidified microstructure significantly affect the mechanical properties of spot welds [90], [93]. A refined and uniform grain structure may be formed inside the RSW nugget of AZ31. A fast cooling rate as well as dendrite fragmentation due to forced convection of molten pool contributed to the refined grain structure. In the nugget, normally equi-axed dendrites existed; however a columnar dendritic structure was developed near the fusion boundary due to high thermal gradient (Figure 2-17a). Liu et al. investigated the effect of columnar dendritic structure on the nugget strength during monotonic TS loading [90], [91]. They reported that the nugget strength increased significantly, if the development of columnar structure was minimized. It was found that the size of Al-Mn particles, pre-existing in the base metal, affected the heterogeneous nucleation rate during solidification: large particles contributed more efficiently in crystallization and a more refined grain structure with small columnar dendrite zone was formed as shown in Figure 2-17b. Significant improvement in the weld strength was achieved. The effects of refined equi-axed grain structure in the FZ was claimed to be due to the following factors:

- a. More isotropic behavior of the equi-axed grains compared to columnar dendrites
- b. Reduced segregation of the alloying elements
- c. Enhancement in the fracture toughness of the material due to reduction of the grain size.



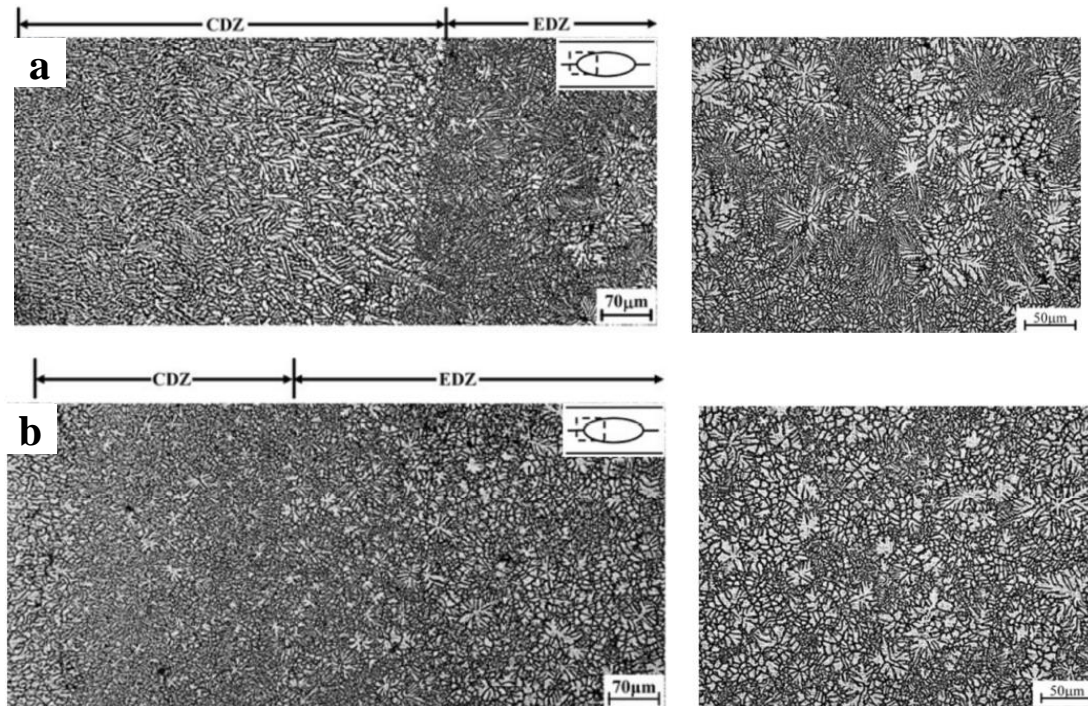


**Figure 2-17 Microstructure variation across RSW of AZ31 (a) Alloy 1 with sub-micron Al-Mn particles, (b) Alloy 2 with micron-sized Al-Mn particles [91]**

Xiao et al. [87] investigated the fatigue life of TS spot weld of AZ31. The results demonstrated better fatigue properties of the spot weld with finer microstructure at the LCF condition. Using transmission electron microscopy, they analyzed the deformed substructure to understand the difference in the mechanisms of deformation between fined-grained and coarse-grained FZ microstructure during TS testing. They claimed that the better performance of the weld with a refined grain size was due to activation of non-basal slip deformation and thus, more effective strain accommodation at the notch root. On the other hand, higher twinning activity was observed in a deformed weld with larger grains as shown in Figure 2-18.

While heterogeneous nucleation led to improvement of the fracture toughness in welds, it significantly reduced the yield strength of the material in the weld. This reduction was associated with the texture change in the fusion zone compared to that in base metal [94]. Figure 2-19 shows that the strong basal texture in the as-rolled sheet metal was turned into a randomized texture in the fusion zone. In this condition, more grains are favorably orientated for basal slip and therefore, plastic yielding starts more readily.

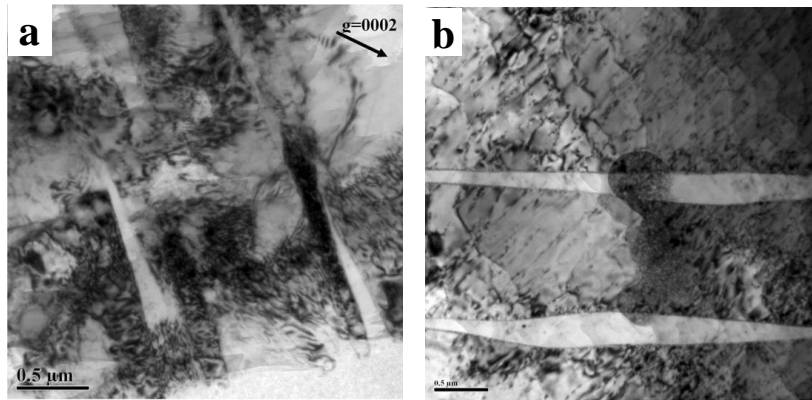


Figure 2-18 Twinning in the fatigued spot weld of AZ31, incident beam //  $[0\ 1\ \bar{1}\ 0]$  [87]

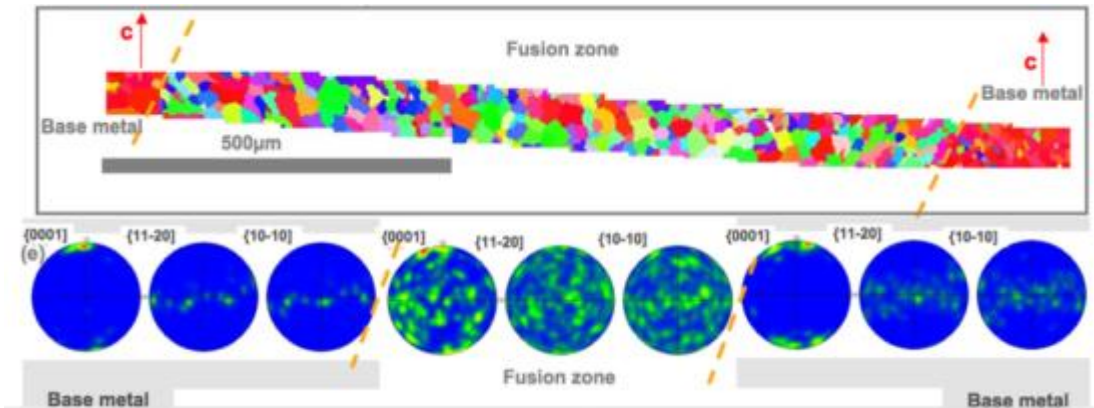


Figure 2-19 EBSD inverse pole figure map across the laser weld of AZ31[94]

### 2.3.2 Liquation and Grain Growth in HAZ

Recrystallization and subsequent grain growth was reported to occur in the HAZ of Mg alloys subjected to a strain hardening process (cold/warm rolling) before welding [56]. The recrystallization temperature of the wrought AZ31 was reported to be in the range of 250-450 °C [95], [96]. The maximum temperature in the HAZ of magnesium was measured to be around 550 °C [97]. Therefore, grain growth in the HAZ is expected. By increasing the solute content, the mobility of the GBs decreased, hence the grain growth was reduced: When a GB moves, the solute atoms migrate along it and induce a drag force which reduces the boundary velocity. The magnitude of the drag force depends on the solute-atom/solvent-atom binding energy and the solute concentration in the GBs. Grain growth is also interrupted by the existence of second phase particles distributed along the GBs [98]. The particles exert a drag force on the GB restricting its motion. The driving force for grain growth (i.e. energy reduction due to decrease in the GB area) might be insufficient to overcome the

drag of the particles and grain growth stagnates. If the microstructure is exposed to a temperature above the dissolution temperature of the second phase, abnormal grain growth is possible to occur [99].

Along with grain growth, liquation has been observed in the HAZ of Mg-Al alloys [100], [101]. Liquation predominantly occurred at either GBs, where maximum solute content existed, or interface of matrix/eutectic phase(s). The HAZ liquation is a non-equilibrium process and results in significant damage in properties of the weld. In some cases crack nucleation was observed due to transient thermal stresses at the liquified regions [89], [102].

## **2.4 Summary**

The major points from the reviewed literature are as follows:

1. Microstructural features such as intermetallics, texture and grain size substantially affect fracture strength, ductility and deformation characteristics of magnesium alloys. Twinning activity was reported to be correlated with fracture process in magnesium alloys
2. Several factors such as sheet thickness, nugget diameter and fracture properties of material in fusion zone and heat affected zone affect fracture mode and mechanical properties of spot weld subjected to tensile shear loading.
3. A highly localized stress field exists at the edge of a nugget when a spot weld is subjected to mechanical loading. Mechanical performance of the spot weld is determined by the fracture strength and ductility of material, existing at the edge of the nugget.
4. For a spot weld with high ratio of nugget diameter to the sheet thickness, plastic zone is more developed into the heat affected zone than in the fusion zone.
5. The welding thermal cycle leads to several forms of microstructural evolution such as grain refinement and texture randomization in the fusion zone and grain growth and grain boundary liquation in the HAZ.

## Chapter 3

### Materials and Methods

#### 3.1 Materials

AZ31, AZ61, AZ80, ZEK100 commercial hot rolled sheets, all 2 mm in the thickness were used for the current research. The AZ series alloys were provided by Pohang's Research Institute of Industrial Science and Technology (RIST) and ZEK100 alloy was provided by Magnesium Elektron of North America (MENA). Table 3-1 lists the chemical composition and tensile properties (in the as-received condition) of the alloys. The stress-strain curves of the materials (in different heat treated conditions) can be found in Appendix A. Rectangular specimens of 100mm×25mm were prepared for the resistance spot welding according to AWS-D17.2 standard [103].

**Table 3-1 Chemical composition (wt. %) of the three AZ alloys and ZEK100 and tensile properties (along sheet's rolling direction) for the magnesium alloys used in this study in as-received condition**

Material		AZ31	AZ61	AZ80	ZEK100
Composition (wt.%)	Al	2.9	6.1	7.7	
	Zn	1.1	1.2	0.7	1.25
	Others	0.3 Mn	0.5 Mn	0.2 Mn	0.5 Zr, 0.22 Nd
Tensile Properties	0.2% offset yield strength (Mpa)	200	200	243	178
	Engineering tensile strength (Mpa)	287	306	351	243
	True Tensile strength (Mpa)	335	355	389	273
	Elongation (%)	19.8	16.9	11.1	16.8

#### 3.2 Resistance Spot Welding and Heat Treatment

Resistance spot welding was performed using a median-frequency DC spot welding machine (Centerline Ltd., Windsor, ON, Canada). The welding parameters used for the RSW of all the welded samples were selected based on the maximum strength of the weld nugget and prevention of expulsion during the welding process. In the whole study, welding time and electrode force were kept constant as 8 cycles (133 ms) and 4kN respectively. Post weld heat treatment was performed in air and atmosphere protected (for temperatures more than 400°C) furnaces. The heat treatment

temperature was selected based on the thermodynamic calculations by FactSage [104] software package for dissolution of the Mg-Al phase in AZ alloys and Mg-Zn phase in ZEK100.

### 3.3 Microstructural Examinations and Mechanical Testing

The specimens were cut from cross sections, hot mounted, ground and mechanically polished. Two etching solutions were considered for revealing the microstructure: 5% nital was used for revealing the morphology of the microstructure in case of columnar-equi-axed dendrites under the optical microscope. The acetic picral solution (4.2 g picric acid, 10 mL acetic acid, 70 mL ethanol, 10 mL water) was used for revealing the GBs and the secondary phases. The microstructures of the weld samples were examined by optical microscopy (OM) and scanning electron microscopy (SEM). A LEO 1550 scanning electron microscope equipped with field emission gun (FEG) and microanalysis system by energy dispersive spectroscopy (EDS) was used for the phase characterization. X-ray diffraction analysis was performed using Rigaku AFC-8 diffractometer with Cu-K $\alpha$  X-ray generated by 50 kV acceleration voltage and 40 mA current. The micro-hardness profiles of the welds were measured on the cross sections using a HMV-2000 Vickers micro-hardness apparatus. Testing was performed with 100 g force and a holding time of 15 seconds. TS specimens were prepared for each condition (i.e. as-welded and the heat-treated conditions), to evaluate the mechanical properties (Figure 3-1a). The fractography of the fractured samples was performed using JEOL JSM-6460 SEM with an Oxford ultra-thin window detector EDS. To study the crack propagation path, the TS testing was stopped immediately after reaching the load-to-failure (Figure 3-1b). The crack-bearing specimens were afterwards examined by the OM, SEM and electron backscattered diffraction (EBSD) to investigate the location and causes of crack formation.

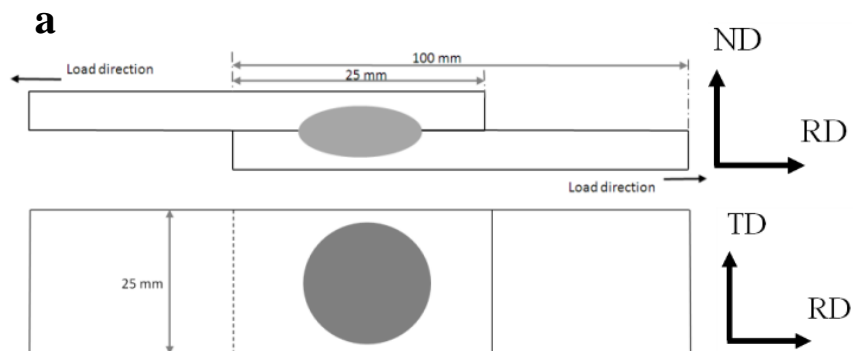
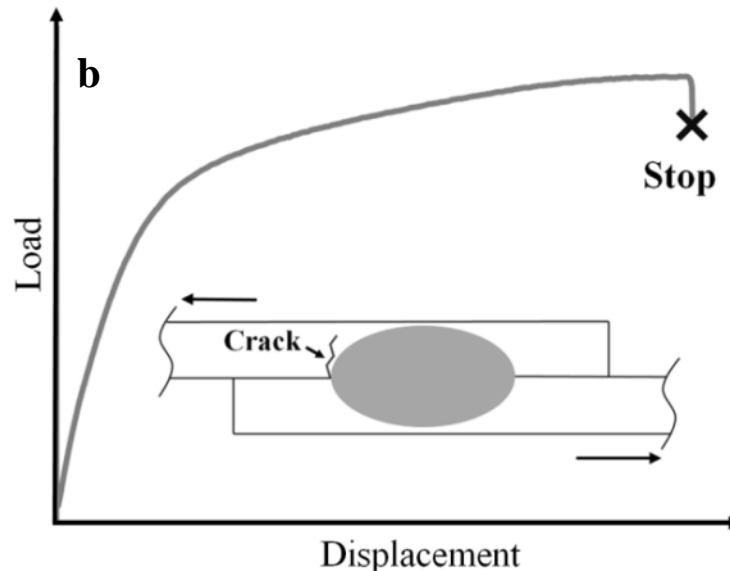


**Figure 3-1 a) Schematic diagram of RSW specimens b) Schematic plot of the tensile shear test for assessment of the crack location**



### 3.4 Advanced Microscopic Analysis

#### 3.4.1 Electron Backscattered Diffraction

EBSD Sample preparation for Mg materials is a difficult task. Several factors affect a successful EBSD analysis. The main issue is very high sensitivity to oxidation [105]. Thus, the last stage of surface preparation should be done immediately before EBSD. Also magnesium demonstrated very high twinning activity when a low tensile force is applied along the c-axis. This would result in significant change in the micro-texture. Since the EBSD samples should be thin, they must be handled very carefully during surface preparation from cutting to final polishing. The applied force during grinding/polishing should be kept very low to avoid large sub-surface damages. Any attempt using automatic polishers available on-campus, was unsuccessful due to high force applied by the loading frame. The preparation procedure used in the current work was arranged according to reports (unpublished) from Dr. M. Danaei (Canadian Centre for Electron Microscopy) and Dr. N. Stanford (Deakin University).

The samples were first cut from the cross section by a precision cut-off machine. A cutoff wheel (Struers 10S15) appropriate for soft materials was used. Normally a thickness of 1 mm material was cut. The samples were not mounted since experience showed that the space between the sample edge and mount is a place ideal for the grinding media build-up. Ejection of these particles during

polishing leads to introduction of scratches. The samples instead were fixed on the surface of a mount using an instant adhesive as illustrated in Figure 3-2. A conductive mount was used to provide electrical conductivity for the electro-polishing process. Two small pieces (of the same material/thickness) were used as support to balance the surface during grinding/polishing.

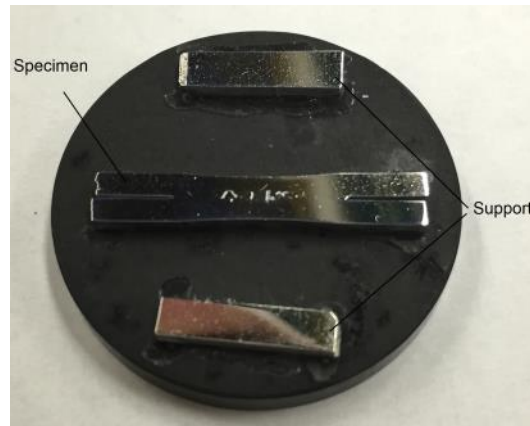


**Figure 3-2 Assembly of specimen on mount for surface preparation for EBSD**

Coarse grinding was performed by 600, 800, 1200 and 4000 grit SiC papers in a fashion to remove the previous scratches by the forthcoming grinding stages. The samples were afterwards electro-polished for the first time using 5% nitric acid in Ethanol in order to remove any possible sub-surface damages imposed by cutting/grinding. A Buehler Electromet-4 electro-polisher was used for electro-polishing. The sample (anode) was fixed faced down and a pin connecting to the negative terminal touched the surface of the mount (Figure 3-3). The electro-polishing parameters (volt/time) were selected based on specimen surface area and type of material. From the experience, electro-polishing was successful when a current of 0.2 A was achieved for a rectangular area of 4 mm× 15 mm.

The samples were afterwards cleaned by ultrasonic vibration in a bath of Ethanol. Mechanical polishing was performed using 3  $\mu\text{m}$  and 1  $\mu\text{m}$  diamond sprays. Anhydrous Ethanol was used throughout the polishing process. Chemo-mechanical polishing was performed for 20 minutes using a mixture of colloidal silica (1/3) and ethylene glycol (2/3) on a Struers MD-Chem polishing cloth. The samples were immersed in a bath of ethanol and ultrasonically cleaned immediately after polishing to prevent formation of a solid film of silica on the surface. The polished samples were polished electrolytically for less than 10 seconds, no more than 5 hours before the EBSD analysis. Experience has shown that longer electro-polishing time results in shadowing of the secondary phase particles as shown typically in Figure 3-4b. From a well-polished sample, one should see the grain/twin

boundaries under the polarized light of the optical microscope as well as the SEM backscattered image (Figure 3-4). Immediately before EBSD, the samples were ion etched under an Ar ion beam for 20 minutes. 4 keV beam energy and 150  $\mu$ A current was applied with rocking angle of 60° and rotation speed of 20 rpm.

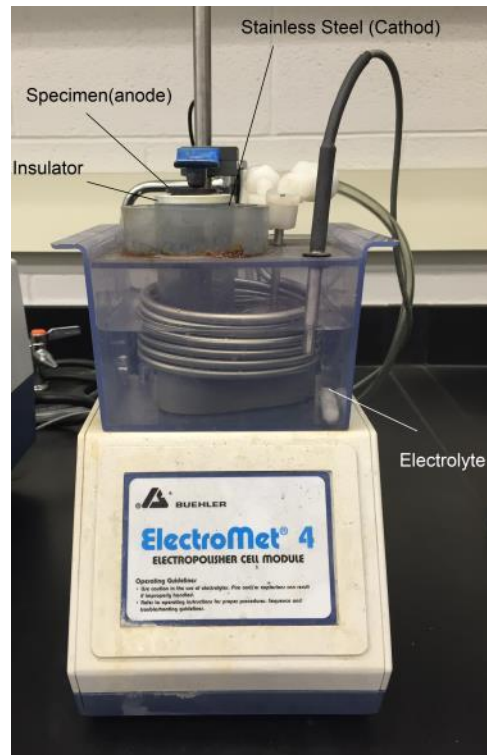


**Figure 3-3 Electro-polishing module**

EBSD analysis was performed using JEOL JSM-7000F equipped with a Schottky field emission gun and an EBSD detector. An acceleration voltage of 20 keV, with a working distance of 15 mm and a sample tilt angle of 70° were utilized. To characterize the twins, small step sizes (0.1-0.4  $\mu$ m) were chosen. The indexing fraction of 65-82% was obtained for the microstructures at the vicinity of the micro-cracks. For analysis of general texture, step size of 1  $\mu$ m was selected. The indexing success for the un-deformed specimens was 88-94%. The maps were cleaned using the “noise reduction” function via CHANNEL 5 software package and afterwards, the identities of the primary and secondary twins were determined in terms of their corresponding Euler angles.



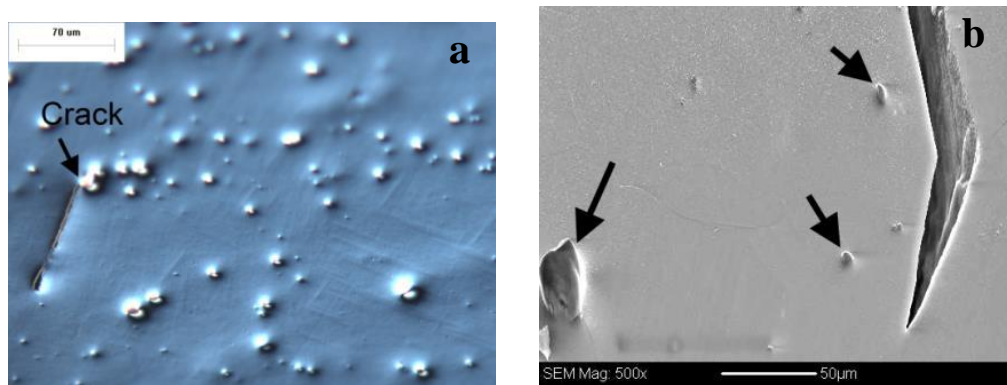


**Figure 3-4 Polished surface appearance (a) viewed under polarized light; (b) viewed by electron backscattered image (the particles which cause shadowing effect are highlighted by black arrows)**

### 3.4.2 Transmission Electron Microscopy

For transmission electron microscopy (TEM), two methods were used to prepared samples:

- a. Jet polishing followed by ion milling for characterization of FZ
- b. Focused Ion Beam (FIB) milling for characterization of HAZ and twinned regions near crack

For the jet polishing method, samples were cut on the AZ80 weld nugget with the thickness of 400 $\mu\text{m}$ . Mechanical thinning of discs was carried out to a thickness of 100  $\mu\text{m}$ . The TEM foils were electro-polished in a Tenupol 5 (Struers, Ballerup, Denmark) double jet polishing unit in a 5.3g lithium chloride (LiCl), 11.16g magnesium perchlorate ( $\text{Mg}(\text{ClO}_4)_2$ ), 500ml methanol, 100ml butyl cellosolve at -45 oC. The foils were afterwards subjected to 2 hrs. ion milling on a Gatan 691 precision ion polishing system (PIPS) in order to remove the surface oxide layer.

The FIB milling was performed with a Zeiss NVision 40. The FIB lift-out method was utilized. A thin layer of Tungsten was deposited on the specimen to protect it during the milling process. The FIB was performed using Ga liquid metal ion source. A Ga beam operating at 30KV excavated the specimen from both sides to a depth of 12 microns. The bottom of the lamella was cut out and the lamella was then lifted out and attached to a TEM grid. The lamella was further thinned to electron transparency using reduced voltage and current. Final thinning was performed at 1kV to reduce any amorphous layer. High resolution transmission electron microscopy (HRTEM) and energy dispersive spectroscopy (EDS) analysis was performed in a JEOL 2010F TEM (field emission gun with a point to point resolution of 0.23 nm) equipped with an EDAX system operating at a voltage of 200kV.

## **Chapter 4**

# **Microstructure and Mechanical Properties of Resistance Spot Weld of AZ Alloys**

### **4.1 Introduction**

In this chapter the experimental results prepared during the first two years of the current project were provided. The work presented in this chapter has been previously published by Niknejad et al. [106][107]. The focus in this chapter was to investigate how the presence of the intermetallics deteriorated the mechanical performance of the weld. Firstly, microstructural features in base metals, heat affected zones and fusion zones were presented. The solidified morphology in the three welds (i.e. AZ31, AZ61 and AZ80) was studied by optical microscopy and discussed. The phase analysis results by scanning electron microscopy, X-ray diffraction and transmission electron microscopy were included. Secondly, mechanical test results were presented which had been prepared by micro-hardness measurements and tensile shear tests. Thirdly, fracture characteristics and micro-mechanisms were investigated. Finally, microstructure-property relationships were discussed in details.

### **4.2 Experiments**

AZ31, AZ61 and AZ80 alloys were used for the resistance spot welding. Welding current was selected to produce a nugget with a maximum ratio of nugget diameter to sheet thickness along with minimum expulsion. The stress intensity at the edge of nugget is significantly dependent on the nugget diameter. Therefore current was selected in such a fashion to produce nuggets with diameters close to each other in the three alloys (AZ31, AZ61 and AZ80). Welding current was kept the same as 28 kA for AZ31 and AZ61 and 26 kA for AZ80. The nuggets formed in AZ31, AZ61 and AZ80 alloys had diameters of 9.12 mm, 9.85 mm and 9.38 mm respectively. The welded samples were also studied in the post-weld heat treated condition. Post-weld heat treatment was performed in atmosphere furnace at 400°C for ½ hr followed by cooling in the air.

### **4.3 Results**

In this section, first the microstructural features in base metal, fusion zone and heat affected zone was presented. Afterwards, mechanical properties and fracture characteristics of spot weld were presented and finally fracture mechanisms were studied by careful microscopic examinations.

### 4.3.1 Microstructural Observations

#### 4.3.1.1 Base Metal

The base metal (BM) microstructures of AZ31, AZ61 and AZ80 are shown in Figure 4-1. A single phase microstructure, having very few second phase particles was observed in the AZ31 and AZ61 base alloys (P1 and P5 in Figure 4-1). The EDS analysis results indicated that these particles were enriched in Al (Table 4-1). Coarse globular Al-rich phase particles were observed in the GBs of the AZ80 base microstructure. The average grain size (from the sheet's transverse direction view) was measured based on the linear intercept method according to the ASTM-E112-96 (2004) to be 4.8  $\mu\text{m}$ , 6.9  $\mu\text{m}$  and 4.3  $\mu\text{m}$  for AZ31, AZ61 and AZ80 respectively. Other than Mg-Al particles, large irregular shaped particles enriched in Al and Mn were also observed (Table 4-1) in microstructures of the three alloys (P1, P3, P4, P6).

#### 4.3.1.2 Fusion Zone

Figure 4-2 shows the microstructure across the RSW nuggets of the Mg alloys. Microstructure in fusion zone (FZ) can be divided into two distinctive regions based on the morphology. A columnar dendrite zone (CDZ) existed adjacent to the fusion boundary. By advancing towards the center of the nugget, the equi-axed dendrite zone (EDZ) existed comprised of the flower-like dendrites. The average length of the columnar dendrite zone was measured to be 320  $\mu\text{m}$ , 170  $\mu\text{m}$  and 80  $\mu\text{m}$  for AZ31, AZ61 and AZ80 RSW respectively. The solidification started from the un-melted (or partially melted) BM grains requiring low undercooling, due to identical crystal structure of substrate and solidifying material. The columnar dendrites grew fast along a crystallographic direction, lined-up favorably with the direction of the maximum temperature gradient. The thermal gradient decreased by advancing from the fusion boundary to the center of nugget, promoting formation of equi-axed dendrites (as observed in Figure 4-2 and Figure 4-3).

Figure 4-3 shows typical microstructures of FZ in the center of the nuggets. The size of dendrites decreased from AZ31 to AZ80. The averaged diameters of the flower-like dendrites were measured to be 31  $\mu\text{m}$ , 20  $\mu\text{m}$  and 16  $\mu\text{m}$  for AZ31, AZ61 and AZ80 welds, respectively.

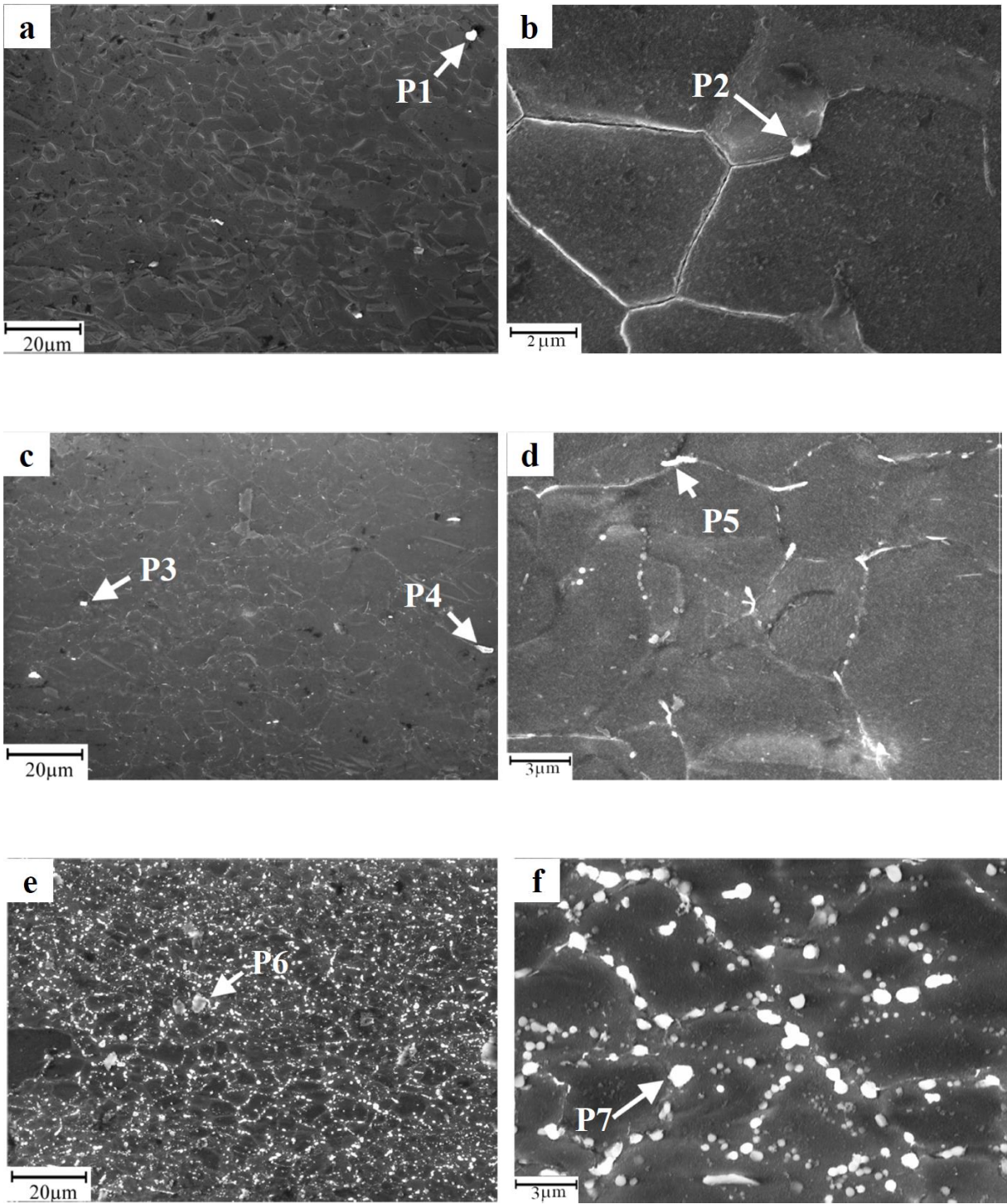


**Figure 4-1 SEM micrographs taken from microstructures of as-received AZ base alloys (a,b) AZ31, (c,d) AZ61, (e,f) AZ80. the EDS analysis results for highlighted particles are shown in Table 4-1**

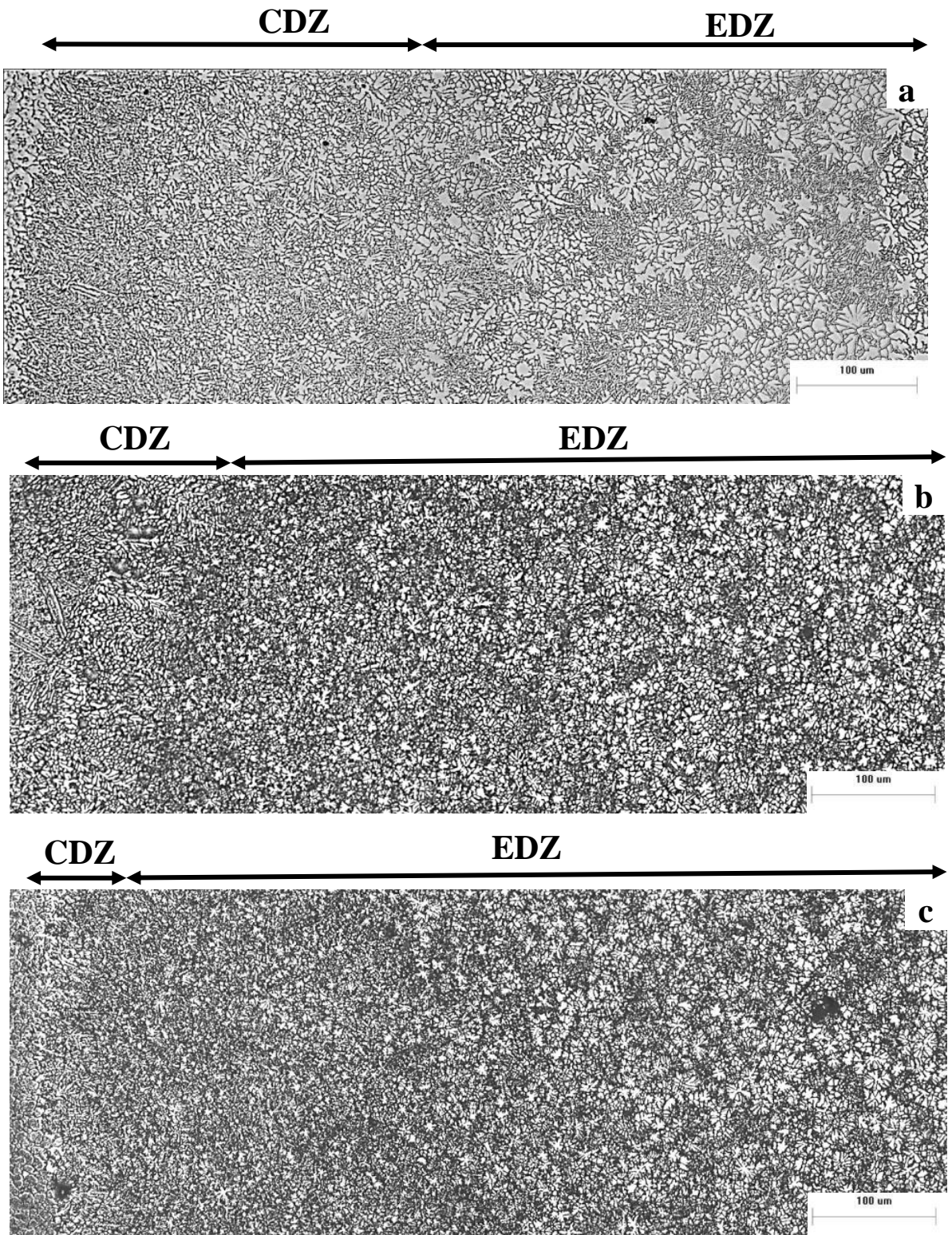


Figure 4-2 Microstructures across the RSW (a) AZ31, (b) AZ61 and (c) AZ80

**Table 4-1 EDS analysis results for the highlighted particles shown in Figure 4-1**

Element	P1	P2	P3	P4	P5	P6	P7
Mg (at. %)	42.3	77.8	65.3	61.85	83.2	12.3	67.3
Al (at. %)	36.2	17.8	24.3	24.8	16.8	58.1	32.7
Zn (at. %)	-	4.4	-	-	-	-	-
Mn (at. %)	21.5	-	10.5	13.35	-	29.6	-

Figure 4-4 shows the SEM micro-graphs, taken from the center of nugget for the three welds. Al-rich phase particles (appeared bright in SEM micro-graphs) were found in the inter-dendritic regions of the three welds. Based on the Mg-Al binary phase diagram, it is expected that these particles are of  $\beta$ -Mg<sub>17</sub>Al<sub>12</sub> phase. The volume fraction of the Mg-Al particles increased from AZ31 to AZ80. Figure 4-5 shows the Mg-rich side of Mg-Al binary phase diagram thermodynamically calculated using FactSage (FT-lite database) [104]. In order to predict the solidification products from the alloying elements other than Al, the averaged content of zinc and manganese in the three alloys (i.e. 1wt. % Zn and 0.33wt.% Mn) were considered in the system for the calculations. The most possible Mg-Al secondary phase to form in the welded microstructure is  $\beta$  phase. The mechanism of solidification can be explained as follows: At the first stage of the solidification,  $\alpha$ -Mg was formed with low concentrations of Al, pushing the solute (Al, Zn) to the molten pool. Due to the growth of  $\alpha$ -Mg primary phase and the lack of time for diffusion in the solid state, the solute contents in the remaining molten pool was progressively increased which led to eutectic reaction and formation of divorced  $\beta$  intermetallics in interdendritic regions. The volume fraction of the eutectic liquid ( $f_e$ ) during non-equilibrium solidification of a liquid with solute concentration of  $C_0$  can be estimated by the Scheil equation [108]:

$$f_e = \left(\frac{C_0}{C_E}\right)^{\frac{1}{1-k}} \quad (\text{eq.4.1})$$

where  $k$  is the equilibrium segregation coefficient and  $C_E$  is the solute concentration at eutectic point. According to eq.4.1, the volume fraction of eutectic liquid during welding increases with increasing the solute content of base metal from AZ31 to AZ80 which results in larger volume fraction of the  $\beta$  intermetallics.

Zinc was also dissolved into the  $\beta$  phase forming Mg<sub>17</sub>(Al,Zn)<sub>12</sub> compound. Figure 4-6 shows a typical microstructure of AZ80 at the fusion boundary. Very large Al-Mn particles exist at the fusion

boundary (within FZ) in the three welds. Such Al-Mn particles existed within the BM microstructures of the AZ alloys but with much smaller dimensions (Figure 4-1 a,c,e). Such large particles were also observed within the center of the nuggets but not as frequently as along the fusion boundary. These particles are likely to be formed as a result of chemical reaction in the liquid state.

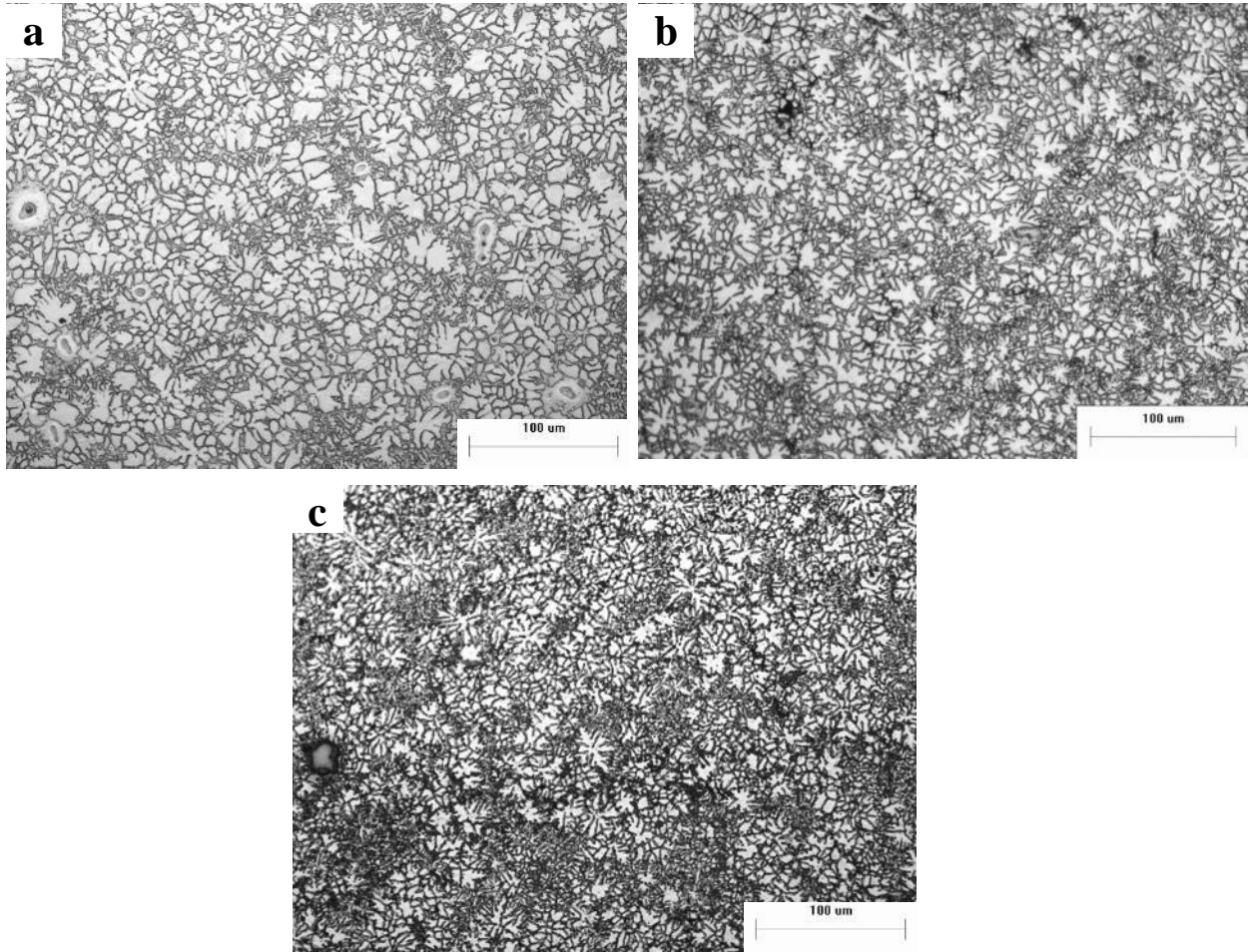


**Figure 4-3 Optical micrographs taken from center of the FZ in the center of nugget in (a) AZ31; (b) AZ61; (c) AZ80**

Figure 4-7 shows the solidification model of AZ80 based on the thermodynamic calculations by FactSage [104]. Scheil-Gulliver equations [108] ( $D_s = 0$ ) were utilized for modeling of the solidification. The model predicted formation of  $Al_8Mn_5$  at early stage of solidification (Figure 4-7b). Although the model also predicted formation of  $Al_{11}Mn_4$  phase, its weight percentage was significantly lower than  $Al_8Mn_5$ . Similar predictions were made for the AZ31 and AZ61. It is likely that the large Al-Mn particles (formed due to chemical reaction of the Al and Mn atoms during welding) were dragged away from the weld pool to the fusion boundary; however smaller particles

remained suspended into the melt as observed typically in Figure 4-4a. The equilibrium model suggested the  $Al_xMn_5$  phase transformation with decreasing the temperature as follows:  $Al_8Mn_5 \rightarrow Al_{11}Mn_4 \rightarrow Al_4Mn \rightarrow Al_{99}Mn_{23}$ . Such sequence of phase transformation is doubted since the present system is far away from equilibrium condition.

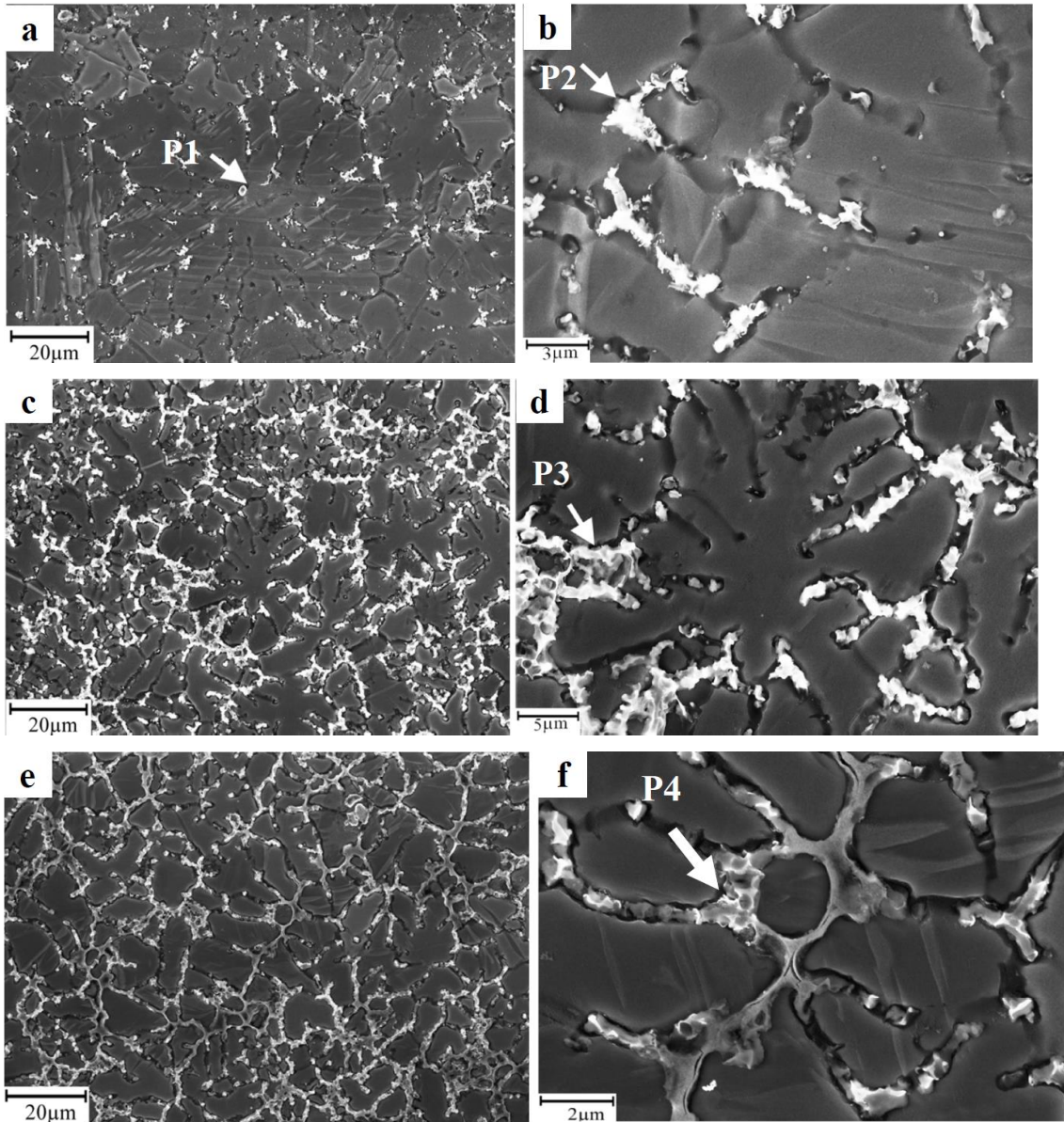


**Figure 4-4** SEM micro-graphs taken from FZ in AZ31 (a,b); AZ61 (c,d); AZ80 (e,f). The EDS analysis results for the highlighted particles are shown in Table 4-2



TEM study detected the nano-sized Al-Mn particles in the FZ. Figure 4-8 shows a typical image of the Al-Mn rich intra-granular particles highlighted by white arrows. As observed, the nano-sized Al-Mn particles frequently have elongated morphologies. It was confirmed by the previous studies (on the AZ31 alloy with the same chemical composition as it is currently under study) that these Al-Mn particles are of  $\text{Al}_8\text{Mn}_5$  phase [91]. These particles remained un-melted during welding, since the melting temperature of the  $\text{Al}_8\text{Mn}_5$  (1048°C to 1191°C [109]) is higher than the highest temperature of the weld in RSW of magnesium alloys (around 770°C [110]). A large  $\beta$  particle was observed on a nano-sized Al-Mn particle in Figure 4-8. During solidification, the nano-sized  $\text{Al}_8\text{Mn}_5$  particles were able to act as nucleation sites for the formation of the  $\text{Mg}_{17}\text{Al}_{12}$ . This is consistent with the previous study [111] which reported that the  $\beta$  phase formed preferentially in the Mn-rich areas.

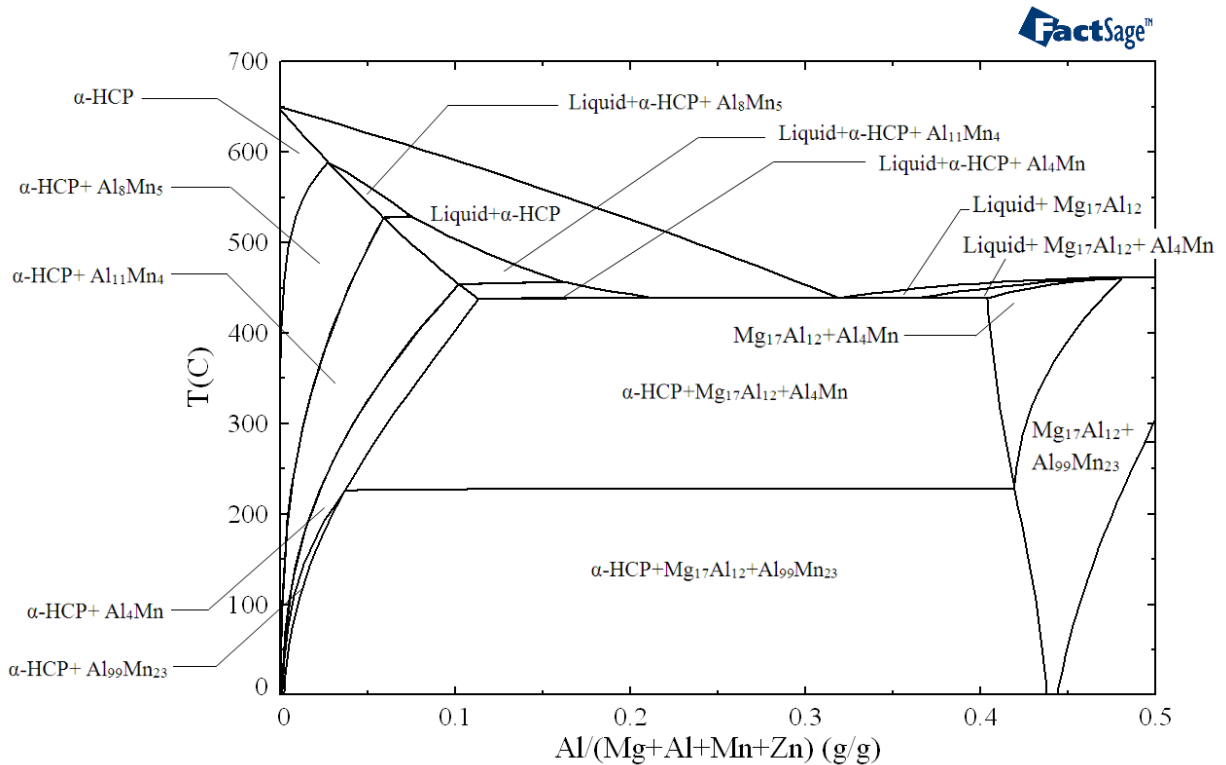


Figure 4-5 Mg-Al phase diagram predicted by thermodynamic calculations (Zn: 1wt. % and Mn: 0.33wt. %)

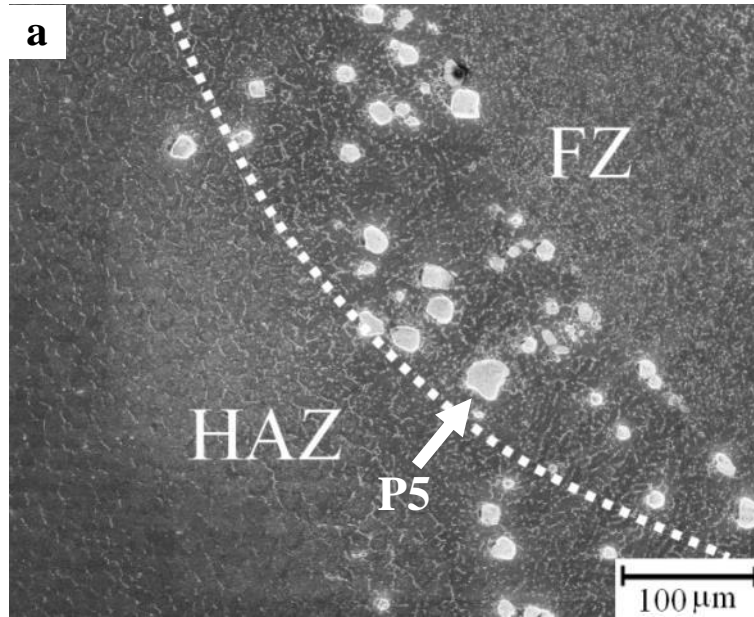


Figure 4-6 Microstructure at the fusion boundary of AZ80

Table 4-2 EDS analysis results for the highlighted particles shown in Figure 4-4

Element	P1	P2	P3	P4
Mg (at. %)	14.1	70.7	64.3	64.3
Al (at. %)	66.2	25.6	32.9	34.2
Zn (at. %)		3.8	2.8	1.5
Mn (at. %)	19.8		-	-

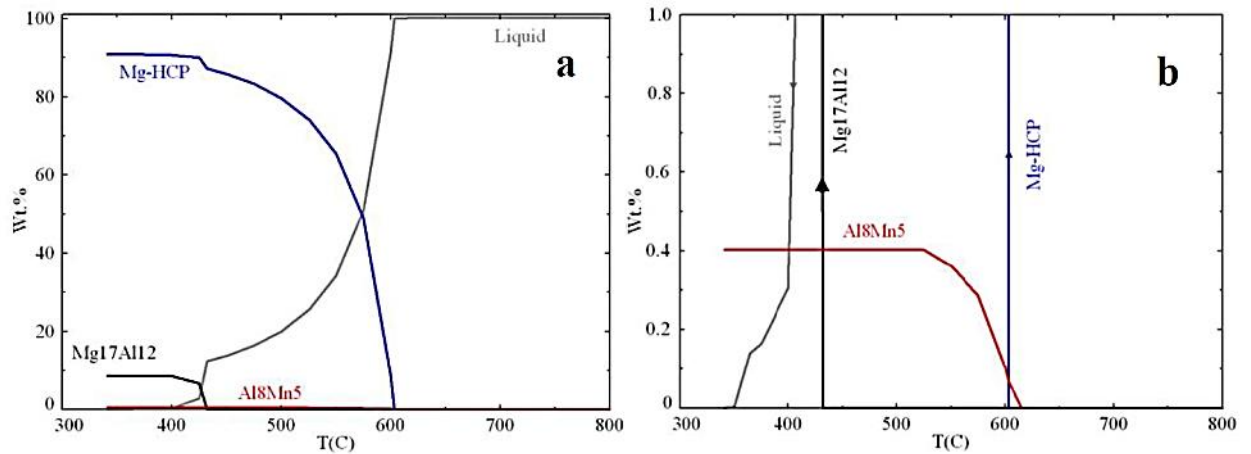


Figure 4-7 Solidification model for AZ80 alloy (Scheil cooling calculations) (a) Overall solidification behavior (b) Formation of  $Al_8Mn_5$

Enhanced columnar to equi-axed transition and grain refinement, by increase in the solute content from AZ31 to AZ80, could be attributed to increase in the constitutional supercooling (CS) ahead of solidification front. As illustrated schematically in Figure 4-9, the extent of CS can be defined by the area limited to the actual thermal gradient and “critical temperature gradient” ( $\frac{dT_L}{dx}$ ) which is proportional to the concentration of the solute in the liquid metal ( $C_0$ ) [112]:

$$\frac{dT_L}{dx} = \frac{mC_0(1-k)v}{kD} \quad (\text{eq.4.2})$$

where  $k$  is the equilibrium segregation coefficient,  $m$  is the liquidus slope,  $v$  is the solidification rate and  $D$  is the diffusivity coefficient in liquid state. Thus, the critical temperature gradient increases as the liquid metal is enriched more in solute content. Assuming that the actual temperature gradient was the same in solidification of the three welds, it is expected that  $CS_{AZ80} > CS_{AZ61} > CS_{AZ31}$ .

The CS-driven nucleation model proposed by Winegard and Chalmers suggested that the increase in supercooling promoted the heterogeneous nucleation rate ( $N_{\text{het}}$ ) on the available substrate particles [113]. In the current study, Al-Mn particles (either pre-existing in the BM or formed during the early stage of solidification) were able to act as heterogeneous nucleation sites. The heterogeneous nucleation was reported to take place in the RSW microstructure by the Al-Mn particles, pre-existing in the BM of magnesium alloys [91]. As the solute content and hence CS increased from AZ31 to AZ80, it is expected that  $N_{\text{het}}(\text{AZ31}) < N_{\text{het}}(\text{AZ61}) < N_{\text{het}}(\text{AZ80})$ .

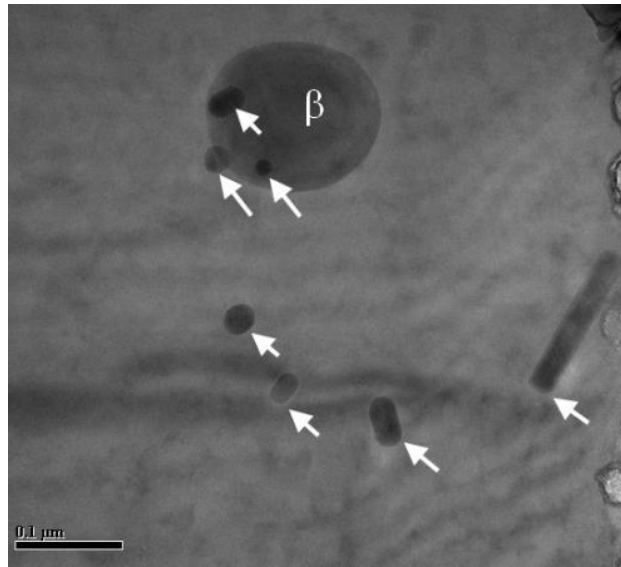


**Figure 4-8** TEM image of the sub-micron Al-Mn and  $Mg_{17}Al_{12}$  particle. The Al-Mn particles are shown by white arrows

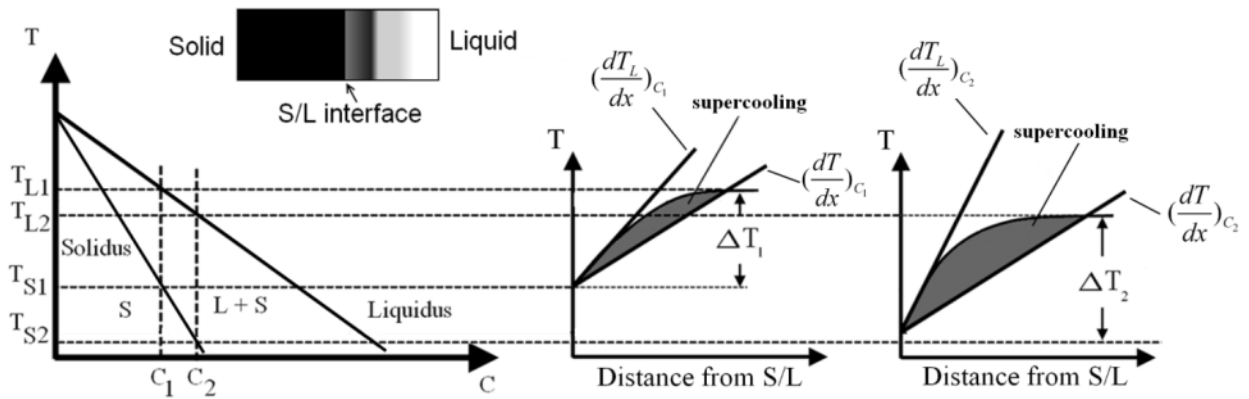


**Figure 4-9** Schematic diagram of supercooling for solidification of imaginary alloys 1, 2 ( $C_2 > C_1$ )

#### 4.3.1.3 Heat Affected Zone

The  $\beta$  intermetallics were frequently observed as worm-like shape at the GBs of heat affected zone (HAZ) in the three welds (Figure 4-10). The mechanisms responsible for the formation of Mg-Al phase in HAZ are explained as follows:

*AZ61 and AZ80:* During the strip casting of the high Al content base alloys (AZ61 and AZ80), the  $\beta$  particles grew in the inter-dendritic regions. Due to subsequent thermo-mechanical treatment, the  $\beta$  particles were partially dissolved in  $\alpha$ -Mg matrix; however a fraction of particles remained un-

dissolved as observed in Figure 4-1 d,f. A high density of the large spherical  $\beta$  particles was detected in the GBs of the final hot rolled structure of AZ80 alloy (Figure 4-1f). During resistance welding, due to very rapid heating of the HAZ, the intermetallic phase lacked the time for dissolution in the matrix by the solid state diffusion. Thus, they remained untransformed above the solvus temperature. Via further heating to the eutectic temperature ( $T_E$ ), the remaining  $\beta$  phase reacted with the surrounding  $\alpha$  matrix and formed liquid eutectic ( $C_E$ ) at GBs.

*AZ31:* It appeared that GB liquation in AZ31 (Figure 4-10b) was not triggered by particle/matrix reaction during HAZ thermal cycle, since few  $\beta$  particles pre-existed in GBs of BM microstructure (Figure 4-1b). It is suggested that the mechanism of GB liquation in AZ31 was different from the one in the high Al magnesium alloys. Huang et al. proposed a mechanism of GB liquation in the HAZ of the BM free of the second phase particles [114]: It was reported that both aluminum and zinc have tendencies to segregate towards the GBs, during magnesium sheet metal production [111]. Lippold et al. proposed that solute segregation occurs during HAZ thermal cycle by solid state diffusion which leads to further solute enrichment of GBs [115]. The segregated atoms remained dissolved within the matrix, lowering down the melting temperature. Due to thermal cycle of HAZ, melting occurred preferentially in the GBs of the BM microstructure, while the intra-granular regions remained unmelted. Melting and subsequent non-equilibrium solidification led to the formation of divorced eutectic phase. Figure 4-10 b,d,f also show presence of  $\beta$  phase as globular particles inside the grains. Some of these particles were separated by the polishing job as their location was left as pores. Due to inhomogeneity of the composition inside the grains, local melting inside the grain occurred which led to formation of these spherical particles. Close observation revealed regions, essentially adjacent to the GB particles, free of the spherical particles. These particle free zones (PFZs) are highlighted in Figure 4-10 b,d,f. During solidification of the solute rich GB melt, first  $\alpha$  phase were formed depleted of the solute pushing the solute atoms to the remaining liquid [116]. Thus, the  $\beta$  particles were unlikely to form in this solute-free region i.e. PFZ.

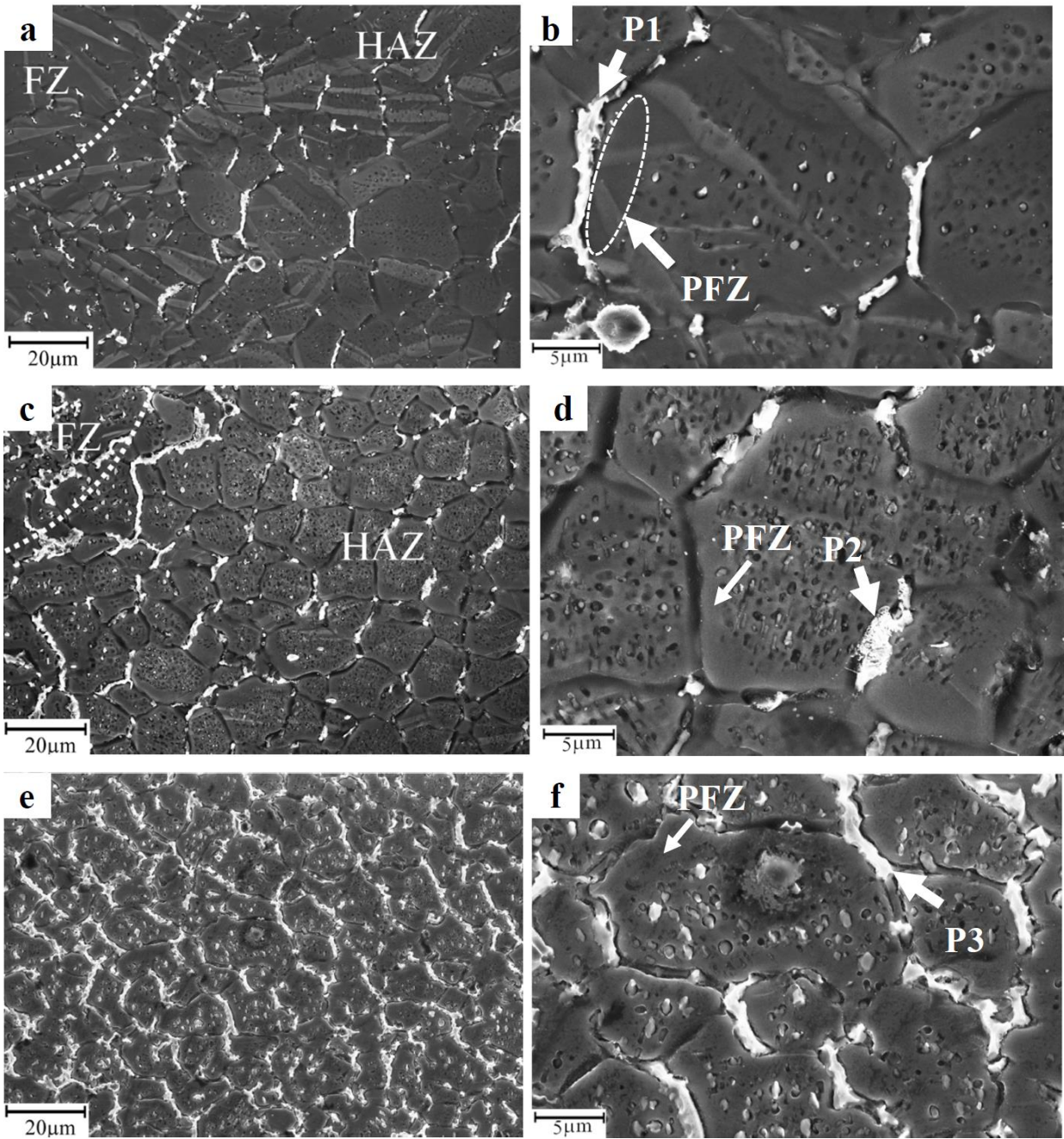


**Figure 4-10** SEM micrograph taken from microstructures of the HAZ in AZ31 (a,b); AZ61 (c,d); AZ80 (e,f), the EDS analysis results for highlighted particles are shown in Table 4-3

**Table 4-3 EDS analysis results for the highlighted particles shown in Figure 4-10**

Element	P1	P2	P3
Mg (at.%)	70.9	70.7	67.9
Al (at.%)	27.3	25.6	28.8
Zn (at.%)	1.8	3.8	3.4

#### 4.3.1.4 Crystallographic Orientation Relationship in $\alpha$ -Mg/Eutectic-Mg<sub>17</sub>Al<sub>12</sub>

The eutectic growth orientation relationships were studied by TEM analysis for the AZ80 weld in FZ and HAZ. The TEM samples from FZ were prepared by jet-polishing/ion milling. Figure 4-11 shows a TEM image of both inter-granular and intra-granular particles in the FZ which were identified as  $\beta$ -Mg<sub>17</sub>Al<sub>12</sub> with the body centered cubic symmetry and lattice parameter of  $a=10.58 \text{ \AA}$  by the corresponding selected area electron diffraction (SAED) pattern. The analysis of the inter-granular phase using EDS indicated both Al and Zn in the chemical composition which is consistent with the previous SEM observations. Figure 4-11b shows the high resolution (HR) image corresponding to the area bounded by a white circle observed in Figure 4-11a i.e.  $\alpha/\beta$  interface. The incident beam was along the  $[1 \bar{1} 1]_{\beta}$ . From the Figure 4-11b, planar OR was found as:

$$(10\bar{1}1)_{\alpha} \parallel (\bar{1}01)_{\beta}$$

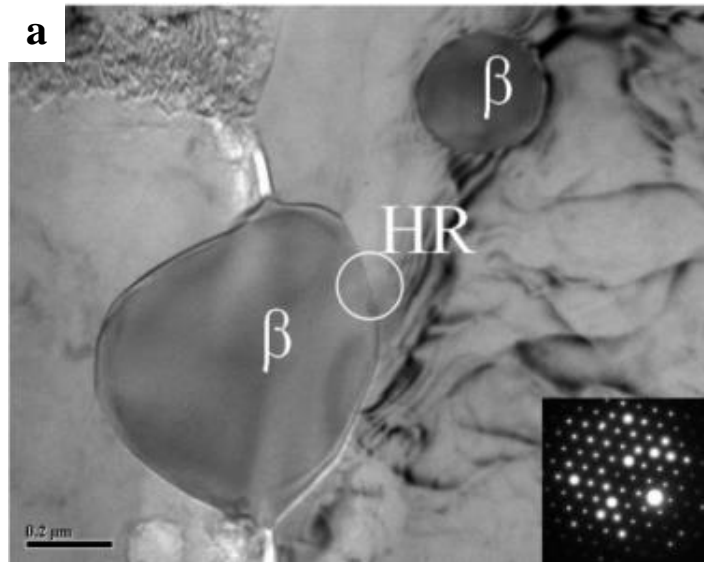


**Figure 4-11 (a) TEM micro-graphs from the inter-granular and intra-granular  $\beta$  particles in FZ of AZ80, (b) HRTEM image for the area marked by white circle in (a), the incident beam was along  $[1 \bar{1} 1]_{\beta}$  direction**

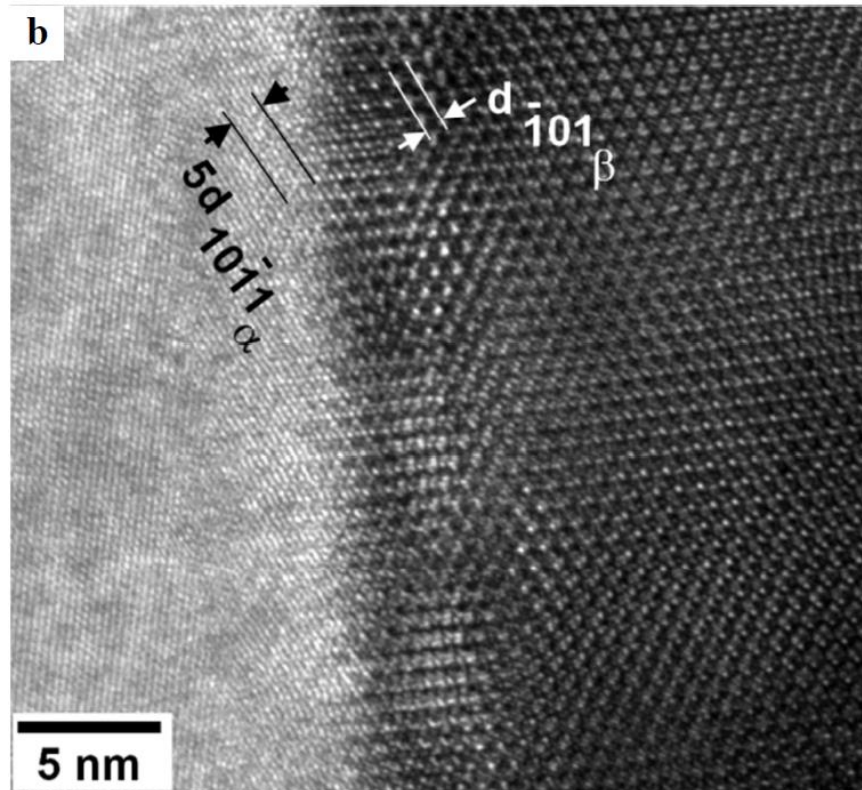


**Figure 4-11 continued**

Figure 4-12 shows another GB particle and its HR image at the interface. the planar relationship for this interface can be defined as:

$$(0\ 0\ 0\ 2)_\alpha \parallel (0\ 1\ 1)_\beta$$

The TEM samples from HAZ were prepared by FIB process. Figure 4-13 shows the location of the FIB extracted sample. Figure 4-14 demonstrates a typical intra-granular  $\beta$ . Figure 4-14 b,c,d show the SAED patterns taken from  $\alpha$ ,  $\beta$  and  $\alpha/\beta$  interface respectively, with the electron beam parallel to  $[5\ \bar{1}\ \bar{4}\ 3]_\alpha$  and  $[\bar{1}\ 1\ 1]_\beta$ . From schematic diagram of Figure 4-14 e it is clear that the diffraction spot of  $(3\ 3\ 0)$  of  $\beta$  was superimposed with that of  $(0\ \bar{1}\ \bar{1}\ 1)$  of  $\alpha$ . The crystallographic planar relationship between the  $\beta$  particle and  $\alpha$  matrix in this site (zone 3 in Figure 4-14a) was determined to be:  $(0\ \bar{1}\ \bar{1}\ 1)_\alpha \parallel (3\ 3\ 0)_\beta$ .



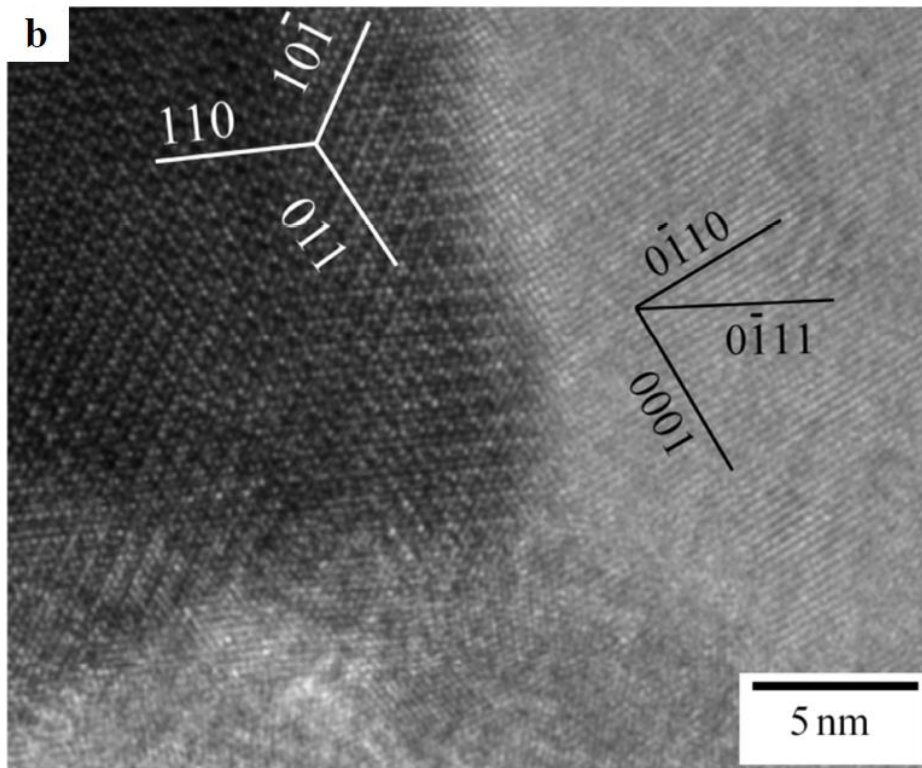
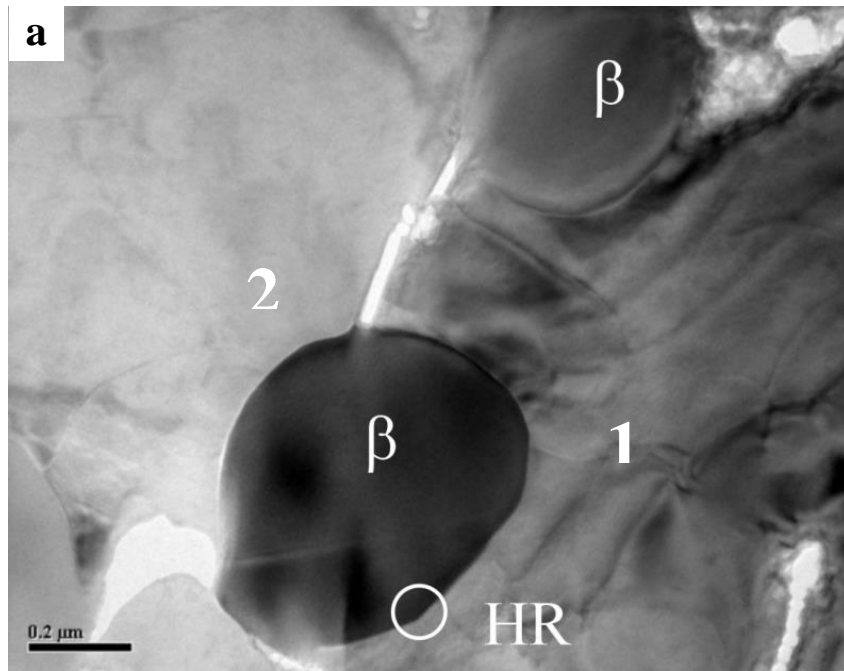
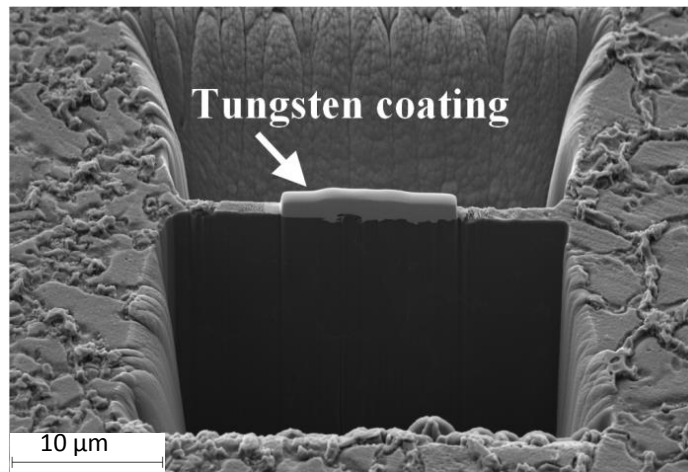


Figure 4-12 TEM micrographs from  $\beta$  particle in the FZ of AZ80 (a) TEM image of inter-granular particle; (b) HRTEM image for the area marked by a white circle in (a) the incident beam was along the  $[2\bar{1}\bar{1}0]_{\alpha}/[1\bar{1}1]_{\beta}$  directions

A divorced eutectic phase essentially grows from the remaining liquid in the inter-dendritic regions at the late stage of the solidification. The growth of eutectic phase is done in such a way that certain OR will be established with minimum interfacial energy [117]. It was proposed by Shiflet and van der Merwe that the minimum interfacial energy is obtained when the close packed or nearly close packed atomic rows match at the interface [118]. Moreover, a set of close packed or nearly close packed planes from the two phases should be arranged in such a way to achieve the edge to edge matching [119]. It has been found that the  $\{3\ 3\ 0\}$  (41.9% close-packed) and  $\{4\ 1\ 1\}$  (44.6% close-packed) are both the nearly close-packed planar types in  $\beta$  lattice with the same d spacing of 2.48 Å [120], [121]. Figure 4-15a shows the atom configuration of the  $\beta$  crystal on the  $(3\ 3\ 0)$  plane. The unit cell was reconstructed based on the position of the Mg and Al atoms as shown in Table 4-4 [45], [122]. In the hcp structure, the most close-packed planes are  $\{0\ 0\ 0\ 2\}$  (100% close-packed) and  $\{\bar{1}\ 0\ 1\ 1\}$  (81% close-packed). Consequently, the determined planar relationships i.e.  $\{0\ 0\ 0\ 2\} \parallel \{3\ 3\ 0\}$  and  $\{1\ 0\ \bar{1}\ 1\} \parallel \{3\ 3\ 0\}$  are expected in order to minimize the interfacial energy. The d-value mismatch calculations also predicted a fairly desired planar matching ( $\delta=4.8\%$  for  $\{0\ 0\ 0\ 2\} \parallel \{3\ 3\ 0\}$  and  $\delta=1.3\%$  for  $\{1\ 0\ \bar{1}\ 1\} \parallel \{3\ 3\ 0\}$ ). The crystallographic OR was determined for the HR-TEM image in Figure 4-12 as follows:

$$[2\ \bar{1}\ \bar{1}\ 0]_{\alpha} // [1\ \bar{1}\ 1]_{\beta}, (0\ 0\ 0\ 2)_{\alpha} // (0\ 3\ 3)_{\beta} \quad \text{OR.1}$$



**Figure 4-13** Area in which the FIB specimen was extracted

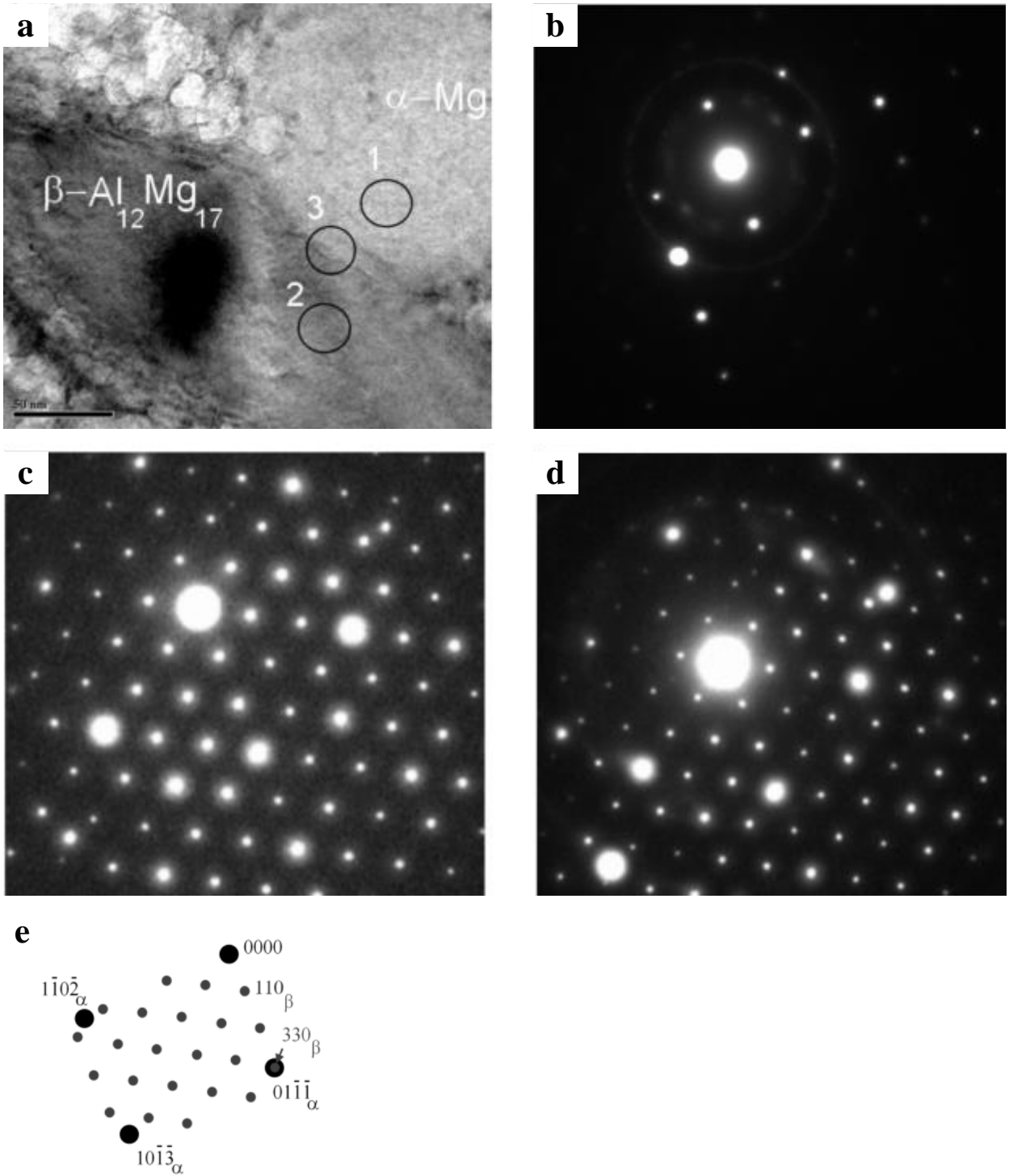


Figure 4-14 (a) TEM image from  $\beta$  particle in the HAZ of AZ80; (b) SAED of Mg matrix in area 1 (Incident beam //  $[5 \bar{1} \bar{4} 3]$ ); (c) SAED of  $\beta$  particle in area 2 (Incident beam //  $[\bar{1} 1 1]$ ); (d) SAED of  $\alpha/\beta$  interface in area 3 and (e) its schematic representation in  $[5 \bar{1} \bar{4} 3]_{\alpha}/[\bar{1} 1 1]_{\beta}$  directions

**Table 4-4 Atom position in  $\beta$  unit cell (the values were taken from Ref. [45])**

Atom	Multiplicity	Site Symmetry	Coordinates: (0,0,0)+ (0.5,0.5,0.5)+		
			x	y	z
Mg	2	$\bar{4}3m$	0	0	0
Mg	8	.m	0.324	0.324	0.324
Mg	24	..m	0.3582	0.3582	0.0393
Al	24	..m	0.0954	0.0954	0.2725

The interatomic misfit along the matching direction for OR.1 was calculated to be 5.3%. Thus high atomic matching is expected to exist at the interface with low strain energy. This has been demonstrated in Figure 4-15b. OR.1 is close to the OR defined by Potter [123]. Such relationship was previously reported for precipitation hardened Mg-Al alloys[124]. It was argued that such atomic row matching satisfied the requirements for the edge to edge matching model in order to obtain a low interfacial energy (i.e interatomic misfit  $\leq 10\%$ ).

In the case of the OR corresponding to Figure 4-14, high interatomic mismatch exists between the two parallel directions along the diffraction pattern zone axis i.e.  $\langle \bar{1} 5 \bar{4} \bar{3} \rangle$  (9.97 Å) of Mg and  $\langle \bar{1} 1 1 \rangle$  of the  $\beta$  (3.05 Å). The  $\langle \bar{1} 5 \bar{4} \bar{3} \rangle$  are not considered as close packed directions in Mg lattice. Consequently another direction pair matching should exist between the two phases. Figure 4-15c shows the atomic arrangement of  $(0 \bar{1} \bar{1} 1)_\alpha$  and  $(3 3 0)_\beta$ . Other than the parallelism of  $[\bar{1} 5 \bar{4} \bar{3}]_\alpha$  and  $[\bar{1} 1 1]_\beta$ , very small misalignment ( $1.2^\circ$ ) exists between the  $[2 \bar{1} \bar{1} 0]_\alpha$  and  $[1 \bar{1} 1]_\beta$ . The  $[1 \bar{1} 1]$  direction is considered as a nearly close packed atomic row in the  $\beta$  lattice. Thus, the following OR can be proposed for this particle:

$$[2 \bar{1} \bar{1} 0]_\alpha \parallel [1 \bar{1} 0]_\beta, (0 \bar{1} \bar{1} 1)_\alpha \parallel (3 3 0)_\beta \quad \text{OR. 2}$$

The interatomic misfit along the matching directions was calculated to be 54.8%. Based on the edge-to-edge matching model [119], this misfit value is significantly large. Therefore, the interfacial boundary between the  $\beta$  particle and  $\alpha$  matrix is expected to be incoherent.

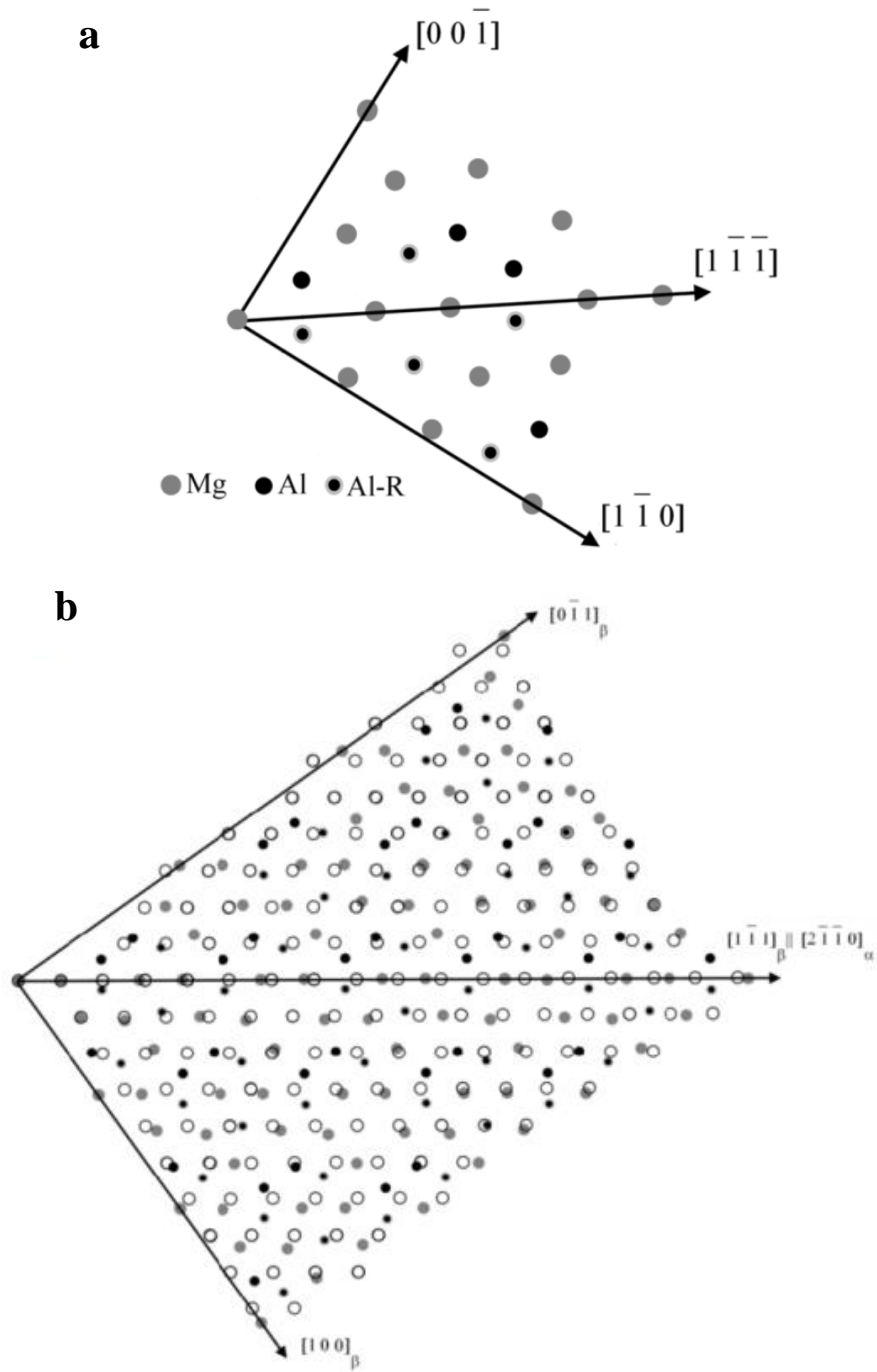
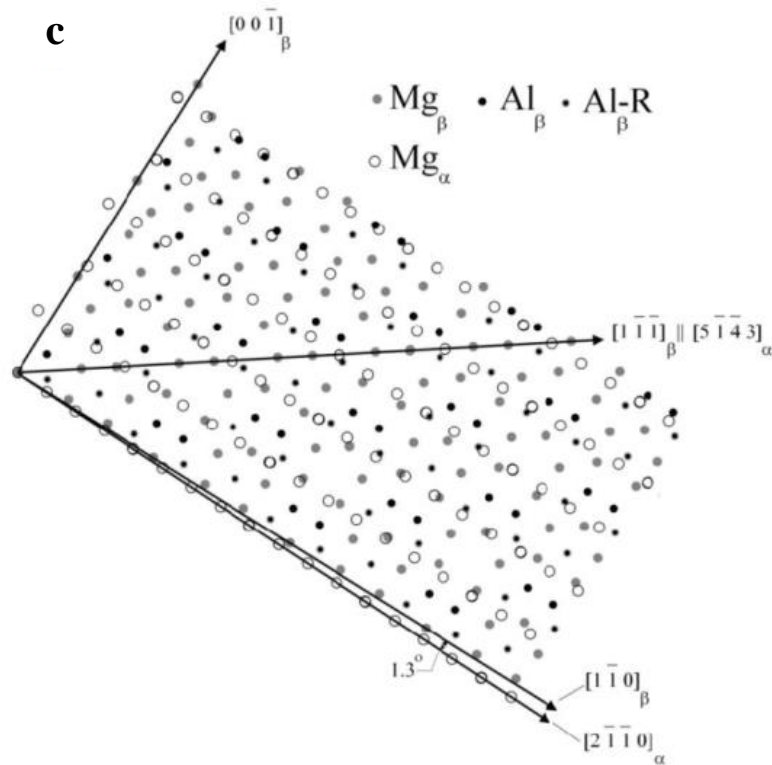


Figure 4-15 (a) Atomic arrangement on  $(3\ 3\ 0)$  plane of  $\beta$  unit cell. The  $\{3\ 3\ 0\}$  planes are not flat, but “corrugated”, i.e. some of the Al atoms (as indicated by Al\_R) have the centers which are not exactly located on the plane. The maximum displacement of the centers of such atoms normal to plane normal is  $1.32\ \text{\AA}$ . Atomic arrangement based on (b) OR.1 and (c) OR.2



**Figure 4-15 continued**

#### 4.3.1.5 Effects of Post-Weld Heat Treatment on the Weld Microstructure

The welded samples were studied in the post-weld heat treated (PWHT) condition. The  $\beta$  intermetallics were partially dissolved into the matrix in FZ and HAZ after PWHT as observed in Figure 4-16. The continuous networks of  $\beta$  particles at the GBs of the HAZ were disrupted and changed to isolated particles (see Figure 4-16). Few GB particles were still remained after PWHT. This indicated that the time for the complete dissolution of intermetallics was insufficient.

It is interesting to note that significant grain growth occurred in HAZ of AZ61 and AZ80 in such a short time of heat treatment (Figure 4-16 d and f). Figure 4-17 compares the grain size in BM, as-welded HAZ and heat treated HAZ microstructures. The HAZ was subjected to grain growth for the three alloys. Grain growth was more pronounced in HAZ of AZ31 ( $\times 2.3$ ) than in the HAZ of AZ61 ( $\times 1.2$ ) and AZ80 ( $\times 1.5$ ). Such an observation can be explained as follows:

During welding process, grain growth occurred in the HAZ at temperatures above the effective grain coarsening temperature (i.e. the single  $\alpha$  phase region in the phase diagram); however, GB liquation retarded further grain growth. The solute-rich liquid film penetrated to the GBs and pinned them due

to wetting action [125], [126]. Since the liquid film had almost the same composition of the adjacent solid, the S-L interfacial energy was low [127] and the liquid film would essentially wet the GBs. No further grain growth occurred until the microstructure cooled down below the solidus of solute-rich liquid. Consequently, the thermal cycle of the HAZ in AZ61 and AZ80 led to grain growth arrest due to significant liquation. Following the dissolution of the GBs in the HAZ of AZ61 and AZ80 during PWHT, further grain growth occurred at large scale as indicated in Fig. 10. The unpinning of the GBs by dissolution of the intermetallics has been reported to lead to abnormal grain growth in the HAZ [128]. Since liquation occurred in HAZ of AZ31 in lower scale, the pinning of the GBs by the wetting action was less than what occurred in HAZ of AZ61 and AZ80. Thus, grain growth occurred near the saturation limit in the HAZ of AZ31 during the welding cycle and no further growth (at large scale) occurred during PWHT.

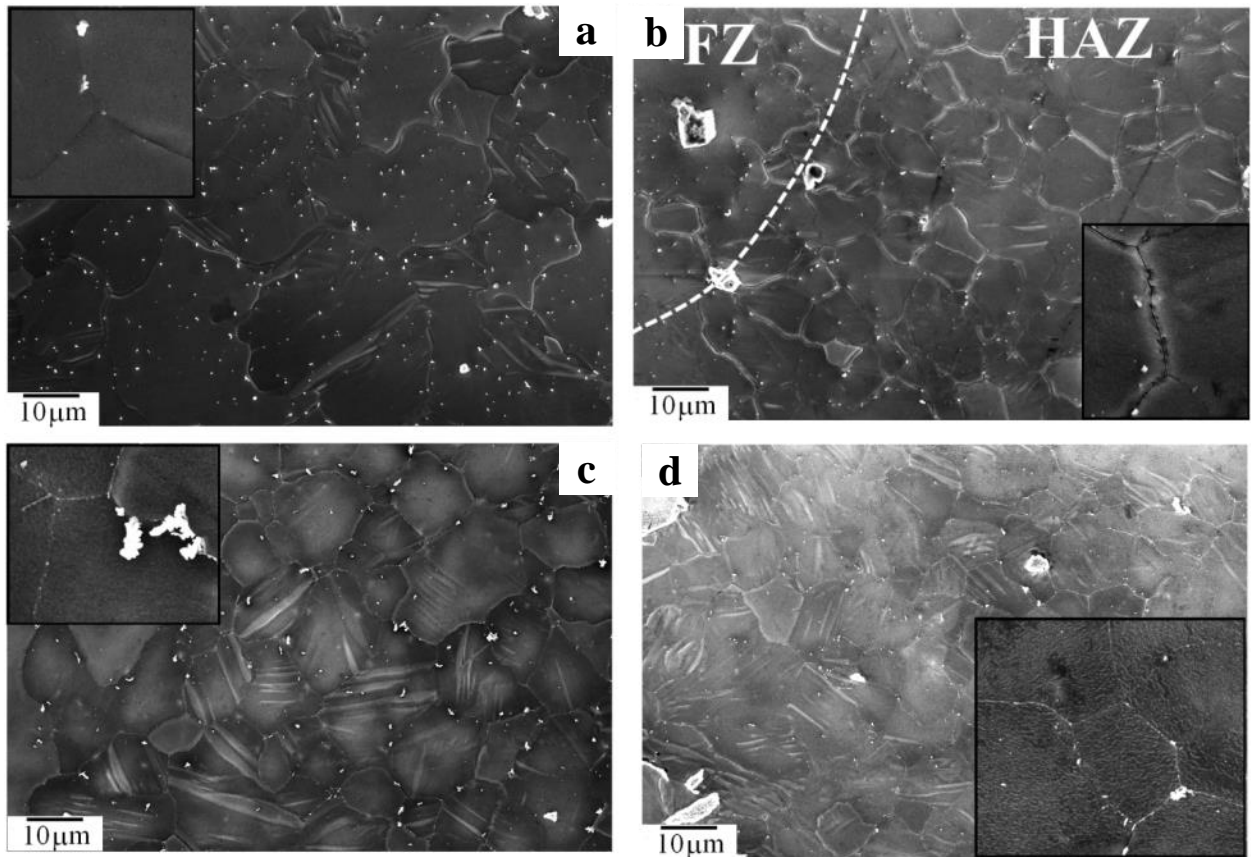


**Figure 4-16 SEM micrographs taken from microstructures of the post weld heat-treated FZ and HAZ for AZ31 (a,b), AZ61 (c,d) and AZ80 (e,f)**

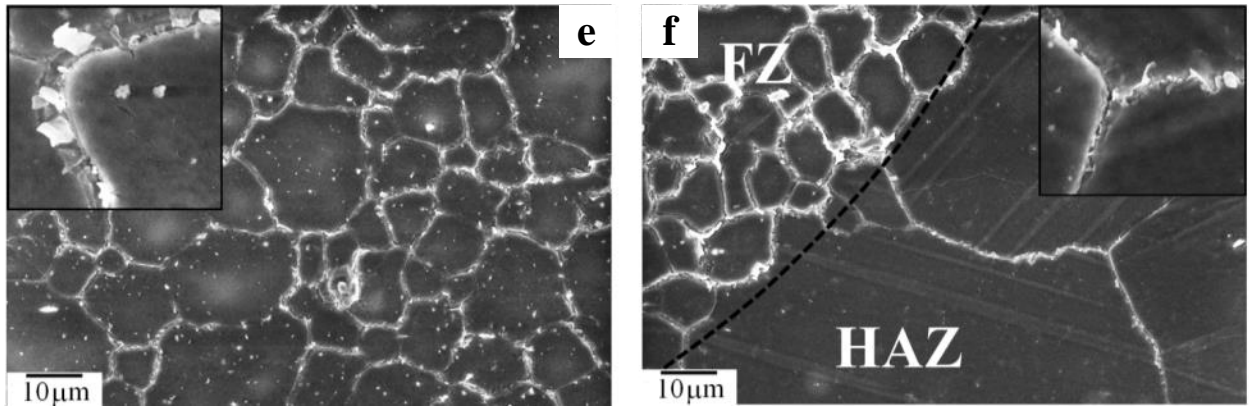


Figure 4-16 continued

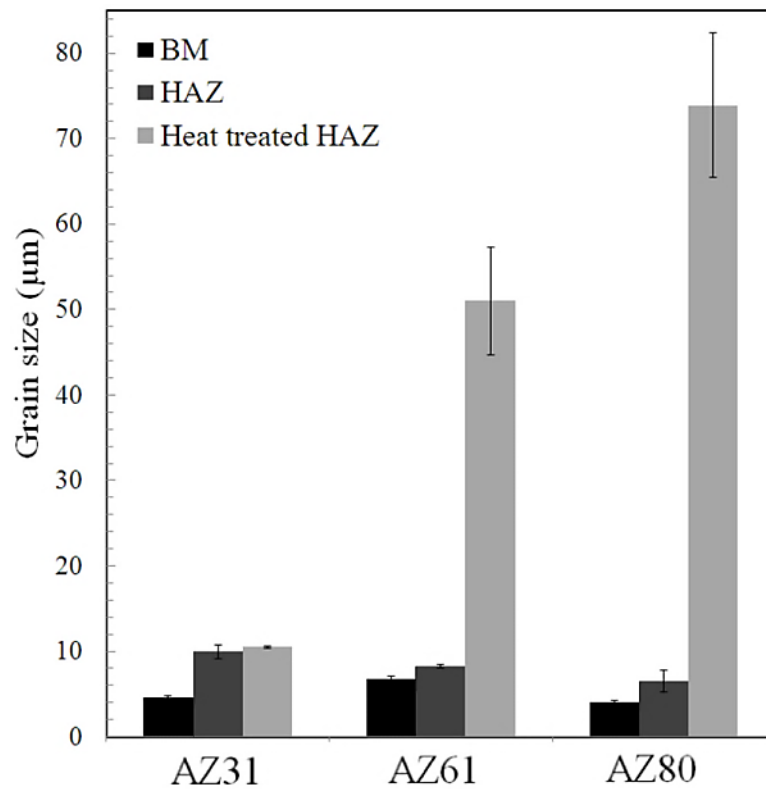


Figure 4-17 Grain size in BM, HAZ and heat-treated HAZ for AZ31, AZ61 and AZ80

X-ray diffraction (XRD) spectra in Figure 4-18 further confirmed the effect of PWHT on dissolution of  $\beta$ . The XRD results showed the presence of  $\beta$  IMCs in both FZ and HAZ. After PWHT, the  $\beta$  peak intensity of both FZ and HAZ almost disappeared.



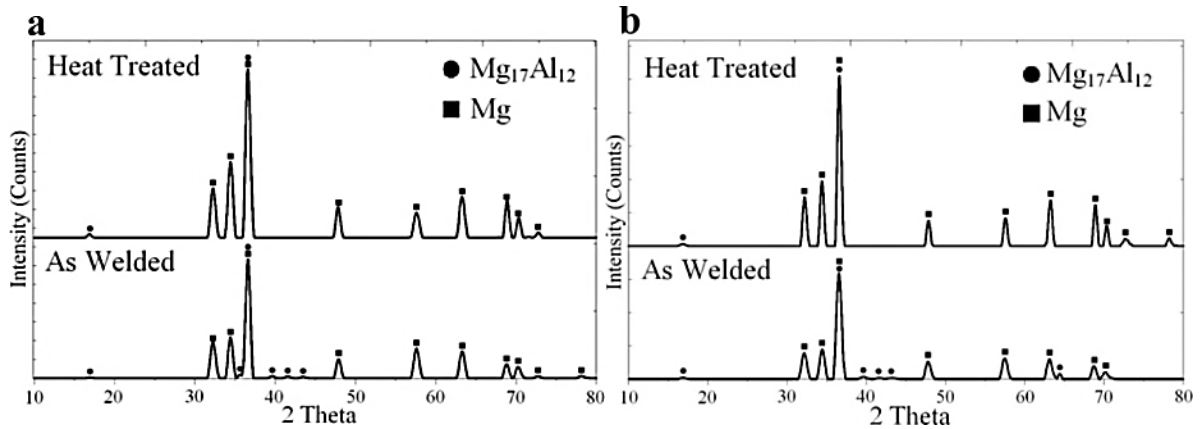


Figure 4-18 XRD spectra from a) FZ b) HAZ of AZ80

### 4.3.2 Mechanical Properties and Fracture Analysis

Figure 4-19a shows the Vickers micro-hardness values for the RSW of AZ31, AZ61 and AZ80 in the as-welded and post-weld heat treated conditions. For each alloy, the hardness values of the FZ and the HAZ are lower compared to that of the associated BM. The decrease in hardness of HAZ can be associated with the static recrystallization and subsequent grain growth.

Post weld heat treatment appeared to decrease the hardness of HAZ and FZ for AZ61 and AZ80. The values measured by the micro-hardness indentation did not reflect the hardness of the  $\alpha$ -Mg. Since  $\beta$  intermetallics existed in both grains and grain boundaries, the hardness values (calculated from the size of the indentations) are the overall hardness of soft  $\alpha$  and hard  $\beta$ . By the application of heat treatment and hence significant removal of the intermetallics, the hardness contribution of  $\beta$  phase decreases. Consequently, the decrease in the hardness of FZ and HAZ after the heat treatment does not essentially indicate the decrease in the hardness of the Mg matrix. On the other hand, an increase in the hardness values of the FZ was detected after heat treatment for the AZ31. Compared to the weld microstructure of AZ61 and AZ80, fewer  $\beta$  intermetallics were formed in FZ and HAZ of AZ31. Consequently the contribution of the intermetallics in micro-hardness measurement was insignificant and the hardness of  $\alpha$  matrix became more pronounced in measurements.

Figure 4-19b compares the load-to-failure and elongation-to-failure of the spot welded Mg alloys in both as-welded and heat-treated conditions. The tensile shear responses of the welds (5 specimens for each weld/condition) are plotted in Appendix B. Although the grip displacement does not indicate the actual specimen elongation, it can be used as a qualitative comparison of the nugget ductility in different welds/conditions. It should be noted that more accurate measurements of nugget elongation

(by accommodation of an extensometer) was performed in the works presented in chapters 5 and 6 for AZ61, AZ80 and ZEK100 spot welds.

It is interesting that the load-to-failure for the spot welds (in as-welded condition) increased as the strength of the BM decreased (Table 3-1). The load-to-failure and elongation-to-failure of AZ80 weld was the lowest among the three weld, but improved significantly by the application of PWHT. The improvement in load-to-failure of the weld by PWHT was calculated to be +2.3%, +11.4% and +43.6% for AZ31, AZ61 and AZ80, respectively. The fracture mode of the AZ61 and AZ80 welds changed from nugget pullout (Figure 4-20b) to through-thickness (Figure 4-20c) after PWHT, while post weld heat treatment had no obvious effect on the failure mode of AZ31 which was interfacial failure (Figure 4-20a). In summary, PWHT favorably affected mechanical properties of RSW of AZ61 and AZ80; however, such effects were not substantial for RSW of AZ31.

In order to further study the effects of PWHT on failure mode and fracture characteristics, tensile shear test was stopped at the peak load (Figure 3-1b) and the cross section of tested samples were metallographically investigated. Figure 4-21 shows the typical cross-sectional crack path for AZ61 and AZ80 welds in as-welded condition. Cracks always started from the notch where the two BM surfaces were joined by the nugget. The crack initiated and propagated along the fusion boundary but mainly located in the HAZ. As indicated by the black and white arrows in Figure 4-22, secondary micro-cracks close to the primary crack also existed. The black arrows point to micro-cracks which occurred inside or traversed through the  $\beta$  particles. The white arrows point to micro-cracks at the  $\beta/\alpha$  interfaces. Thus, the  $\beta$  intermetallics in the HAZ can be considered preferred crack propagation paths during TS loading of RSW joints made with high Al content Mg alloys.

In post-weld heat treated AZ61 and AZ80 coupons, crack propagated on a different path as illustrated in Figure 4-23. Cracks occasionally initiated away from the edge of nugget (as observed typically in Figure 4-23b). After initiation, the crack propagated inside the HAZ and far away from the fusion boundary. The  $\beta$  particles were not observed along the crack pathway of the post-weld heat treated samples as illustrated typically in Figure 4-24. High twinning activity was detected near the crack edges, suggesting that plastic deformation took place at the vicinity of notch before crack initiation.

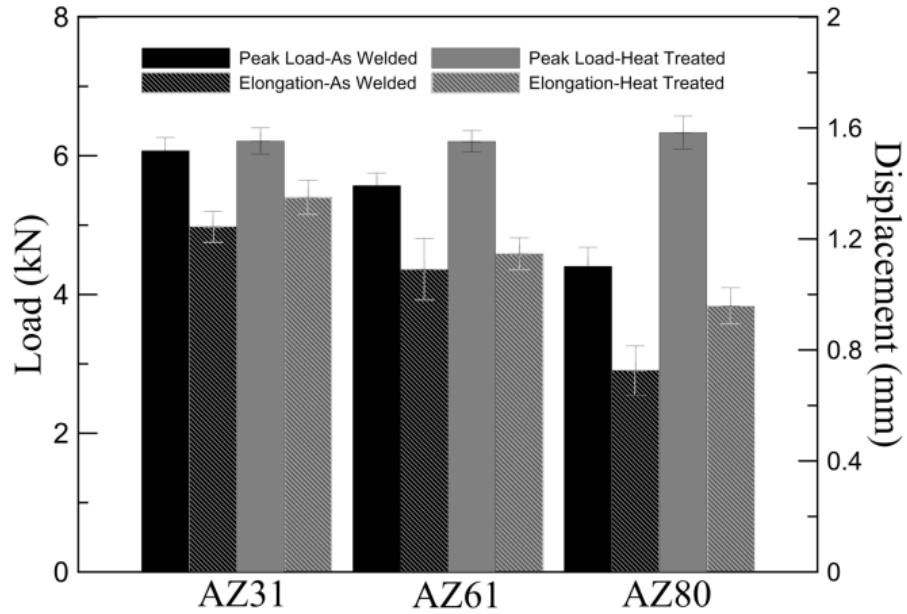
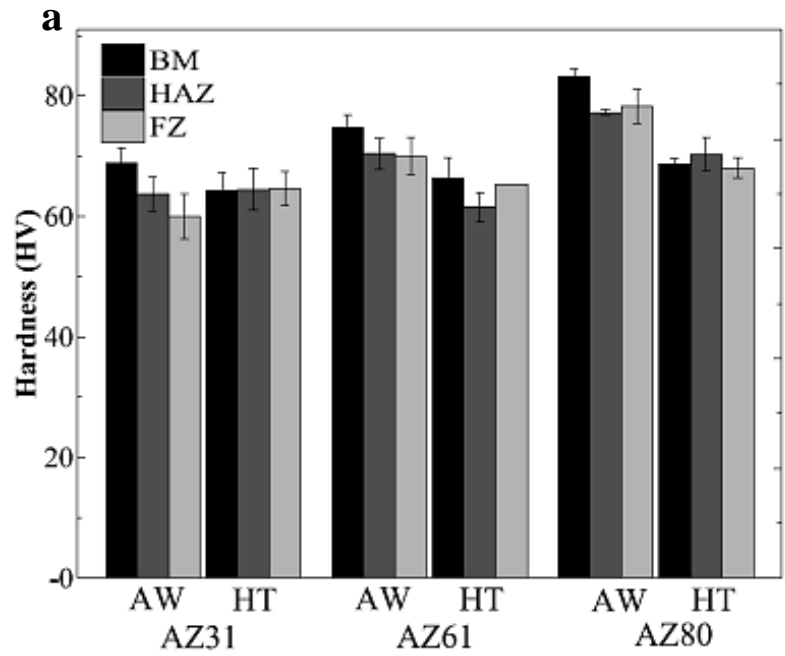


Figure 4-19 (a) Micro-hardness values of the BM, HAZ and FZ of RSW in as-welded and heat-treated conditions (b) Load-to-failure and displacement at failure load for the spot welded specimens (5 specimens for each joint/condition) in as-welded and heat treated conditions

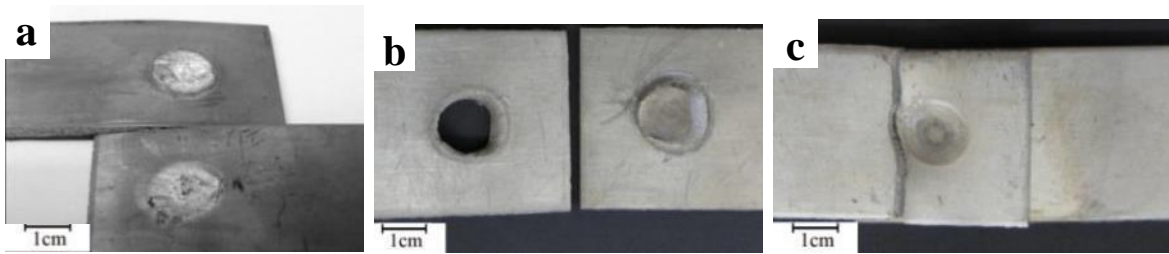


Figure 4-20 Illustration of fracture modes: (a) Interfacial (b) Nugget pull-out (c) Through-thickness

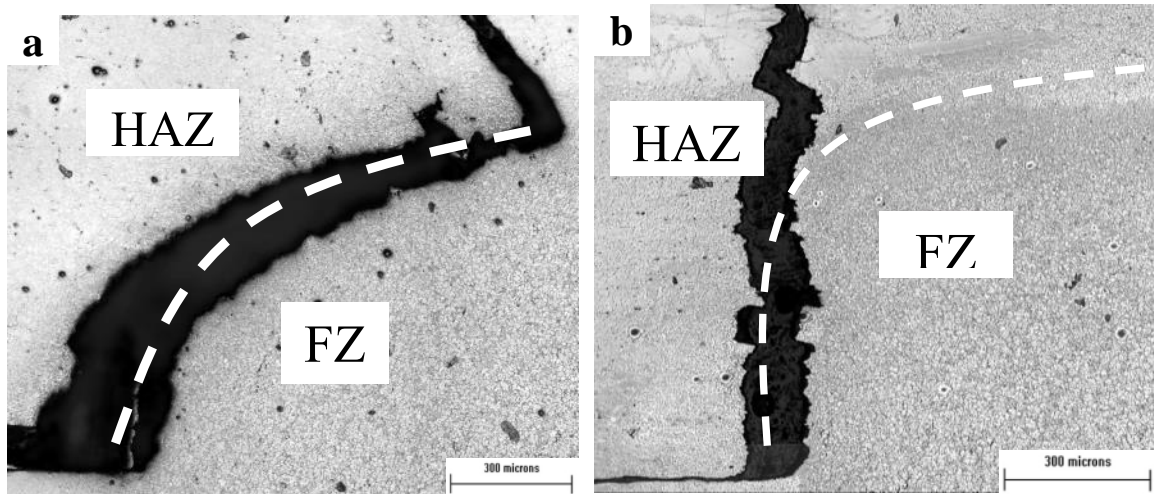


Figure 4-21 Typical crack pathway for RSW in the as-welded condition (a) AZ61; (b) AZ80

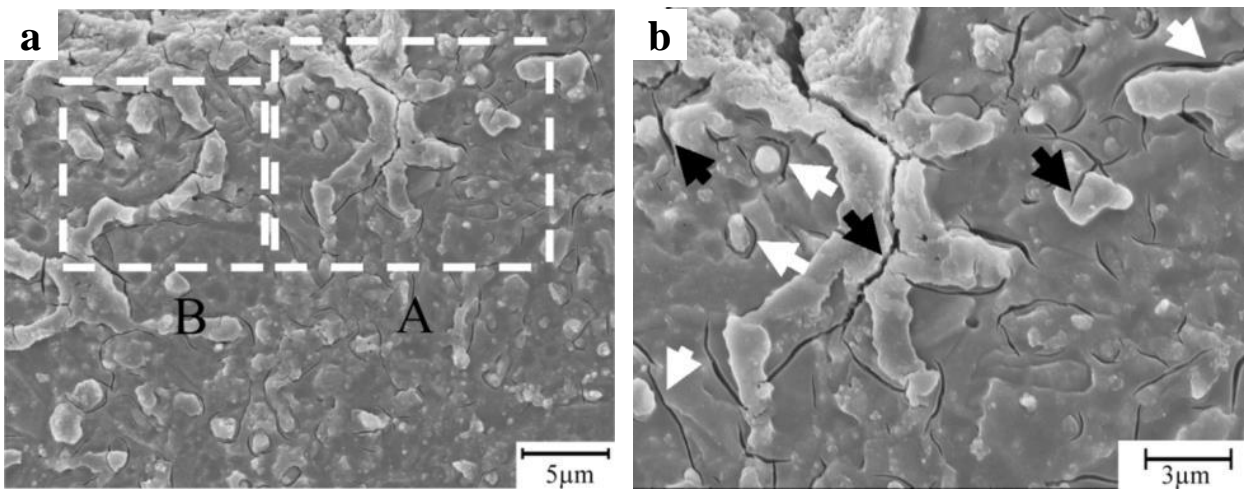


Figure 4-22 (a) Microstructure near the primary crack in the AZ80 spot weld in as-welded condition (b) Area A at higher magnification (c) Area B at higher magnification.

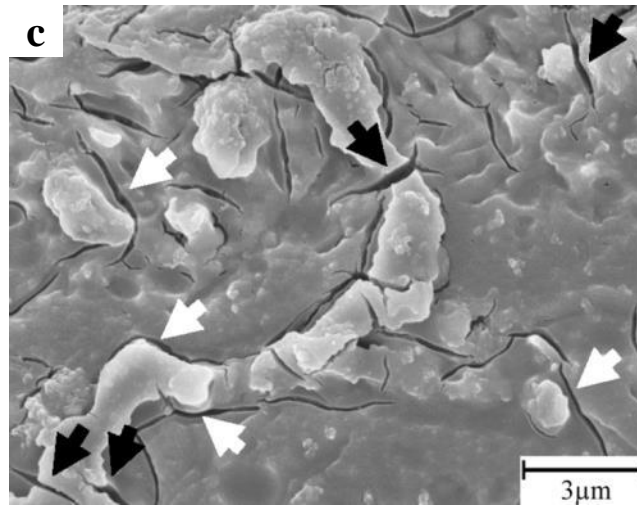


Figure 4-22 continued

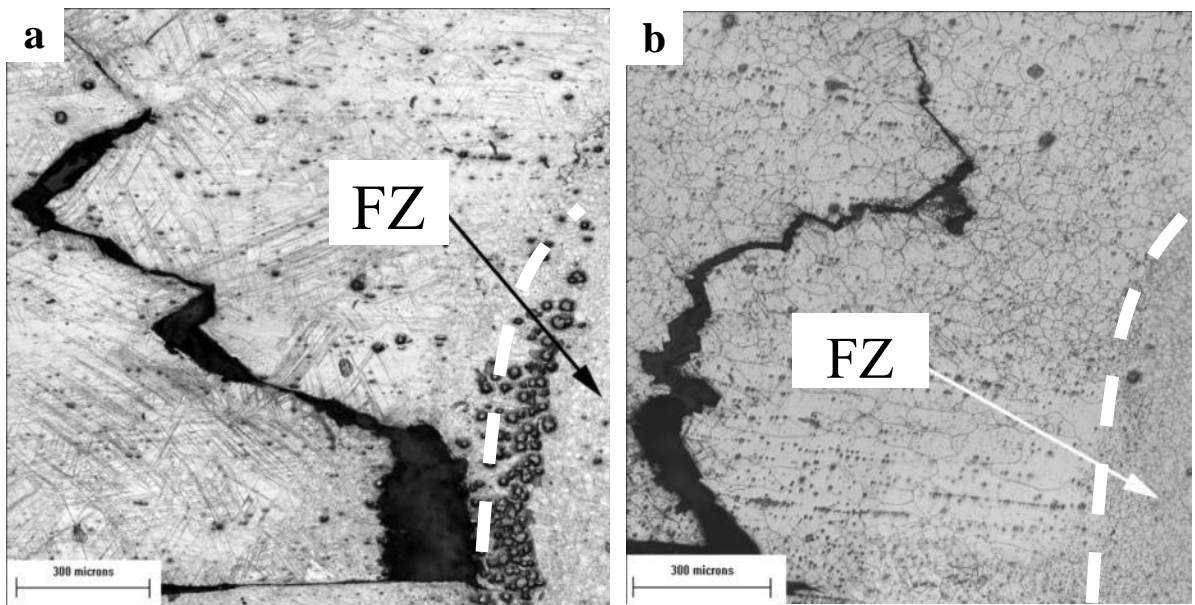
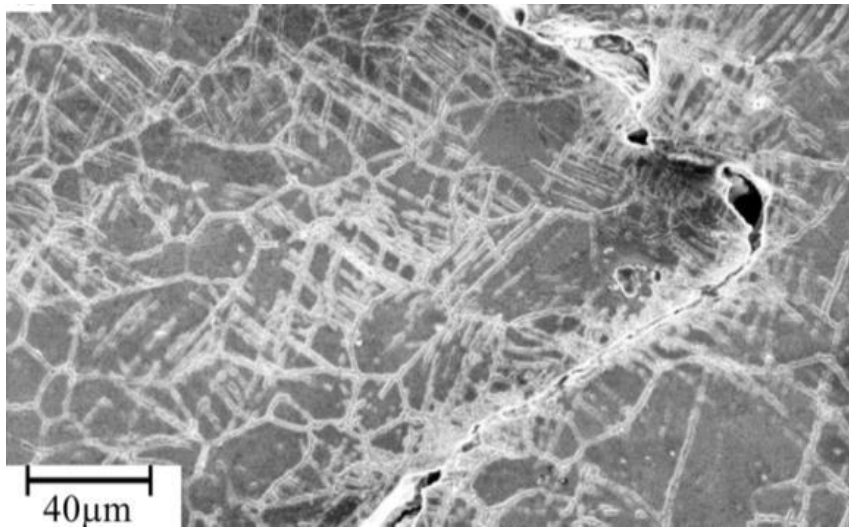


Figure 4-23 Typical crack propagation path of the RSW in the heat-treated condition (a) AZ61; (b) AZ80



**Figure 4-24 Microstructure near the crack for the AZ80 RSW in the heat-treated condition**

Figure 4-25 shows the fracture surface of an AZ80 TS specimen in the as-welded condition. Based on the fracture morphology, the fracture surface can be divided into three sections as illustrated schematically in Figure 4-25a. Figure 4-25 b and c are the low magnification SEM images of these three sections while Figure 4-25 d and e are high magnification images of section 1 and 2, respectively.

Section 1 was located at the FZ/HAZ interface and appeared to have a dendritic structure (Figure 4-25d), which indicates that very weak joining occurred at the faying surface close to the notch of the nugget. Located in HAZ, Section 2 appeared to exhibit cleavage-like steps as shown in low magnification in Figure 4-25. Careful examination of the fracture surface in Section 2 revealed a high density of micro-voids (Figure 4-25e). The EDS analysis, from the fracture surface of Section 2, indicated presence of  $\beta$  particles near the micro-voids (P2, P3, P5 in Table 4-5). Finally, section 3 demonstrated a shear fracture through BM due to over loading.

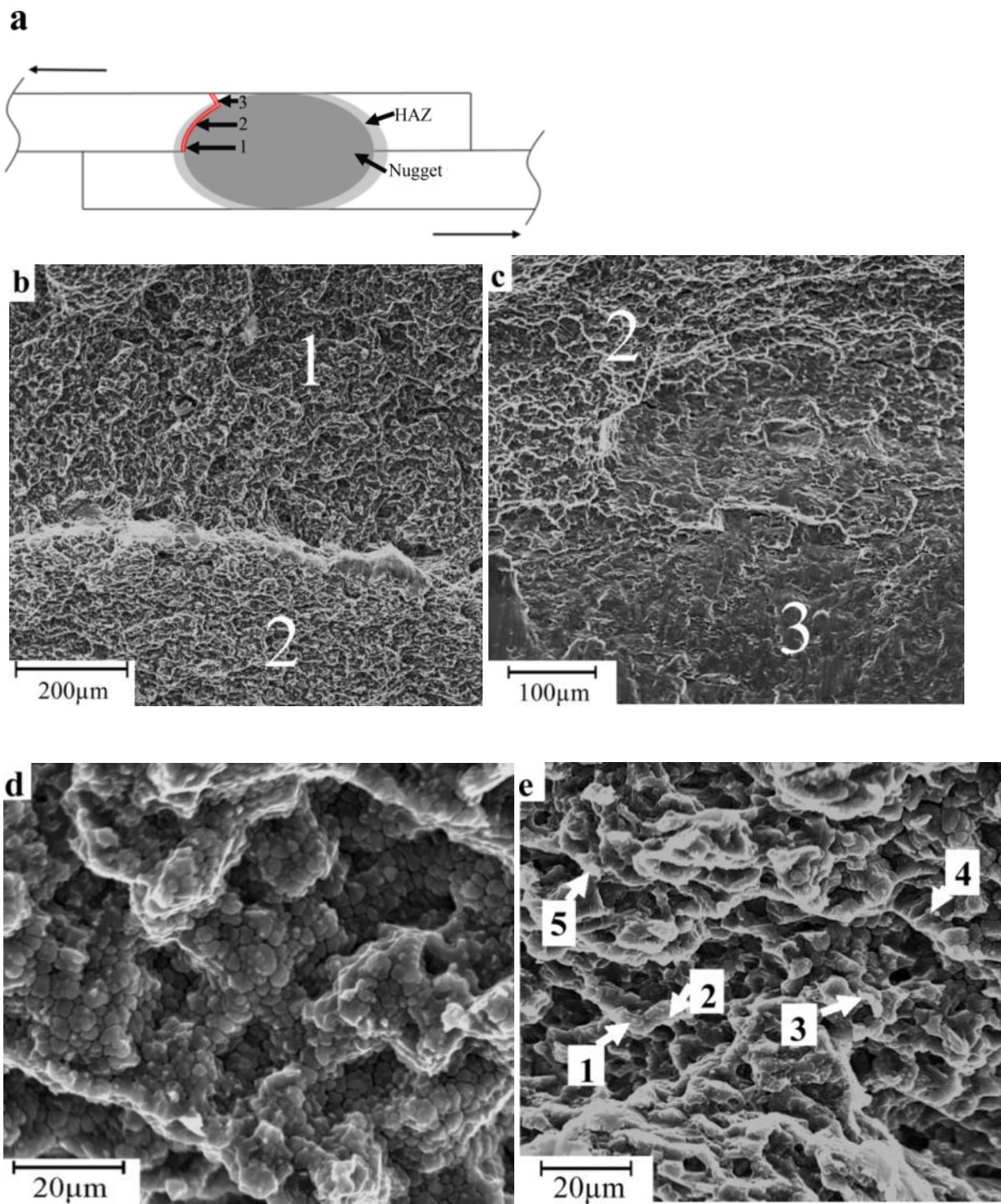
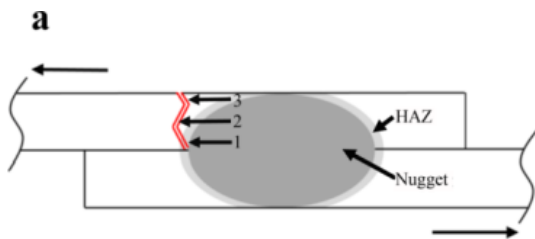


Figure 4-25 Fracture surface of AZ80 RSW in as-welded condition: (a) Scheme of the fracture location showing three sections; (b) Fracture surface in section 1 and 2; (c) Fracture surface in section 2 and 3; (d) Magnified image of fracture surface in section 1; (e) Magnified image of fracture surface in section 2

**Table 4-5 EDS analysis results for the particles shown in Figure 4-25e**

Particles	1	2	3	4	5
Mg (at.%)	84.6	83.5	82.5	81.5	77.6
Al (at.%)	15.4	16.5	17.5	18.5	22.4

Figure 4-26 illustrates the fracture surface of AZ80 RSW in PWHT condition. The fracture morphologies were different from those of the as-welded sample. The fracture surface of the post-weld heat treated sample could be divided into 3 sections as shown in Figure 4-26b and their locations are schematically illustrated in Figure 4-26a. Fracture surface at Section 1 demonstrated dimpled-like morphology (Figure 4-26c). Section 2 was mostly related to the through-thickness fracture in the HAZ/BM region. The SEM image in Figure 4-26d shows a transgranular fracture surface, which is similar to the fracture surface of the AZ80 base alloy, solution heat treated at 400°C for ½ hr (Figure 4-26e). No evidence of intermetallics was detected on the fracture surface of post weld heat-treated sample. Section 3 had the same morphology as found in the Section 3 of the as-welded sample.



**Figure 4-26 Fracture surface of the spot weld in the heat-treated condition: a) Scheme of the fracture location b) Fracture surface in section 1, 2, 3 c) Magnified image of fracture surface in section 1 d) Magnified image of fracture surface in section 2 e) Fracture surface in AZ80 BM in heat-treated condition**



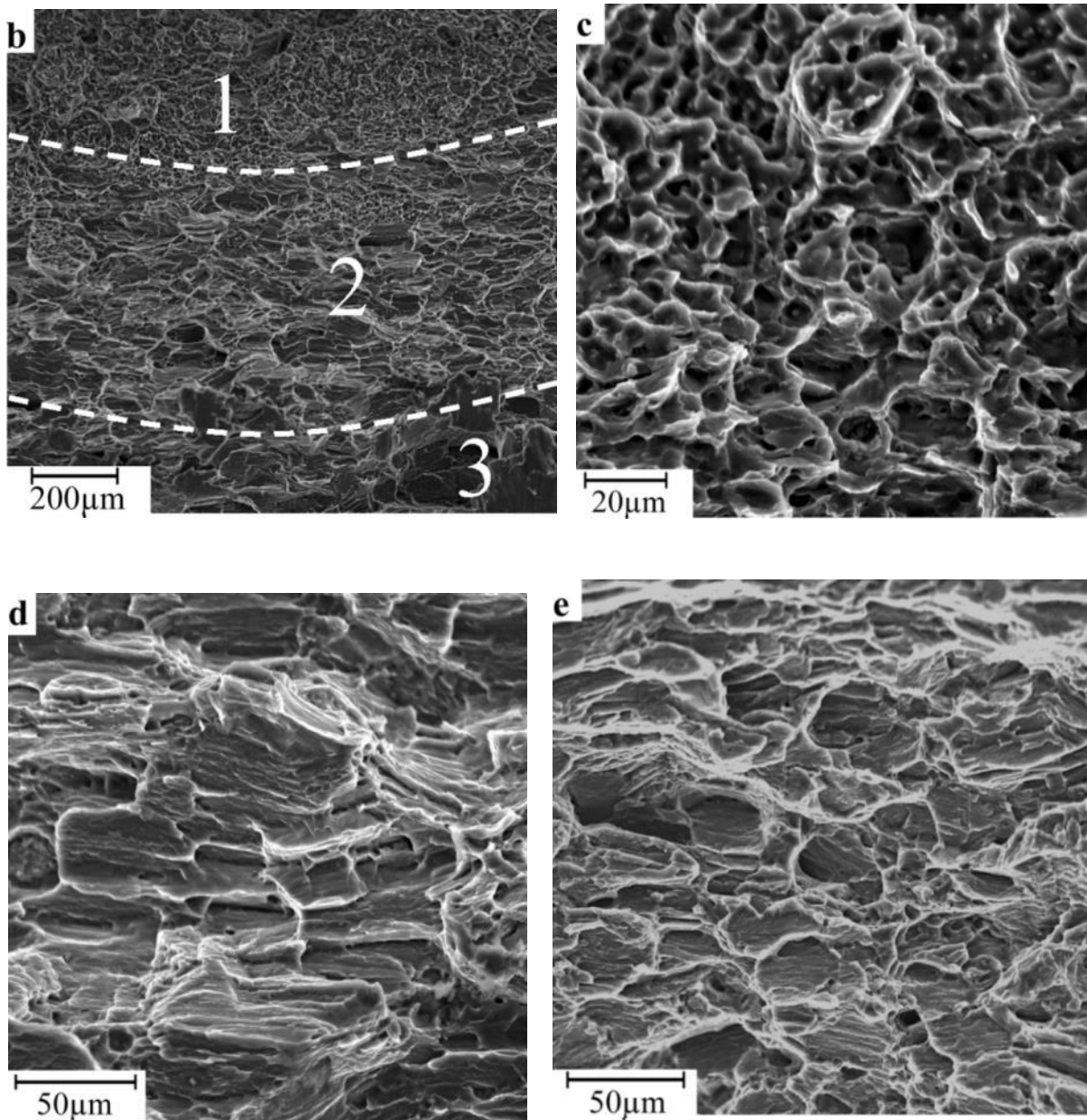


Figure 4-26 continued

#### 4.4 Discussion on Microstructure-Property Relationships

It was observed that the HIGHER the Al content of the magnesium BM, the more eutectic  $\beta$  phase formed and hence the more deterioration in mechanical properties of the weld occurs. The current results contradict the previous reports made on electron beam weld of the AZ alloys which indicated that as the Al content of magnesium alloy increases, the weld strength increases [53], [54]; however

the current results can be justified by considering the stress concentration at the edge of nugget. The ductility of the HAZ in AZ61 and AZ80 was deteriorated due to formation of intermetallics at the GBs. The crack initiated preferentially along the fusion boundary in the HAZ for the RSW of AZ61 and AZ80 via coalescence of micro voids/cracks, which were formed by two distinctive mechanisms:

#### *1. Intrinsic fracture of intermetallics*

As indicated by black arrows in Figure 4-22 c,d, the intermetallics were ideal sites for crack initiation and propagation. When the Mg-Al intermetallic compound grew too thick, it became significantly brittle. A similar phenomenon has been previously observed in Mg-to-Al dissimilar welds [129]–[131]. The presence of hard brittle second phase in the GBs of the soft solute-depleted matrix was reported to deteriorate the mechanical properties of HAZ [114].

#### *2. De-cohesion at $\alpha/\beta$ interface*

In this study OR 1 was confirmed between a GB particle and grain 1, as demonstrated in Figure 4-12a, with fairly high atomic matching; however, no OR was found between the same particle and grain 2. It can be proposed that the eutectic growth occurred on grain 1 (or dendrite) and therefore the OR was fixed. The divorced eutectic phase was not able to build an OR with the adjacent solidifying grain (grain 2) since the restrictive crystallographic matching of the particle with grain 1 was unlikely to produce a favourable OR with the grain 2 [98]. This is also true for the GB particles in the HAZ. In the case of OR 2, poor atomic matching exist at the interface. Moreover, as the particle/matrix interface grows larger (as the particle size increases), the atomic matching becomes more difficult and the coherency strains are replaced by dislocations. Therefore, it is implied that the interfacial energy between the  $\beta$  particles and Mg matrix is high and a high concentration of dislocations exists at the interface. Due to high interfacial energy, de-cohesion at particle/matrix interface is expected [132]. Due to existence of localized stress field at the edge of nugget, micro-cracks were formed at particle/matrix as observed in Figure 4-22. The increase in crack propagation rate during fatigue test, by the growth and coherency loss of the particles, was reported in over-aged aluminum alloys [133]. The particles present within the Mg grains promoted early void nucleation during plastic flow [129], [132]. Formation of micro-cracks and micro-voids in the HAZ eased crack initiation in high Al weld samples. The initiated crack preferred to propagate along the GBs as they contained the continuous network of  $\beta$  intermetallics. Possible fracture path in the FZ was tortuous due to dendritic morphology of the microstructure. Thus, the crack preferentially propagated along the GBs in the HAZ.

Unlike AZ61 and AZ80, low volume fraction of  $\beta$  phase exist in HAZ of AZ31 (Figure 4-16). Thus, HAZ microstructure was more resistant against fracture. The crack preferably initiated/propagated into the developed columnar structure of the FZ in AZ31 leading to interfacial fracture. The developed columnar structure formed near the fusion boundary of AZ31, is the preferred crack growth path [91]. Since in case of AZ31 weld, the crack initiation was not associated with the fracture of intermetallics, mechanical performance of spot weld was higher than those in AZ61 and AZ80.

The  $\beta$  particles are dissolved into the Mg matrix via PWHT. Thus, the potential sites for the easy crack propagation were effectively removed in weld microstructures of AZ61 and AZ80. Within the heat treated microstructure, crack initiation appeared to be associated with the plasticity at the vicinity of the notch. This can be confirmed via observation of heavily twinned microstructure near the crack region (Figure 4-24). A linkage between fracture and twinning activity was previously found in magnesium alloys [31], [33], [34], [60], [62].

It was proposed by Meyers that the twinning becomes more difficult with grain refinement in hcp materials [134]. The improvement in fracture toughness of magnesium alloys has been reported with grain refinement [61], [64]. Due to grain refinement during solidification of AZ61 and AZ80, fracture was resisted highly in the FZ. This refined microstructure of the FZ was stable even after the PWHT as shown in Figure 4-16 c and e. On the other hand, severe grain growth occurred during PWHT in the HAZ for these two alloys. Therefore, in the case of AZ61 and AZ80 alloys, twins formed more readily in the HAZ than in the FZ. Cracks appeared to initiate within such twins inside the HAZ microstructure.

In RSW of AZ31, grains are coarser in FZ than in HAZ in case of (Figure 4-16). The Large grain size in FZ of AZ31 was associated with low heterogeneous nucleation rate as explained in section 4.3.1.2. These grains became coarsened during the PWHT. Moreover, elongated grains adjacent to the fusion boundary are unfavourable to mechanical properties. On the other hand, HAZ grains remained small during the PWHT of AZ31 weld (Figure 4-16b). Therefore, failure in RSW of AZ31 remained unchanged by application of PWHT.

## 4.5 Summary

This work has been concerned with the effects of intermetallic compounds on the mechanical performance of the resistance spot welded AZ alloys in tensile shear loading. The following conclusions have been drawn:

1.  $\beta$ -Mg<sub>17</sub>Al<sub>12</sub> eutectic phase was formed in fusion zone and heat affected zone of the AZ31, AZ61 and AZ80 alloys due to non-equilibrium solidification during resistance welding. Eutectic growth was in such a fashion that matching of closed packed planes were established at the interface i.e.  $\{3\ 3\ 0\}$  of  $\beta$  phase with  $\{1\ \bar{1}\ 0\ 1\}$  or  $\{0\ 0\ 0\ 2\}$  of the  $\alpha$ -Mg matrix.
2. Columnar to equi-axed transition and grain refinement were enhanced, as Al content of base alloy increased. Increase in the solute content increased constitutional supercooling, which led to promotion of heterogeneous nucleation during solidification and subsequent grain refinement.
3. Grain growth occurred at large scale in heat affected zone of AZ61 and AZ80 during post-weld heat treatment.
4. The weld strength order AZ31>AZ61>AZ80 is opposite to that of base materials of AZ31<AZ61<AZ80, since easy crack initiation at the  $\beta$ /matrix interfaces in the heat affected zone of AZ61 and AZ80 occurred.
5. The post weld solutionizing heat treatment improved the load-to-failure and elongation-to-failure of RSW with high Al content. The fracture mode changed from nugget pull-out to through-thickness and the crack pathway was shifted towards heat affected zone far away from fusion boundary. Observation of twinning near the crack pathway of heat-treated samples indicated activation of plastic deformation mechanisms at the vicinity of the notch, which brought resistance against crack initiation.
6. With the absence of intermetallics, failure location was associated with the grain size of the microstructure: fracture occurred through the heat affected zone for AZ61 and AZ80 welds due their larger grains compared to those in the fusion zone. On the other hand, cracks preferentially initiated/propagated in the fusion zone of AZ31, where larger grains existed compared to the heat affected zone.

## Chapter 5

# The Role of Double Twinning on Transgranular Fracture in Magnesium AZ61 in the Localized Stress Field of Spot Weld

### 5.1 Introduction

It was found in Chapter 4 that presence of intermetallics deteriorated the mechanical performance of spot welded AZ61 and AZ80 magnesium alloys. Fracture occurred preferentially through the  $Mg_{17}Al_{12}$  intermetallics before plasticity began, at the vicinity of notch. By removal of these particles by the post-weld heat treatment, plasticity occurred near the notch during tensile shear loading. Therefore, the strength and ductility of spot weld was substantially improved. In this chapter attempts were made to find a correlation between plasticity, specifically twinning activity, and fracture in the HAZ of AZ61 spot weld in the post-weld heat treated condition.

This work is based on careful EBSD investigation within the coarse grains within which transgranular fracture was observed. In this chapter, firstly, the twin variants in the fracture grains were identified. Secondly, the shear stresses resolved on the basal slip systems were calculated using Schmid law. The numerical calculations were followed by TEM observations of the basal slip activity within the grains and the twinned segments. Finally, the effects of double twinning activity on ductile fracture in magnesium was discussed. The work presented and described in this chapter has been reviewed for publication by Niknejad et. al. [135].

### 5.2 Background on Double Twinning

A complex doubly twinned structure appears when the c-axis of Mg crystal is compressed. The matrix reorientation by the primary  $\{1\ 0\ \bar{1}\ 1\}$  twinning ( $g_{CT}$ ) followed by secondary  $\{1\ 0\ \bar{1}\ 2\}$  twinning ( $g_{ET}$ ) produces the orientation of the double twinned material ( $g_{DT}$ ). Since there exist 6 variants for both primary and secondary twinning, 36 orientations are expected for the double twin variants:

$$g_{DT}(i, j) = g_{ET}(i)g_{CT}(j), \quad i = 1, 2, \dots, 6 \text{ and } j = 1, 2, \dots, 6 \quad \text{eq.5.1}$$

The misorientation matrix between the parent crystal and double-twinned daughters ( $M_{P/DT}$ ) can be found by [136]:

$$M_{P/DT} = g_{DT}g_P^{-1} \quad \text{eq.5.2}$$

The rotation axis/angle pair for each double twin relative to parent can be found from  $M_{P/DT}$ . The 36 double twinning reorientations can be reduced to 4 twin variants based on the axis/angle pair as shown in

Table 5-1. Figure 5-1 shows how the crystal is reoriented by the variant 1 and variant 4 double twinning. Crystallographic reorientation by the 36 possible double twinning was predicted by MTEX Matlab toolbox [137] and shown on the pole-figure of Figure 5-2.

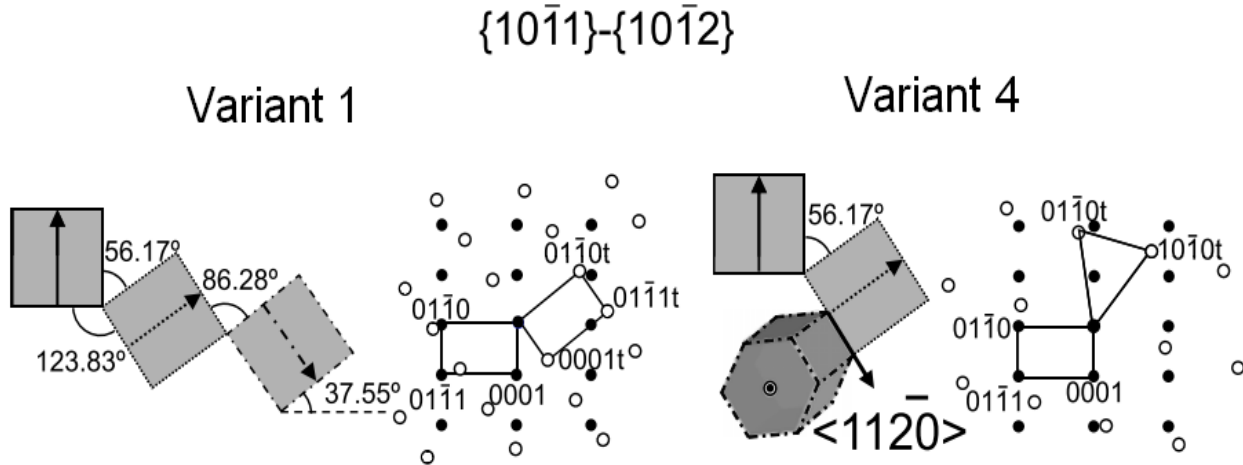
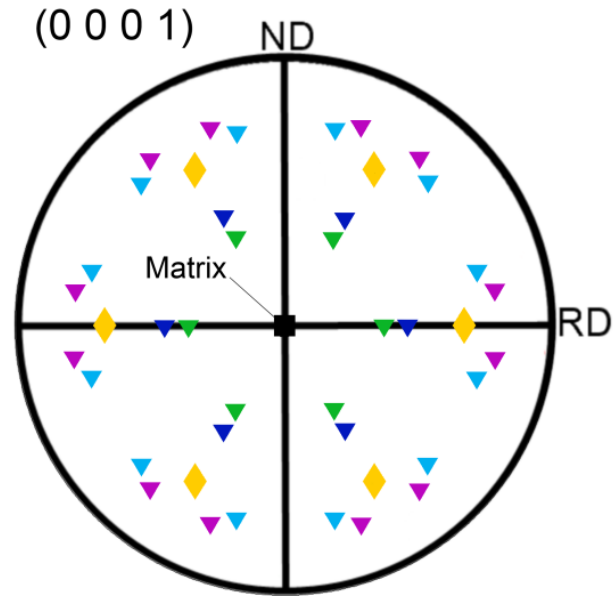


Figure 5-1 Schematic diagram of hcp lattice rotation via variant 1 and 4 double twinning and their diffraction patterns (taken from Ref. [34])

Table 5-1 Rotation axis/angle pair for  $\{10\bar{1}1\}$  twinning and  $\{10\bar{1}1\}-\{10\bar{1}2\}$  double twinning variants and the symbols used in this study for presentation of different twin variants

Twin type	$\{10\bar{1}1\}$	$\{10\bar{1}1\}-\{10\bar{1}2\}$			
Twinning variants		I	II	III	IV
Misorientation (axis/angle)	$\langle 1\bar{2}10 \rangle / 56.17^\circ$	$\langle 1\bar{2}10 \rangle / 37.5^\circ$	$\langle 1\bar{2}10 \rangle / 30.1^\circ$	$\langle \bar{1}33\bar{1}71.5 \rangle / 66.5^\circ$	$\langle \bar{1}53\bar{1}51.2 \rangle / 69.9^\circ$
Color on highlighted twin boundary	Yellow	Blue	Green	Light Blue	Fuchsia
Orientation symbols on pole figure	◆	▼	▼	▼	▼



**Figure 5-2 Stereographic projection of  $\{0\ 0\ 0\ 1\}$  poles of the six  $\{1\ 0\ \bar{1}\ 1\}$  primary twins and 36 double twin variants. The symbols representing the orientations are as per Table 5-1**

### 5.3 Experiments

AZ61 sheet was used for spot welding. Rectangular specimens of 100 mm\*35 mm along the sheet's rolling direction (RD) and transverse direction (TD) respectively, were joined by resistance spot welding. The same welding parameters as described in Chapter 4 were applied (welding current: 28 kA, welding time: 8 cycles, electrode pressure: 4 kN). The samples were afterwards heat treated at 420 °C for 60 minutes in order to dissolve the secondary phase particles. The heat treatment was carried out at higher temperature and for longer time than what was done in the work presented in chapter 4 (i.e. 400 °C for 30 minutes), in order to dissolve the  $\beta$  intermetallics as much as possible and hence to increase the EBSD indexing rate. Such change in the heat treatment procedure, had negligible impact on the grain structure and mechanical performance of the spot weld. Figure 5-3a shows EBSD map from the microstructure near the notch. Grain size distribution results indicated that the microstructure in the HAZ was subjected to abnormal grain growth during post weld heat treatment (Figure 5-3b). The majority of grains in HAZ have c-axes close to the sheet's normal direction (ND), due to initial strong basal texture of the as-received alloy. On the other hand, the texture in the FZ is fully randomized due to heterogeneous nucleation effect during solidification. Tensile shear tests were conducted parallel to the sheet's RD on the samples. In order to accurately measure the specimen elongation during tensile shear test, the test coupons were assembled by the spacers (as shown schematically in Figure 5-4) to accommodate an extensometer. The spacers were spot welded to the test coupons to prevent slipping at the gripping zone.

Figure 5-5 shows mechanical response in tensile shear testing of spot welds in as welded and heat treated conditions. Post weld heat treatment obviously improved the strength and ductility of spot weld. In heat treated spot welds, cracks initiated from the notch at loads of 5.9-6.1 kN. In order to investigate the cracking mechanisms during loading, the tensile shear test was stopped before failure and a cross section was studied metallographically.

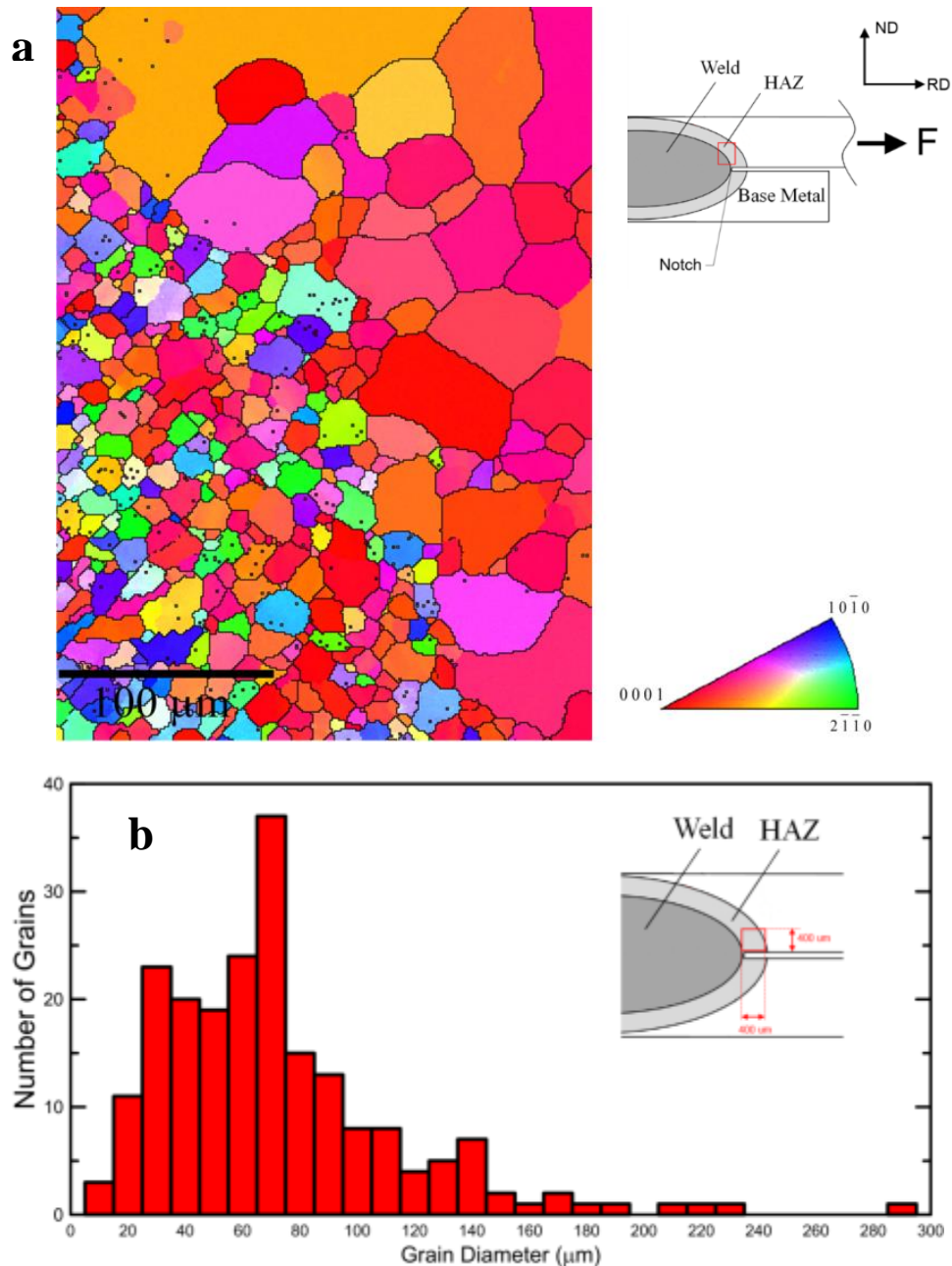


Figure 5-3 (a) Typical microstructure near the spot weld notch as encircled in the schematic drawing of spot weld; the projection direction of inverse pole-figure map is parallel to sheet normal direction (ND); (b) Grain size distribution in HAZ of AZ61 (heat treated at 420 °C for 60 minutes); the area from which the grains were picked for the measurements, is highlighted in the schematic drawing



The micro-textures were studied via scanning electron microscope (SEM) equipped with a field emission gun and an EBSD detector. An acceleration voltage of 20 keV, with a working distance of 15 mm and a sample tilt angle of 70° were utilized. Due to very fine size of the twin bands, small step sizes (0.1-0.4 μm) were chosen. The indexing fraction of 65-75% was obtained for the microstructures at the vicinity of the micro-cracks. The maps were cleaned and afterwards, the identities of the primary and secondary twins were determined by CHANNEL 5 software package.

Using focused ion beam (FIB) technique, samples were extracted from the fractured grains for transmission electron microscopic (TEM) analysis. A thin layer of tungsten was deposited on the specimen to protect it during the milling process. FIB was performed using Ga liquid metal ion source.

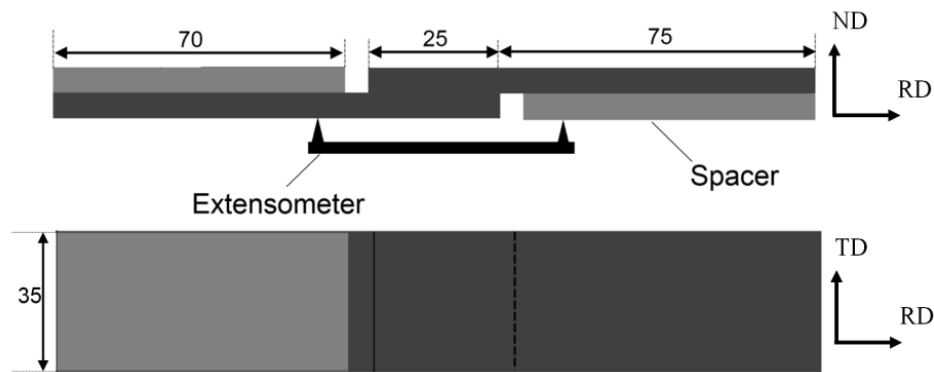


Figure 5-4 Schematic drawing of welding assembly and accommodation of extensometer

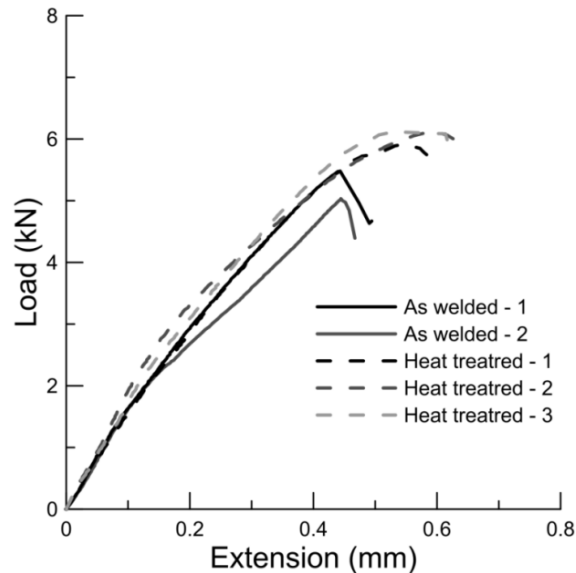


Figure 5-5 Tensile shear response of AZ61 spot weld in as-welded and heat treated conditions

## 5.4 Schmid Law Model Description

In order to understand the role of double twinning on transgranular fracture, activity of plastic deformation mechanisms in the microstructure was predicted using Schmid law. Numerical calculations were conducted using MTEX Matlab toolbox (open-source). The classical Schmid law proposes that a critical value of resolved shear stress ( $\tau_{RSS}^{(r)}$ ) must be reached if a given slip system is activated in a deformed crystal. The twinning shear or slip may be defined in terms of the  $r$ th shear/slip plane normal ( $n_i^r$ ) and shear direction/Burgers vector ( $b_i^r$ ), where both  $n_i^r$  and  $b_i^r$  are unit vectors, defined based on specimen coordinate system (i.e. x||RD-y||ND-z||TD).

$$b_i^r = \begin{bmatrix} b_{RD} \\ b_{ND} \\ b_{TD} \end{bmatrix}, n_i^r = \begin{bmatrix} n_{RD} \\ n_{ND} \\ n_{TD} \end{bmatrix}$$

The resolved shear stress ( $\tau_{RSS}$ ) on defined slip plane and slip direction is determined by the projection of stress state on the  $r$ th slip system [138]:

$$\tau_{RSS}^{(r)} = R_{ij}^{(r)} \sigma_{ij} \quad \text{eq.5.3}$$

Where  $\sigma_{ij}$  is the second rank Cauchy stress tensor and  $R_{ij}$  is second rank Schmid tensor which may be obtained by the Einstein summation.

$$R_{ij}^{(r)} = \frac{1}{2} (b_i^r n_j^r + b_j^r n_i^r), \sigma_{ij} = \begin{bmatrix} \sigma_{RD} & \sigma_{RD,ND} & \sigma_{RD,TD} \\ \sigma_{ND,RD} & \sigma_{ND} & \sigma_{ND,TD} \\ \sigma_{TD,RD} & \sigma_{TD,ND} & \sigma_{TD} \end{bmatrix} \quad \text{eq.5.4}$$

The local stresses for defining stress tensor were obtained from an elastic/plastic finite element (FE) simulation of tensile shear loading of spot weld. The analysis was conducted by FE-code (Ansys® Academic Research-Mechanical, Release 16.0).

Figure 5-6 shows the half-model with the applied boundary conditions. The edge of spot weld was assumed to be a blunt notch with a radius of 0.076 mm according to the measurements in this study as well as previous study on FE simulation of spot weld [86]. The nugget diameter (i.e. the distance from the notch tip from one side to the other) was 9.85 mm. The von-Mises yielding criterion was used along with the multi-linear isotropic hardening [139] to define the plastic flow. The multi-linear behavior was selected based on the data from stress-strain ( $\sigma_t - \epsilon_t$ ) curve obtained for uniaxial tensile test on the material in heat treated condition (i.e 420 °C for 60 min). Profuse twinning was observed near the notch, before crack initiation, when applied load was 5.2 kN (as shown in Figure 5b). Therefore, the stress and strain analysis was done with the applied load of 5.2 kN. Since the stress condition is not uniform across

the notch, a unique stress tensor was defined for each set of EBSD data based on its location relative to the notch as shown schematically in Figure 5-7.

It should be noted that Schmid law calculations must be performed based on specimen orthonormal coordinate system (RD-ND-TD). Thus, a transformation from the crystal coordinate system to specimen coordinate system must be defined. The numerical procedure regarding to this conversion is explained in details in Ref. [140].

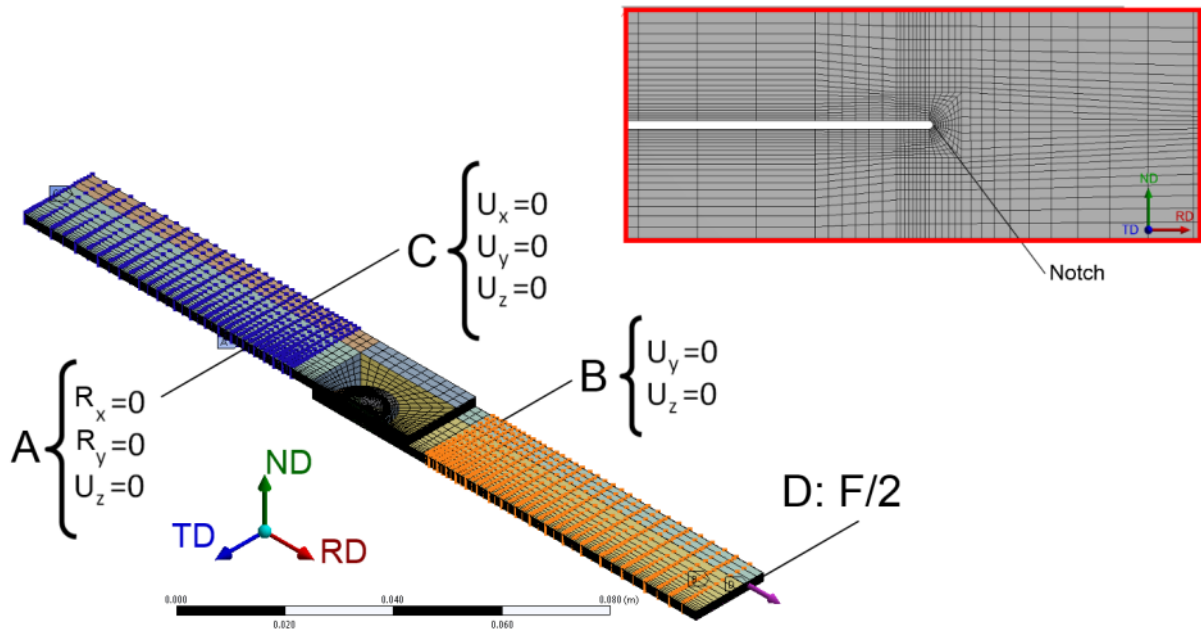


Figure 5-6 Finite element half-model presentation of spot weld and cross section near the notch

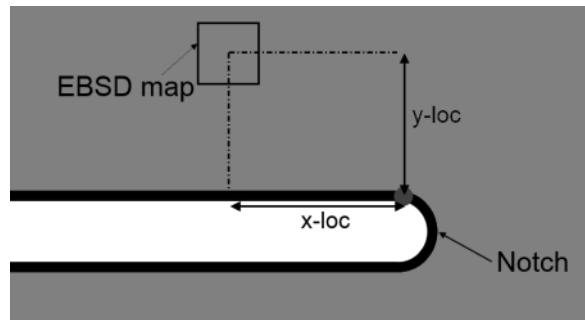


Figure 5-7 x-y location of EBSD area relative to the notch

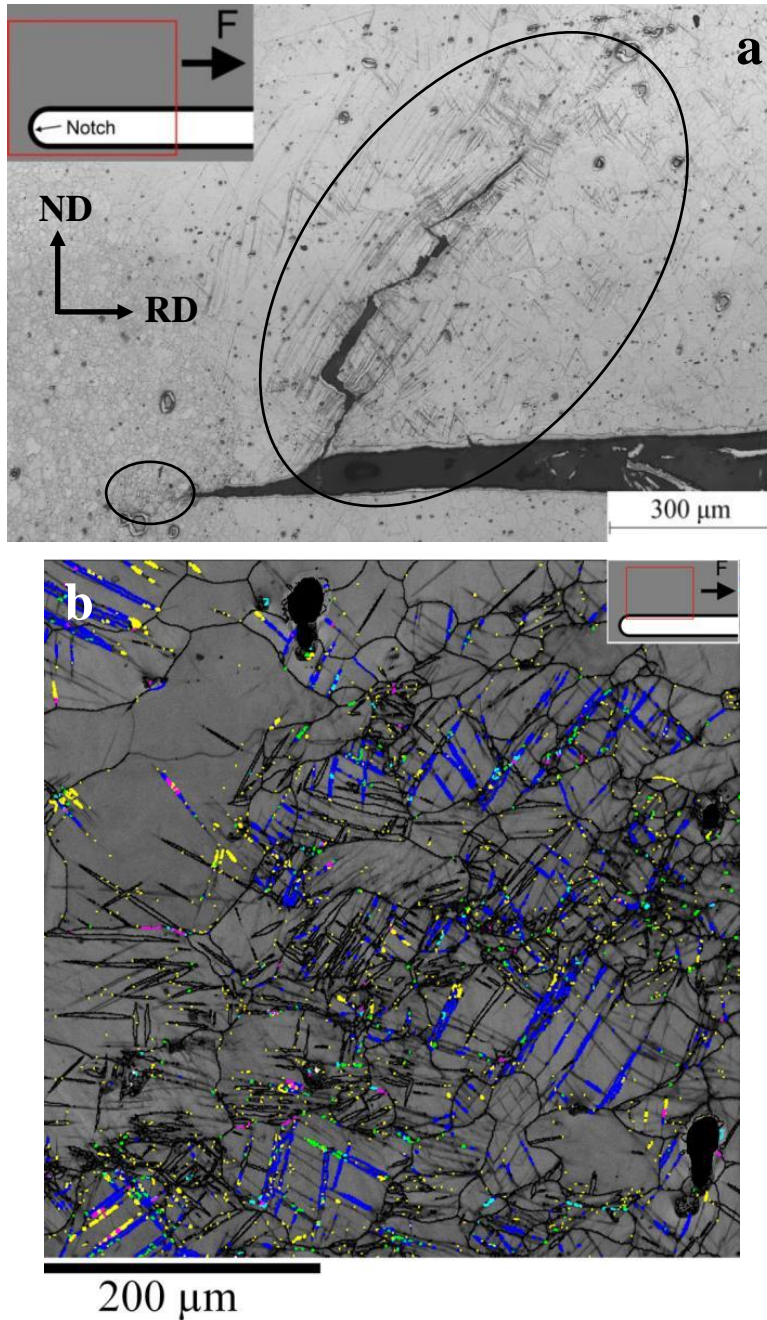
## 5.5 Results

### 5.5.1 Observation of Transgranular Cracks and Twin Variants

Figure 5-8a shows an overview of initiated crack produced during tensile shear test. Plastic zone created ahead of the notch can be distinguished from the twinned region as encircled in Figure 5a. Plasticity occurred on a large scale above the notch, but only a small plastic zone was developed in front of the notch. The crack initiated from the notch and propagated towards the thickness of the material. The crack exhibited very sharp edges, and its pathway changed abruptly from one grain to another. Twinning occurred profusely near the crack pathway. Microstructural examination revealed high twinning activity at the vicinity of notch, before crack initiation as observed typically in Figure 5-8b. The twins were mostly identified as variant I double twins with boundary misorientation of  $\langle 1 \bar{2} 1 0 \rangle / 37.5$ .

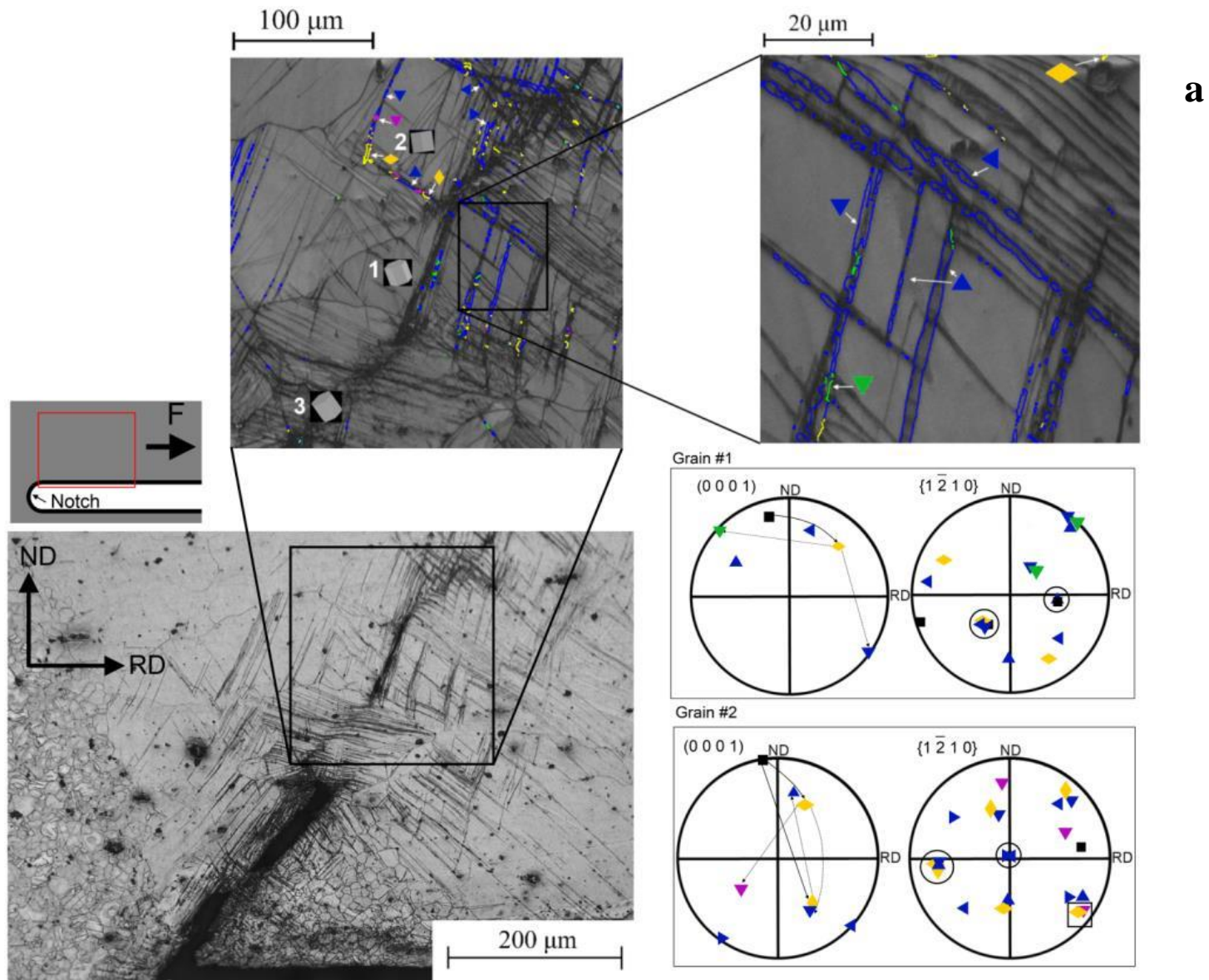
Careful investigations revealed micro-cracks, generated within the grains close to the primary crack pathway. These grains were deformed heavily by twin bands. Figure 5-9 shows typical microstructures near the micro-cracks observed within the grains (via optical microscopy). These micro-cracks were generally close to the primary crack which initiated from the notch (as shown typically in Figure 5-8). On the EBSD maps, the identified twin boundaries are highlighted in different colors as per Table 5-1. The highlighted twin boundaries were drawn with angular allowance of  $\pm 5^\circ$ . A Large number of primary  $\{1 0 \bar{1} 2\}$  twinning incidences also occurred in the microstructure but they are not highlighted in the figures. In contrast to  $\{1 0 \bar{1} 2\}$  twins which demonstrated high lateral growth, primary  $\{1 0 \bar{1} 1\}$  and secondary twinned segments appeared as thin lamellae.

Figure 5-9a shows an overview of a region where cracking occurred. The double twin variants were identified within the coarse grains; however very few double twin traces were found in grain 3 which had a different orientation compared to the majority of grains whose c-axes are close to sheet's ND. It appeared that grain 3 (which is located in the mid-pathway of the primary crack) did not suffer from transgranular fracture. Closer EBSD analysis was done on grain 1 with  $0.1 \mu\text{m}$  step size as shown in the second EBSD map of Figure 5-9a. The intersecting double twinned segments are clear and their orientations are illustrated in the corresponding pole-figures. They were mostly identified as variant I double twins. The orientation of micro-crack is very close to habit planes of those double twins which were more developed compared to their intersecting counterparts. Grain 4 also showed high double twinning activity. Only the twin variants I and IV were observed. It is shown in the corresponding pole-figures that the secondary twins were products of four primary  $\{1 0 \bar{1} 1\}$  twinning systems. The variant I secondary twins involved rotation around the common  $\langle 1 \bar{2} 1 0 \rangle$  axis of the matrix and the primary twins and type IV involved rotation around a different  $\langle 1 \bar{2} 1 0 \rangle$  axis of the primary twin.



**Figure 5-8 (a) Typical microstructure near the notch after crack initiation during tensile shear test. Plastic zones are encircled; (b) EBSD Kikuchi band contrast map presenting microstructure near the notch before crack initiation in tensile shear test (applied load: 5.2 kN). The twin boundaries are identified as per Table 1-1**

As can be seen in the optical micrographs presented in Figure 5-9, the orientations of the micro-cracks are similar to the orientation of the small twins appeared dark in the as-etched microstructure. The EBSD revealed that they are mainly of variant I (Table 1-1) double twins. This is direct evidence of double twinning involvement in transgranular crack initiation.



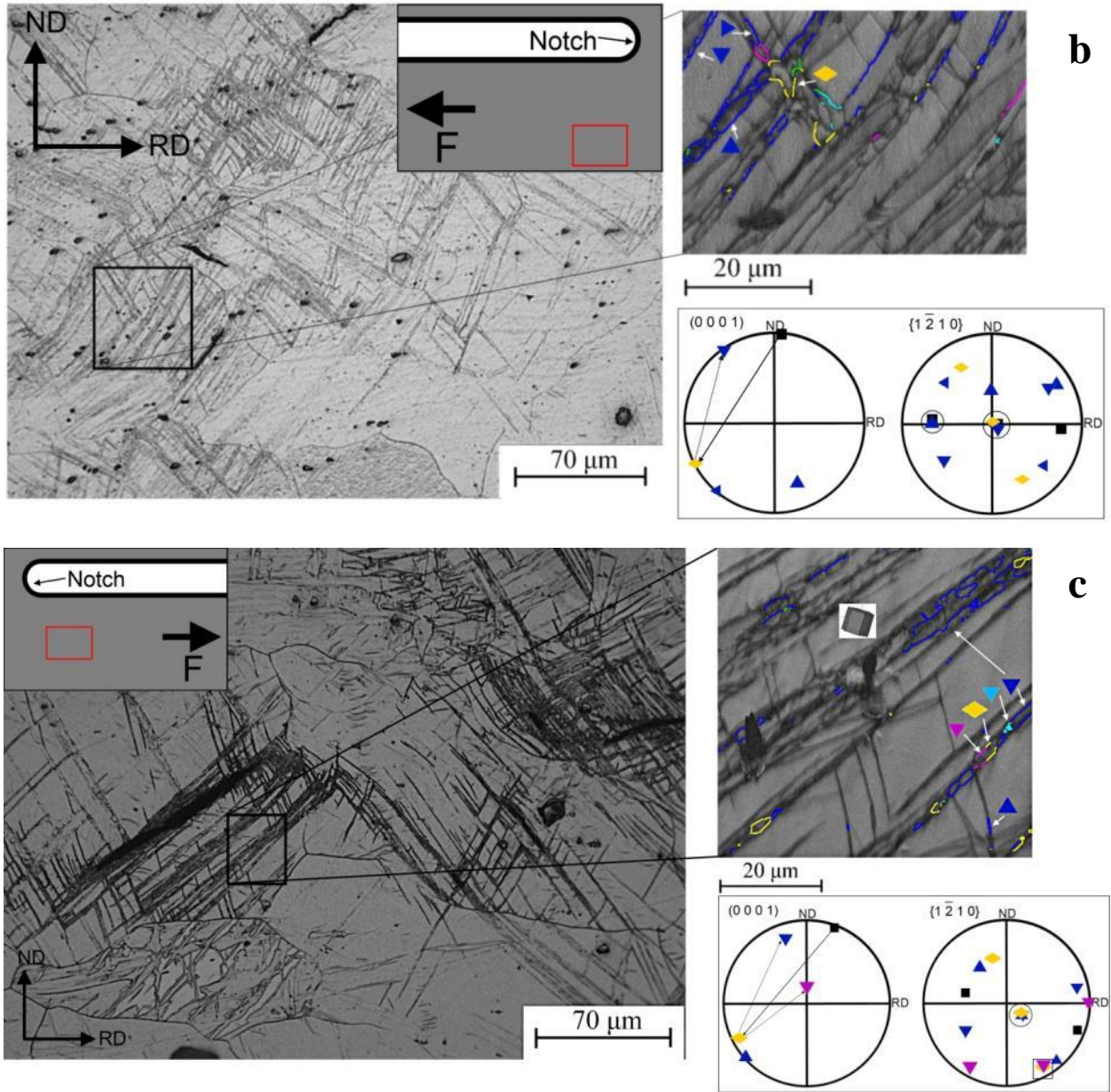


Figure 5-9 Typical microstructures near the edge of spot weld after tensile shear test as shown in the schematic drawings. The EBSD Kikuchi band contrast maps presents the microstructure within the grains suffered from transgranular fracture as shown in the optical micrographs. The twin boundaries are identified as per Table 1-1. In the accompanying pole-figures, dark square represents the orientation of the parent grain, rhombic represents the orientation of primary  $\{10\bar{1}1\}$  twins and triangle represents the orientation of the double twins. The  $\langle 1\bar{2}10 \rangle$  rotation axes are circled in the corresponding pole-figures.

Figure 5-10 shows a typical microstructure near the fracture edge from ND view. The observation of micro-crack near the fracture edge confirms that transgranular micro-cracks had been formed before general failure occurred, and fracture edges were sharp. In most cases, they had the same orientation as the twinning habit planes. It is evident that the orientation of the micro-crack changed from grain 1 to grain 2. As can be seen in grain 2, the habit plane of the variant IV twin was different from those of variant I. It appeared that the micro-crack developed into the grains keeping the identical orientation as those of the habit plans for the variant I twins. This indicated that the crack preferentially initiated within the variant I twins. The EBSD analysis revealed that the twin segments are mostly of variant I twins in both grains specifically near the micro-crack. In both grains the intersecting twins were also observed; however the EBSD was not successful in indexing of them (as highlighted by black arrow in EBSD map of Figure 5-10). The habit planes of the two intersecting twins are parallel to the two  $\langle 1 \bar{2} 1 0 \rangle$  directions corresponding to the matrix crystal. Taking into account that the c-axis of the matrix is close to the normal direction, it can be suggested that non-indexed twins also occurred by the  $\langle 1 \bar{2} 1 0 \rangle$  rotation (either variant I or II). It appeared that twinning in the two grains occurred exactly at the identical points on the shared grain boundary. No twin was found in the central part of the map in both grains. It appeared that the reorientation of the matrix within the intersecting twin in grain 1 (highlighted by black arrow in EBSD map), acted as a barrier for the nucleation/growth of the twins in this region. It appeared that the twin nucleation in the particular locations of grain boundary in one grain, triggered twin nucleation in the other. This phenomena can be explained by the theory of the strain accommodation proposed by Jonas et al. [141]: “The formation of a twin is accompanied by shearing the matrix. Thus, when a twin is nucleated at a grain boundary, the neighboring grain, which shares the same grain boundary, will experience the shearing”. Thus, the twins nucleated in the grain 2 from the grain boundary at certain points where the shearing stresses are experienced.

In general, variant I (which involved rotation of  $\langle 1 \bar{2} 1 0 \rangle/37.5^\circ$ ) is favored compared to the other variants of double twinning. This is consistent with the previous studies on AZ31 alloy during in-plane tensile test [141]. Also very small segments of primary  $\{1 0 \bar{1} 1\}$  twins were found within the crack-bearing grains, suggesting a nearly complete transformation of these twins by the secondary  $\{1 0 \bar{1} 2\}$  twinning. The pole figures corresponding to  $\{1 \bar{2} 1 0\}$  poles, indicated that in most cases, the double twinning involved rotations about those  $\langle 1 \bar{2} 1 0 \rangle$  axes of the parent grains which were closest to the sheet’s transverse direction (TD). This suggested that a correlation exist between the



twin variant selection and Schmid law. At last, it should be noted that no trace for double twinning activity was detected within the grains far away ( $>700\ \mu\text{m}$  along the sheet's ND) from the notch i.e. low stressed regions.

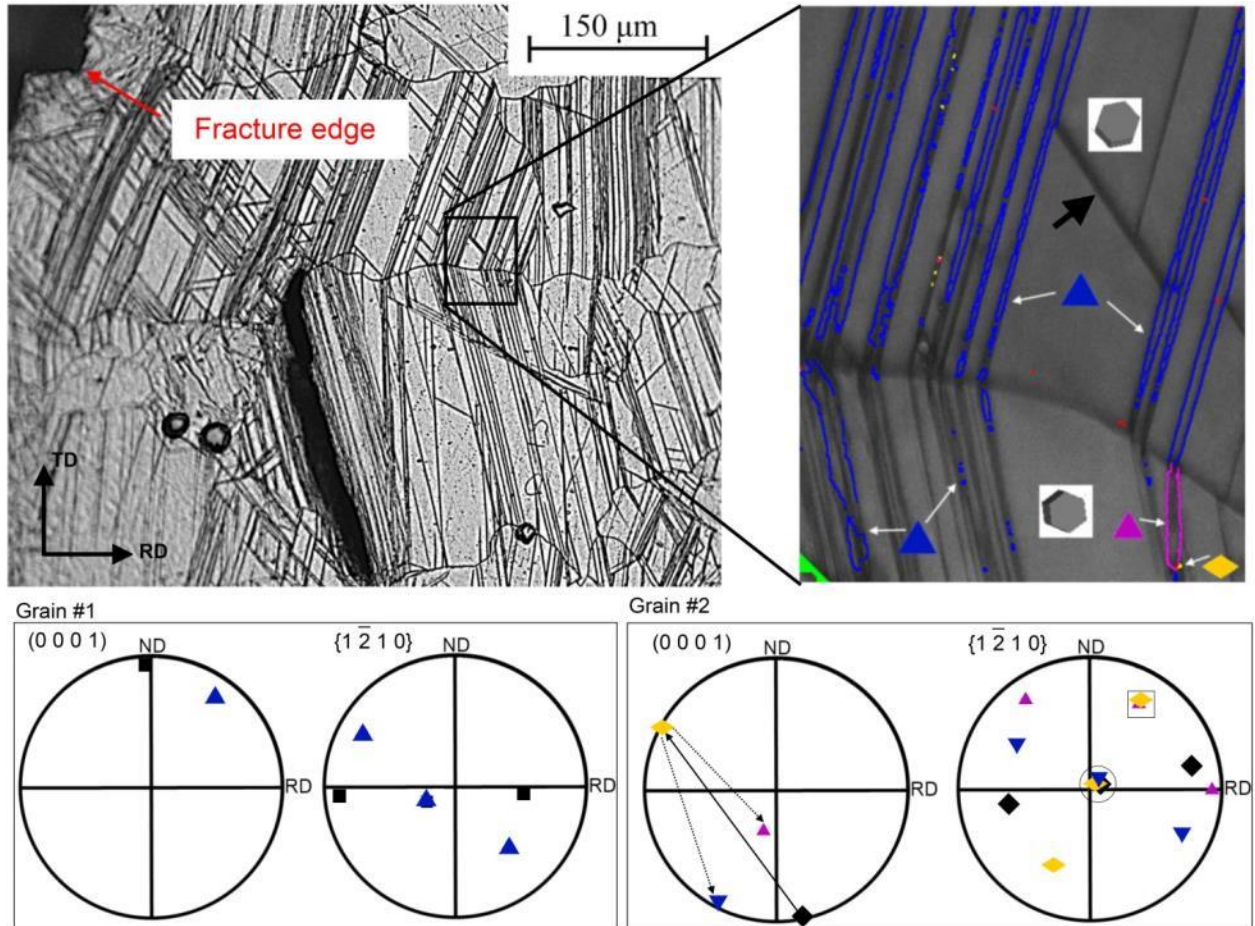


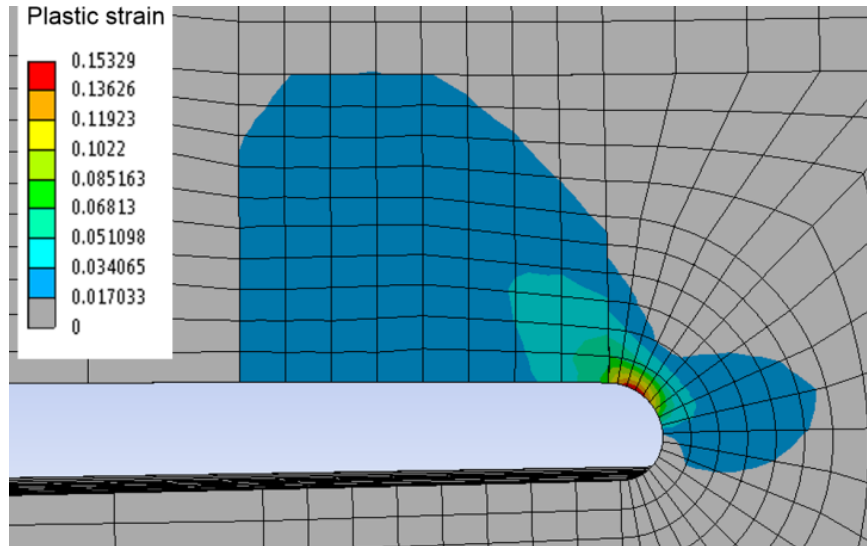
Figure 5-10 Typical optical micrograph and the EBSD map near the fracture edge from ND view

## 5.5.2 Prediction of Deformation Mechanisms at the Vicinity of Notch

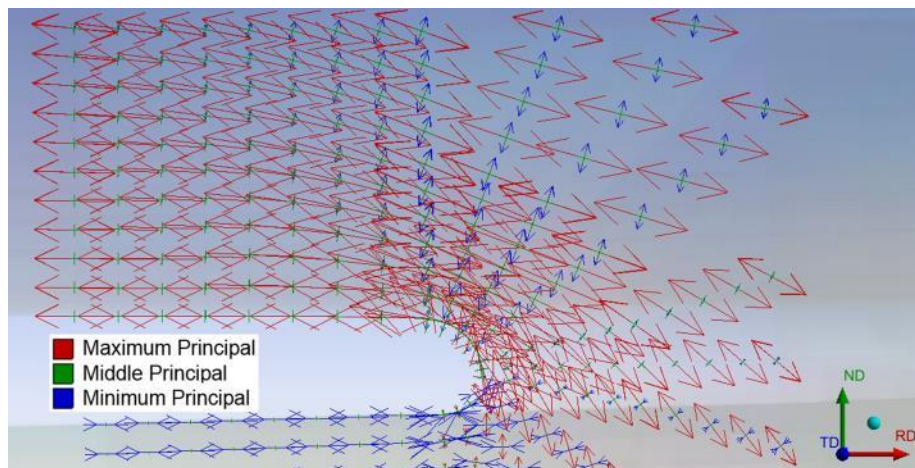
### 5.5.2.1 Plastic Zone and Stress Condition at Notch

Figure 5-11 plots the predicted plastic zone produced ahead of the notch during the tensile shear test. Large plastic zone was predicted above the notch (i.e. within HAZ). Small plastic zone was predicted in front of the notch progressing into FZ. The plastic zone prediction is consistent with the plastic zone distinguished from microstructural observations (Figure 5-8a). The region near the notch

experienced a triaxial tensile stress state as shown in Figure 5-12. The stress field above the notch (i.e. where crack initiation occurred), is such that the maximum (close to RD) and minimum (close to ND) principal stresses are rotated about the TD axis to an angle of 0-17°. This rotation is due to application of the shear stress ( $\tau_{RD-ND}$ ) due to a combination of tension- and bending-induced normal stress i.e.  $\sigma_{ND}$  [85]. The middle principal stress is acting along TD and its magnitude is about the ½ that of maximum principal stress.



**Figure 5-11 Predicted plastic zone created ahead of the notch**



**Figure 5-12 Principal stresses near the notch during tensile shear loading**

Table 5-2 shows the defined stress tensor applied for the EBSD maps presented in Figure 5-9 and Figure 5-10. Stress tensor for each EBSD map was obtained based on its x,y coordinates relative the notch (as shown in Figure 5-7).

**Table 5-2 Definition of stress tensors corresponding to the EBSD areas shown in Figure 5-9 and Figure 5-10 with their measured x-y locations relative to notch**

Figure	(x,y) location of EBSD relative to notch ( $\mu\text{m}$ )	$\sigma_{ij}$ (MPa)
5-9a	(315,286)	$\begin{bmatrix} 247 & 31 & 0 \\ 31 & 22 & 0 \\ 0 & 0 & 132 \end{bmatrix}$
5-9b	(533,547)	$\begin{bmatrix} 232 & 29 & 0 \\ 29 & 23 & 0 \\ 0 & 0 & 121 \end{bmatrix}$
5-9c	(142,751)	$\begin{bmatrix} 237 & -56 & 0 \\ -56 & 83 & 0 \\ 0 & 0 & 145 \end{bmatrix}$
5-10	(384,100)	$\begin{bmatrix} 223 & -45 & 0 \\ -45 & 1 & 0 \\ 0 & 0 & 113 \end{bmatrix}$

## 5.5.2.2 Calculation of Resolved Shear Stress on Deformation Systems

### 5.5.2.2.1 Basal Slip Activity within Grains and Twins

Numerical results for basal slip activity in the microstructures of Figure 5-9 and Figure 5-10 are presented in Figure 5-13 (detailed procedure for calculations shown in Appendix C). The grains within which the cracking occurred mostly possessed unfavorable orientation for the basal slip. In case of the primary  $\{1\ 0\ \bar{1}\ 2\}$  twins, the crystal rotation did not generally lead to increase in the resolved shear stress. It can be understood from Figure 5-13a that the double twins, with the same orientation as the crack in grain 1, led to substantial increase in basal slip activity. Interestingly, the reorientation of the crystal within the intersecting double twins (highlighted by black arrows in Figure 5-13a), did not favor the basal slip. It is also shown in Figure 5-13a that grain 3 is in favorable orientation for basal slip. It can be suggested that the imposed strains are efficiently accommodated via basal glide in this grain and thus it did not demonstrate high twinning activity. This can be a justification for resistance of grain 3 to transgranular fracture (as shown in the optical micrograph in Figure 5-9a). It can be inferred from Figure 5-13 a-d show that the double twins with the same orientation as the previously observed micro-cracks provide high activity for basal glide. The twins of

variants I and II generally, demonstrated "easy-for-slip" orientation; however this was not the case for the variant III and IV twins (as highlighted by black arrows in Figure 5-13 c and d).

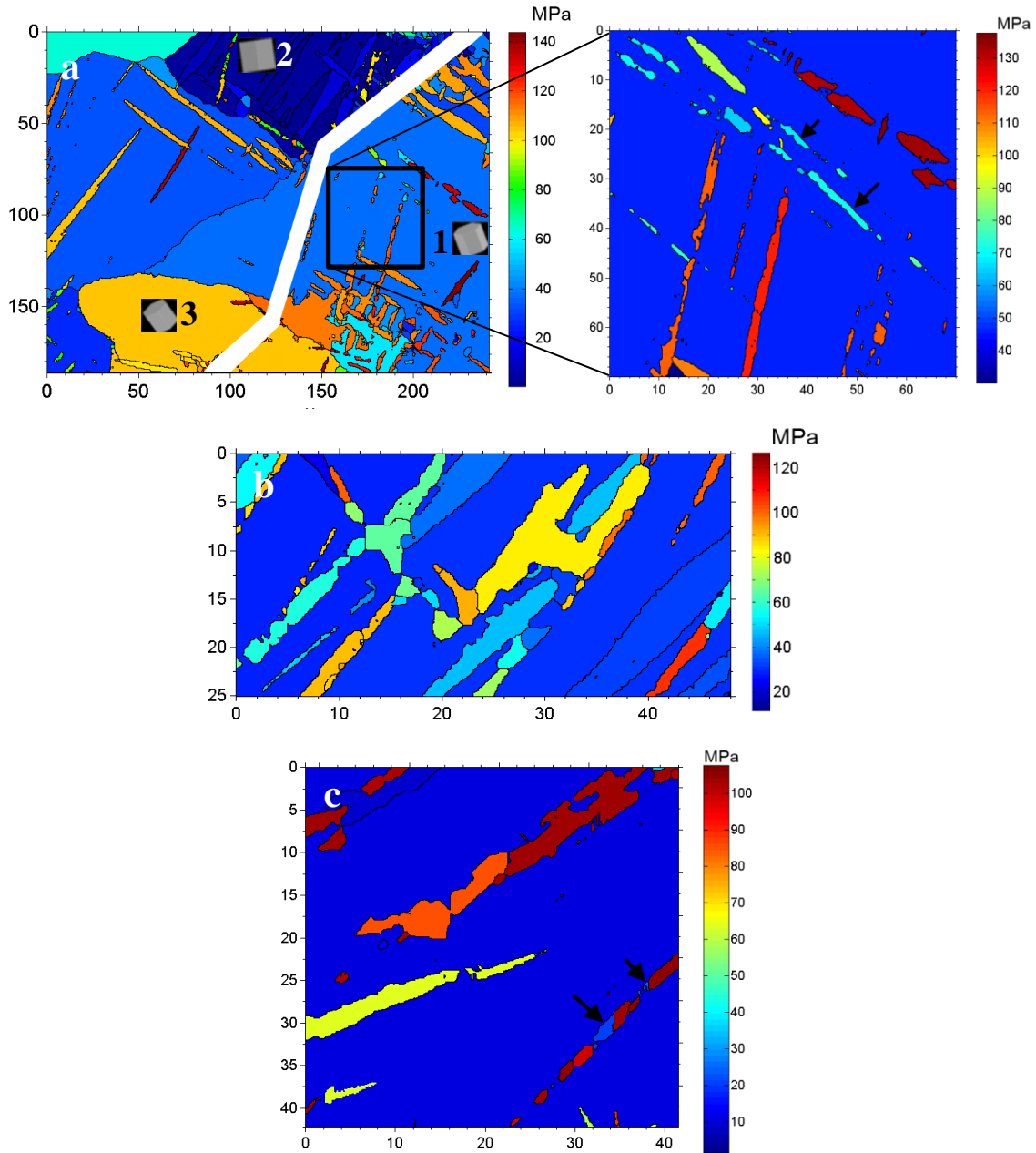
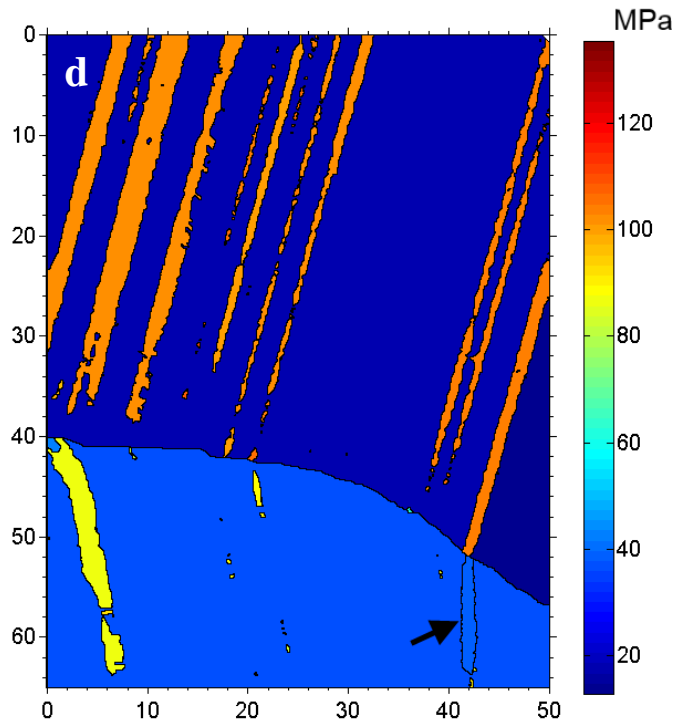


**Figure 5-13 Prediction of maximum resolved shear stress applied on basal slip systems for the EBSD data shown in Figure 5-9a (a), Figure 5-10b (b), Figure 5-10c (c) and Figure 5-10 (d). The black arrows show those double twins variants which did not demonstrate high activity for basal slip**



#### 5.5.2.2.2 Strain Accommodation in Fractured Grains

In the second part of the numerical analysis, attempts were made to find a correlation between strain accommodation capability and cracking susceptibility. In this regard, the grains within which transgranular fracture occurred were selected. Figure 5-14 shows inverse pole-figures reflecting the orientation of tensile stress axis in reference frame of parent crystal with the calculated Schmid factor for basal slip (Figure 5-14a),  $\{10\bar{1}2\}$  twinning (Figure 5-14b) and  $\{10\bar{1}1\}$  twinning (Figure 5-14c). The direction of maximum principal stress acting on each fractured grain was transformed to the crystallographic direction and superimposed on the inverse pole-figures as highlighted by the black dots. Figure 5-14 indicated that while the fractured grains possessed unfavorable orientation for the basal slip and  $\{10\bar{1}2\}$  twinning, their potential to undergo  $\{10\bar{1}1\}$  twinning is high. This explains high double twinning activity within the fractured grains. From Figure 5-14b, it can be understood that the stress is applied in such way that it produced very low (or in many cases negative) shear stresses resolved on extension twinning systems.

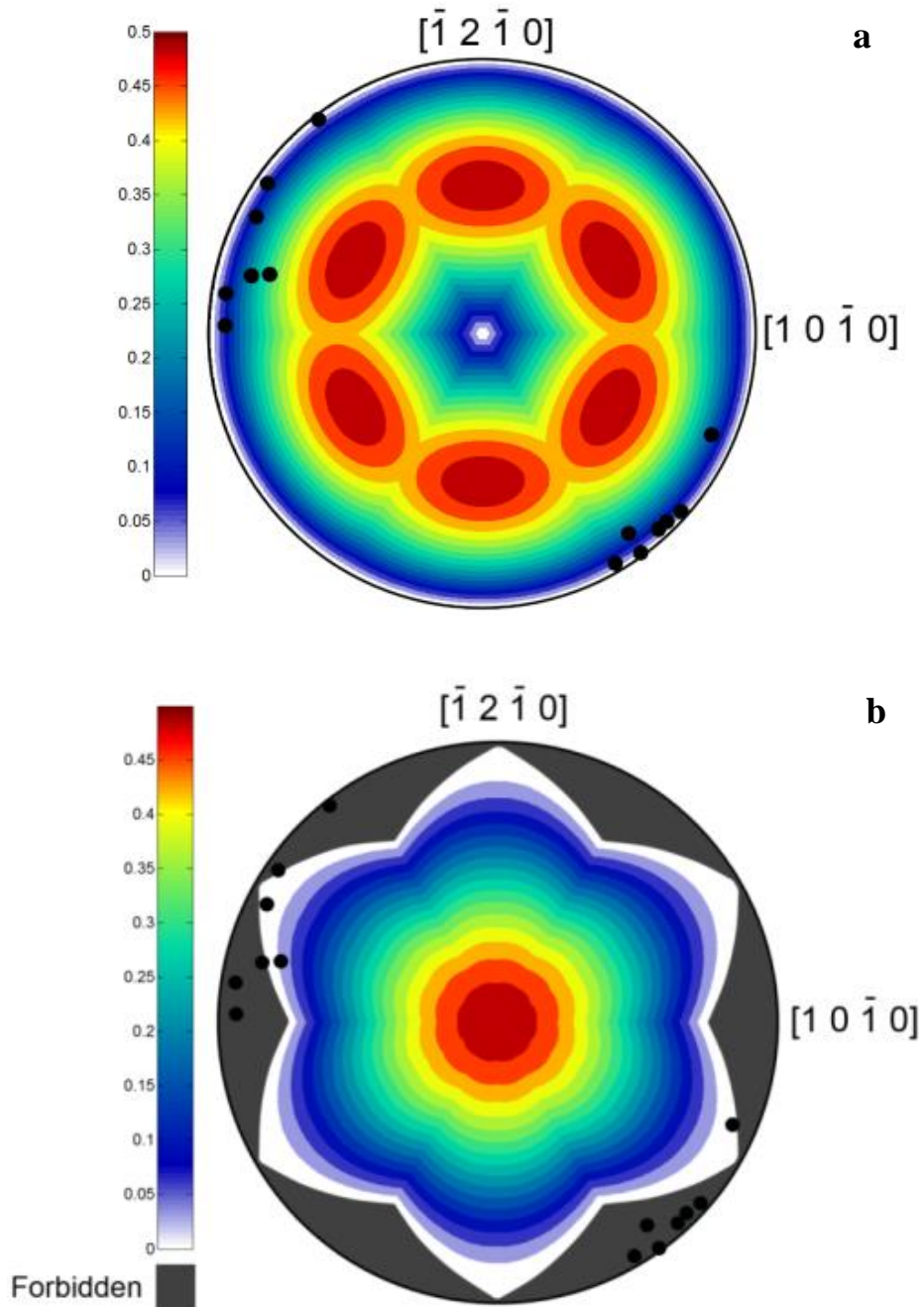
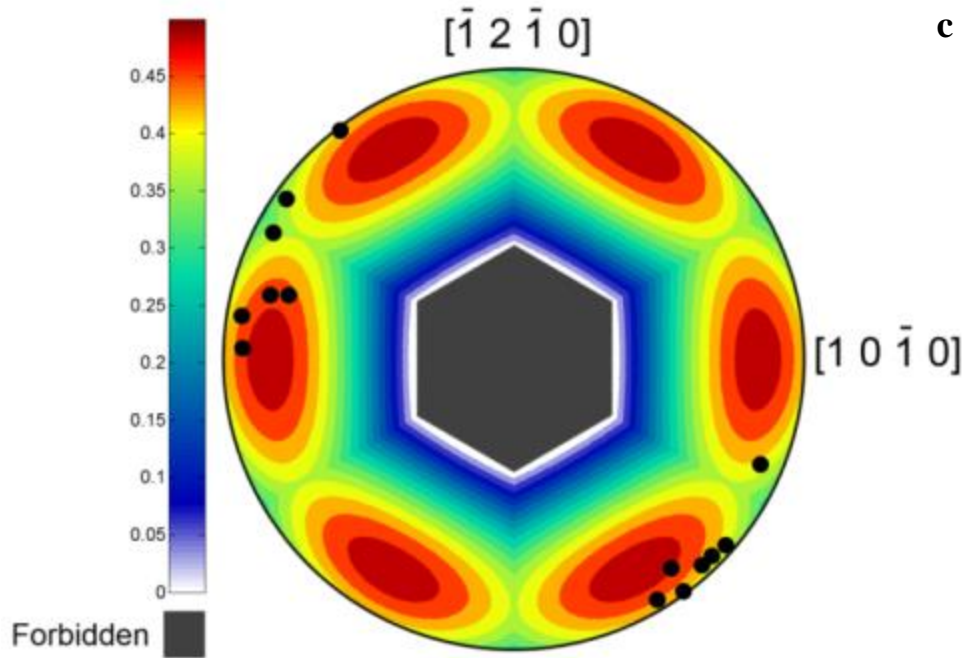


Figure 5-14 Maximum Schmid factor predictions of basal slip (a),  $\{10\bar{1}2\}$  twinning (b) and  $\{10\bar{1}1\}$  twinning (c). The inverse pole-figures reflect the orientation of tensile stress axis in reference frame of parent crystal. The spots were obtained from the transformation of the directions corresponding to maximum principal stress from the specimen reference frame to the crystallographic frame of the parent grains in which the cracks were observed.



### 5.5.3 TEM Observations of Slip Activity in Matrix and Double Twin

Figure 5-15 shows microstructure and corresponding diffraction patterns from a TEM sample taken from a region near a transgranular micro-crack. The twin boundaries are visible in the back-scattered image (Figure 5-15a) with the same orientation as the micro-crack. High density of the doubly twinned segments was observed in the TEM sample. The diffraction pattern revealed all of them as variant I with  $\langle 1 \bar{2} 1 0 \rangle / 38 \pm 3^\circ$  misorientation (as shown typically in Figure 5-15 b and c). Unlike a TEM study of the double twins made by Cizek et al. [31], no traces of the primary  $\{0 1 \bar{1} 1\}$  twinning was found in the current study. This observation along with the EBSD data imply that the  $\{0 1 \bar{1} 1\}$  twins are extremely unstable and therefore transformed mostly via the secondary twinning. High dislocation activity and high density of crystallographic faults were observed within the twinned segments as shown typically in Figure 5-16. Figure 5-16a shows a STEM image of a typical double twin. Tilting was done in such a fashion that the intensity of the basal poles were reduced and that of  $\{0 1 \bar{1} 1\}$  increased (Figure 5-16b). In this condition ( $g \cdot b \neq 0$  [65], [142]), the basal-type dislocations can be seen as straight segments along the basal traces in both matrix and twin. From a comparison in Figure 5-16 a and b, one could find significantly higher activity of basal dislocations in the twinned

segment than in the matrix. Figure 5-16c shows low angle grain boundaries with constituents dislocations along with stacking fault regions in a doubly twinned material. The diffraction pattern within this region revealed  $\sim 7^\circ$  misorientation about the  $\langle 1\bar{2}10 \rangle$  axis due to the activity of dislocations. Such crystallographic defects were not observed within the matrix.

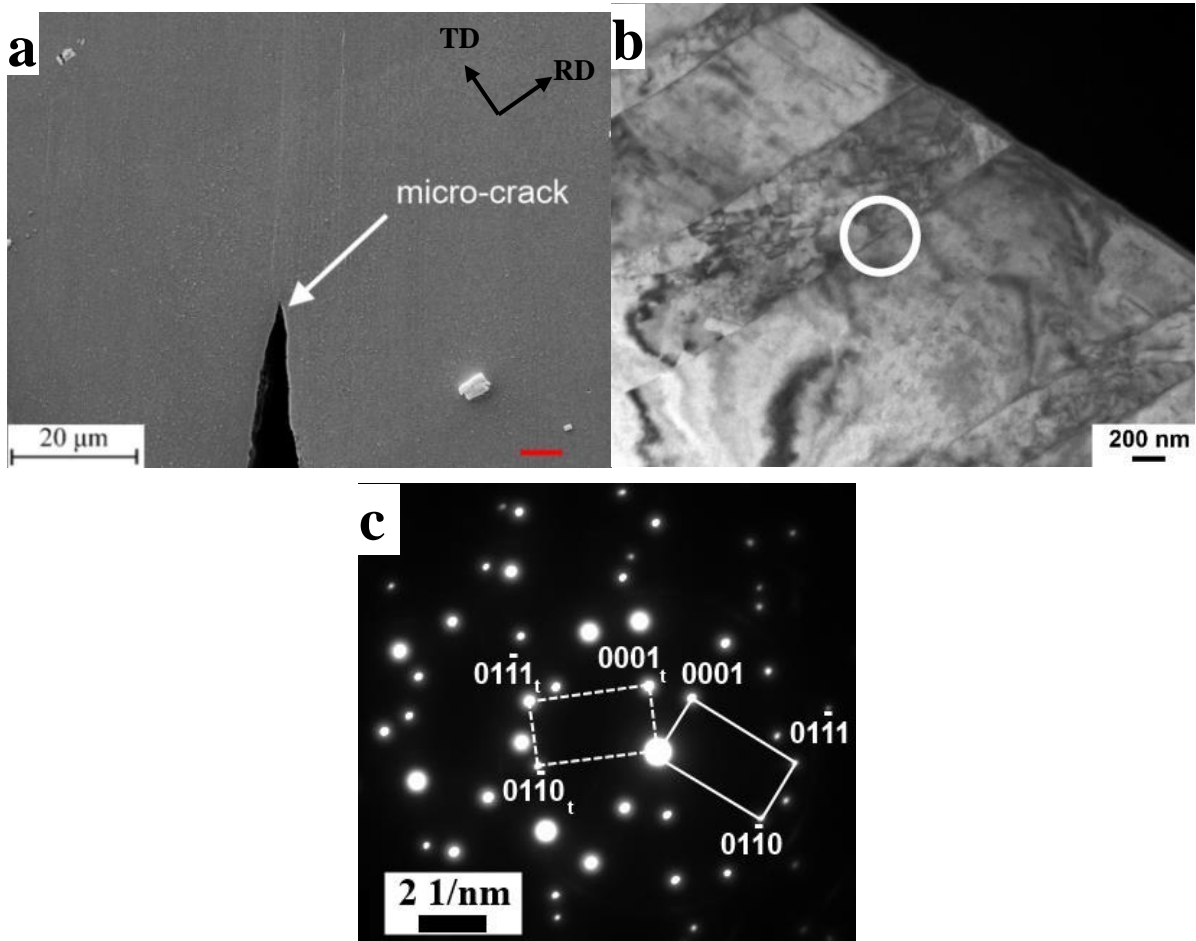
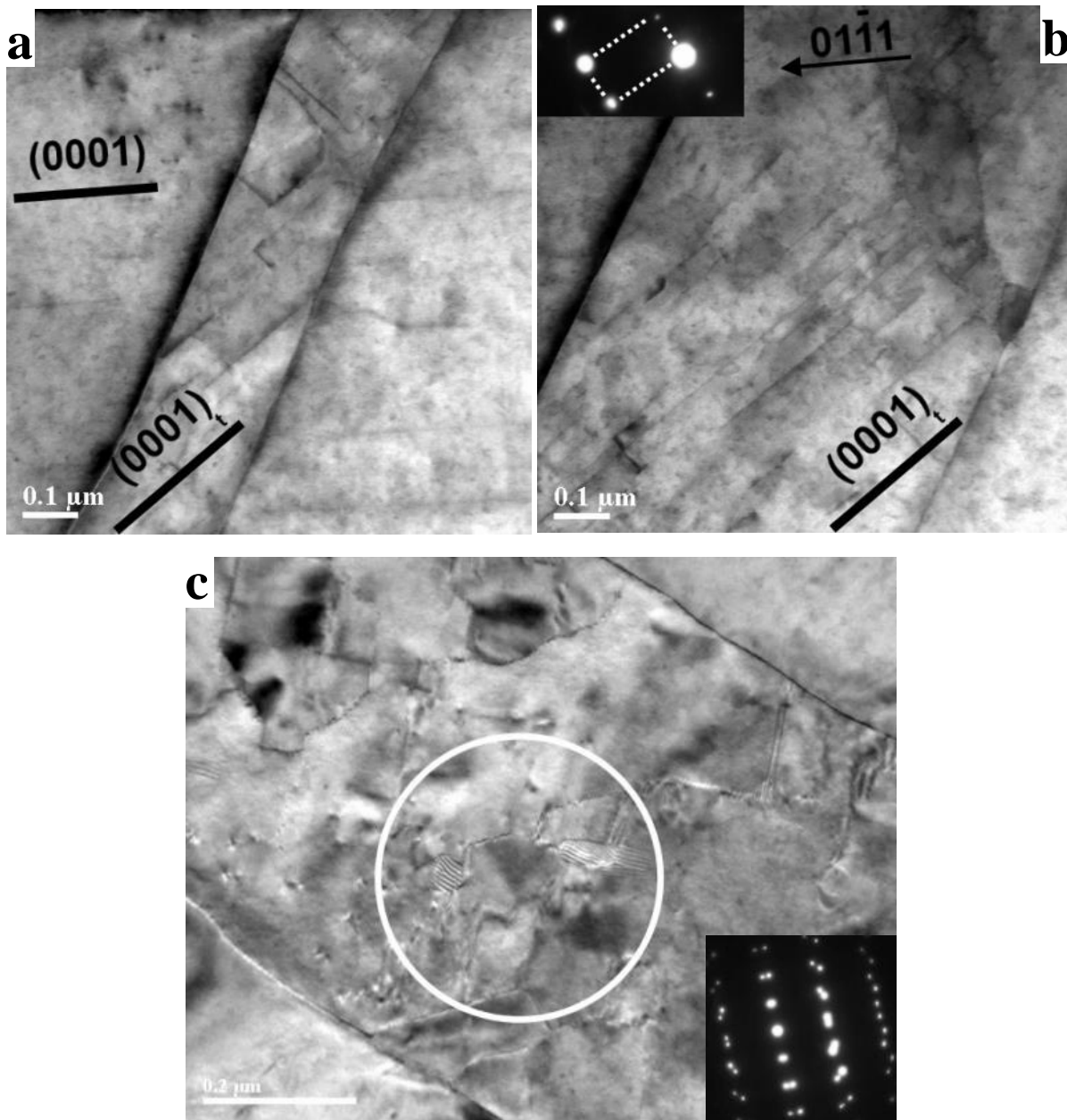


Figure 5-15 (a) FIB surface image of a fractured grain (twin boundaries are visible in BS mode); (b) TEM image from the double twins; (c) diffraction pattern showing a misorientation of  $\langle 1\bar{2}10 \rangle / 38^\circ$  at the twin boundary as encircled in (b)





**Figure 5-16 (a) STEM image from a double twin and matrix; (b) two beam diffraction condition from a double twin: the diffraction vector ( $g$ ) is shown by black arrow; (c) microstructure within a double twin showing dislocation arrays forming a low angle grain boundary**

## 5.6 Discussion

### 5.6.1 Schmid-type Behavior of $\{1\ 0\ \bar{1}\ 1\}$ Twinning

Due to strongly textured microstructure near the notch, the majority of the grains had c-axes almost perpendicular to the direction of maximum principal stress (as shown in Figure 5-12). In this condition a tensile stress produced contraction strains along the c-axis and thus activation of  $\{1\ 0\ \bar{1}\ 1\}$  twinning was expected. In order to study the Schmid-type behavior of the  $\{1\ 0\ \bar{1}\ 1\}$  twinning, the  $\tau_{RSS}$  values that applied on the six possible primary  $\{1\ 0\ \bar{1}\ 1\}$  twinning systems (in a given grain) were calculated. This procedure was done for 78 grains and the primary  $\{1\ 0\ \bar{1}\ 1\}$  twinning systems in these grains were identified from their orientations. In this study only those  $\{1\ 0\ \bar{1}\ 1\}$  twinning systems which contributed to formation of the variant I and II double twins (experimentally observed) were considered. The calculation procedure for variant selection is explained in details in Appendix D. Figure 5-17 a and b shows the frequency of occurrence of  $\{1\ 0\ \bar{1}\ 1\}$  twinning variants in terms of their  $\tau_{RSS}$  values and ranks respectively. Almost 60% of the twinning systems identified by EBSD were subjected to stress range of 70-100 MPa (Figure 5-17a). The CRSS for  $\{1\ 0\ \bar{1}\ 1\}$  twinning in AZ31 was previously determined to be ~100MPa in AZ31 alloy [19], [32]. It can be inferred from Figure 5-17b that almost 61% of the primary  $\{1\ 0\ \bar{1}\ 1\}$  twins formed in accordance with the most and second most heavily stressed systems. In those grains with only one variant activated, 62% of twinning occurred based on the first and second highly stressed systems (Figure 5-17c). It can be implied from these findings that Schmid law is a suitable approach to predict the occurrence of  $\{1\ 0\ \bar{1}\ 1\}$  twinning. This is consistent with the findings of Barnett et al. [32]. The deviation from the Schmid-type behavior occurred more frequently in the finer grains (<20  $\mu\text{m}$ ) than the coarse grains (>40 $\mu\text{m}$ ).

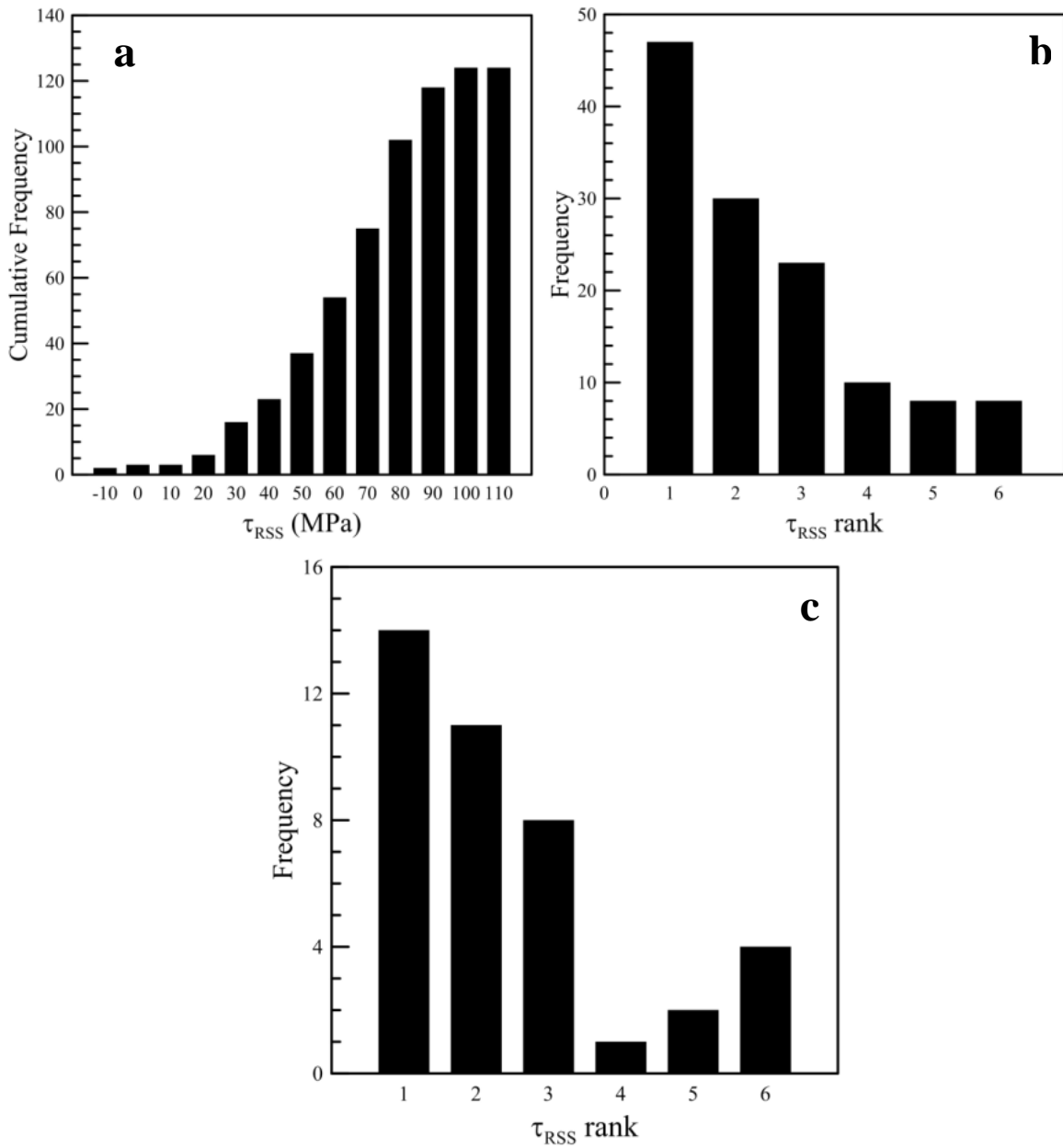


Figure 5-17 (a) Cumulative frequency of primary  $\{1\ 0\ \bar{1}\ 1\}$  twinning incidences in terms of their  $\tau_{RSS}$  value; (b) frequency of  $\{1\ 0\ \bar{1}\ 1\}$  twinning incidences in terms of their  $\tau_{RSS}$  rank for all grains and (c) for cases with one twin per grain

## 5.6.2 Strain Accommodation and Cracking

The above discussion implied that the  $\{1\ 0\ \bar{1}\ 2\}$ - $\{1\ 0\ \bar{1}\ 1\}$  double twins were likely to form in grains only when their primary  $\{1\ 0\ \bar{1}\ 1\}$  twinning systems were subjected to high shear stresses. Figure 5-13 demonstrates that the applied shear stresses resolved onto the basal slip systems of the fractured grains, are very low. The maximum  $\tau_{RSS}$  value for the basal glide corresponding to fractured grains were determined to be within the range of 15-45 MPa. The numerically determined CRSS values for basal slip in Mg-Al-Zn alloys are largely different from one report to another within the range of 10-50 MPa [20], [143], [144] depending on the method of analysis. This implies that a competition exist between twinning and slip systems. The former was subjected to a high resolved shear stress but with high CRSS, while the latter is under low stress but with low CRSS. It is expected that the basal glide systems were not activated until the applied load was close to the magnitude of load-to-failure.

It is possible that the strains in the grain were accommodated partially by the prismatic slip due to high basal texture; It was confirmed that the prismatic slip undergoes solute softening while basal slip is hardened by addition of common alloying elements within the solubility limits [145]; however the lattice resistance against the prismatic slip is still high (CRSS was determined to be within the range of 90-100 MPa for AZ31 [20], [146], [147]). Moreover, a high magnitude of normal stress was generated along the sheet's TD ( $\sigma_{TD}$  as defined in Table II) near the notch which reduced the shear stresses on the prismatic planes. Thus, like basal slip, prismatic slip was likely activated when the applied load was close to load-to-failure.

At the same time the  $\tau_{RSS}$  on the  $\{1\ 0\ \bar{1}\ 1\}$  planes could reach up to the value for CRSS. The stress state relative to the fractured grains orientations is such that it produces high shear stress on two or more  $\{1\ 0\ \bar{1}\ 1\}$  planes. This is the reason why the micro-cracks were observed within the grains having intersecting twin boundaries. The twins were mostly developed from one grain boundary to the as observed in Figure 5-9 and Figure 5-10. The twins nucleated preferentially in certain points on the grains boundaries with stress concentration which is majorly due to intersection of a twin within a neighboring grain with the shared grain boundary (as observed typically in Figure 5-10). Also the finer intersecting twins nucleate mostly from the boundaries of their more developed counterparts (as shown typically in Figure 5-9a and Figure 5-10). Due to very small width, the contraction/double twins did not change the general texture. But the crystal reorientation by double twinning, produced

high resolved shear stresses on basal slip systems. Although at this point basal slip was likely to start in the matrix (since  $\tau_{RSS}$  reached CRSS) its activity was limited (as shown typically in Figure 5-16) since the crystal reorientation by twinning acted as an obstacle against it. Therefore, massive basal slip activity occurred in the thin double twin lamellae to accommodate the imposed strains in the individual grains. This led to early void nucleation and transgranular cracking. The calculation results showed that the doubly twinned segments of variants I and II are more favorably orientated for the basal glide than those of variants III and IV. The reason why the double twins of variant I were observed more frequently than the other types was previously explained by the minimization of the compatibility strains imposed by the secondary  $\{1\ 0\ \bar{1}\ 2\}$  twinning inside the primary  $\{1\ 0\ \bar{1}\ 1\}$  twin [32]. Since the misorientation angle between the habit planes of the two successive twinning systems in variant I are smallest ( $18.8^\circ$ ) among the four variants, they face less barriers against the lateral growth.

The grains poorly oriented to activate the  $\{1\ 0\ \bar{1}\ 1\}$  twinning (such as grain 3 in Figure 5-9a), were more likely to accommodate the strains by basal glide. Consequently it can be suggested that such grains were less prone to the strain localization and transgranular cracking. It should be noted that the cracking is expected to finally occur in these grain if they were in the middle of the primary crack pathway. Since the cracks form in the neighboring grains, the local stresses are further intensified.

### 5.6.3 Grain Size Effects

The grain growth in HAZ is non-uniform and small grains ( $10\ \mu\text{m} < d < 30\ \mu\text{m}$ ) were frequently observed along with the coarse grains. Though, transgranular cracking was mostly observed in the coarse grains than the finer ones. The reason can be attributed to the fact that the twinning activity is higher in coarse grained structure (i.e. more potential sites for the crack nucleation) than the fine grains. It was confirmed that the critical stress to activate twinning increases more rapidly than the that for slip, with decreasing grain size [65], [134].

## 5.7 Summary

This work has been concerned with characterization of micro-mechanisms leading to transgranular fracture in magnesium AZ61 in a localized stress field. Microstructural and numerical analyses at the fracture zone led to the following conclusions:

1. High double twinning activity was observed at the vicinity of notch during mechanical loading. The transgranular micro-cracks were generated with the identical orientation as the double twin habit planes. The double twins which involved rotation of  $\langle 1 \bar{2} 1 0 \rangle / 37.5^\circ$ , formed more readily in the microstructure than those of the other three variants.
2. The strong basal texture in microstructure at the vicinity of notch provided favorable condition for activation of  $\{1 0 \bar{1} 1\}$  twinning. The experimentally observed primary  $\{1 0 \bar{1} 1\}$  twinning systems demonstrated a Schmid-type behavior. The majority of the  $\{1 0 \bar{1} 1\}$  twinning systems were activated when the resolved shear stress reached a range of 70-100 MPa.
3. The crystal reorientation due to double twinning, which involved  $\langle 1 \bar{2} 1 0 \rangle / 37.5^\circ$  crystallographic rotation, triggered massive basal slip activity, leading to early void nucleation and transgranular fracture.
4. Those grain with difficult orientation for basal activity demonstrated more tendencies to plastically deform by  $\{1 0 \bar{1} 1\}$  twinning and are more susceptible to shear localization and transgranular fracture.

# Chapter 6

## Microstructural Effects on Mechanical Properties and Failure of AZ80/ZEK100 Spot Weld

### 6.1 Introduction

It was discussed in chapter 5 that formation of  $\{1\ 0\ \bar{1}\ 1\}$ - $\{1\ 0\ \bar{1}\ 2\}$  double twins within the grains in the HAZ led to shear localization and transgranular fracture. Double twinning readily occurred in the HAZ of AZ61 since the stress condition and strong basal texture produced high shear stresses on the  $\{1\ 0\ \bar{1}\ 1\}$  primary twinning systems. Hypothetically, if the microstructure changes so activation of  $\{1\ 0\ \bar{1}\ 1\}$  twinning systems is delayed, the fracture process will be delayed as well. In this chapter, the effects of texture and grain size on fracture properties were of concern. In this regard, fracture in AZ80/ZEK100 dissimilar joint was studied. ZEK100 demonstrated a relatively more randomized texture compared to the AZ series magnesium alloys. Moreover, it demonstrated very high resistance against grain growth during isothermal heat treatment. It was shown in this study that the HAZ in ZEK100 is able to accommodate the inelastic strain more effectively than the HAZ in AZ80 and thus in a fracture competition between ZEK100 and AZ80 in a dissimilar joint, failure occurred preferentially in AZ80. The work presented and described in this chapter will be submitted for publication by Niknejad et al. [148].

### 6.2 Experiments

AZ80 and ZEK100 sheets were used for the dissimilar and similar welding. In case of dissimilar welding (AZ80/ZEK100), welding current was selected as 36 kA. To have a better understanding of fracture competition between AZ80 and ZEK100, TS tests were also conducted on the spot welds of similar joints of the two alloys i.e. ZEK100/ZEK100 and AZ80/AZ80. In order to normalize the effect of nugget size, welding current (26 kA and 36 kA for AZ80/AZ80 and ZEK100/ZEK100 joints respectively) was selected in a fashion to produce joints with almost identical nugget diameters (9.67 mm and 9.38 mm for ZEK100/ZEK100 AZ80/AZ80 joints, respectively). The post-weld heat treatment (PWHT) was performed on the similar and dissimilar joints at 420°C for 0.5 hr followed by cooling in air. The PWHT temperature was selected based on the thermochemical calculations by FactSage software [104] in order to dissolve the Mg-Al and Mg-Zn intermetallic compounds across the weld.

3 specimens were mechanically tested by TS test in each condition. Tensile loading was parallel to the rolling direction of the sheets. In order to accurately measure the specimen elongation during the TS test, the test coupons were assembled with the spacers to accommodate the extensometer.

### 6.3 Calculation of Energy-to-Failure for a Unit of Spot Weld

The mechanical properties of a spot weld, in quasi-static tensile shear test, are normally quantified by the maximum amount of force a weld can withstand; however no information regarding the weld ductility is obtained from such measurement. On the other hand, the strain hardening exponent in hcp metals under tension is significantly lower than that of bcc and fcc metals. This has been related to the lack of slip systems in the hcp lattice along with localized texture softening [19], [32]. Thus, the localized plasticity at the notch may not result in significant increase in the measured load. Therefore, weld ductility should be taken into account in order to discuss the microstructural effects.

It has been suggested that fracture, during tensile shear loading, initiates when the material is no longer able to tolerate the imposed strain energy [4], [149]. In this study the resistance of RSW against fracture was evaluated via calculation of energy-to-failure which may be determined from the area under the load vs. displacement (as shown schematically in Figure 6-1) up to failure [10]. The energy-to-failure ( $E_c$ ) may be normalized for a unit of weld nugget, accounting for material thickness ( $t$ ) and nugget diameter ( $d$ ) [150]:

$$E_c = \frac{\int_0^{x_c} F dx}{\pi dt} \quad \text{eq.6.1}$$

Where  $F$  is the applied load,  $dx$  is the differential displacement and  $x_c$  is the specimen displacement at the peak load.

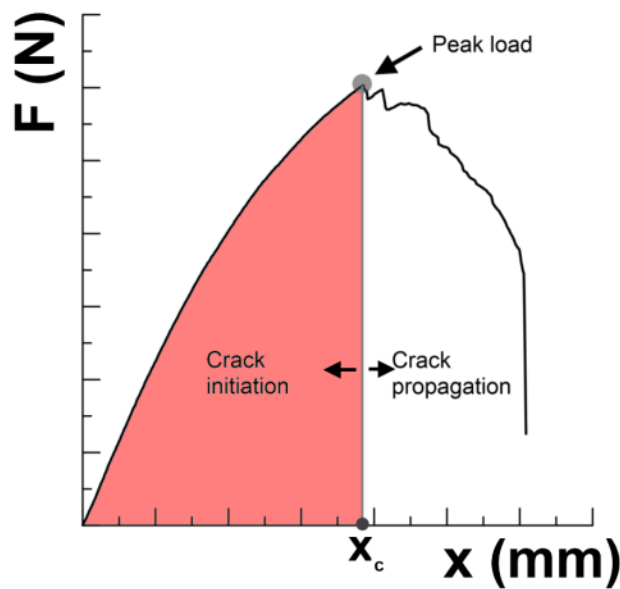


Figure 6-1 Schematic of load ( $F$ ) vs. extension ( $x$ ) in TS test of a spot weld; the area for calculation of energy-to-failure is highlighted



## 6.4 Results

### 6.4.1 Microstructural Observations

#### 6.4.1.1 BM Microstructure

Figure 6-2 shows SEM image of ZEK100 BM from the sheet's TD view. Based on the chemical composition as shown in Table 6-1, three types of particles were observed in the microstructure: particles which are likely to be a ternary compound of Mg-Zn-Nd (P1 and P2), particles enriched in Nd (P3) and particles enriched in Ca (P4). Based on thermochemical analysis using the FactSage software package (Figure 6-4a), the Mg-Nd particles were likely to be of  $Mg_{41}Nd_5$ .

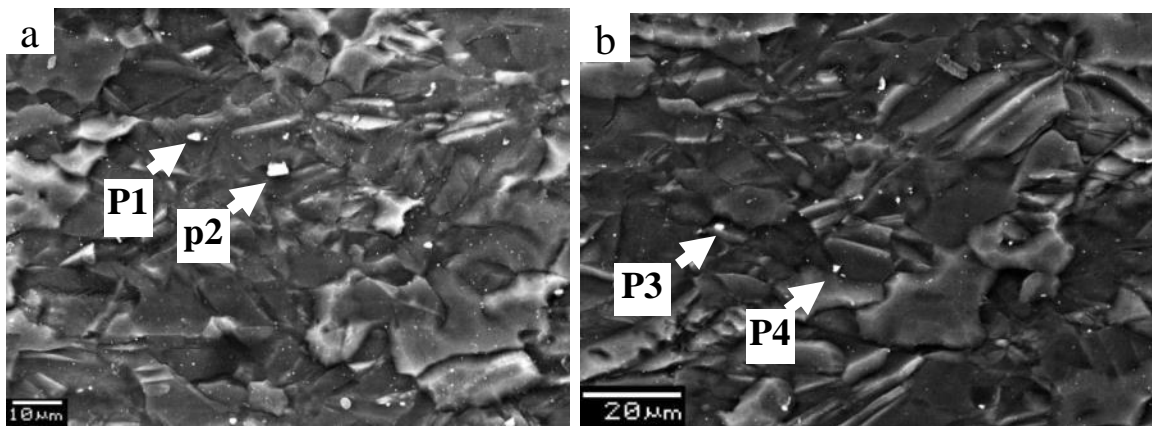


Figure 6-2 SEM micrographs taken from microstructure of the as-received ZEK100 alloy, the chemical composition of the particles shown by arrows are illustrated in Table 6-1

Table 6-1 Chemical composition (weight percent) of the particles shown in Figure 6-2

	Mg	Zn	Nd	Zr	Ca	Fe
P1	52.03	23.16	24.81	-	-	-
P2	39.27	27.93	32.9	-	-	-
P3	65.8	-	34.2	-	-	-
P4	83.17	-	-	-	16.83	-

#### 6.4.1.2 Weld Microstructure and Phase Analysis

Figure 6-3a shows the nugget shape of a dissimilar joint. The half-nugget produced in the AZ80 side was significantly larger than that in the ZEK100 side. Figure 6-3b shows the dependence of nugget size on the welding current for the similar welding (i.e. ZEK100/ZEK100 and AZ80/AZ80 joints). With the same welding parameters, the weld nugget produced in the AZ80 was larger than the one in ZEK100. The

difference in the weld pool size was associated with the difference in the melting point of the two alloys. It was found via FactSage thermochemical calculations that the equilibrium melting temperatures of AZ80 and ZEK100 base alloys are 603.2°C and 647.7°C respectively (Figure 6-4). Consequently, with the assumption of balanced temperature distribution in the two sheet metals during resistance welding, a larger weld pool is expected to be produced in the AZ80 side.

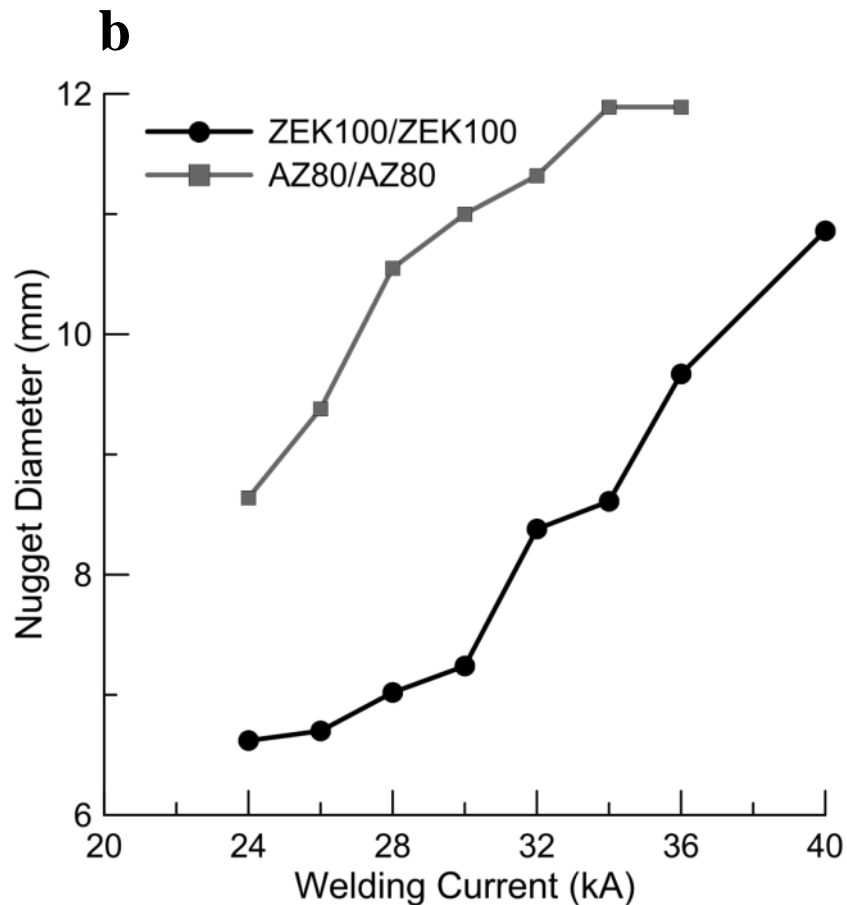
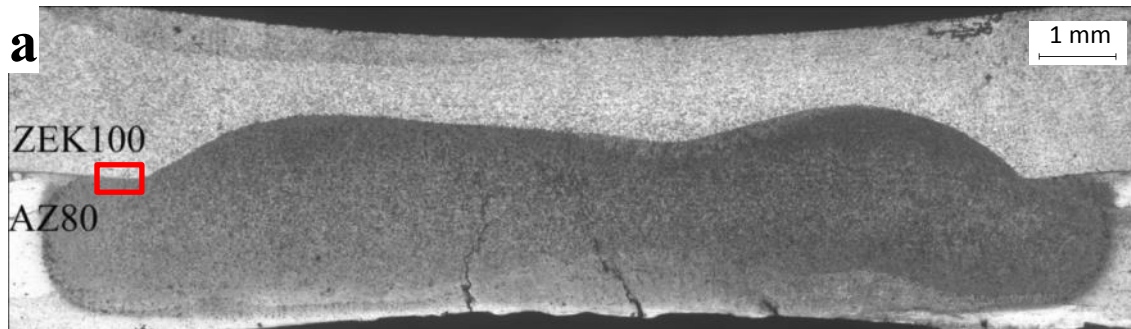
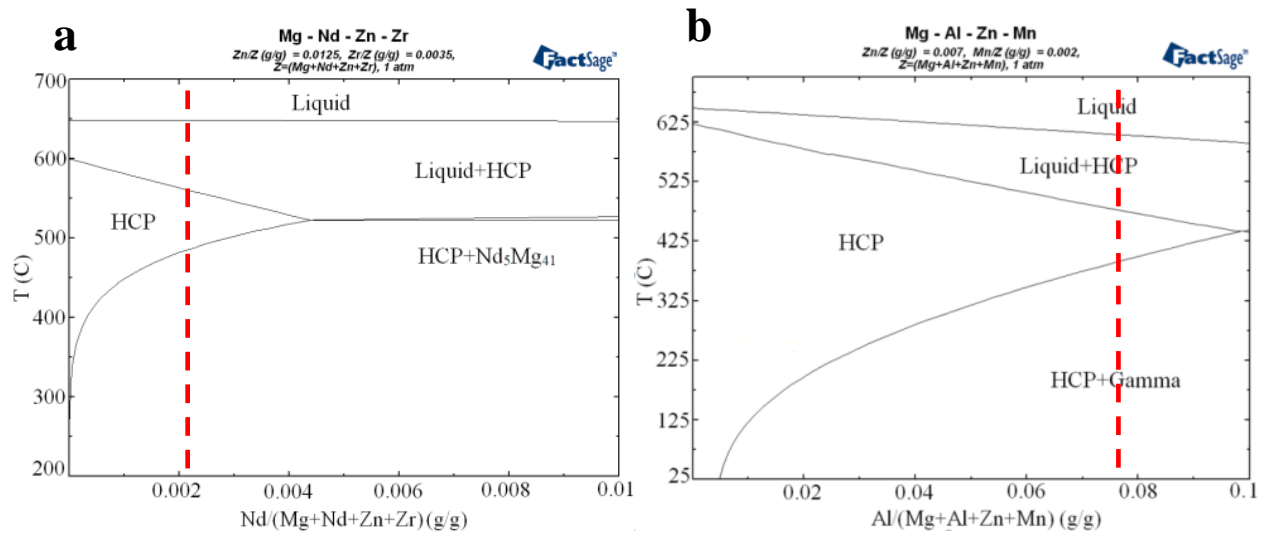
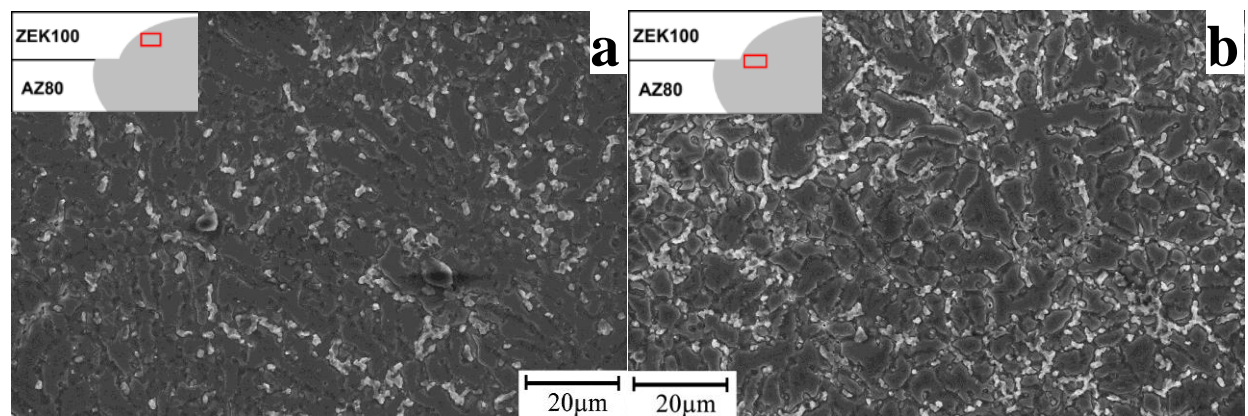


Figure 6-3 (a) Overview of the nugget produced in ZEK100/AZ80 joint; (b) Nugget diameter vs. welding current for AZ80/AZ80 and ZEK100/ZEK100 spot welds



**Figure 6-4** Mg-rich area of binary phase diagrams (a) Mg-Nd (Zn:1.25wt.%, Zr:0.35wt.%) and (b) Mg-Al (Mn:0.2wt% , Zn:0.7wt.%). The dashed lines show the chemical composition in ZEK100 (a) and AZ80 (b)

Figure 6-5 a-c shows the initial microstructure of FZ near the edge of the nugget from ZEK100 to AZ80 side. The  $Mg_{17}Al_{12}$  intermetallic compound (IMCs) were observed even in the extreme top side of the half-nugget in ZEK100 side (Figure 6-5a); however the volume fraction of IMCs decreased by progressing from the half-nugget produced in the AZ80 side (Figure 6-5c) to the one produced in ZEK100 side (Figure 6-5a). The volume fraction of IMCs was maximum near the nugget edge where the AZ80 melt was in contact with the un-melted ZEK100 substrate and thus the least dilution of Al-rich liquid occurred.



**Figure 6-5** SEM micrographs taken from FZ close to the edge of ZEK100/AZ80 nugget at (a) ZEK100 side; (b) near the boundary of the two sheets and (c) AZ80 side

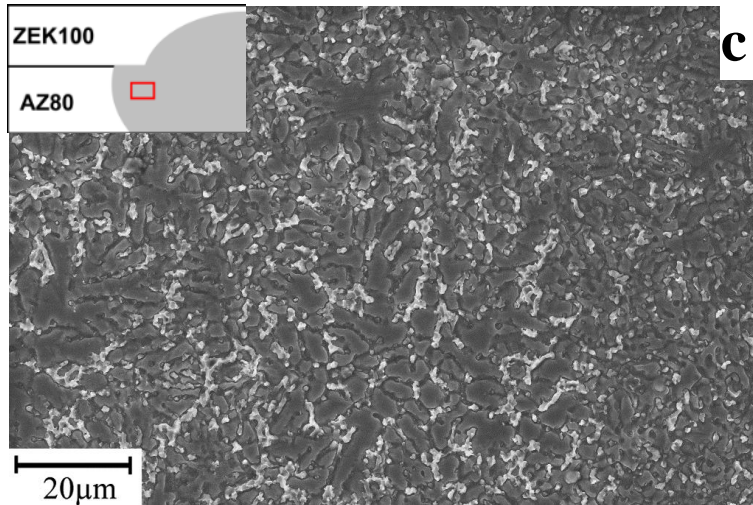


**Figure 6-5 continued**

Figure 6-6 shows typical phase particles (other than  $Mg_{17}Al_{12}$ ) which were formed during solidification of the FZ. The EDS results for the particles highlighted by white arrows are presented in Table 6-2. The relatively large (5-12 $\mu m$ ) particles, enriched in Al and Mn are likely to be of  $Al_8Mn_5$  phase. Two other particles enriched in Al-Ca and Al-Zr were also observed in the FZ.

Figure 6-7 shows the AZ80/ZEK100 interface near the nugget edge. It was observed that the discontinuity between the two sheet metals progressed into the FZ of the AZ80 side. Thus, the notch root no longer existed at the HAZ of AZ80 but progressed into the FZ of AZ80. By advancing from the nugget edge toward the center, a complete joint appeared in the interface free of any discontinuity. During welding, ZEK100 un-melted BM grains at the nugget edge acted as a substrate for nucleation of crystals in the AZ80 melt. The melt from the AZ80 was in close contact with the ZEK100 un-melted substrate and wetted the grains completely. The solidification started via an epitaxial growth from ZEK100 substrate.

**Table 6-2 Chemical composition of the particles shown in Figure 6-6**

	P1	P2	P3	P4	P5	P6
Mg K	50.3	84.2	57.8	59.7	47.2	76.6
Al K	24.3	8.5	7.5	19.3	24	13.6
Mn K	25.4	-	-	21	28.8	9.7
Zn	-	-	-	-	-	-
Zr	-	-	34.7	-	-	-
Ca	-	7.3	-	-	-	-

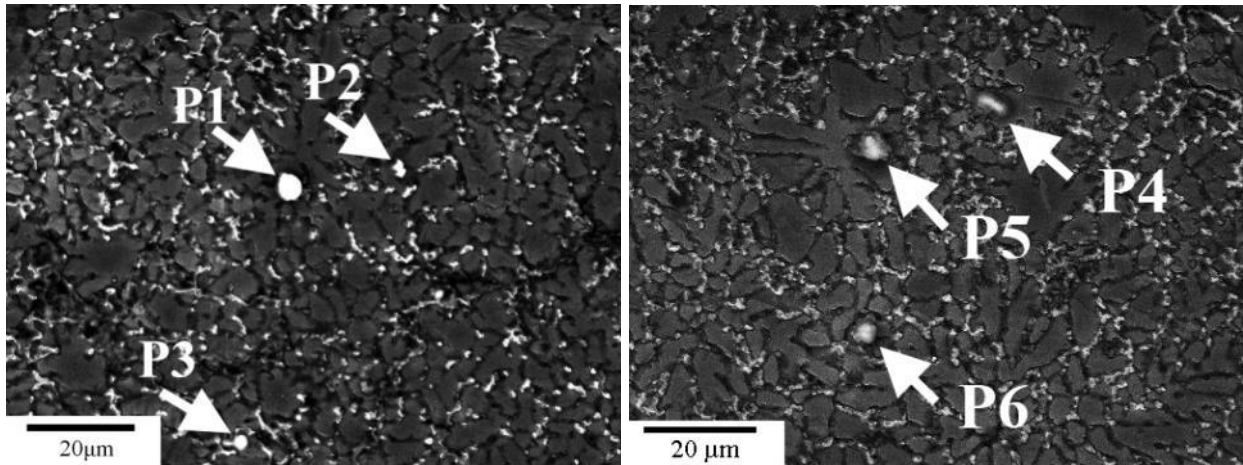


Figure 6-6 SEM micrographs taken from FZ of ZEK100/AZ80 (the chemical compositions of the highlighted particles are shown in Table 6-2)

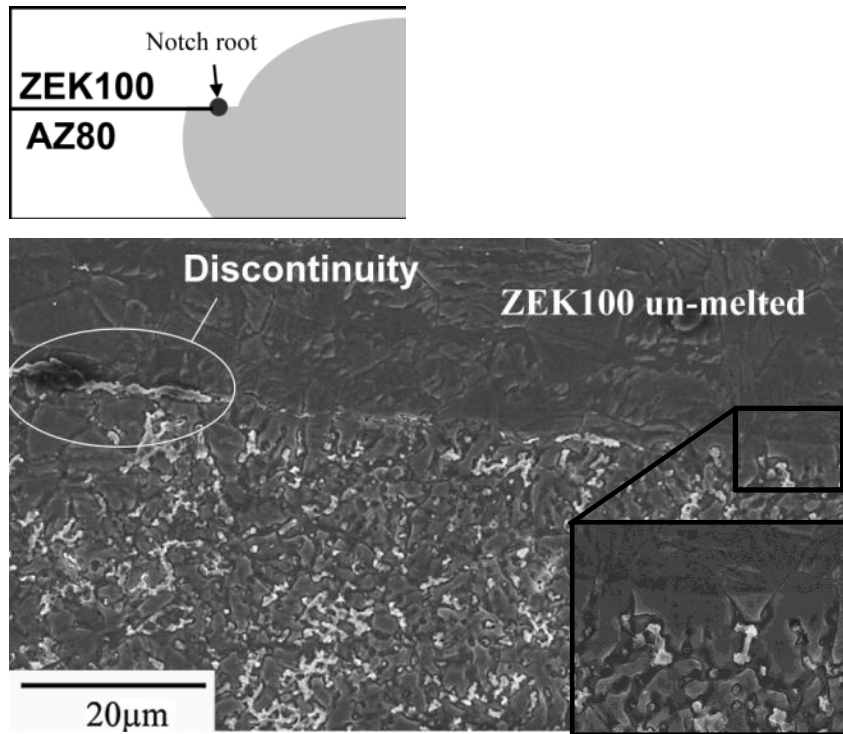


Figure 6-7 SEM micrograph at the edge of the nugget as highlighted in Figure 6-3a

#### 6.4.2 Mechanical Characteristics and Failure mode

Figure 6-8 shows tensile shear response of RSW coupons produced by AZ80/ZEK100, ZEK100/ZEK100 and AZ80/AZ80 joint combinations. Failure mode is also plotted schematically for each joint/condition. Figure 6-9 summarizes the mechanical test results for the similar and dissimilar joints. It is clear from Figure 6-8a and Figure 6-9 that the AZ80/ZEK100 weld in the as welded condition suffered from poor

ductility. Figure 6-10a shows the cross section of the AZ80/ZEK100 weld after the TS test. The crack initiated at the notch-tip in the interface and propagated within the FZ of AZ80 through the thickness towards the free surface. The joint produced in the AZ80/ZEK100 interface was strong enough so the crack did not travel along the interface.

By application of PWHT on AZ80/ZEK100 nugget, the ductility as well as load-to-failure were substantially improved. Figure 6-10b shows the cross section of the AZ80/ZEK100 weld in heat treated condition after TS test. It is interesting that the through-thickness crack initiated and propagated within the HAZ of AZ80, far from the notch root. Unlike the crack appearance in the as welded nugget, the crack in the heat treated nugget appeared to have sharp edges and its pathway changed abruptly. This observation implied that the AZ80/ZEK100 joint in the heat treated condition suffered from poor ductility of HAZ on the AZ80 side.

The nugget of ZEK100/ZEK100 demonstrated a superior combination of strength/ductility over that of AZ80/AZ80. This is associated with the fact that the nugget of ZEK100/ZEK100 was able to more effectively accommodate plastic deformation than that of AZ80/AZ80. Failure mode of AZ80/AZ80 joint implies that the early fracture (in both as welded and heat treated conditions) was caused due to the low ductility of HAZ; however the microstructure of HAZ in ZEK100/ZEK100 nugget demonstrated higher ductility than that of FZ so the fracture occurred in interfacial mode (Figure 6-11). The PWHT appeared not to affect the mechanical performance and failure mode of ZEK100/ZEK100 nugget; however it significantly improved the mechanical response of AZ80/AZ80 joint and changed the failure mode from nugget pull-out to through thickness.

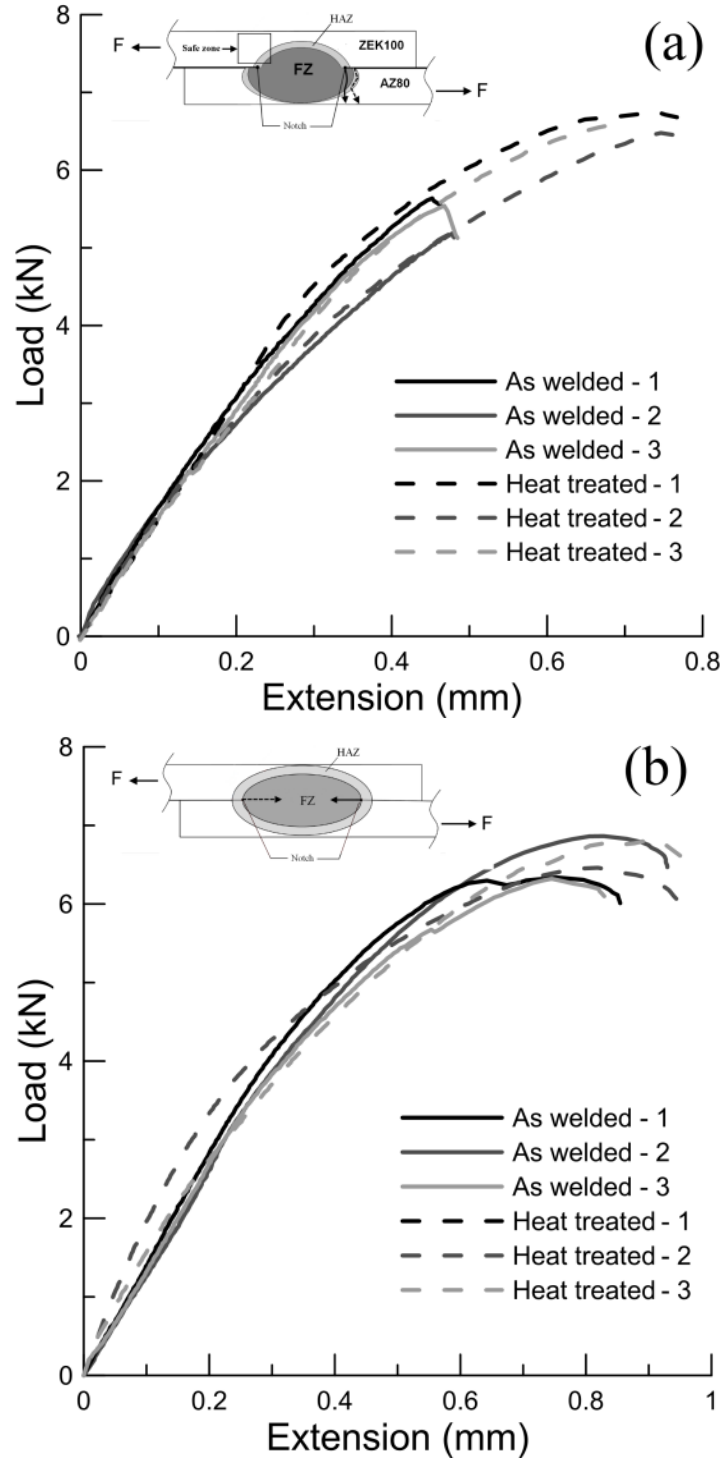


Figure 6-8 Tensile shear response of the spot welds for (a) ZEK100/AZ80 (nugget diameter in ZEK side: 9.51 mm); (b) ZEK100/ZEK100 (nugget diameter: 9.67 mm) and (c) AZ80/AZ80 (nugget diameter:9.38 mm) joint combinations in the as welded and heat treated conditions; The arrows (solid for as welded and dashed for the heat treated) on the schematics demonstrate the fracture mode/location.

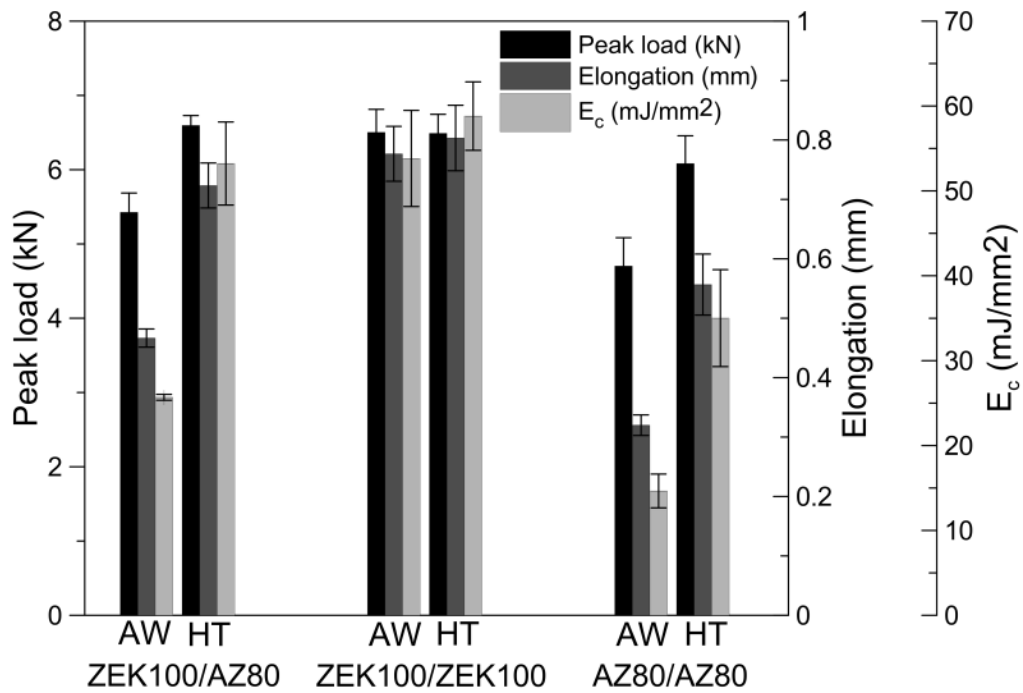
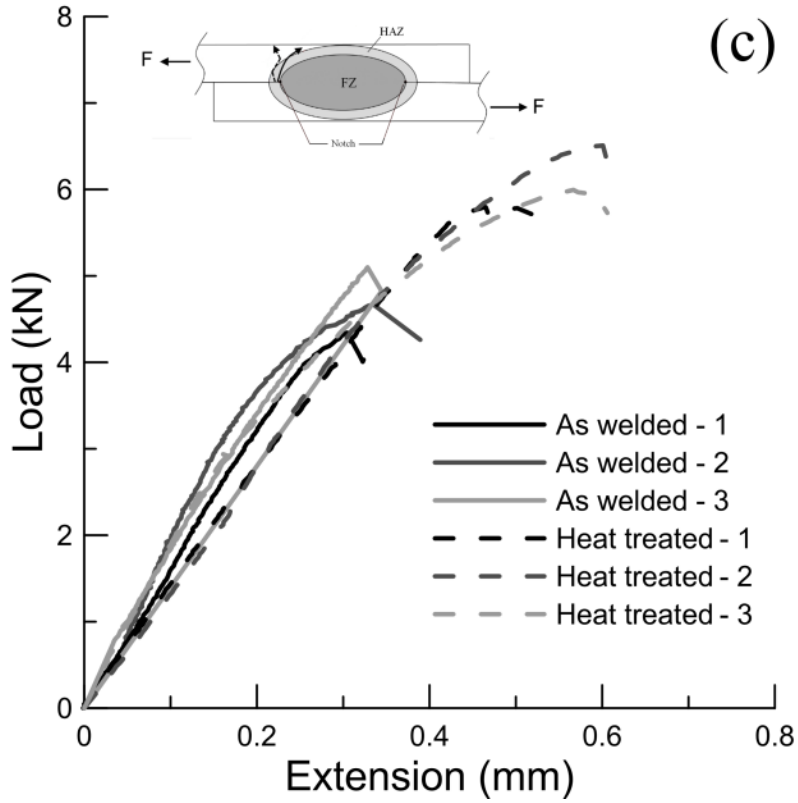


Figure 6-9 Tensile shear test results for three RSW coupons (for each joint/condition) for ZEK100/AZ80, ZEK100/ZEK100 and AZ80/AZ80



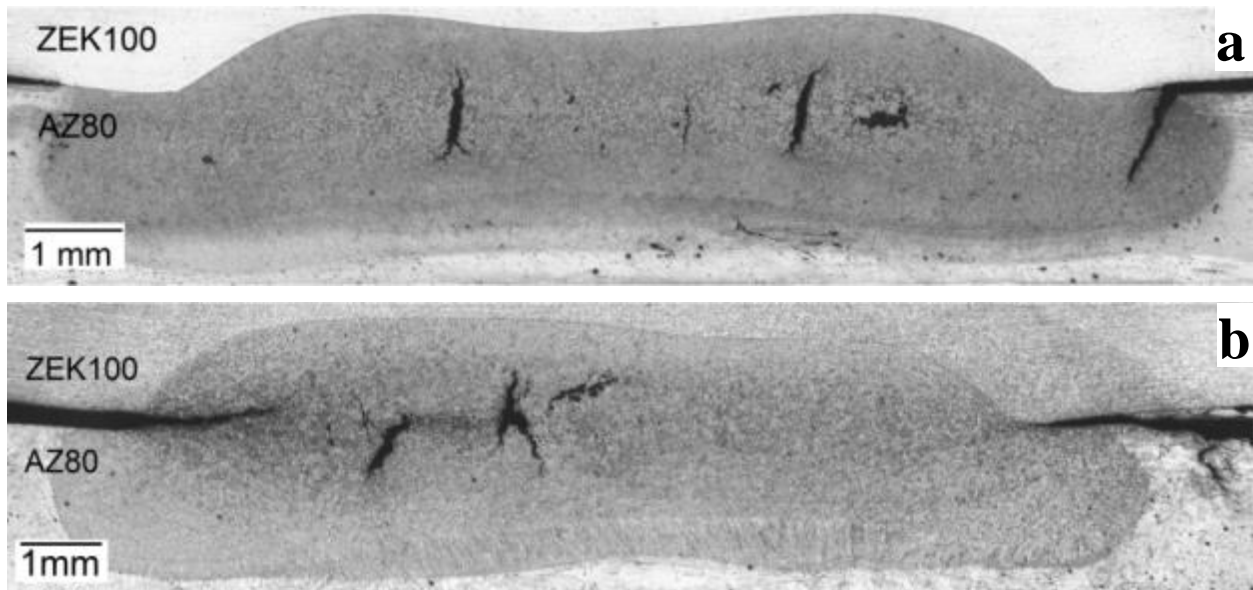


Figure 6-10 Overview of AZ80/ZEK100 nugget after the tensile shear test (stopped at load-to-failure): (a) As welded and (b) heat treated conditions

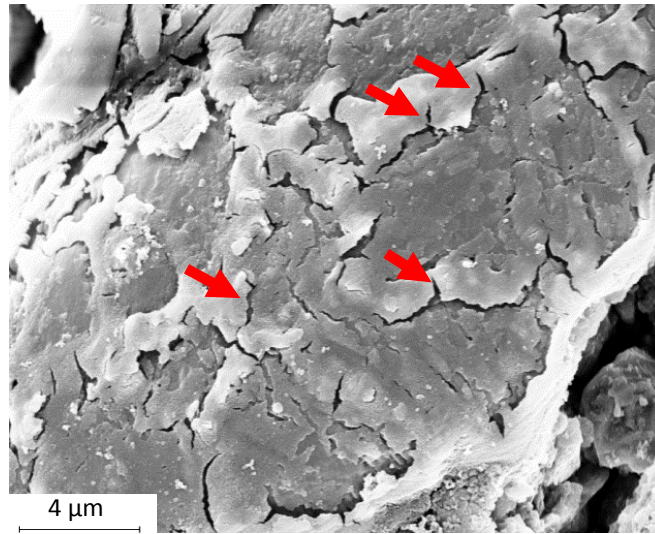


Figure 6-11 Failure in ZEK100/ZEK100 weld in as welded condition

### 6.4.3 Fracture Mechanisms and Microstructural Effects

#### 6.4.3.1 As Welded Condition

Figure 6-12a shows the microstructure near the developed crack into the FZ. A high density of micro-cracks was observed. Such micro-cracks mostly generated within the  $Mg_{17}Al_{12}$  IMCs or at the  $Mg/Mg_{17}Al_{12}$  interface. Fracture preferentially occurred in FZ of AZ80, since this region was found to have the highest volume fraction of IMCs (Figure 6-5c).



**Figure 6-12 Microstructure near crack in ZEK100/AZ80 weld**

#### 6.4.3.2 Post-Weld Heat Treated Condition

Close investigation of the fracture zone in AZ80/ZEK100 nugget in the heat treated condition, revealed high twinning activity (Figure 6-13a). These twins appeared to start from one grain boundary to another with very low lateral growth. In most cases, the orientation of the crack is the same as the orientation of the twins. Twinning activity was observed to be lower in the HAZ of ZEK100 (Figure 6-13b). From this observation as well as the load vs. displacement plot, it can be concluded that cracking is associated with plasticity in the post weld heat treated weld. The fracture process zone also demonstrated traces of transgranular micron-scale cracks/voids (as highlighted by white arrows in Figure 6-13a) with the same orientation of the habit planes of the fine twins formed profusely within the fractured grain. Via the application of EBSD analysis, these twins were characterized as  $\{1\ 0\ \bar{1}\ 1\}-\{1\ 0\ \bar{1}\ 2\}$  double twins with a misorientation of  $\langle 1\ \bar{2}\ 1\ 0 \rangle / 37.5^\circ$  (Figure 6-14). The doubly twinned segments were reoriented so that the basal poles were rotated from the sheet's normal direction (ND) towards RD, and thus the twins are favorably oriented for the basal slip activity. In order to understand why fracture occurred preferentially in the HAZ of AZ80, a comparison of microstructure near the notch root at AZ80 and ZEK100 sides was carried out:

By application of PWHT, the  $Mg_{17}Al_{12}$  IMCs in the FZ and HAZ of AZ80 were dissolved in the  $\alpha$ -Mg matrix (Figure 6-15). This led to improved mechanical performance of the dissimilar joint (Figure 6-9a). Figure 6-15 also shows that PWHT resulted in abnormal grain growth in HAZ of AZ80; however the HAZ in ZEK100 retained its fine-grained microstructure.

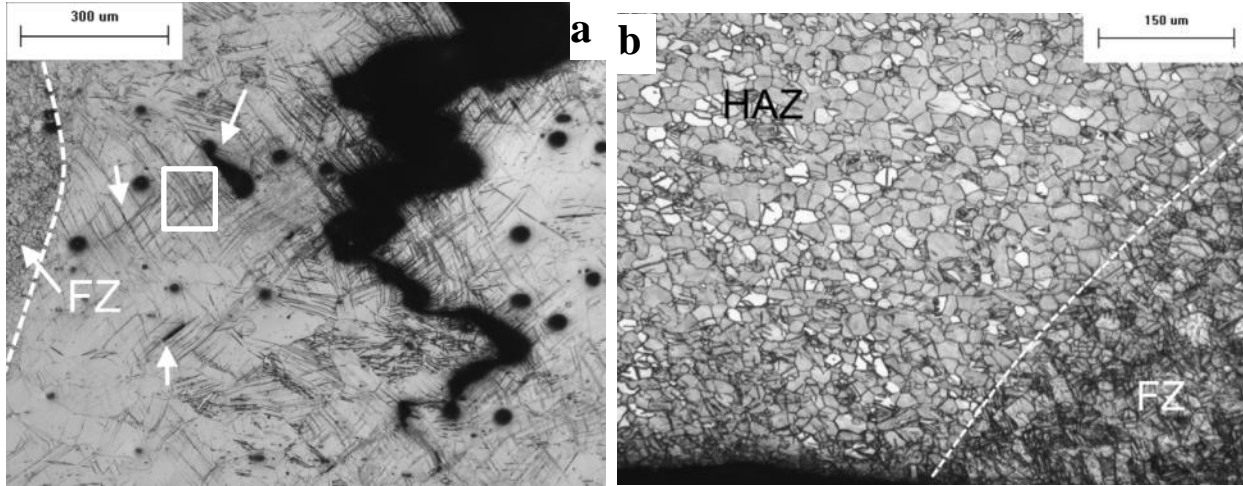


Figure 6-13 Microstructure at the edge of AZ80/ZEK100 nugget in heat treated condition after TS test (stopped at peak load); (a) AZ80 side i.e. fracture process zone and (b) ZEK100 side (the side which experienced tensile stresses)

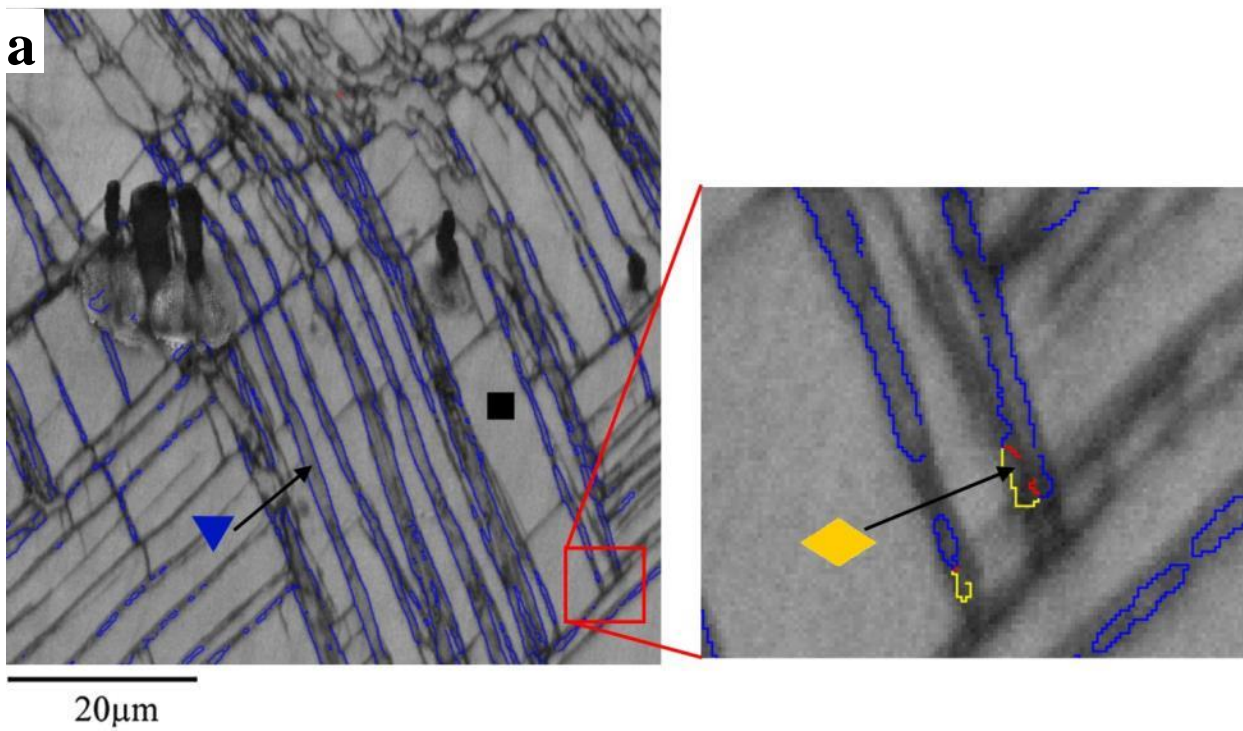


Figure 6-14 (a) EBSD Kikuchi band contrast maps from the area highlighted in Figure 6-13a: The twin boundaries were highlighted as yellow ( $\langle 1 \bar{2} 1 0 \rangle / 56.2 \pm 5^\circ$ ) accounting for the primary  $\{1 0 \bar{1} 1\}$  twinning and as blue ( $\langle 1 \bar{2} 1 0 \rangle / 37.5^\circ$ ) accounting for  $\{1 0 \bar{1} 1\}$ - $\{1 0 \bar{1} 2\}$  double twinning; (b) Corresponding pole-figures showing the crystallographic orientations within the matrix and the twinned segments

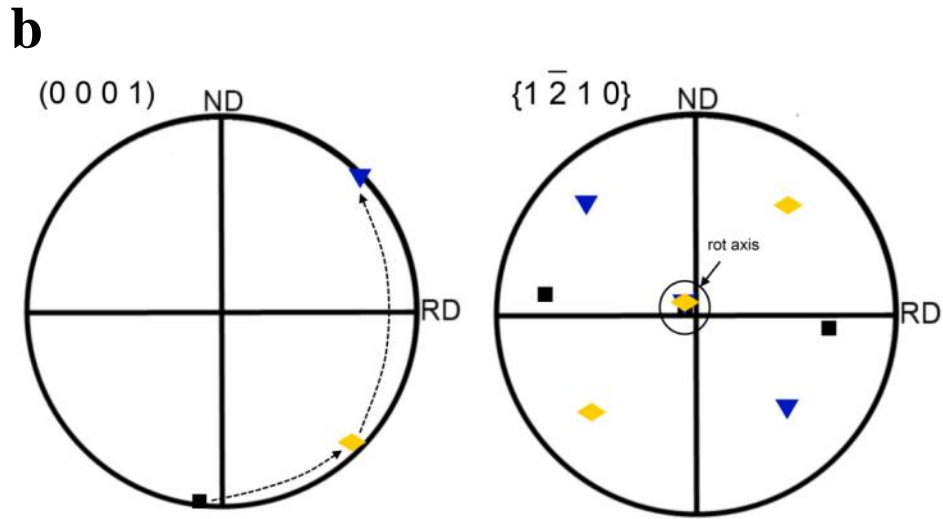


Figure 6-14 continued

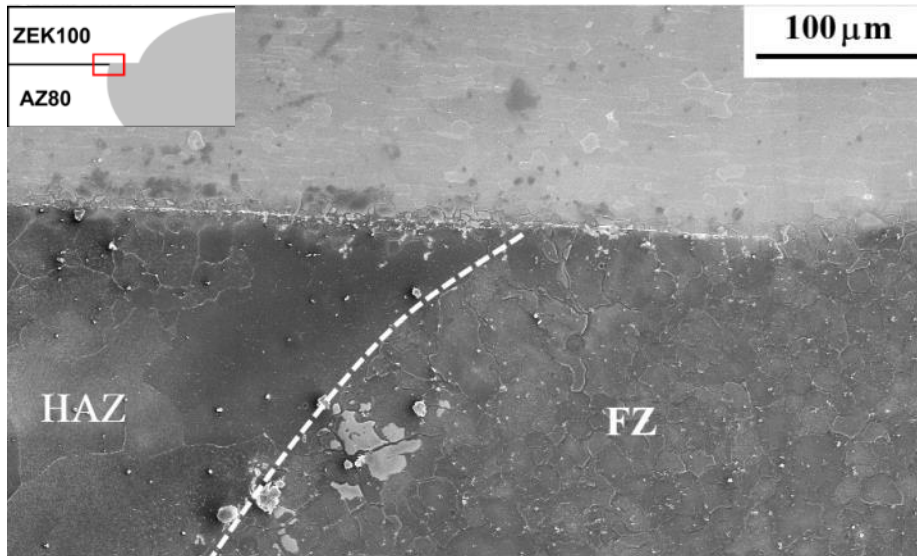


Figure 6-15 Microstructure at the edge of nugget in heat treated condition

Figure 6-16 shows the EBSD results from the AZ80 BM near HAZ in PWHT condition. The inverse pole-figure map shows the orientation of the sheet's ND with respect to the crystal frames. It is obvious from the pole-figures that the c-axes of most of the grains are closely aligned with the sheet's ND. It should be noted that such strong texture also exists in coarse-grained microstructure of HAZ as demonstrated typically in Figure 6-14. On the other hand, the HAZ of ZEK100 demonstrated a more randomized texture (Figure 6-16b). Despite a relatively weaker texture compared to AZ80, a considerable portion of the grains in ZEK100 are aligned so that their c-axes are tilted away from sheet's ND to TD.

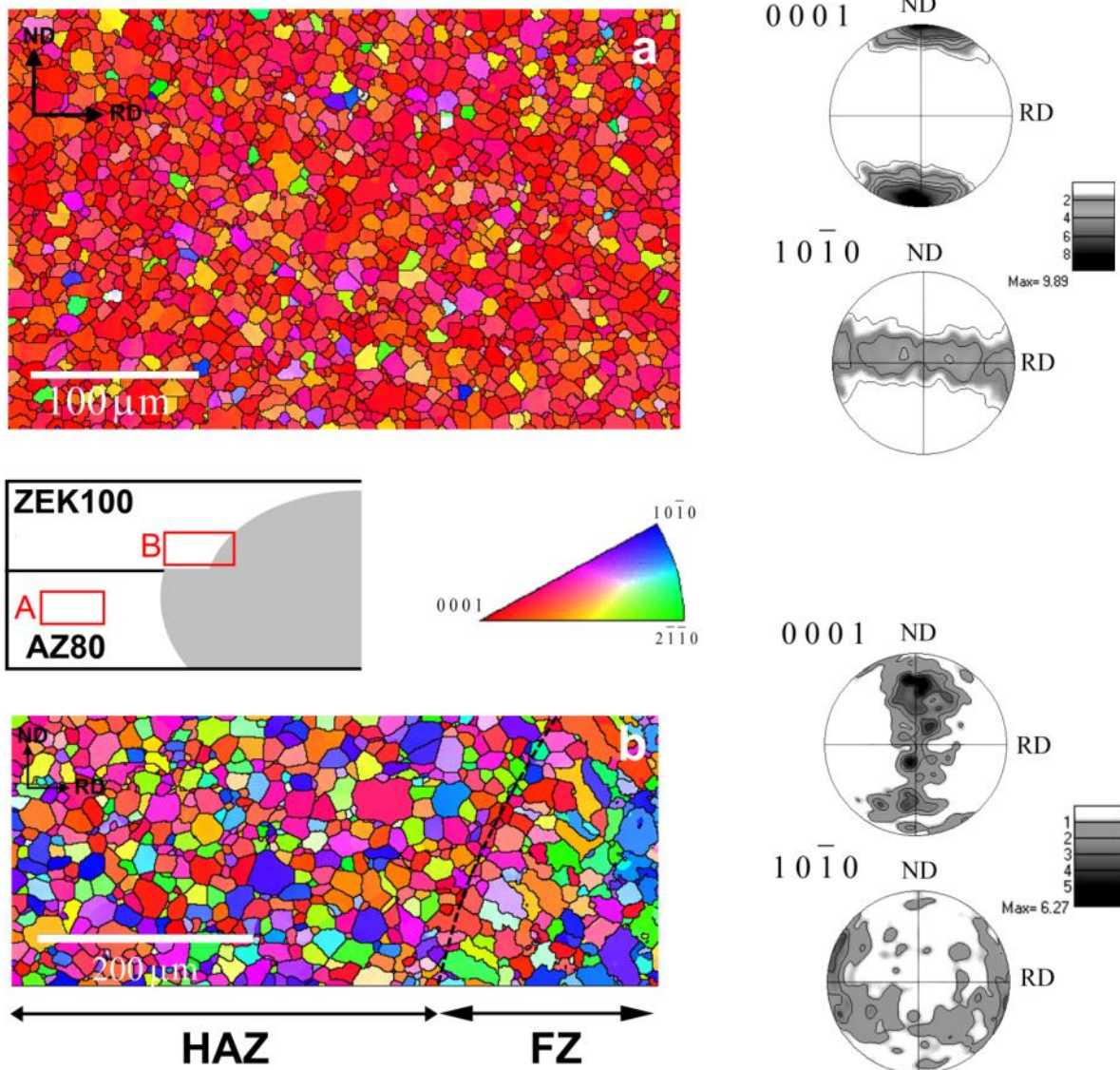


Figure 6-16 EBSD inverse pole-figure maps from the microstructures corresponding to (a) area A and (b) area B as highlighted in the schematic drawing. The pole-figures in (b) demonstrate the texture only in HAZ of ZEK100

## 6.5 Discussion

In this section the structure-property relationships in AZ80/ZEK100 joint (in both as welded and heat treated conditions) are discussed:

The stress concentration at a notch root may be decreased by local plastic yielding in a ductile material [83]. Thus, the stress intensity is expected to reduce in a material with better ability to accommodate the

plastic strains. For the dissimilar weld in the as welded condition, the local plastic yielding at the notch root of the spot weld was preceded by the micro-crack generation in FZ, leading to premature failure with negligible ductility (Figure 6-8a) and low values of energy to failure (Figure 6-9). No twinning activity was observed in the microstructure near the notch after TS test. In fact the inelastic strains are accommodated, not via plastic deformation but via crack nucleation due to brittle fracture of  $Mg_{17}Al_{12}$  IMCs or de-cohesion at  $Mg/Mg_{17}Al_{12}$  interface [106], [107].

With the absence of IMCs in post weld heat treated weld, the inelastic strains can be more effectively accommodated by slip/twinning activity. This increased the nugget ductility and consequently energy-to-failure (Figure 6-8). The stress-strain analysis from chapter 5 showed that plasticity is more localized within the HAZ compared to the FZ in a TS specimen, which is in agreement with previous studies [9], [149]. Moreover, it was found that the stress along the loading direction (in this study parallel to sheet's RD) dominates the stress field in HAZ. Therefore, at high magnitude of the applied force, the HAZ stretched plastically parallel to the sheet's RD. Due to conservation of volume during plastic deformation, contraction occurred in the lateral directions (i.e. parallel to sheet's ND and TD). This contraction is constrained by the material surrounding the plastic zone which is still in elastic state; however the material is less constrained along the sheet's ND since the notch is located the interface of the two sheet metal surfaces (the stress normal to a free surface is zero). Thus, a relatively large tensile stress acted parallel to the sheet's TD. Such a stress distribution created a maximum shear stress on those planes whose normal is oriented  $45^\circ$  to the sheet's RD and ND (as illustrated by Mohr's circle of Figure 6-17a). Such shearing condition and resulting necking along the thickness of the sheet was predicted using finite element analysis of spot weld [9].

In the case of a HAZ microstructure with strong basal texture (such as AZ80 in this study), the stress state was such that the shear stresses resolved on the basal planes (i.e.  $\vec{c}, \vec{\sigma}$ ) of the grains are very small (as shown schematically in Figure 6-17b) and thus  $\langle a \rangle$  type dislocations slip on basal planes, as the major plastic deformation mechanism in hcp structured materials, is very limited. The stress condition (as aforementioned in the previous paragraph) produced a high shear stress on the pyramidal planes of crystal lattice. Such elastic stress could be relieved by either slip of  $\langle c + a \rangle$  dislocations on the pyramidal planes or  $\{1\ 0\ \bar{1}\ 1\}$  contraction twinning. The activation of  $\langle c + a \rangle$  slip mode in a coarse-grained material is extremely difficult at ambient temperature [151], [152] due to very high hcp lattice resistance. With further intensification of elastic stresses, the  $\{1\ 0\ \bar{1}\ 1\}$  contraction twinning was activated; The strains are not able to be accommodated effectively by contraction twinning due to significant resistance of the matrix against twin lateral growth [141]. As stated in chapter 5, the primary  $\{1\ 0\ \bar{1}\ 1\}$  twins immediately transformed to double twins. The crystal reorientation due to double-twinning (specifically those twin

variants leading to  $\langle 1 \bar{2} 1 0 \rangle / 37.5^\circ$  crystal rotation as observed in Figure 6-14), provided a favorable orientation for basal slip (as shown schematically in Figure 6-17b). Thus, shear deformation is localized in the thin laths of the double twins leading to local necking and transgranular micro-cracking. The primary crack in the spot welds initiated/propagated via bridging through such micro-cracks.

From the discussion above, it can be concluded that the HAZ of AZ80, is not able to accommodate strains effectively and therefore it is susceptible to premature fracture; however the nugget in PWHT condition demonstrated a higher ductility in the dissimilar weld (Figure 6-8a), compared to that of AZ80/AZ80 in the same condition (Figure 6-8c). It is suggested that the HAZ of the ZEK100 side, effectively accommodated the inelastic strains near the notch root owing to the two following reasons:

*a. Randomized texture:* Significant improvement of tensile ductility was reported due to texture weakening in the as-rolled magnesium alloys [153]. Within the microstructure of the HAZ at ZEK100 side, with reduced intensity of basal fiber texture, more grains were favorably oriented for the dislocation slip compared to that at AZ80 side. It should be noted that due to broader spread of basal poles towards the sheet's TD than RD, a great number of grains were still oriented in such a fashion that Schmid factor is low for the basal slip; however, considering the stress state and the dominant basal pole inclination towards the sheet's TD, the prismatic dislocation slip was likely to be activated (as shown schematically in Figure 6-17b). At the same time, activity of the  $\{1 0 \bar{1} 1\}$  and  $\{1 0 \bar{1} 1\}$ - $\{1 0 \bar{1} 2\}$  double twins was reduced, since the pyramidal planes are less under stress (compared to the situation for HAZ of AZ80 side). Thus, shear localization was delayed in ZEK100.

*b. Effects of grain size:* The HAZ of ZEK100 appeared to be resistant against grain growth during welding and PWHT thermal cycles. Such resistance to grain growth was reported to be due to the grain boundary pinning effects of the Zn-Zr particles [154]. It is confirmed that ductility of magnesium alloys are improved significantly via grain refinement [17]. The reason was principally attributed to the fact that activation of twinning modes may be preceded by activation of dislocation slip on both basal and non-basal planes. The activation of non-basal slip in fine grained microstructure was attributed to intensification of plastic compatibility stresses near the grain boundaries and triple junctions [65]. On the other hand, the  $\{1 0 \bar{1} 1\}$  contraction twins and  $\{1 0 \bar{1} 1\}$ - $\{1 0 \bar{1} 2\}$  double twins became less active within a fine-grained microstructure [65], [155]. Somekawa et al. demonstrated the reduced size of the twinned zone near a propagating crack-tip by grain refinement of magnesium [62]. Such decrease in the twinning activity diminished the potential sites for the transgranular fracture.

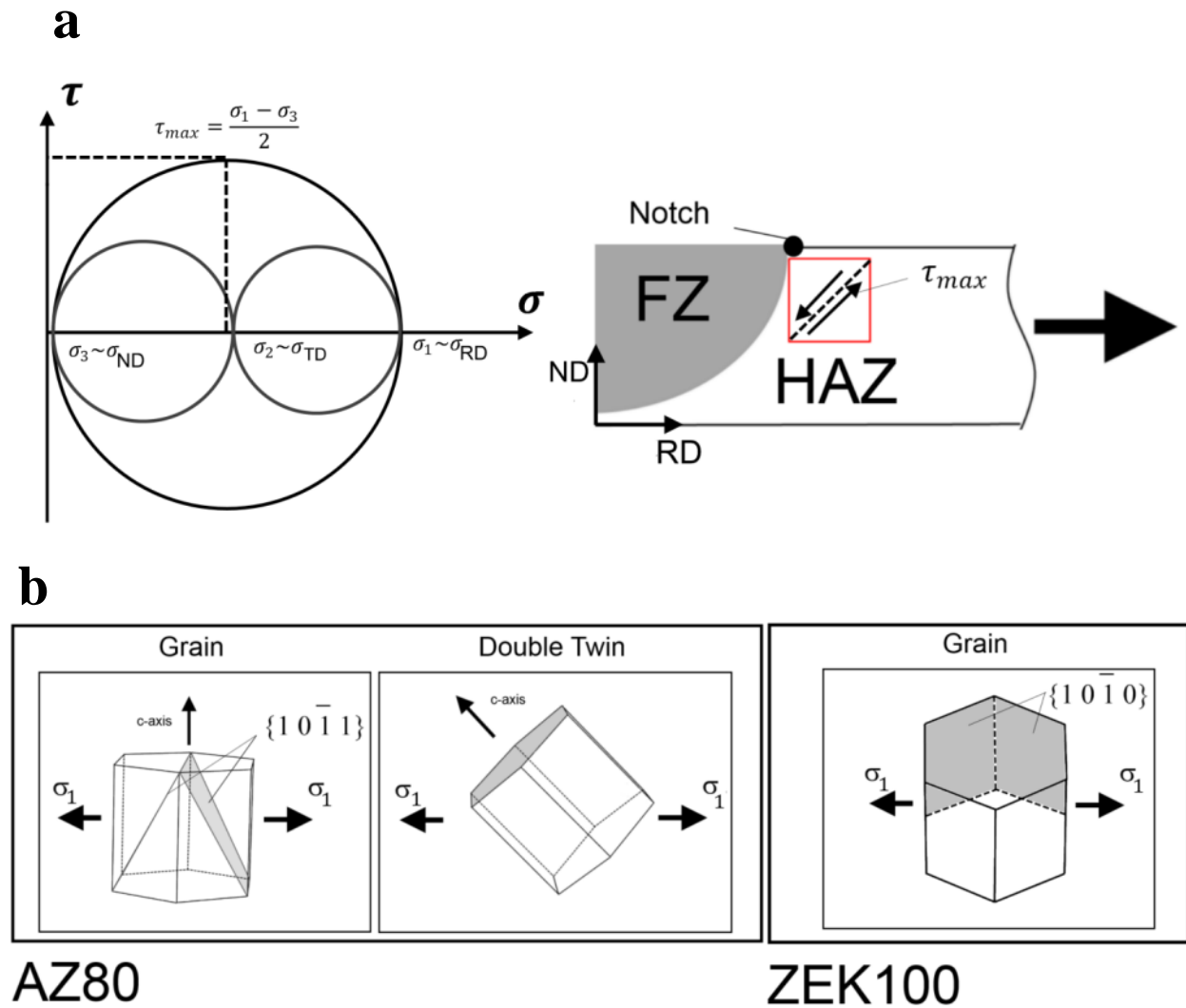


Figure 6-17 (a) Schematic drawing of stress condition in HAZ at the edge of spot nugget and (b) effect of crystallographic orientation on the activity of deformation micro-mechanisms based on stress condition in HAZ of AZ80 and ZEK100

## 6.6 Summary

The micro-mechanisms involved in fracture initiation of resistance spot weld of AZ80/ZEK100 were studied in the current work. The failure was quantified via calculation of energy-to-failure. The following conclusions were made:

1. For the dissimilar joint in as welded condition, premature failure occurred at the notch root with very low value of energy-to-failure. The mechanical performance of the nugget was improved significantly by the application of post weld heat treatment.



2. With the absence of intermetallic compounds in the microstructure across the weld, effects of crystallographic texture and grain size on nugget ductility as well as failure mode became important.
3. Fracture in post-weld heat treated spot weld, initiated preferentially the heat affected zone of AZ80. This was associated with ineffective strain accommodation due to coarse-grained microstructure along with high basal texture.
4. The heat affected zone of ZEK100 was resistant against fracture initiation since it was able to accommodate the plastic strains more effectively due to its fine-grained microstructure and randomized texture.

## Chapter 7

# Microstructural Effects on Notch Strength and Ductility of Magnesium Alloys

### 7.1 Introduction

It was argued in chapters 4, 5 and 6 that fracture resistance of a magnesium alloy depends strongly on combined effects of stress condition and microstructure. The key point to achieve a tough material is to prevent (or delay) the activation of fracture micro-mechanisms. The combined effect of microstructure and stress condition was simulated and studied in this chapter by studying the notch effect on magnesium materials.

The study of notch effect is of great importance for assessing the sensitivity of the engineering materials to geometrical discontinuities such as grooves, screw threads and holes. Since the material is subjected to biaxial/multi-axial stress state ahead of a stress raiser, failure may occur without significant plastic deformation during monotonic or cyclic loading [156]. Several analytical and numerical analysis methods such as Neuber's stress analysis, slip line field theory, finite element analysis and energy approach, have been utilized so far to understand the notch effect on the mechanical properties of metals such as strength and ductility [83], [157]–[159]; however a general understanding of the notch effect which applies to all types of materials is lacking. The reason has been attributed to the lack of comprehensive fracture criteria which are applicable for all types of materials. Despite this shortcoming, it has been generally accepted that the less notch-sensitive materials are able to more effectively accommodate the inelastic strains at the notch root by plastic deformation [11], [160].

There have been numerous published works on the effects of crystallographic texture on mechanical properties of magnesium alloys subjected to a uniaxial tension or compression; however there has been a lack of experimental data on the effects of texture on their mechanical performance in a triaxial stress field. Normally, the sensitivity of materials to stress concentration in monotonic loading, is assessed via tensile testing of notched specimens [161], [162]. In this study, the notch strength and notch sensitivity of the Mg materials were investigated using double-edged notched tensile (DENT) specimens. In monotonic tensile loading of notched specimens (i.e. the nominal stress exceeds the yield point), fracture in ductile materials is associated with plasticity and shear localization [163]. Therefore, in order to investigate the notch sensitivity of Mg materials, attempts were made to predict the plastic deformation mechanisms to be activated within the microstructure ahead of the notch root. The work presented and described in this chapter will be submitted for publications by Niknejad et al. [164].

## 7.2 Experiments

AZ31, AZ61, AZ80, ZEK100 commercial hot rolled sheets, all 2 mm in thickness were used for the current research. The tensile notch response of Mg alloys with different grain sizes, in as-received (AR) and heat treated conditions (as introduced in Table 7-1), were evaluated. Tensile properties and average grain size of the alloys in the aforementioned conditions are plotted in Figure 7-1.

**Table 7-1 Heat treatment procedures for different conditions of the alloys**

Condition	Heat treatment temperature (°C)	Heating time (hr)
AR	-	-
1h	420	1
6h	420	6
10h	420	10

All the notched dog-bone shaped specimens (Figure 7-2a) were machined in a fashion that the gauge longitudinal direction is parallel to the sheet's rolling direction (RD). The gauge length was 10 mm with a squared cross section of 2 mm × 2 mm. V-shaped notches, 0.3 mm and 0.5 mm deep with a tip radius of 0.1 mm were introduced. In order to investigate the texture effect, the notches were introduced at the middle of the gauge length with notch tips pointing aligned with the sheet's normal direction (ND) and transverse direction (TD) for ND and TD specimens, respectively (as shown schematically in Figure 7-2a). Therefore, for ND and TD specimens, the notch front was aligned with the sheet's TD and ND, respectively. In order to clearly demonstrate and explain the stress condition at the notch root, a second coordinate system was introduced based on specimen directions i.e. loading (L), width (W) and thickness (B) directions. Tensile tests on notched samples were carried out with an Instron 5548 Microtester equipped with hydraulic gripping system in order to reduce the specimen slipping to minimum. The net-section stress applied on the material ( $\sigma_{nss}$ ) is defined as:

$$\sigma_{nss} = \frac{F}{B \times W_{net}} \quad \text{eq.7.1}$$

Where  $F$  is the applied load and  $W_{net}$  is the net width at the notched region (as shown in Figure 7-2a). The actual  $W_{net}$  was measured by optical microscope since the machined notch depth in different specimens were in order of  $\pm 0.03$  mm different than the designated values.

Texture of Mg alloys in the 10h heat treated condition (Table 7-1) was examined using electron backscattered diffraction (EBSD). The EBSD specimens were prepared from the sheet's ND. Step size of 1  $\mu\text{m}$  was selected for an area of 0.5 mm×0.5 mm for each specimen. The indexing rate was between 91-94%.

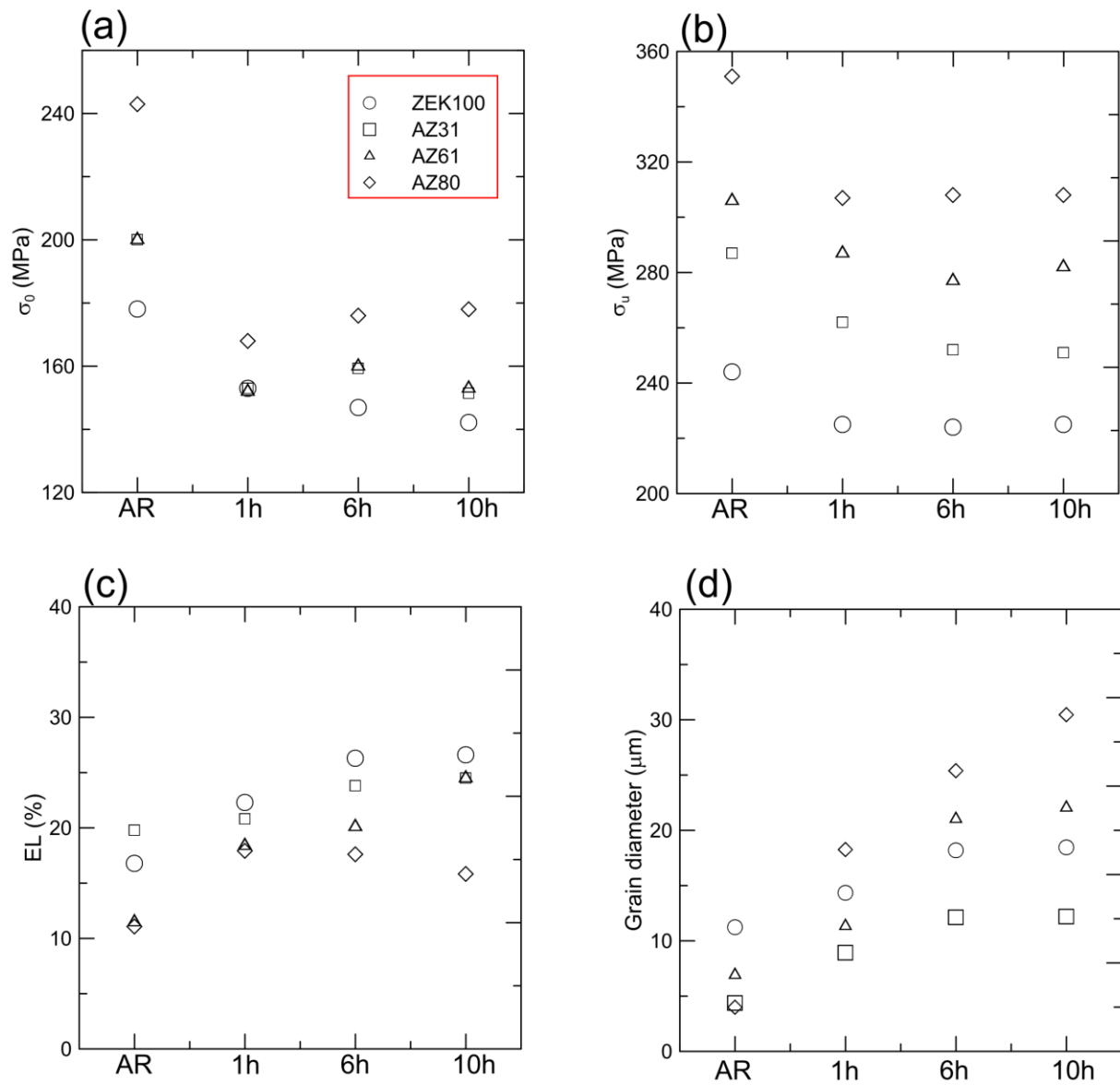


Figure 7-1 Tensile properties (along rolling direction) in different heat treatment conditions as explained in; Table 7-1 (a) Yield strength ( $\sigma_0$ ); (b) True tensile strength ( $\sigma_u$ ); (c) Elongation (EL) and (d) grain size (from ND view)

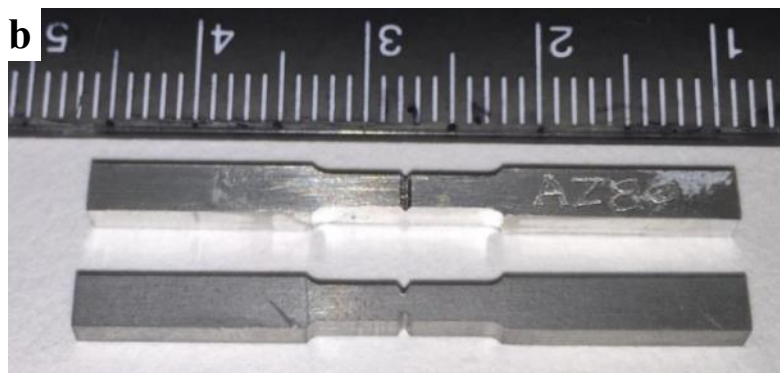
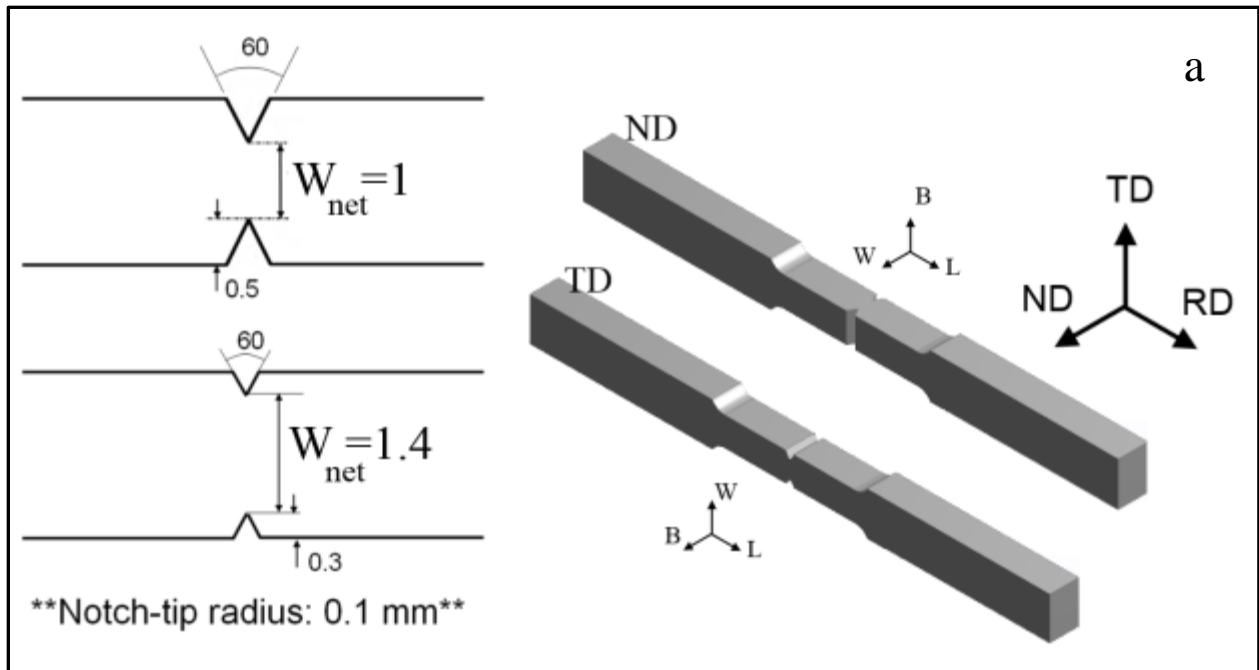


Figure 7-2(a) Schematic drawing of the DENT specimens (ND and TD) and the corresponding dimensions; The sheet (RD-TD-ND) and specimen (L-W-B) coordinate systems are defined. Note that in ND specimens:  $L \parallel RD, W \parallel ND, B \parallel TD$  and in TD specimens:  $L \parallel RD, B \parallel ND, W \parallel TD$ . (b) Typical DENT (ND and TD) specimens; (c) Notch appearance from cross sectional view (notch depth: 0.5 mm)



**Figure 7-3 Instron 5548 Micro-tensile tester**

## **7.3 Results**

### **7.3.1 Tensile Notch Response**

Figure 7-4 and Figure 7-5 show tensile notch response of the Mg materials as net-section stress ( $\sigma_{nss}$ ) vs. grip displacement in different heat treatment conditions. Although the measured displacement values do not represent the actual specimen elongation, they can be used for qualitative comparison. For each material/condition, the notch tensile strength (NTS) value was higher than its tensile strength. Moreover, the NTS increased as the notch depth increased. This indicates the “notch strengthening” effect which is typical of ductile materials [161], [162]. Generally, notch ductility was improved by the application of heat treatment.

The graphs show a different performance of the AZ alloys (AZ31, AZ61 and AZ80) in ND and TD specimens. The elongation-to-failure in TD specimens was higher than that in ND specimens for the same material/condition. This difference became more significant in heat treated alloys. On the other hand, ZEK100 alloy appeared to be less sensitive to the notch orientation. The tensile notch response of ZEK100 alloy in ND and TD specimens did not significantly change (except the 0.3 mm deep notch in 1h condition as shown in Figure 7-4b).

In order to quantify the intrinsic ability of the materials to deform locally at the vicinity of the notch, one can use the term “notch yield ratio” (NYR) defined as [12]:

$$NYR = \frac{NTS(MPa)}{\sigma_0(MPa)} \quad \text{eq.7.2}$$

Where  $\sigma_0$  is the yield strength for material/condition. Figure 7-6 shows the NYR vs. yield strength of the Mg materials in different conditions. For the same material, the NY-R value increased via decrease in its  $\sigma_0$ . This is consistent with the previous reports on notch strength of the aluminum alloys [12]. For an alloy, a softer microstructure is more able to locally accommodate the plastic strains. The NYR value of AZ80-AR is significantly lower than the other materials/conditions. The AZ80-AR demonstrated poor ductility accompanied by sudden fracture after reaching the peak stress (Figure 7-4a and Figure 7-5a); however notch response of AZ80 alloy was significantly improved by heat treatment.

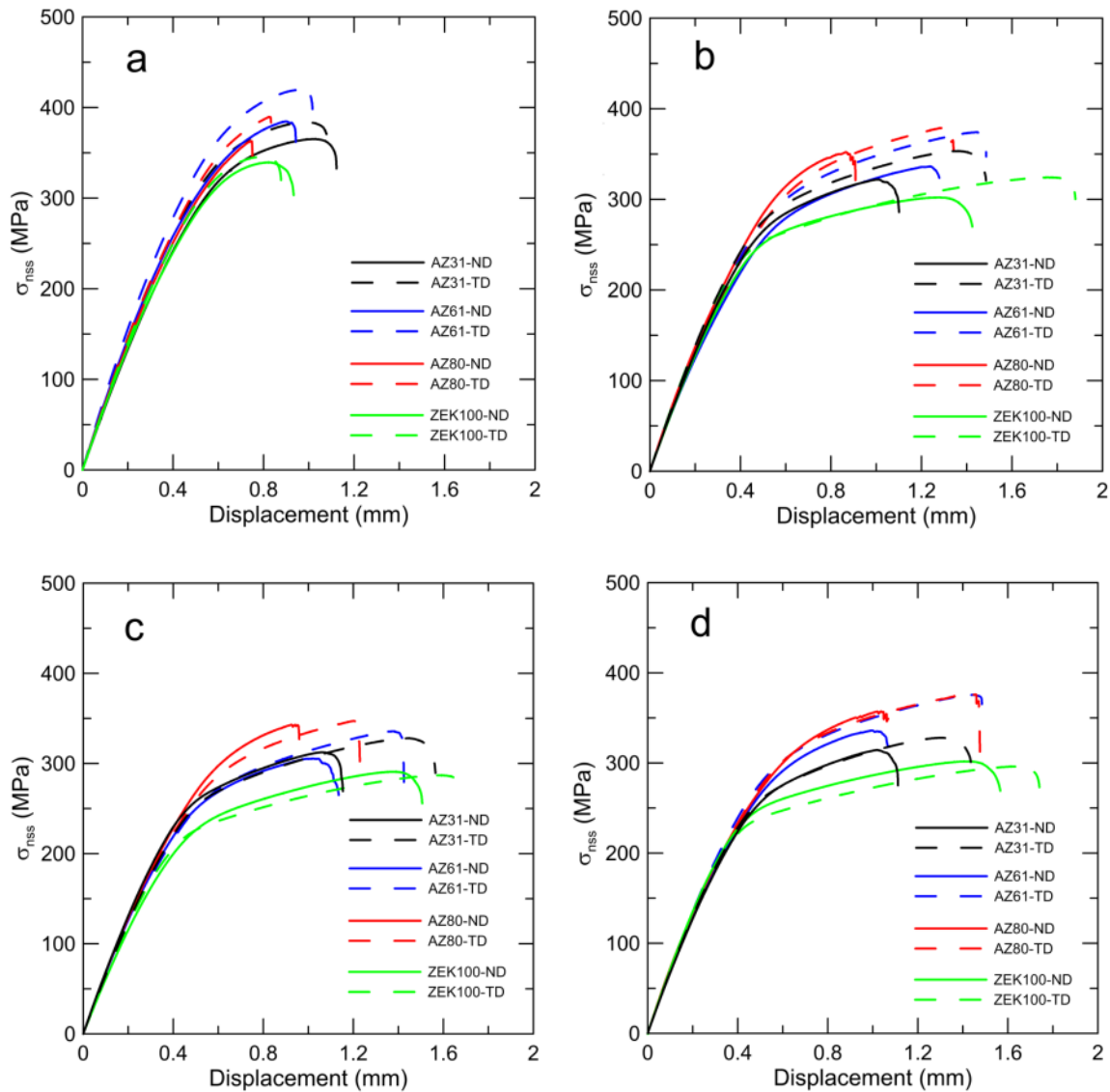


**Figure 7-4 Tensile notch response for the Mg alloys in (a) AR; (b) 1h, (c) 6h and (d) 10h conditions. Specimens have a notch depth of 0.3 mm**

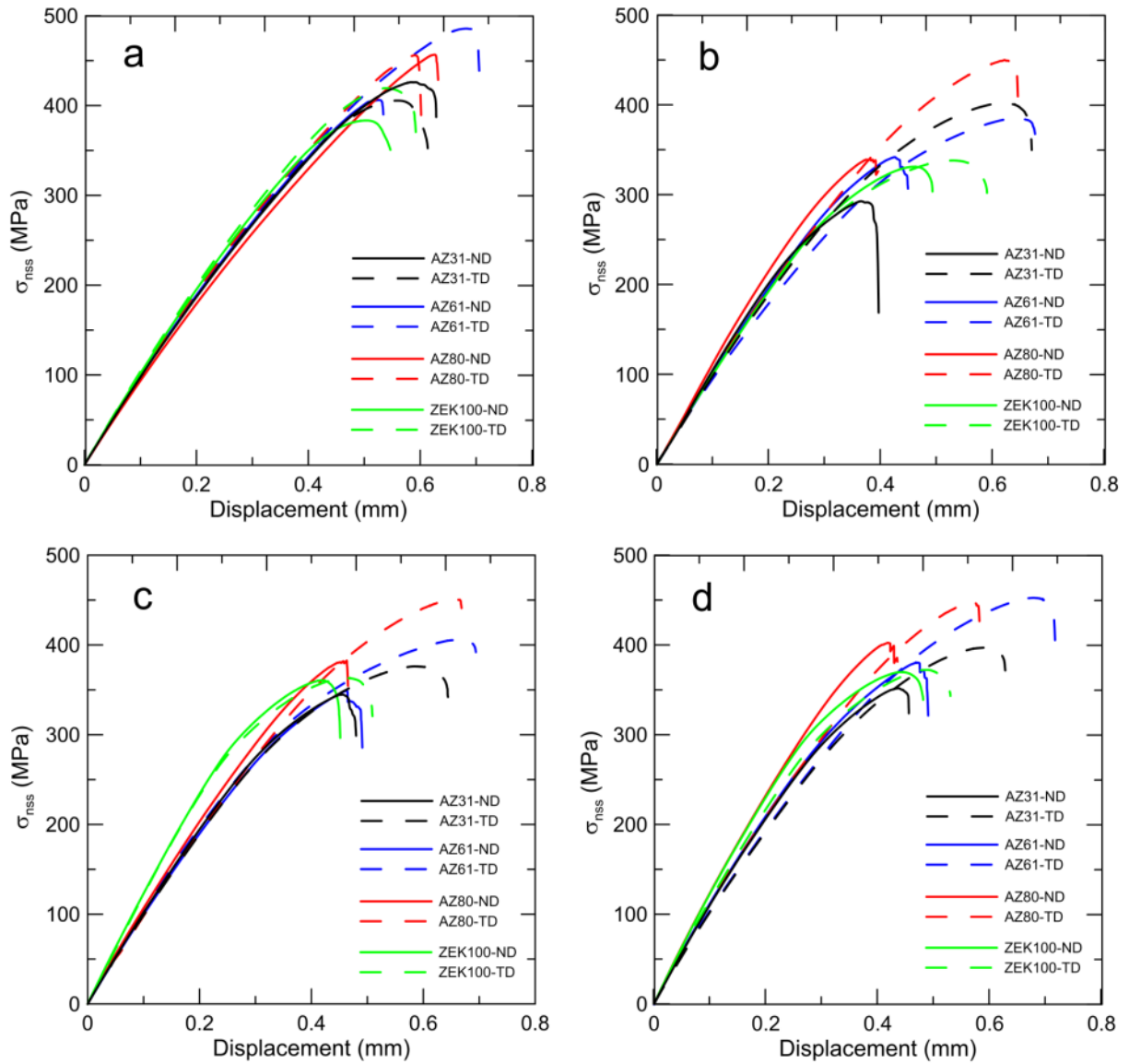


**Figure 7-5 Tensile notch response for the Mg alloys in (a) AR; (b) 1h, (c) 6h and (d) 10h conditions. Specimens have a notch depth of 0.5 mm**



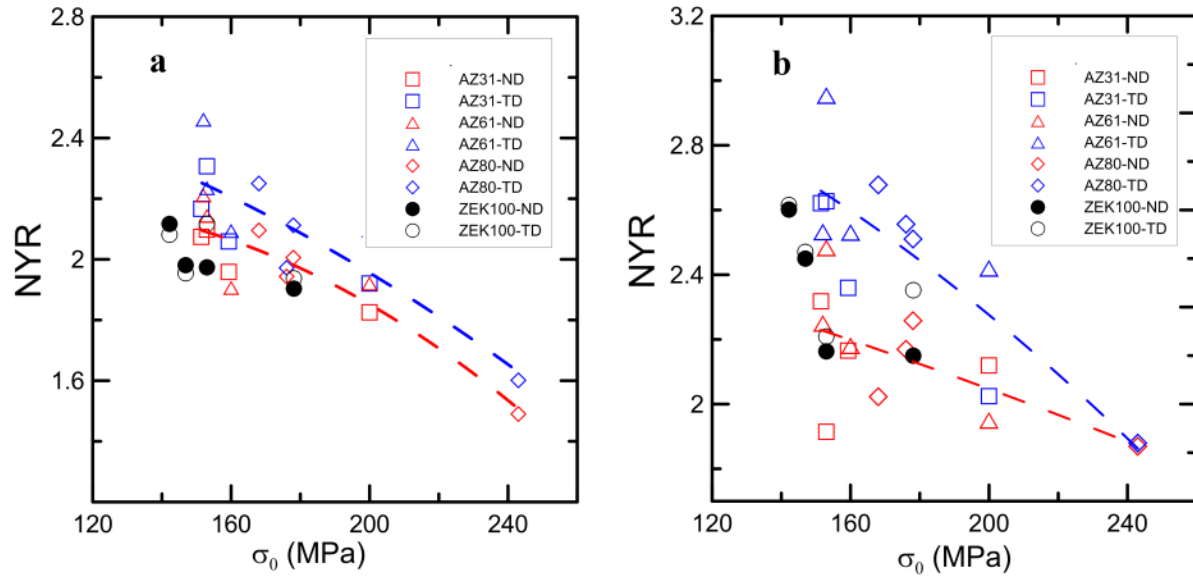


Figure 7-6 Notch yield ratio vs. tensile yield strength for magnesium alloys (a) Notch depth: 0.3 mm; (b) Notch depth: 0.5 mm

### 7.3.2 Fracture Characteristics

The inability of AZ80-AR to accommodate the plastic deformation can be assessed in its microstructure. Figure 7-7 shows AZ80-AR microstructure close to the notch after fracture. Close SEM investigation near the fracture edge revealed a high density of micron-scale cracks and voids. The micro-voids were normally caused by Mg/Mg<sub>17</sub>Al<sub>12</sub> interfacial de-cohesion (Figure 7-7b) and the micro-cracks were caused by brittle fracture of Mg<sub>17</sub>Al<sub>12</sub> (Figure 7-7c). This phenomenon, significantly reduced the localized ductility of the material. However, via heat treating of the alloy in the single phase region of the Mg-Al binary phase diagram, the particles were dissolved into the  $\alpha$ -Mg. This resulted in improvement of notch ductility as shown in Figure 7-4b-d, Figure 7-5b-d and Figure 7-6.

Fracture characteristics of AZ alloys in ND and TD specimens were different. A shear-type fracture occurred in ND specimens with the fracture edges approximately 45° relative to the loading direction (Figure 7-8a). Such shear-type appearance was not observed for the TD specimens. On the other hand, shear-type fracture occurred in ZEK100 in both ND and TD specimens (Figure 7-8b).

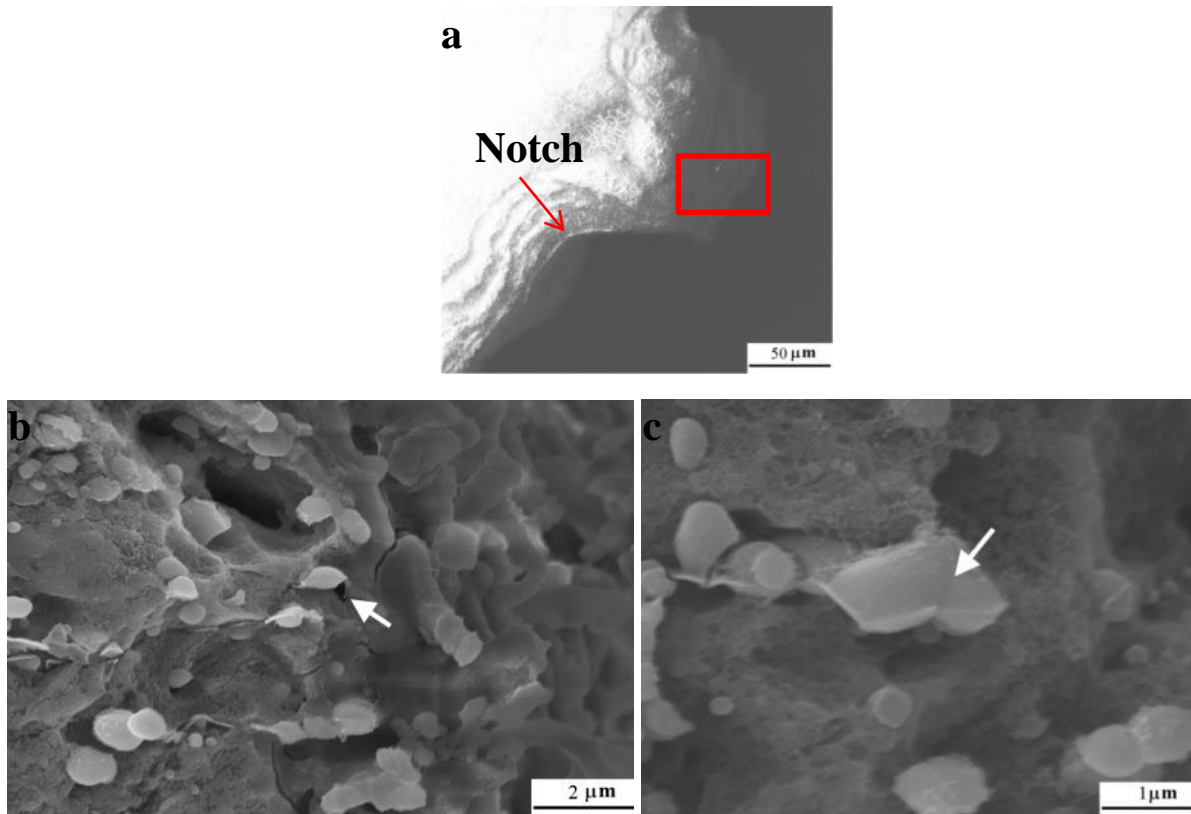


Figure 7-7 (a) Notch appearance in AZ80-AR after fracture, notch depth: 0.3 mm; (b) Mg/Mg<sub>17</sub>Al<sub>12</sub> decohesion; (c) Brittle fracture of Mg<sub>17</sub>Al<sub>12</sub>

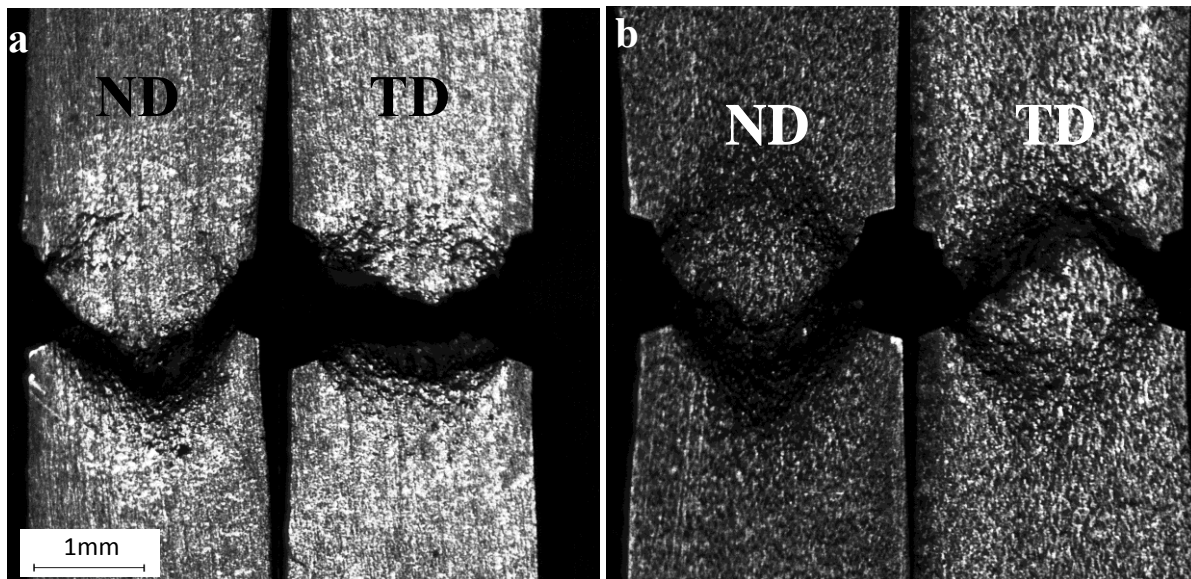
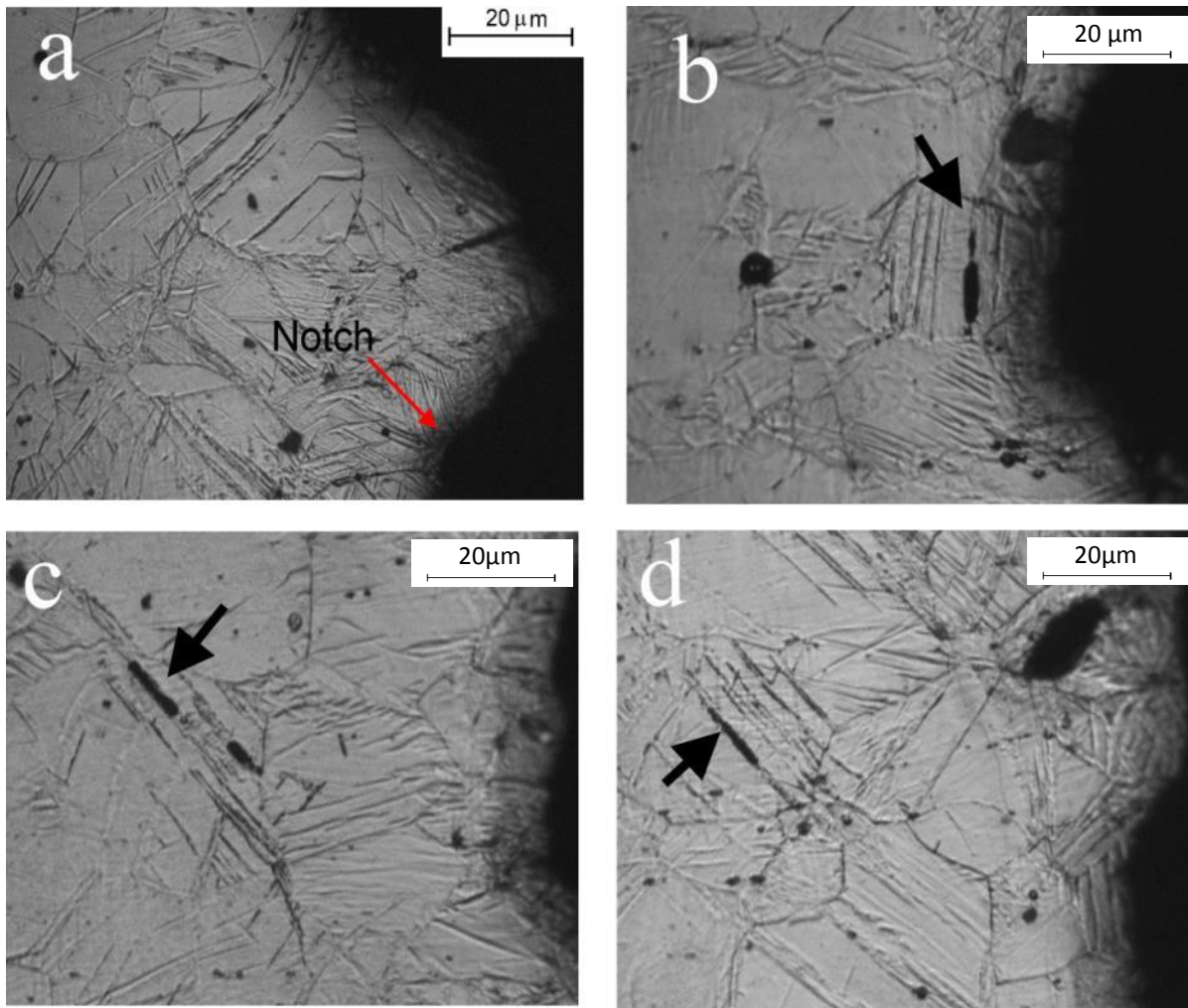


Figure 7-8 Cross section of the notched specimens after fracture for (a) AZ61-10h and (b) ZEK100-10h; Notch depth:0.3mm

Fracture in all samples (except AZ80-AR), involved mainly twinning activity near the notch as shown typically in Figure 7-9. The twin boundaries were mostly straight and they demonstrated very low lateral

growth which are of typical nature of  $\{10\bar{1}1\}$  contraction twins. Figure 7-9b-d shows transgranular micro-cracks near the fracture edge with the same orientation as the twinning habit planes (inside the fractured grains as highlighted by black arrows). These observations indicated a direct correlation between twinning activity and fracture.



**Figure 7-9 Typical microstructures near the notch of fractured specimens (AZ61-6h, ND); notch depth: 0.3 mm**

### 7.3.3 Micro-texture Analysis

Figure 7-10 shows the EBSD results from the magnesium alloys in the 10h condition. The inverse pole-figure maps show the orientation of the sheet's ND with respect to the crystal frames. It can be inferred from the pole figures (Figures 10 a-c) that the AZ alloys generally took up a strong basal texture. Unlike AZ61 and AZ80, a relative spread of basal poles towards the sheet's TD was observed in AZ31 (Figure 7-10a). Texture in ZEK100 alloy was completely different than the AZ alloys: despite its more

randomized texture, a great proportion of grains were rotated so that their basal poles were inclined from the sheet's ND towards TD (Figure 7-10d).

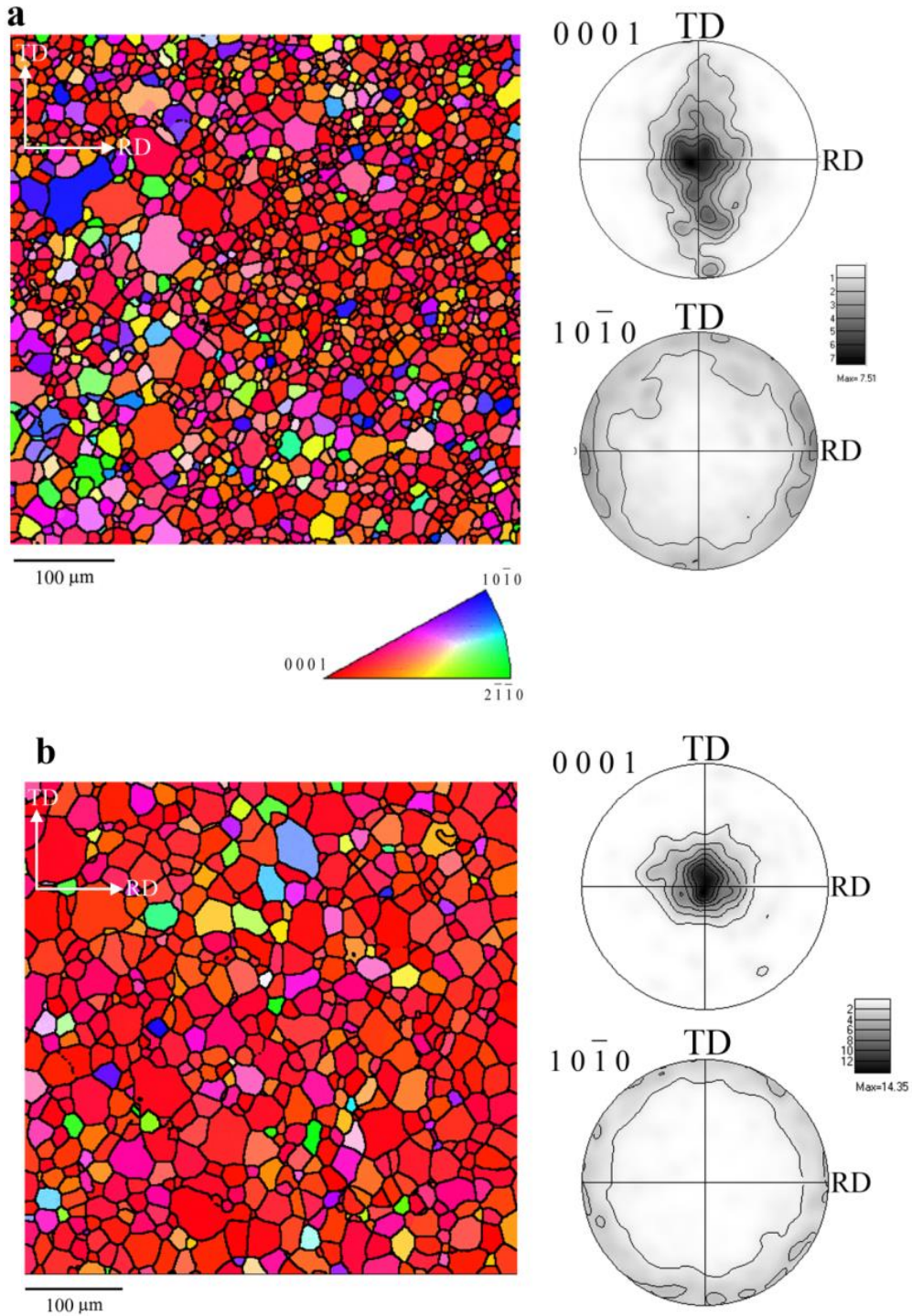


**Figure 7-10** EBSD IPF maps (relative to sheet's ND) of the microstructures 10h condition corresponding to (a) AZ31; (b) AZ61; AZ80 and (d) ZEK100. The associated pole-figures demonstrate the general texture relative to the sheet's ND

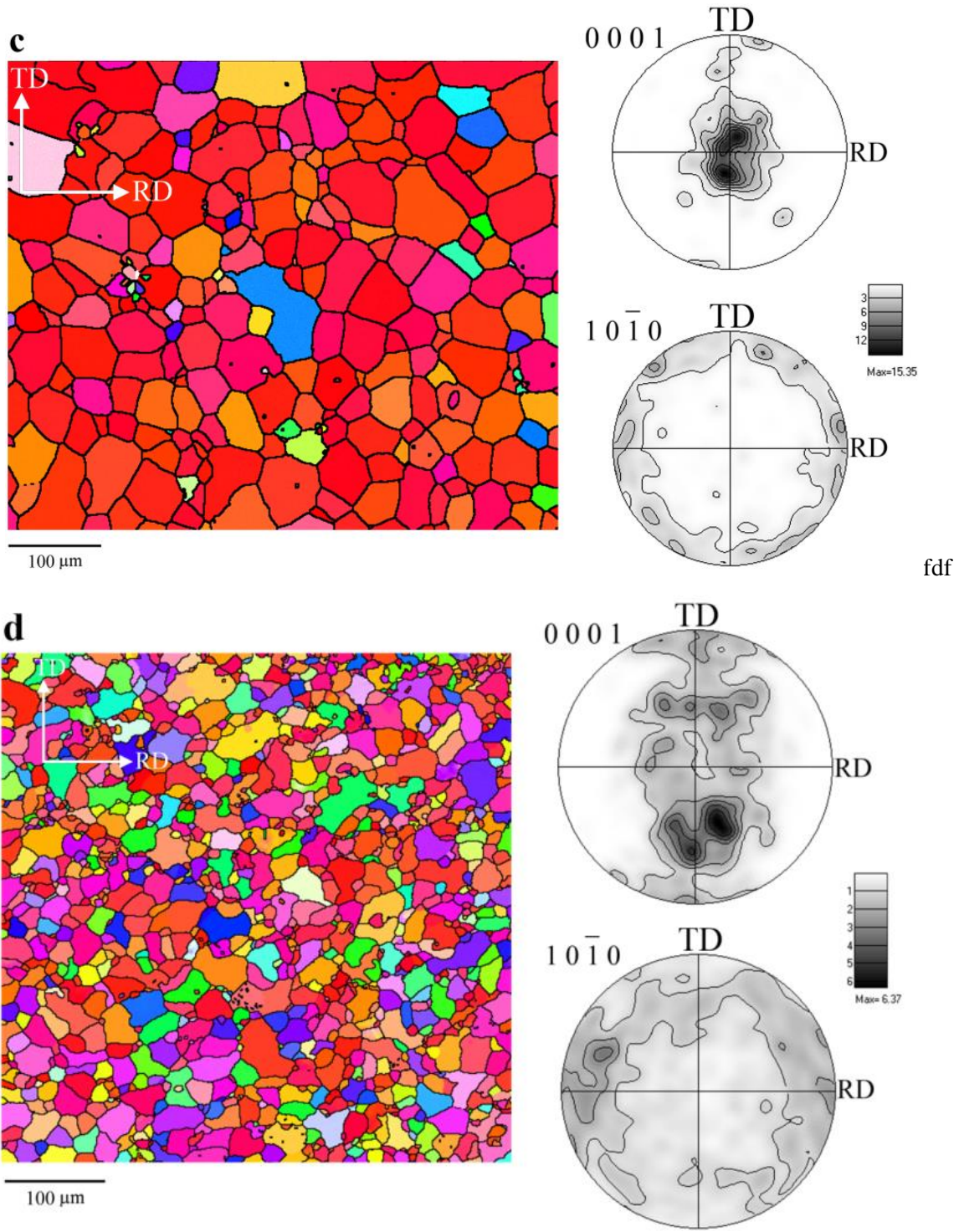


Figure 7-10 continued

## 7.4 Prediction of Deformation Mechanisms at Notch Root

In this work numerical calculations of resolved shear stresses were performed to predict the activity of slip/twinning mechanisms at the notch root during local yielding. The model was explained in details in section 5.4. The stress tensor for calculation of resolved shear stresses was defined as follows:

$$R_{ij}^{(r)} = \frac{1}{2}(b_i^r n_j^r + b_j^r n_i^r), \quad \sigma_{ij} = \begin{bmatrix} \sigma_{RD} & \sigma_{RD,TD} & \sigma_{RD,ND} \\ \sigma_{TD,RD} & \sigma_{TD} & \sigma_{TD,ND} \\ \sigma_{ND,RD} & \sigma_{ND,TD} & \sigma_{ND} \end{bmatrix} \quad \text{eq.7.3}$$

Note that this definition of stress tensor is different than the one defined in eq.5.4. The reason is that the EBSD results presented in chapter 5 were taken in a condition that electron beam direction (z-view) was parallel to the sheet's TD; however in the study in the current chapter, the beam direction was parallel to the sheet's ND. Therefore, coordinate system in this study was defined as: x||RD-y||TD-z||ND. Stress conditions (in the form of stress tensors) near the notch root, were obtained from the FE model as explained in section 7.4.1. The Schmid law modeling was carried out using M-Tex toolbox. In the present numerical approach, the activation of twinning was treated according to the positive direction of twinning shear direction.

### 7.4.1 Stress Analysis at Notch Root

Elastic/plastic finite element (FE) simulation of DENT specimens was conducted by FE-code Ansys 16 to define the stress tensors near the notch root. Figure 7-11 shows a half-model used in the current study. The stress distributions at the notch root (only for specimens with notch depth of 0.5 mm) were obtained when  $\sigma_{nss} = \sigma_0$ . The elastic properties were selected based on the properties of pure Mg (E=45 GPa and  $\nu=0.35$ ). The von Mises criterion was selected as the yield function and plastic flow was defined based on experimental tensile test (along the sheet's RD) data as shown in Appendix A. The elastic/plastic analysis was only carried out for the materials in 10h (Table 7-1) condition.

The plastic zone created ahead of the notch root (at  $\sigma_{nss} = \sigma_0$ ) was predicted by FE model as shown typically in Figure 7-12a for AZ31 at the mid-thickness plane (B=1). Due to stress concentration at the notch root, yielding began at early stage ( $\sigma_{nss} < \sigma_0$ ) [11]. In the interior of the specimen however, a triaxial stress condition existed and a higher external load was required to make the material yield. Therefore, only a small portion of the material near the notch root contributed to the tensile plastic deformation. Consequently, a notched sample demonstrated lower elongation than a uniform-sectioned sample [160]–[162].

Once a crack initiated at the notch root during monotonic loading, general fracture occurred. Figure 7-12a shows that plasticity was confined to a small volume (up to  $\sim 100\mu\text{m}$  ahead of the notch). In order to make

a correlation between plasticity and fracture in the notched specimens, stress analysis was focused within the plastic zone to predict the activated micro-mechanisms responsible for strain accommodation.

Figure 7-12b shows the stress condition at 50  $\mu\text{m}$  away from the notch of AZ31-10h. The stress state near the notch root was triaxial (due to local yielding) with the principal stresses acting in tension along the specimen's coordinate axes (i.e. L, B, W). Figure 7-13 shows that except a small section close to the specimen surface ( $B=0$ ),  $\sigma_L > \sigma_B > \sigma_W$ . This is in conformity with the previously published works on notch stress analysis [11], [43], [165]. It can be inferred from Figure 7-13 that except for a small region near the surface ( $0\text{mm} < B < 0.2\text{mm}$ ) variation of normal stresses ( $\sigma_L$ ,  $\sigma_W$ ,  $\sigma_B$ ) along the specimen's thickness is negligible. Therefore, stress conditions at the mid-thickness ( $B=1\text{ mm}$ ) were used for definition of stress tensors ( $\sigma_{ij}$  as defined in eq.7.3) in order to calculate the shear stresses resolved on the deformation mechanisms. Table 7-2 shows the stress tensors defined ahead of the notch root (for Mg alloys in the 10h condition), in case of ND and TD specimens.

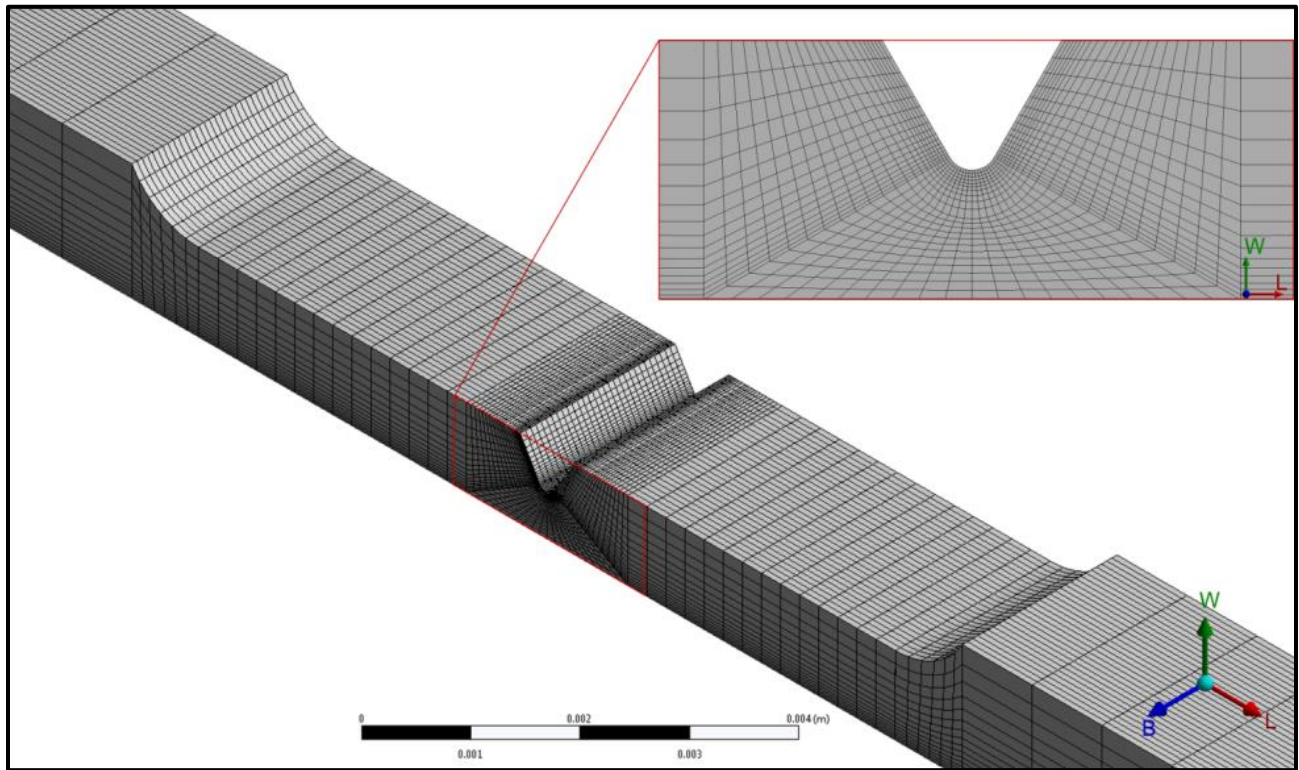


**Figure 7-11 Three dimensional half-model used for the notch stress analysis**

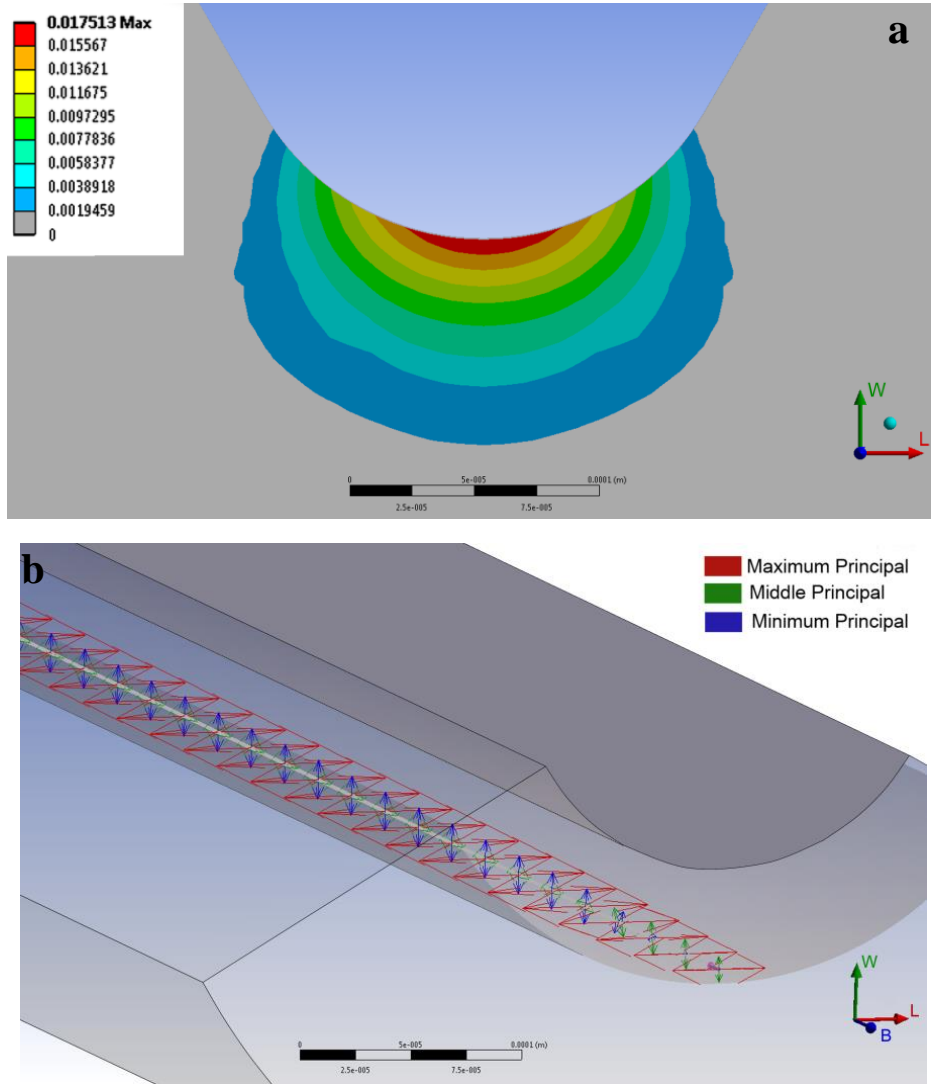
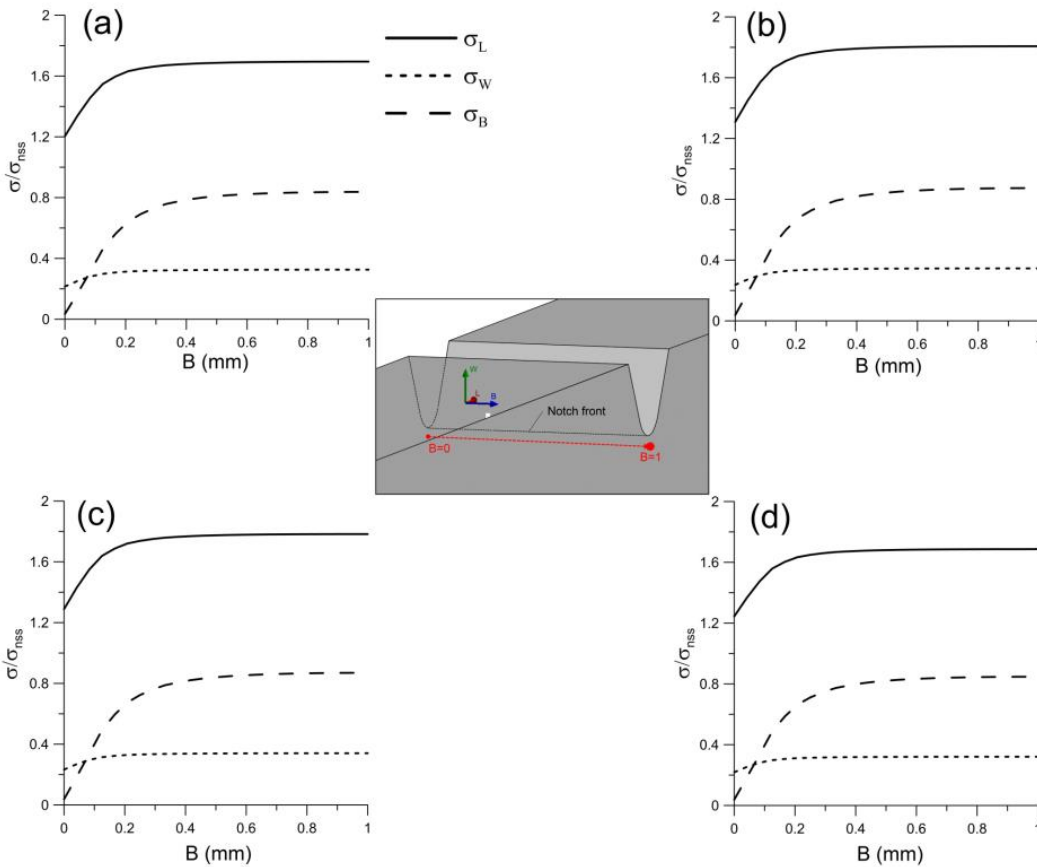


Figure 7-12 Stress and strain analysis at the notch root for AZ31-10h when  $\sigma_{nss} = \sigma_0$ . (a) Plastic zone at the notch root for mid-thickness (B=1) section; (b) Principal stress directions along the thickness at 50  $\mu\text{m}$  away from notch root;

Table 7-2 Stress tensors (MPa) obtained from FE model for the alloys in 10h condition in ND and TD specimens ( $\sigma_{nss} = \sigma_0$ )

	AZ31	AZ61	AZ80	ZEK100
ND specimen	$\begin{bmatrix} 257 & 0 & 0 \\ 0 & 127 & 0 \\ 0 & 0 & 49 \end{bmatrix}$	$\begin{bmatrix} 277 & 0 & 0 \\ 0 & 134 & 0 \\ 0 & 0 & 53 \end{bmatrix}$	$\begin{bmatrix} 317 & 0 & 0 \\ 0 & 155 & 0 \\ 0 & 0 & 61 \end{bmatrix}$	$\begin{bmatrix} 240 & 0 & 0 \\ 0 & 121 & 0 \\ 0 & 0 & 46 \end{bmatrix}$
TD specimen	$\begin{bmatrix} 257 & 0 & 0 \\ 0 & 49 & 0 \\ 0 & 0 & 127 \end{bmatrix}$	$\begin{bmatrix} 277 & 0 & 0 \\ 0 & 53 & 0 \\ 0 & 0 & 134 \end{bmatrix}$	$\begin{bmatrix} 317 & 0 & 0 \\ 0 & 61 & 0 \\ 0 & 0 & 155 \end{bmatrix}$	$\begin{bmatrix} 240 & 0 & 0 \\ 0 & 46 & 0 \\ 0 & 0 & 121 \end{bmatrix}$





**Figure 7-13 Stress distribution (according to specimen coordinate system) along the thickness at 50  $\mu\text{m}$  away from notch root for (a) AZ31; (b) AZ61; (c) AZ80 and (d) ZEK100 all in 10h condition**

#### 7.4.2 Calculation of Resolved Shear Stresses for Deformation Mechanisms

Calculation of shear stresses resolved on deformation mechanisms was conducted using eq.5.3 and stress tensors as defined in Table 7-2. The calculation procedure is explained in detail in Appendix C. Figure 7-14 shows the contour plots of the maximum shear stresses resolved on basal slip, prismatic slip, extension twinning and contraction twinning systems of the grains examined by EBSD analysis. The calculations were performed based on stress field, operating ahead of the notch root for ND and TD specimens. Figure 7-15 plots the averaged values of numerical results for each microstructure/specimen. In all Mg alloys, the basal slip systems of most of the grains were not heavily stressed by the notch root stress field. From the contour plots of Figure 7-14, in case of AZ alloys, a high activity for  $\{10\bar{1}1\}$  contraction twinning is expected for microstructure near the notch in ND specimens, while in case of TD specimens, the prismatic slip systems are more highly stressed. Such a difference is more pronounced in the case of AZ61 and AZ80 than in AZ31. ZEK100 demonstrated a different behavior: it appeared that the notch orientation did not substantially change the activity of slip/twinning systems. The magnitudes of

shear stresses resolved on the contraction twinning and prismatic slip systems are almost identical in ND and TD specimens.

In general, very low (in case of ND specimens negative value) stresses are applied on the extension twinning systems for all the Mg alloys ahead of the notch. This is due to the fact that the maximum principal stress is applied tension almost perpendicular to c-axis of most grains. In case of TD specimens since a large tensile stress is applied along the sheet's ND (i.e. along c-axis of most of grains), the resolved shear stresses on the extension twinning systems are relatively larger; however it should be noted that even possible activation of extension twinning in most of the grains did not contribute to plastic elongation along the loading direction (L).

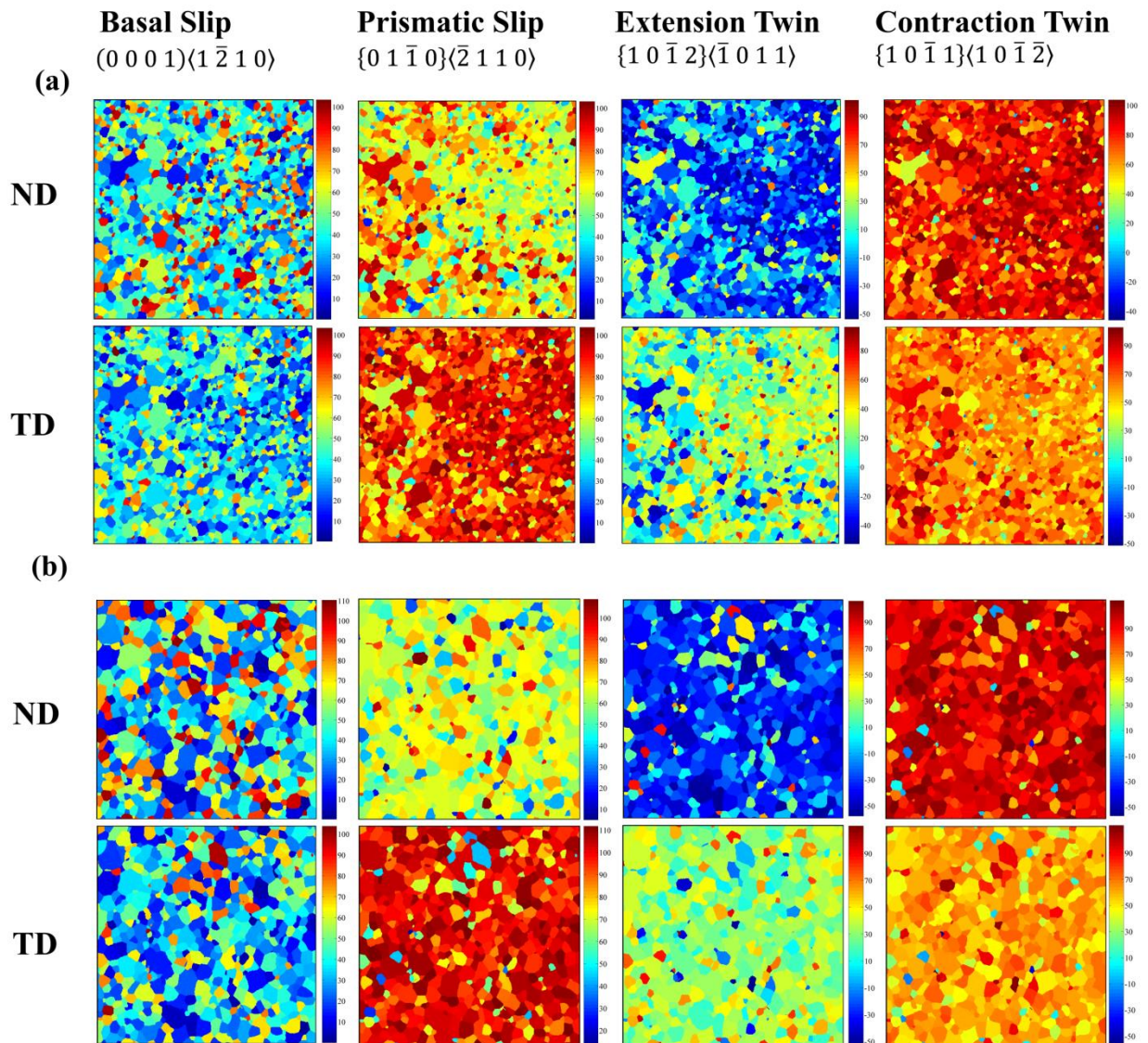


Figure 7-14 Contour plot of maximum resolved shear stress (MPa) on the deformation systems for microstructures subjected to notch stresses in ND and TD specimens (a) AZ31-10h, (b) AZ61-10h, (c) AZ80-10h, (d) ZEK100-10h

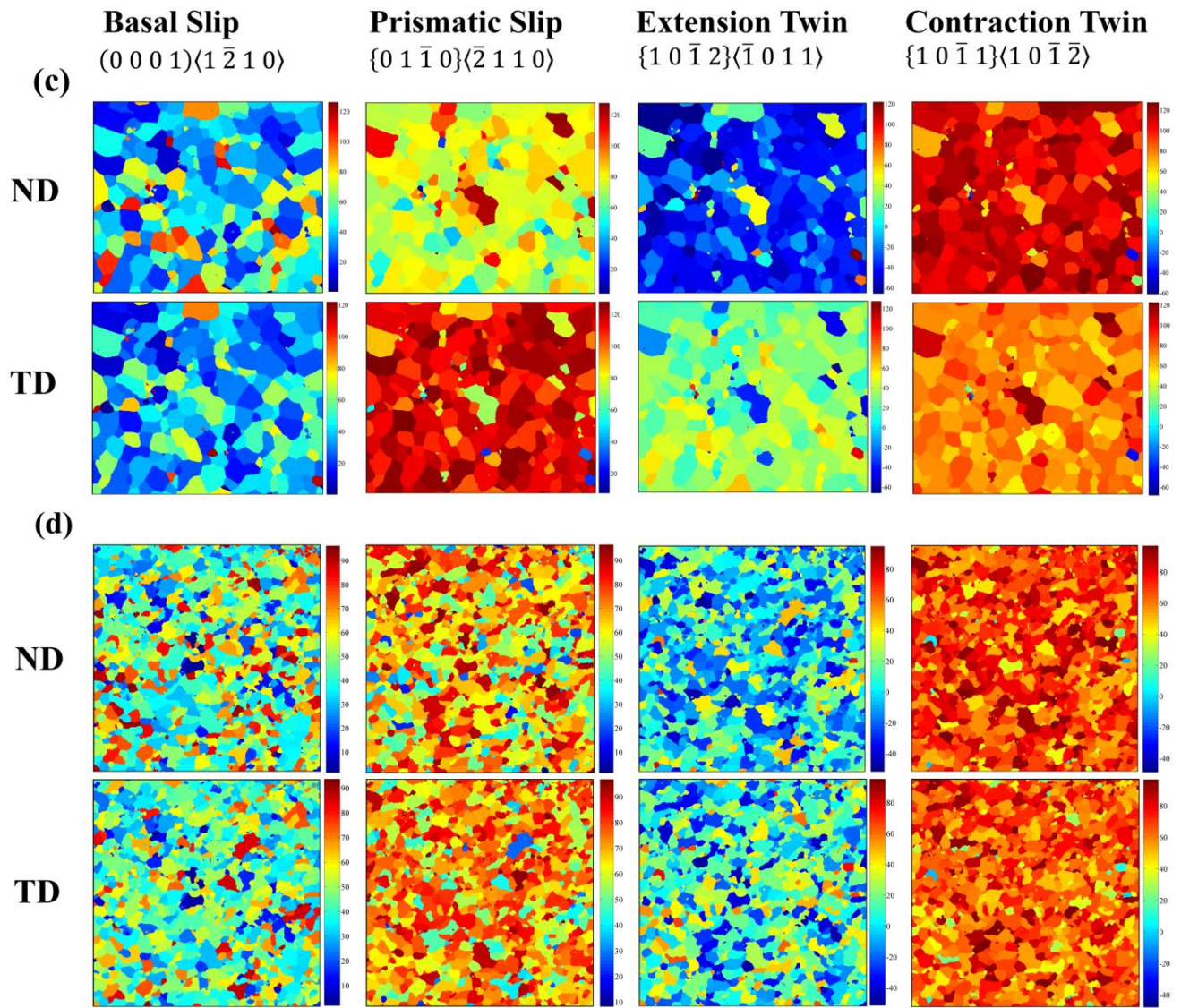


Figure 7-14 continued

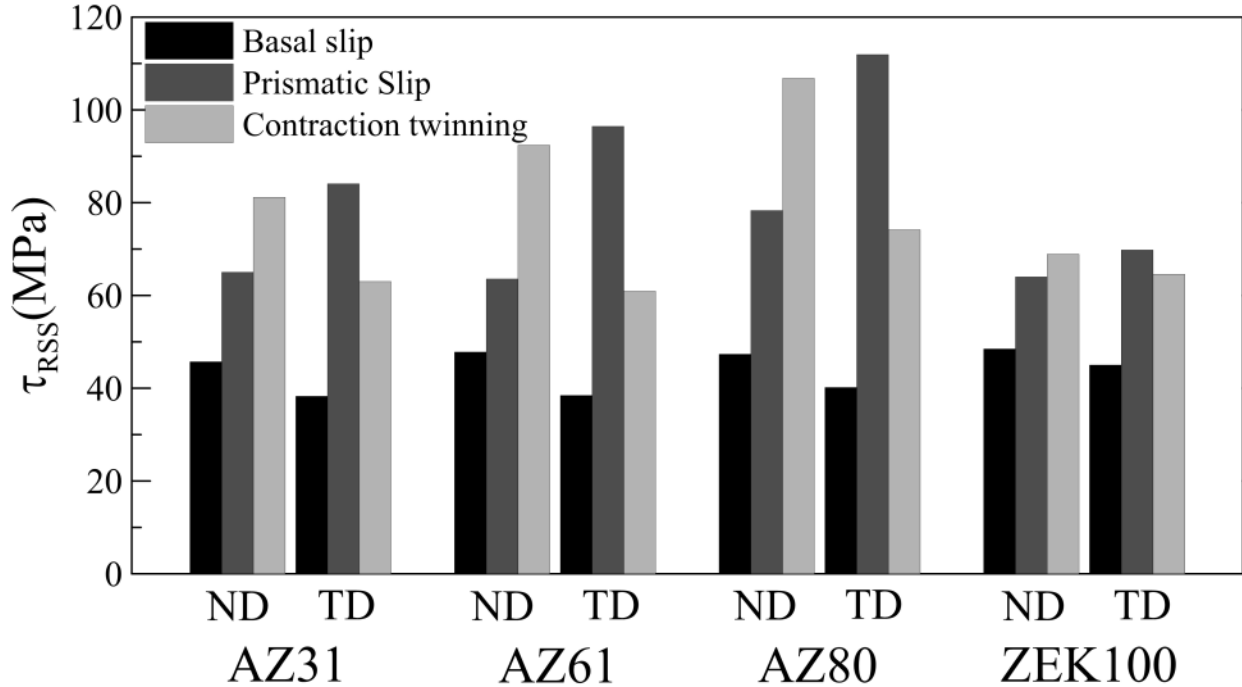


Figure 7-15 Averaged resolved shear stress values on different deformation systems calculated as shown in Figure 7-14

## 7.5 Discussion

Plastic deformation at the notch root results in stress relaxation and notch blunting which lowers the stress intensity [165]. This is the main reason why the heat treated (i.e. more ductile) alloys had higher NYR value. When material at the vicinity of a notch was subjected to a nominal stress close to its yield strength, it attempted to stretch plastically in the direction parallel to the loading direction (L). Due to the conservation of volume during plastic deformation, contraction occurred along lateral directions; however the contraction was constrained by the bulk of the specimen which remained in an elastic state. This led to introduction of tensile stresses along the other two principal directions (i.e. B and W); however the material at the notch root was less constrained along the specimen's width direction (W) due to proximity to a free surface. The material's plastic flow was more constrained along the thickness direction (B). Therefore, the maximum principal stress applied tension along the loading direction and the middle principal stress applied tension along the thickness ( $\sigma_W < \sigma_B$ ) [11], [165]. Such stress distribution created maximum shear stress on those planes whose normal created a 45° angle with W and L as shown schematically in Figure 7-16a.

For a hcp material with strong basal texture (in this study the AZ alloys), such stress distribution created low magnitude of shear stress on the basal slip systems. Though, soft basal slip mechanism is likely to be activated within the localized stress field ahead of a notch. The critical resolved shear stress (CRSS) for basal slip was approximated to be 10-45 MPa for Mg-Al-Zn alloys [20], [143], [144] which is less than

the averaged  $\tau_{RSS}^{basal}$  at notch root (Figure 13). At the same time other deformation systems were likely to be activated to accommodate the contraction strains along the other principal directions (i.e. W and B).

In case of ND specimens, the shear stress resolved on the pyramidal planes was maximum; In such stress condition, the Schmid factor corresponding to  $\{1\ 0\ \bar{1}\ 2\}$  extension twinning was negative for most of grains due to the polarity of twinning. Therefore, the strains should be largely accommodated via  $\{1\ 0\ \bar{1}\ 1\}$  contraction twinning (Figure 7-16b). From what has been mentioned in chapters 5 and 6, contraction twinning is not able to effectively accommodate the plastic strains. Subsequent transformation of  $\{1\ 0\ \bar{1}\ 1\}$  twins by secondary  $\{1\ 0\ \bar{1}\ 2\}$  twinning provided a favorable orientation for basal slip activity in doubly-twinned segments. Shear deformation was localized in the thin lamellae of the double twins leading to local necking and transgranular fracture [19], [32]. The twin-induced transgranular fracture can be observed typically in Figure 7-9. This explained the shear-type fracture of AZ alloys in ND specimens (Figure 7-8a). From what has been mentioned above, it can be suggested that the stress condition at the notch root of ND specimens, reduced the possibility of homogenous plastic deformation and thus a premature fracture occurred.

On the other hand, in case of TD specimens the notch root stress condition created large shear stresses on the prismatic planes of the grains (Figure 7-16b). The CRSS corresponding to prismatic slip is lower than that for pyramidal slip. Via several numerical and experimental methods, it has been shown that the ratio of  $\frac{CRSS_{prism}}{CRSS_{basal}}$  decreases from 48-87 in pure magnesium to 1.1-5.5 in Mg-Al-Zn alloys [35], [37], [40]. Agnew et al. demonstrated the dominant contribution of prismatic slip (over basal and non-basal slip and extension twinning) to strain accommodation in a strongly textured material when tension is applied perpendicular to c-axis of most of the grains [146].

It can be suggested that prismatic slip contributed extensively to strain accommodation at the notch root in the TD specimens leading to a more homogeneous plastic deformation. Moreover, the shear stresses resolved on the  $\{1\ 0\ \bar{1}\ 1\}$  planes were lower compared to ND specimens. Thus, a delayed activation of  $\{1\ 0\ \bar{1}\ 1\}$  twinning occurred and fracture was resisted more in the TD specimens.

In case of ZEK100 alloy, the tensile notch response appeared to be insensitive to the notch orientation. Due to spread of basal poles from ND to TD, the orientation of most of the grains relative to the maximum shear stress direction remained unchanged in ND and TD specimens (as shown schematically in Figure 7-16c).

Finally, it should be stated that the assumption of  $\sigma_{nss} = \sigma_0$  was only to study the onset of plasticity ahead of the notch root. At higher values of  $\sigma_{nss}$  (close to NTS of specimen), the plastic zone produced ahead of a notch would be larger; however the triaxial stress condition is not expected to change significantly since the plastic zone is still surrounded by the elastic material, away from the notch.

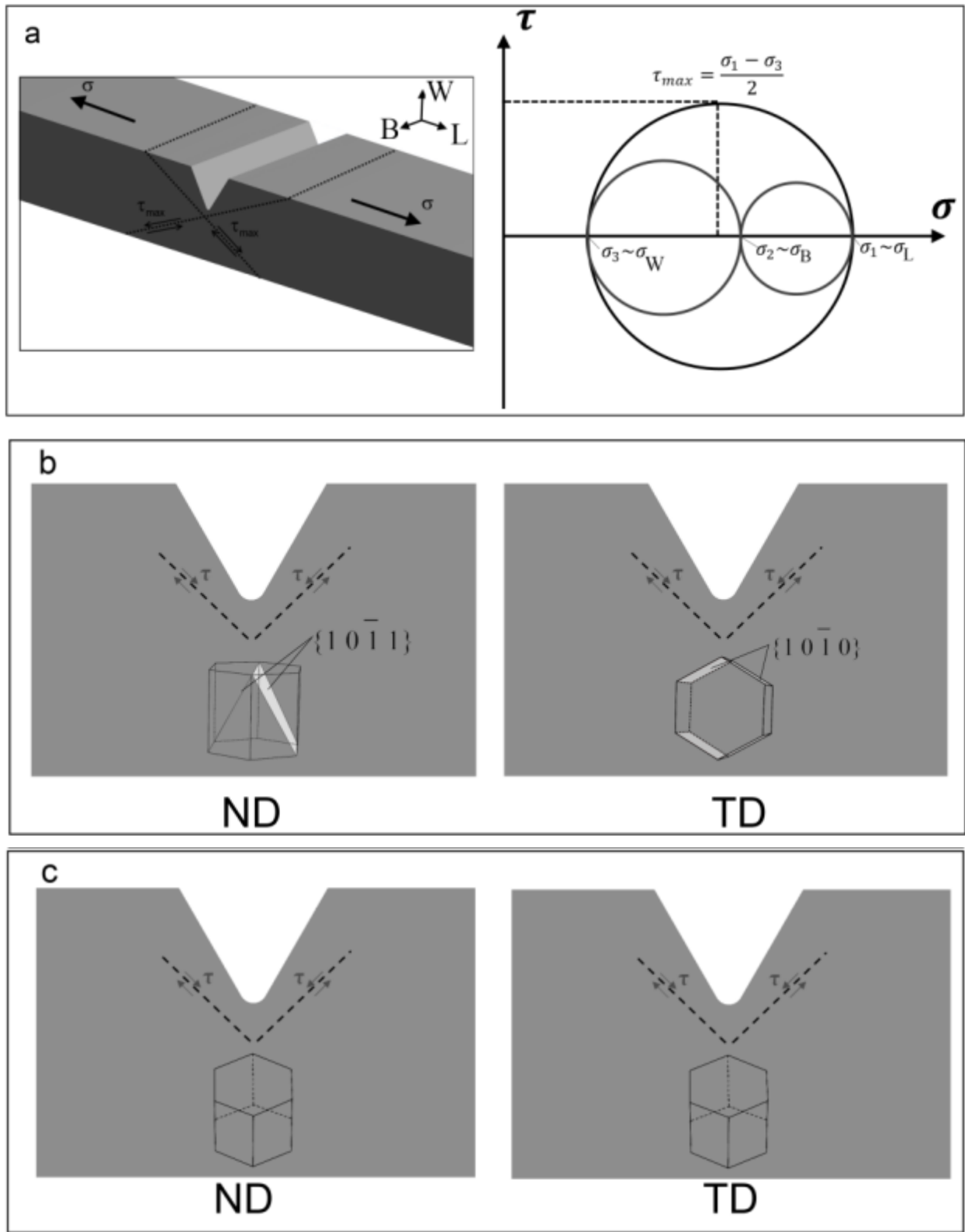


Figure 7-16 (a) Schematic drawing of stress condition at notch root using Mohr's circle; (b) heavily stressed deformation systems in crystal near the notch in ND and TD specimens in case of AZ alloys; (c) general crystallographic orientation relative to the stress condition in ZEK100

## 7.6 Summary

Notch strength and notch sensitivity of magnesium alloys were investigated in this work. The following conclusions can be drawn:

1. AZ80 alloy in as-received condition demonstrated poor notch ductility along with premature failure. Early fracture was associated with easy fracture at  $Mg_{17}Al_{12}$  intermetallics.
2. AZ magnesium alloys with sharp texture, demonstrated superior mechanical performance when a notch was introduced along the sheet's transverse direction than when it was introduced along the sheet's normal direction. The numerical results indicated that the sensitivity of the AZ alloys to the notch orientation is due to activity competition between prismatic slip deformation and contraction twinning.
3. When notch was along the sheet's normal direction, contraction twinning became more readily active. This led to early shear localization and transgranular fracture. When notch was along the sheet's transverse direction, the contraction twinning systems were less under stress. Therefore, localized shearing was delayed. On the other hand, higher activity of prismatic dislocation slip led to a more homogenous deformation ahead of a notch parallel to the sheet's transverse direction.
4. Due to more randomized texture, ZEK100 alloy appeared to be less sensitive to the notch orientation. The numerical results also showed no significant difference in the activity of deformation systems when the notch was along the sheet's normal direction or transverse direction.

## Chapter 8

### Conclusions and Outlook

In the current work, fracture characteristics of magnesium alloys subjected to complex stress condition at the edge of spot weld were investigated. More specifically, fracture micro-mechanisms leading to crack initiation, in different microstructures were characterized and explained by analytical and numerical approaches. The effects of microstructural features such as intermetallics, crystallographic texture and grain size on fracture strength, ductility and characteristics in magnesium materials were studied.

The following sections contain the major conclusion of this work and recommendations for future research.

#### 8.1 Conclusions

The following conclusions were made through the current work:

- 1 A highly localized stress field is created at the edge of nugget for a spot weld subjected to external loading. Fracture of spot weld was associated with the inability of the microstructure (existing at the edge of the nugget) to accommodate the inelastic strains.
- 2 Formation of  $\beta\text{-Mg}_{17}(\text{Al,Zn})_{12}$  intermetallic compounds led to deterioration of ductility in HAZ of Mg-Al-Zn alloys. Micro-crack initiation at the  $\beta$  sites, preceded the activation of plastic deformation mechanisms in the HAZ of AZ61 and AZ80 spot welds, subjected to tensile shear loading. The strength and ductility of spot weld were reduced by increase in the Al content of base metal.
- 3 Post-weld solutionizing heat treatment improved strength and ductility of the spot welds with high Al content. The failure mode changed from nugget pull-out (in as welded condition) to through-thickness (in heat treated condition) and crack pathway shifted towards the HAZ/BM. Observation of high twinning activity near the fracture edges, indicated activation of plastic deformation mechanisms in the microstructure at the edge of nugget, which introduced more resistance against crack initiation.
- 4 A correlation was found between fracture initiation in intermetallic-free microstructure of HAZ and  $\{10\bar{1}1\}$ - $\{10\bar{1}2\}$  double twinning activity. Transgranular micro-cracking occurred in the microstructure of HAZ adjacent to the notch. The micro-cracks possessed the same orientation as



the double twin habit planes. The double twins, which involved rotation of  $\langle 1 \bar{2} 1 0 \rangle / 38^\circ$ , formed more readily in the microstructure than those of the other three variants. The experimentally observed primary  $\{1 0 \bar{1} 1\}$  twinning systems demonstrated a Schmid-type behavior. The majority of the twinning systems were activated when the resolved shear stress reached a range of 70-100 MPa.

- 5 Schmid law numerical analysis demonstrated that crystal reorientation due to double twinning (which involved  $\langle 1 \bar{2} 1 0 \rangle / 37.5^\circ$  crystallographic rotation), provided favorable condition for basal slip activity. By TEM observations, higher basal slip activity was observed in the double twinned segments compared to the matrix.
- 6 A correlation between micro-texture and fracture susceptibility was found: The grains with difficult orientation for slip deformation demonstrated more tendencies to plastically deform by  $\{1 0 \bar{1} 1\}$  twinning and were more susceptible to shear localization and transgranular fracture.
- 7 In an intermetallic-free microstructure, the effects of crystallographic texture and grain size became important in determining the nugget ductility as well as failure mode. Coarse-grained microstructures of HAZ in AZ61 and AZ80 along with their sharp basal texture appeared to be highly susceptible to early shear localization and transgranular fracture. On the other hand, the HAZ of ZEK100 demonstrated high ductility since its microstructure was able to accommodate the plastic strains more effectively due to its fine-grained microstructure and randomized texture.
- 8 Notch strength and ductility of magnesium alloys was associated with the combined effect of texture and stress condition: Mg alloys demonstrated low notch strength and ductility when stress condition led to high activity of  $\{1 0 \bar{1} 1\}$  twinning. They demonstrated to be more ductile when slip-based deformation mechanisms were more active than the deformation mechanisms followed by twinning.

The schematic diagram presented in Figure 8-1 summarizes the main conclusions in this work. In a localized stress field, operating ahead of a stress raiser, crack initiates readily in a microstructure with high volume fraction of intermetallics. Therefore, presence of intermetallics must be avoided. This can be achieved by either application of a proper heat treatment procedure or selection of a material with low amount of alloying elements. In a microstructure free of intermetallics, fracture was resisted more if twinning activity (specifically those on  $\{1 0 \bar{1} 1\}$  systems) is suppressed and plastic accommodation ahead

of notch is majorly carried out by dislocation slip. This can be satisfied by selection of a material with randomized texture and fine grain size.

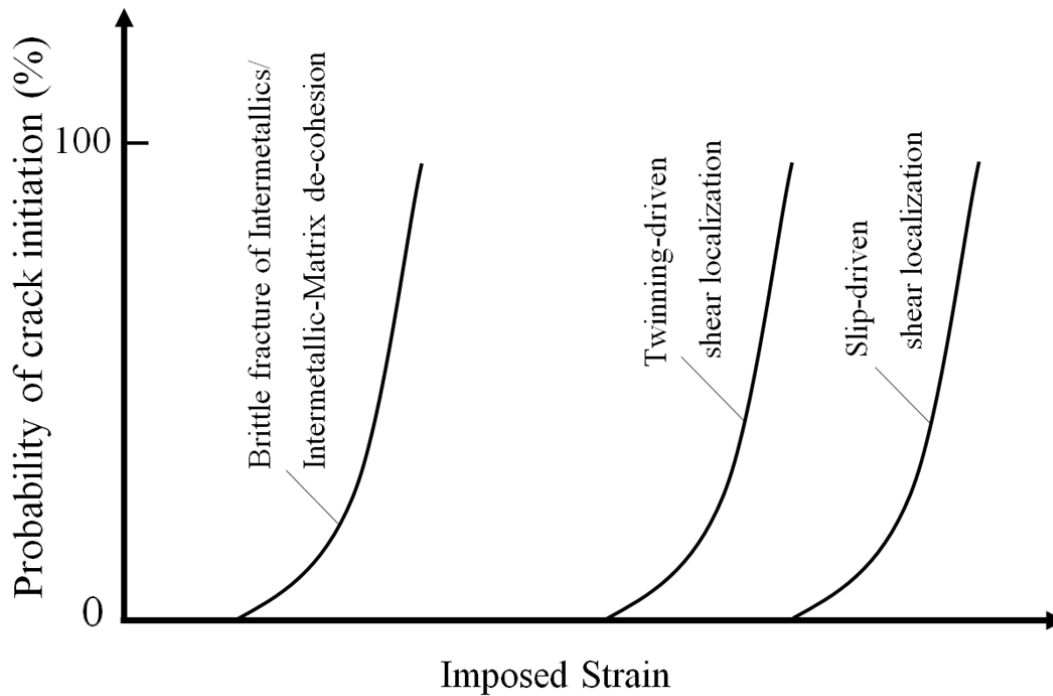


**Figure 8-1 Schematic diagram showing the probability of crack initiation vs. imposed strain based on the type of micro-mechanisms to be activated in a localized stress field**

## 8.2 Outlook

The following topics are suggested for future research:

1. The current research was focused on effects of microstructure on mechanical properties and fracture characteristics of spot weld under monotonic loading. It is suggested to evaluate the microstructural effects (intermetallics, texture and grain size) on fatigue performance of spot weld. It is predicted that these microstructural factors affect stage I (slip-band crack growth) of fatigue damage.
2. More examination of microstructure is needed in order to characterize other deformation mechanisms activated during tensile shear testing of spot weld. It is suggested that prismatic slip contribute largely to plastic accommodation in magnesium materials subjected to notch stress condition. In the current work prismatic slip activity was not characterized and discussed.

3. More detailed study is needed to understand microstructural evolution (such as production of stacking fault regions and dislocation activity) within the double twinned volumes. Careful EBSD observation of the fractured grains revealed twinned volumes which were not identified based on their boundary misorientations. These twins are shown typically in Figure 5-9 b and c. The crystallographic orientation of these twinned segments are different from one to another and roughly close ( $7\text{-}20^\circ$  axial/angular misorientation) to their double twin neighbors. It is possible that the high dislocation activity in double twinned volumes led to recrystallization and production of high angle grain boundaries.
4. The effects of texture on notch strength and ductility must be examined in more detail. In the current research ZEK100 alloy was used as a representation of a randomized textured materials; however this material still possessed a strong texture (since a large volume fraction of grains have basal poles rotated from normal direction towards transverse direction). Moreover, the effect of basal slip activity on notch strength and ductility should be investigated as well. In this regard, it is recommended to evaluate the mechanical performance of ZEK100 spot weld, when tensile shear loading direction is close to the sheet's transverse direction. In this condition, the basal slip systems are subjected to high shear stresses. High basal slip activity can prevent early shear localization and delay fracture in magnesium alloys. This was confirmed by uniaxial tensile testing of ZEK100 along transverse direction. The tensile elongation in this condition was recorded as approximately 45% (more than double of tensile elongation along the sheet's rolling direction). Such increase in ductility should be able to delay fracture as well.
5. Electron backscattered diffraction is a suitable method to characterize the fusion zone in case of crystallography of solidification. It was observed in this study that the texture within the central rejoin of fusion zone is completely randomized due to the heterogeneous nucleation effect during solidification; however the epitaxial growth region must demonstrate crystallographic orientation relationships with the un-melted grains adjacent to the fusion boundary. It is suggested that the developed columnar dendrite zone of fusion zone in spot weld of AZ31 alloy, possessed a preferred crystallographic texture. Texture effect might be a reason for interfacial failure in spot weld of AZ31.
6. In the current work the stress and strain analysis by finite element model was carried out based on von Mises yielding criteria, since the HAZ was dominated by tension along the sheet's rolling direction. However magnesium alloys have demonstrated anisotropic properties in plasticity., and application of a more realistic yielding criteria to account for yield anisotropy (such as Hill's

plasticity) may results in more accurate prediction of stress and strain condition at the notch. Moreover, in this study the same materials properties were assigned to base metal, heat affected zone and fusion zone for stress-strain analysis; however the mechanical properties are affected by the weld thermal cycle in fusion zone and heat affected zone. This differences in mechanical properties (including yield criteria and hardening rule) should be considered for a more accurate stress and strain analysis.

**Appendix A**  
**Tensile Test Data for Magnesium Alloys in Different Heat Treatment**  
**Conditions**

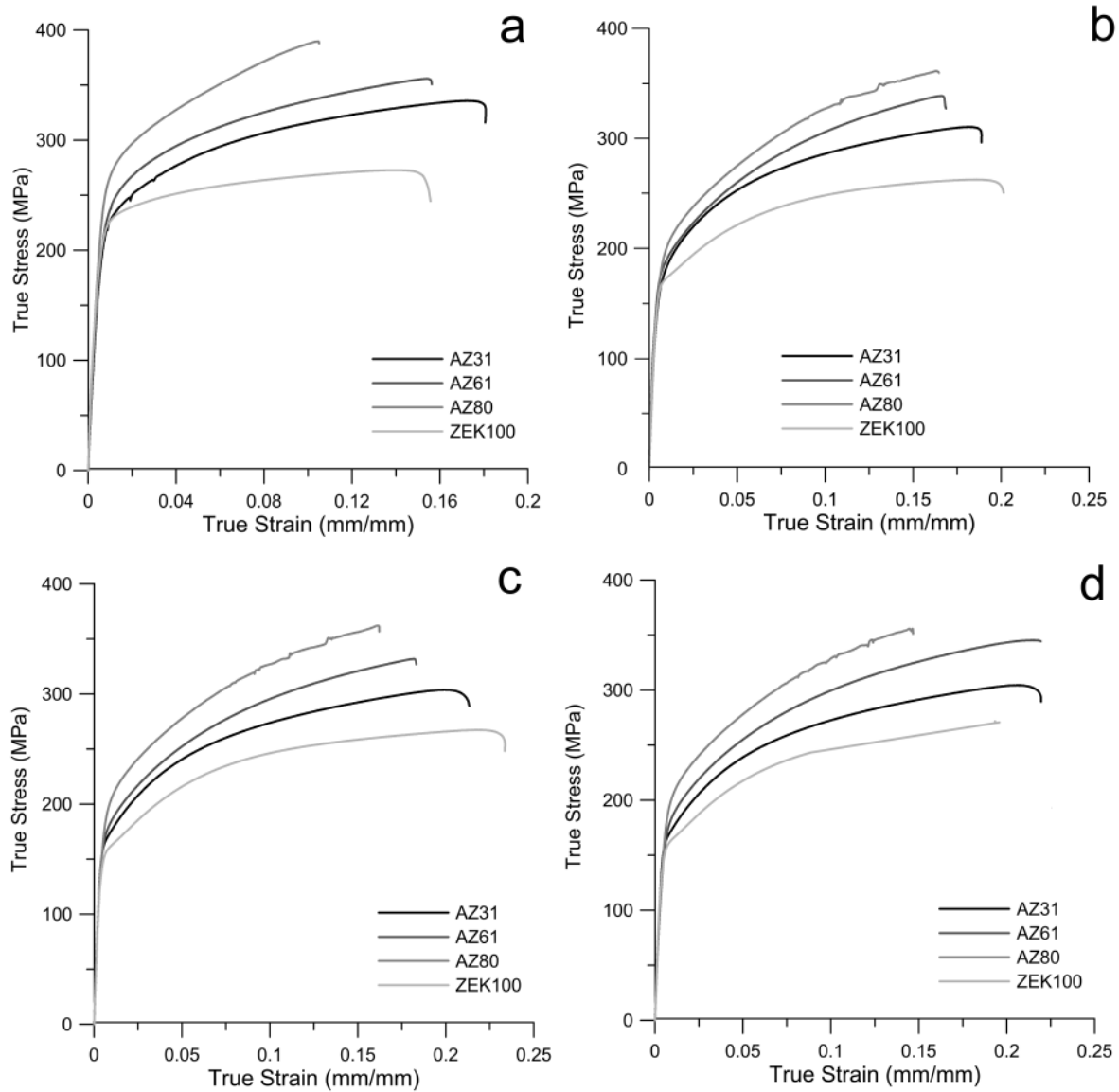


**Figure A.1** Monotonic tensile stress-strain curves for AZ31, AZ61, AZ80 and ZEK100 along rolling direction in (a) as-received; (b) heat treated at 400°C for 1hr; (c) heat treated at 400°C for 6hr and (d) heat treated at 400°C for 10hr conditions

## Appendix B

### Tensile Shear Test Results for the Spot Welds of AZ Alloys

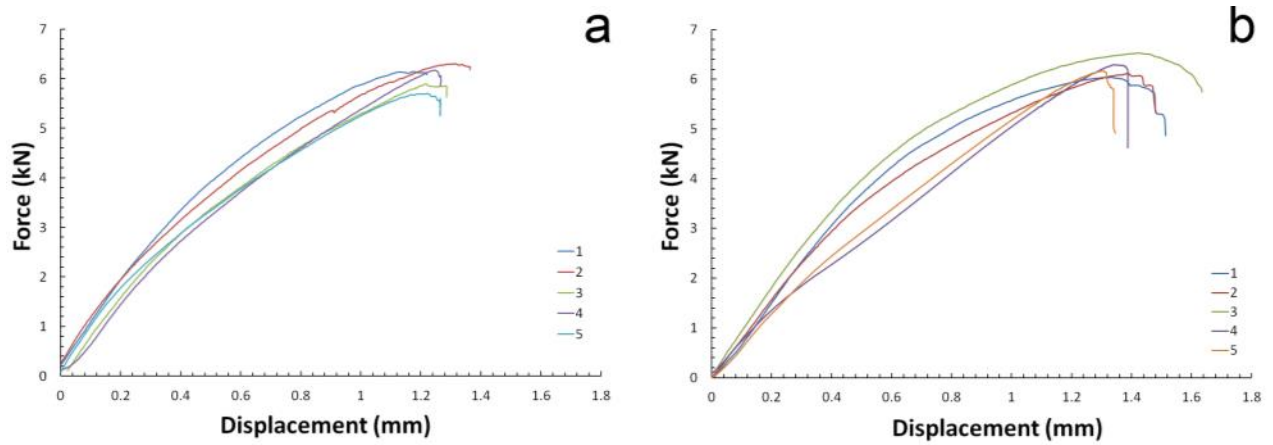


Figure B.1 Force vs. Displacement for spot weld of AZ31; (a) as welded and (b) heat treated

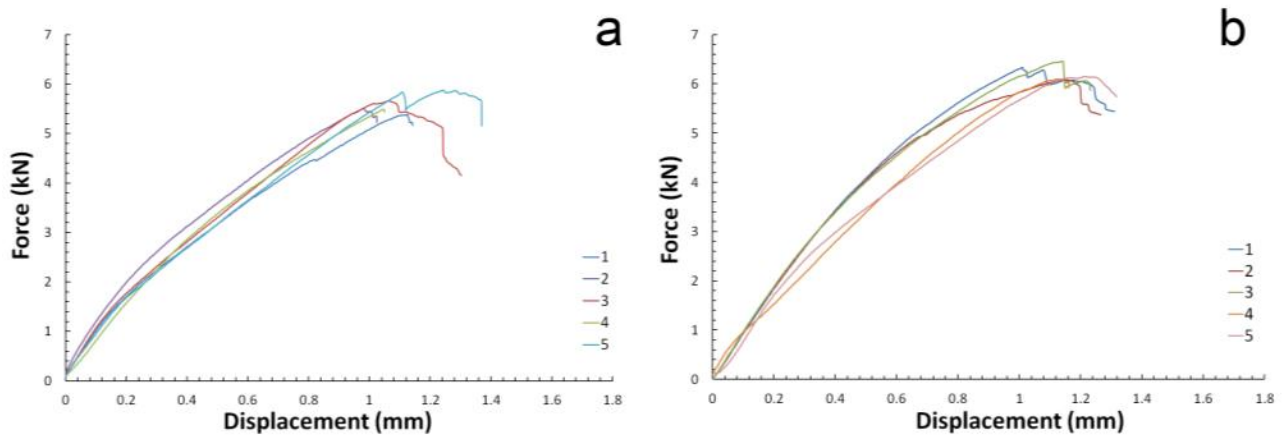
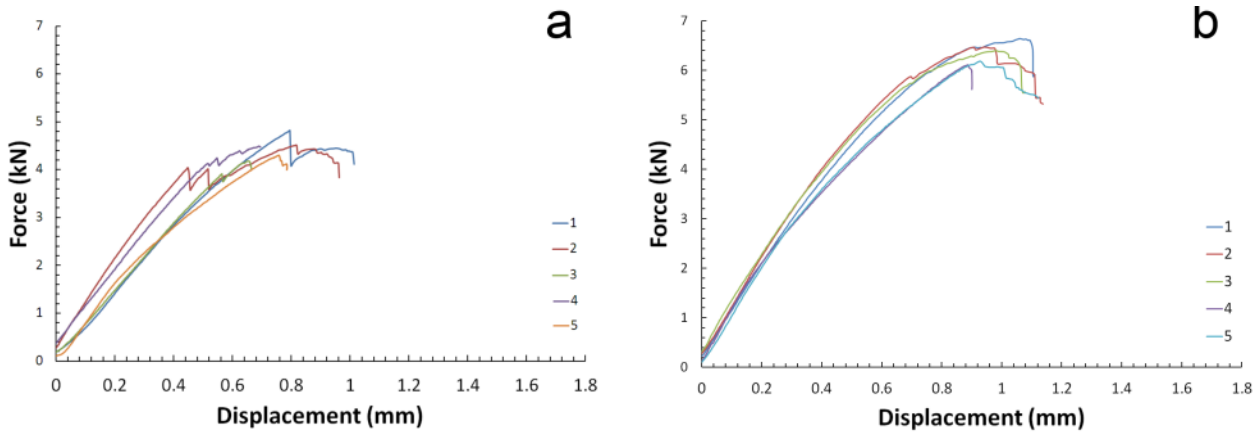


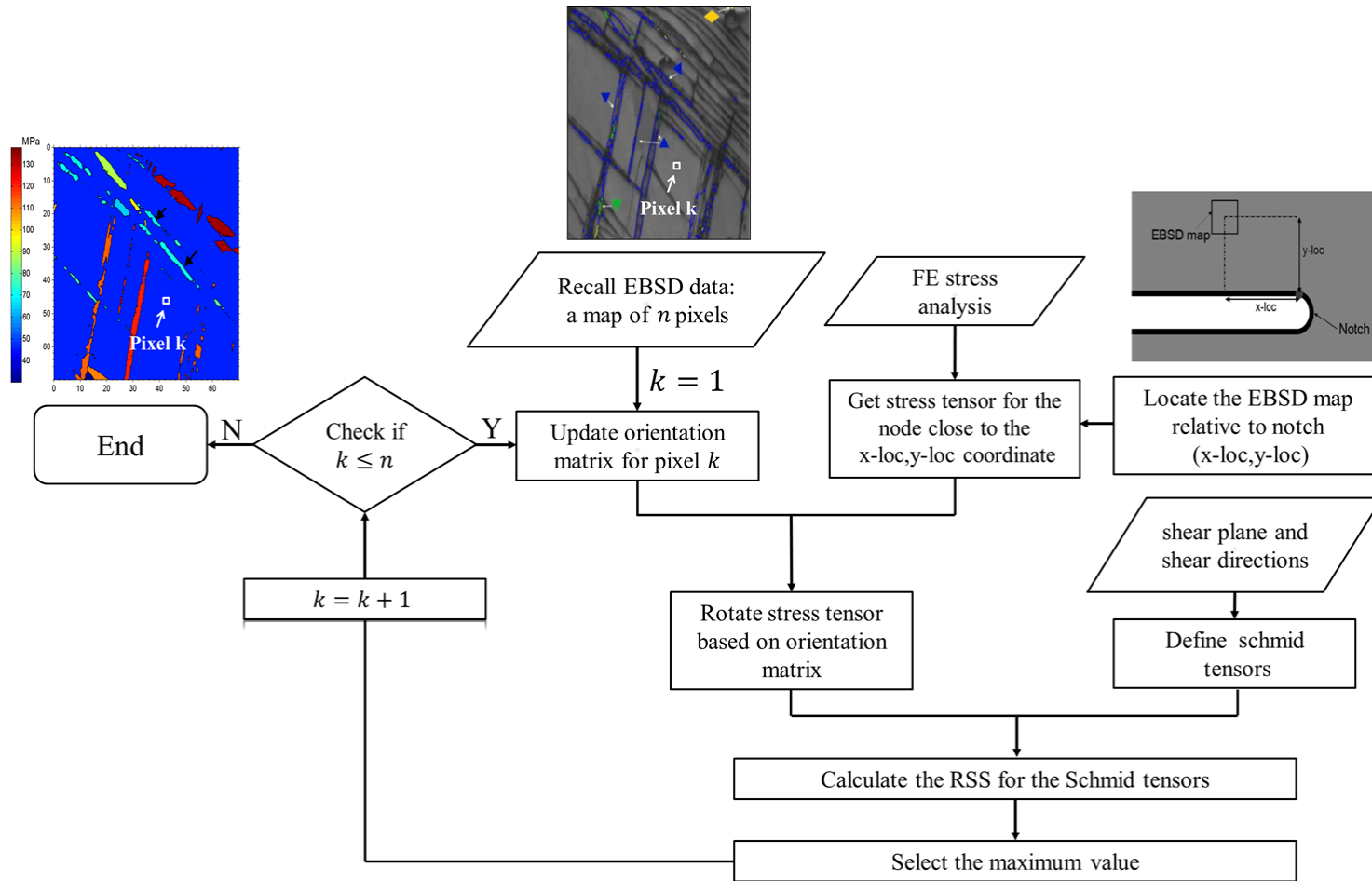
Figure B.2 Force vs. Displacement for spot weld of AZ61; (a) as welded and (b) heat treated



**Figure B.3 Force vs. Displacement for spot weld of AZ80; (a) as welded and (b) heat treated**

## Appendix C

### Flowchart for numerical calculation of resolved shear stress for deformation systems











## Appendix D

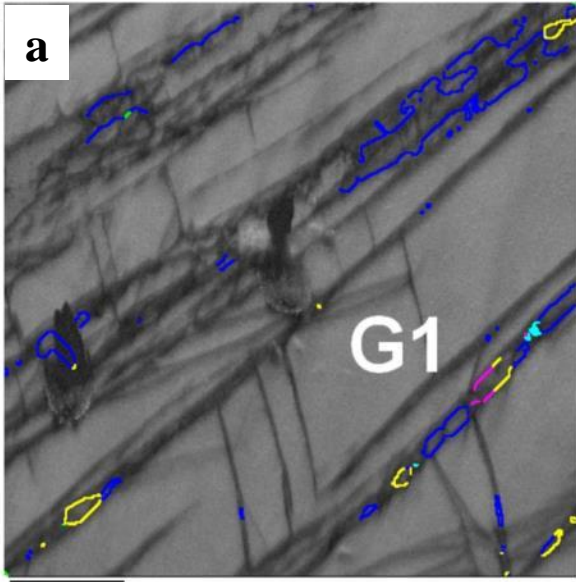
### Determination of Schmid-type behavior of $\{1\ 0\ \bar{1}\ 1\}$ twinning

The procedure for determination of Schmid-type behavior of primary  $\{1\ 0\ \bar{1}\ 1\}$  twinning systems is explained in details with two examples. 78 grains (within which the primary  $\{1\ 0\ \bar{1}\ 1\}$  twinning variants were unambiguously determined) were examined in this study. Figure C.1 shows the EBSD maps and grain numbering order. Only those grains, in which the primary  $\{1\ 0\ \bar{1}\ 1\}$  twin or  $\{1\ 0\ \bar{1}\ 1\} - \{1\ 0\ \bar{1}\ 2\}$  double twins (of variant I and II) were identified, were selected. To determine the Schmid-type behavior, each grain was treated individually as following:

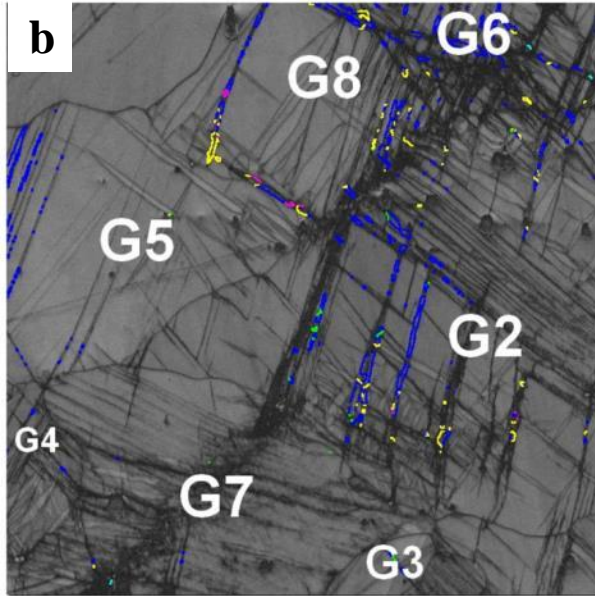
For a matrix (or grain), six primary  $\{1\ 0\ \bar{1}\ 1\}$  twinning variants exist as shown in Table C.1. Thus, 6 possible crystal reorientation can take place by primary  $\{1\ 0\ \bar{1}\ 1\}$  twinning. These six reorientation can be predicted if the matrix orientation is determined (by Euler angles). The procedure for reorientation was done based on the “rotation” command in the MTEX toolbox and plotted in the pole-figures showing traces of  $(0\ 0\ 0\ 1)$  and  $\{1\ \bar{2}\ 1\ 0\}$  poles. The shear stress resolved on each of these six twinning systems was determined based on the defined stress tensor. The stress tensors defined for each EBSD data (as plotted in Figure C.1) are shown in Table C.2. Then, the orientation of the identified twins (by EBSD) were superimposed on the pole-figures (by markers introduced by Table C.3) in order to determine their variants. Variant selection from the identified primary  $\{1\ 0\ \bar{1}\ 1\}$  twins and  $\{1\ 0\ \bar{1}\ 1\} - \{1\ 0\ \bar{1}\ 2\}$  double twins are explained by the following two examples :

**Table C.1 Six  $\{1\ 0\ \bar{1}\ 1\}$  twinning variants and the markers used for their demonstration on the pole-figures**

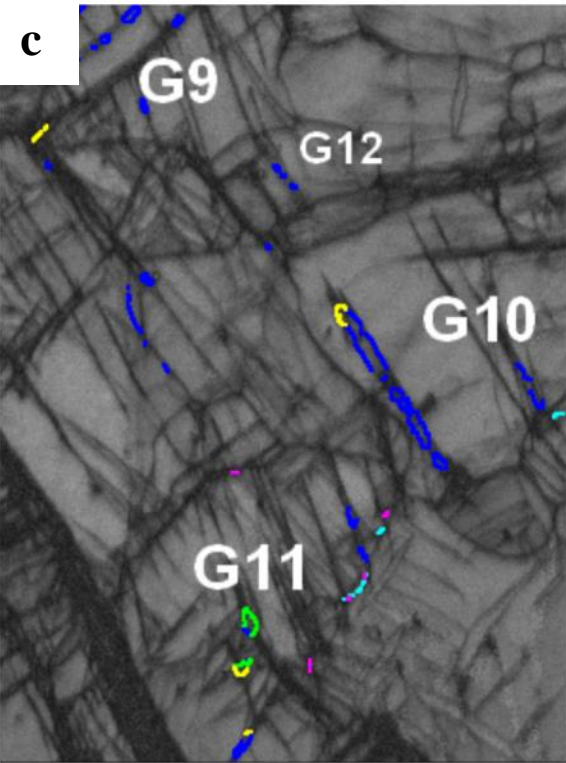
Twin variant #	Shear plane-direction	Marker
1	$(1\ 0\ \bar{1}\ 1)[1\ 0\ \bar{1}\ \bar{2}]$	
2	$(0\ 1\ \bar{1}\ 1)[0\ 1\ \bar{1}\ \bar{2}]$	
3	$(\bar{1}\ 1\ 0\ 1)[\bar{1}\ 1\ 0\ \bar{2}]$	
4	$(1\ 0\ \bar{1}\ 1)[\bar{1}\ 0\ 1\ \bar{2}]$	
5	$(0\ \bar{1}\ 1\ 1)[0\ \bar{1}\ 1\ \bar{2}]$	
6	$(1\ \bar{1}\ 0\ 1)[1\ \bar{1}\ 0\ \bar{2}]$	



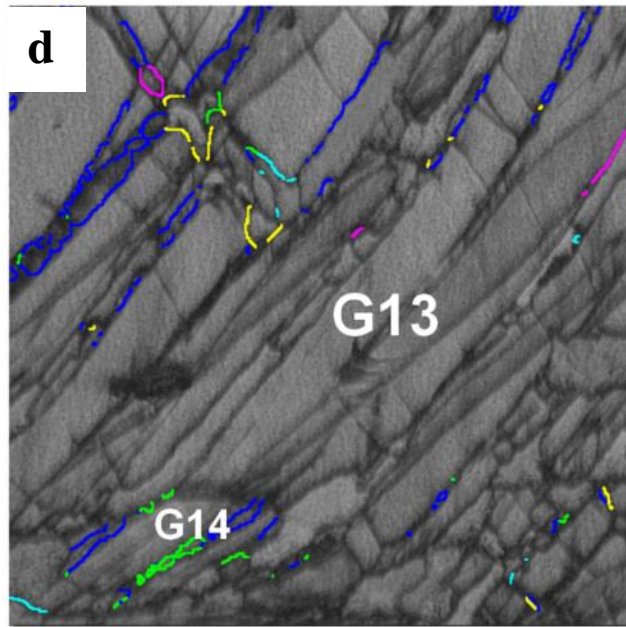
10  $\mu\text{m}$



100  $\mu\text{m}$



10  $\mu\text{m}$



10  $\mu\text{m}$

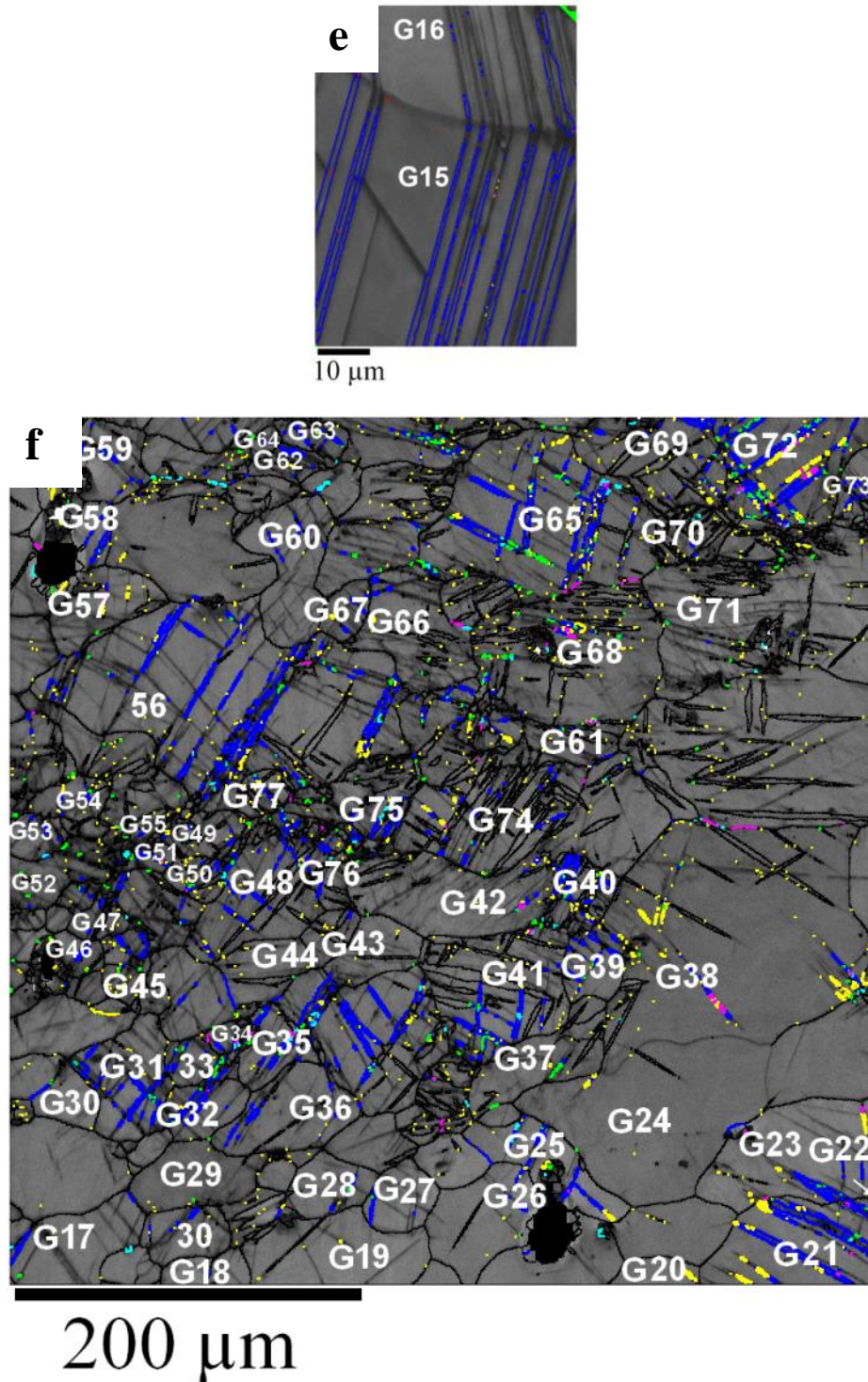





Figure C.1 Grain numbering for the EBSD data used in this study for determination of the Schmid-type behavior of  $\{1\ 0\ \bar{1}\ 1\}$  twinning. Twin boundaries are drawn by yellow for identification of  $\{1\ 0\ \bar{1}\ 1\}$  twinning and blue, green, light blue and fuchsia for identification of  $\{1\ 0\ \bar{1}\ 1\} - \{1\ 0\ \bar{1}\ 2\}$  twinning

**Table C.2 Definition of stress tensors corresponding to the EBSD maps shown in Figure C.1**

Figure	$\sigma_{ij}$ (MPa)
C.1.a	$\begin{bmatrix} 237 & -56 & 0 \\ -56 & 83 & 0 \\ 0 & 0 & 145 \end{bmatrix}$
C.1.b	$\begin{bmatrix} 247 & 31 & 0 \\ 31 & 22 & 0 \\ 0 & 0 & 132 \end{bmatrix}$
C.1.c	$\begin{bmatrix} 230 & -29 & 0 \\ -29 & 24 & 0 \\ 0 & 0 & 120 \end{bmatrix}$
C.1.d	$\begin{bmatrix} 232 & 29 & 0 \\ 29 & 23 & 0 \\ 0 & 0 & 121 \end{bmatrix}$
C.1.e	$\begin{bmatrix} 223 & -45 & 0 \\ -45 & 1 & 0 \\ 0 & 0 & 113 \end{bmatrix}$
C.1.f	$\begin{bmatrix} 227 & 26 & 0 \\ 26 & 25 & 0 \\ 0 & 0 & 117 \end{bmatrix}$

**Table C.3 Marker shapes and colors for identification of  $\{1\ 0\ \bar{1}\ 1\}$  twinning and  $\{1\ 0\ \bar{1}\ 1\}$ - $\{1\ 0\ \bar{1}\ 2\}$  double twinning variants on the pole-figures**

Twin type	$\{1\ 0\ \bar{1}\ 1\}$	$\{1\ 0\ 1\ 1\}$ - $\{1\ 0\ 1\ 2\}$	
Twinning variants		I	II
Misorientation (axis/angle)	$\langle 1\ \bar{2}\ 1\ 0 \rangle / 56.17^\circ$	$\langle 1\ \bar{2}\ 1\ 0 \rangle / 37.5^\circ$	$\langle 1\ \bar{2}\ 1\ 0 \rangle / 30.1^\circ$
Orientation symbols on pole figure			

**C. 1. Direct determination of the twin variants from the experimentally observed  $\{1\ 0\ \bar{1}\ 1\}$  twins**

Figure C.2 shows the  $(0\ 0\ 0\ 2)$  and  $\{1\ \bar{2}\ 1\ 0\}$  pole-figures for orientations corresponding to matrix and its six  $\{1\ 0\ \bar{1}\ 1\}$  twinning variants for grain “G16” (as shown in Figure C.1). The shear stress resolved on each of the six twinning systems was calculated and shown in the table below the figure. The values were ranked from “1” (maximum) to “6” (minimum). The orientation corresponding to the experimentally observed  $\{1\ 0\ \bar{1}\ 1\}$  in G16 was also superimposed on the pole-figure. It is clear that the twinning occurred based on variant #5 i.e. the 1<sup>st</sup> rank. It should be noted that a small angle misorientation between these predicted orientation and actual twin orientation is normal due to high dislocation activity (i.e. low angle boundaries) within twinned volumes.

**C.2. Indirect determination of the twin variants from the experimentally observed  $\{1\ 0\ \bar{1}\ 1\}$  –  $\{1\ 0\ \bar{1}\ 2\}$  twins**

In most cases, the crystal orientations within the  $\{1\ 0\ \bar{1}\ 1\}$  twins were not captured by EBSD such as G15 (Figure C.1); however they can be determined inherently from their double twin daughters. Figure C.3 shows the orientations for G15. The matrix, primary  $\{1\ 0\ \bar{1}\ 1\}$  twin and the resultant  $\{1\ 0\ \bar{1}\ 1\}$  –  $\{1\ 0\ \bar{1}\ 2\}$ , all three share a common rotation axis of  $\langle 1\ \bar{2}\ 1\ 0 \rangle$ -type. From the  $\{1\ \bar{2}\ 1\ 0\}$  pole-figure, the identified double twin (blue triangle) shares a common  $\langle 1\ \bar{2}\ 1\ 0 \rangle$  rotation axis with twin variants #3 and #6. Thus, this double twin resulted from either variant #3 or variant #6 twinning. On the other hand, we

know that there exist a misorientation of  $86^\circ$  between the primary and secondary twinning. Therefore, variant #3 is not able to be the primary twinning system for the observed double twin, while variant #6 is almost perpendicular to the double twin. Thus, variant #6 is the primary  $\{1\ 0\ \bar{1}\ 1\}$  variant, which actually happened in G15. Table C.4 presents the matrix and twin orientations for the 78 grains considered in this work for investigation of Schmid-type behavior of twinning. Table C.5 lists the calculated resolved shear stress values corresponding to each of 6 twinning systems for each grain.

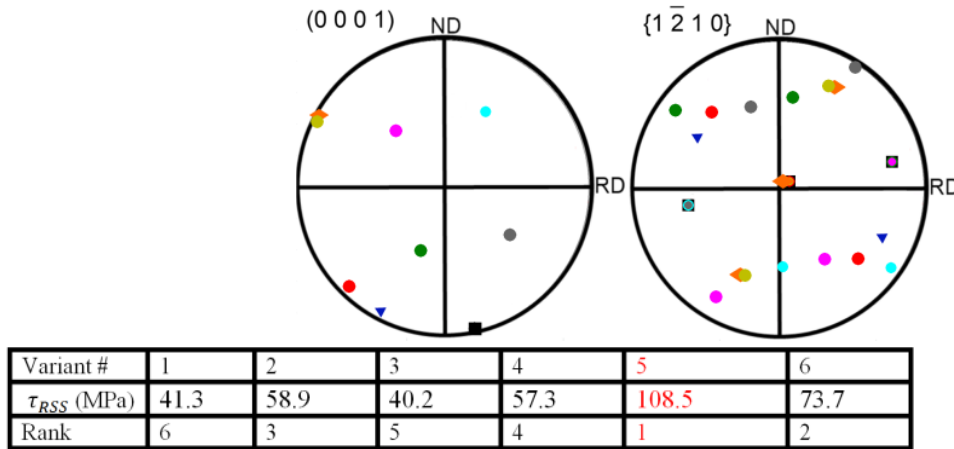


Figure C.2  $(0\ 0\ 0\ 2)$  and  $\{1\ \bar{2}\ 1\ 0\}$  pole-figures for G16 matrix (black square), its six possible  $\{1\ 0\ \bar{1}\ 1\}$  twin variants (circles) and experimentally observed  $\{1\ 0\ \bar{1}\ 1\}$  twin (orange rhombic). The values for resolved shear stress for each twin variant is calculated and shown in the table and the variant which was identified in the grain was highlighted by red font

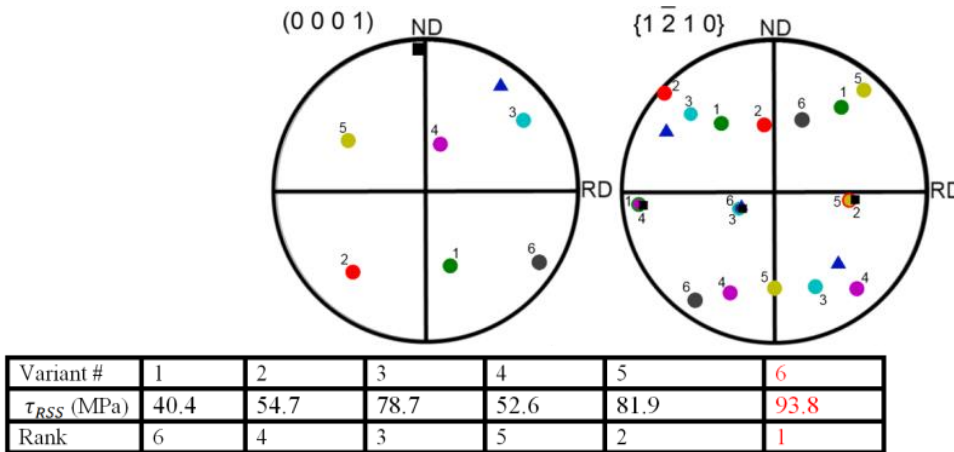
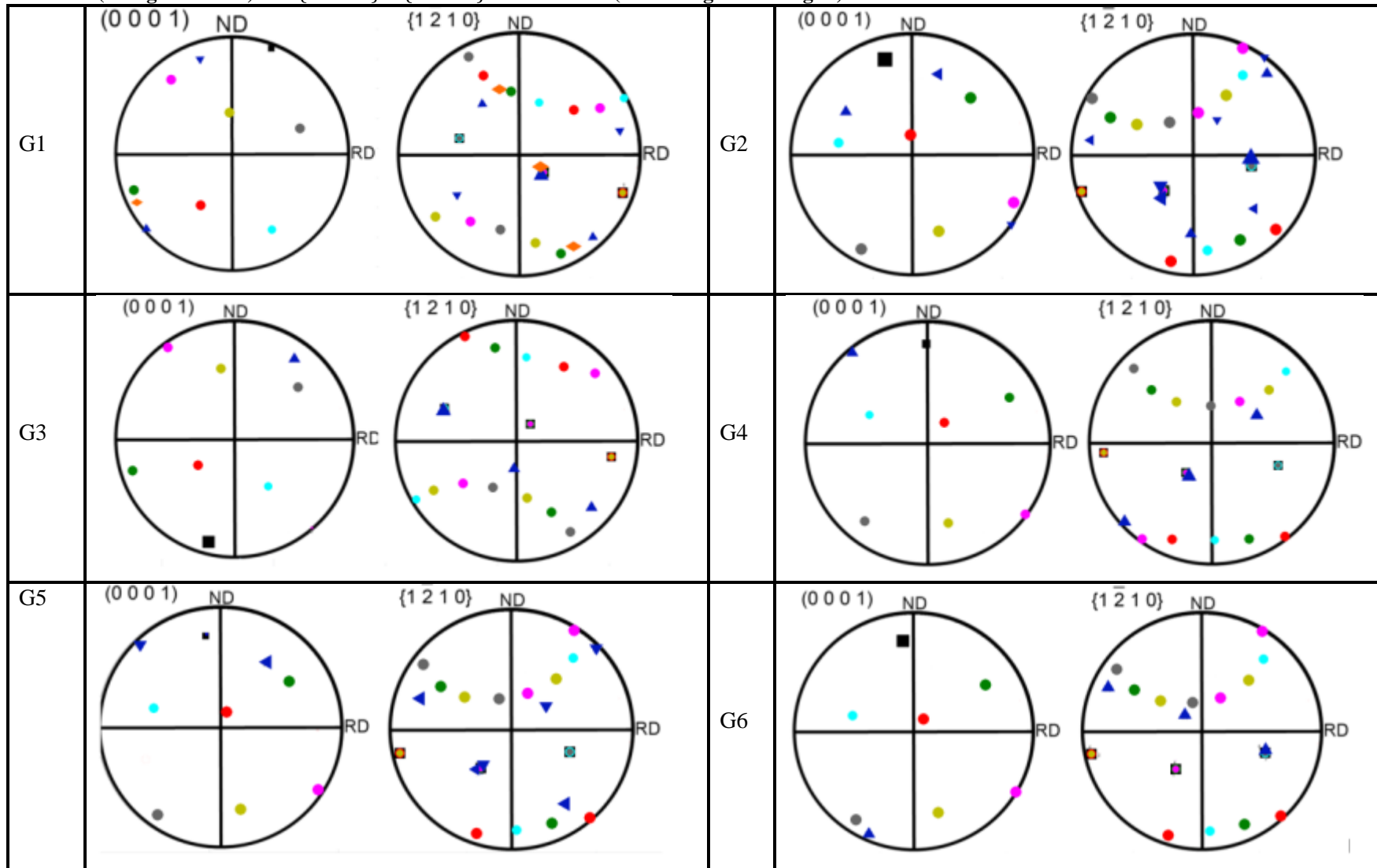
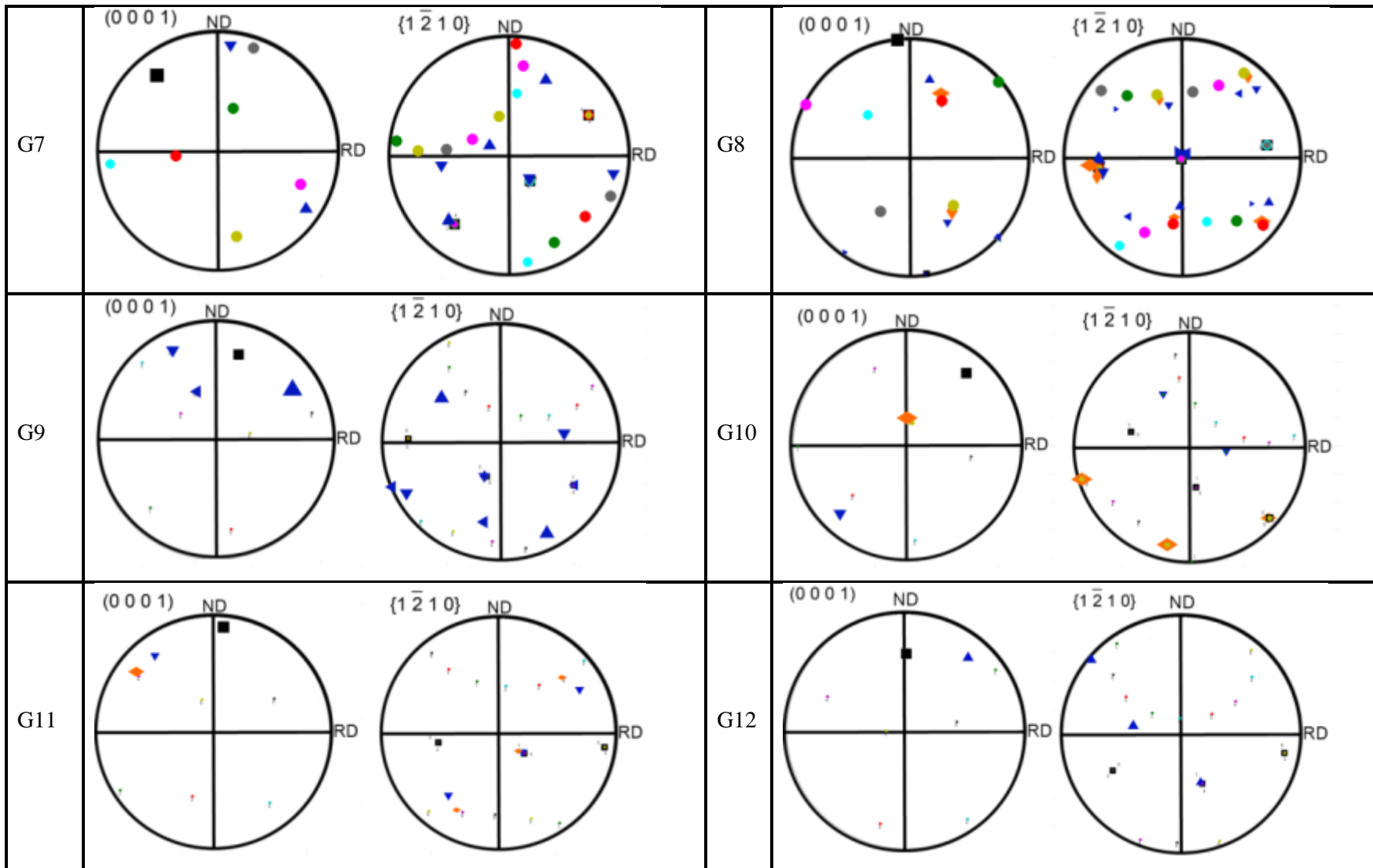
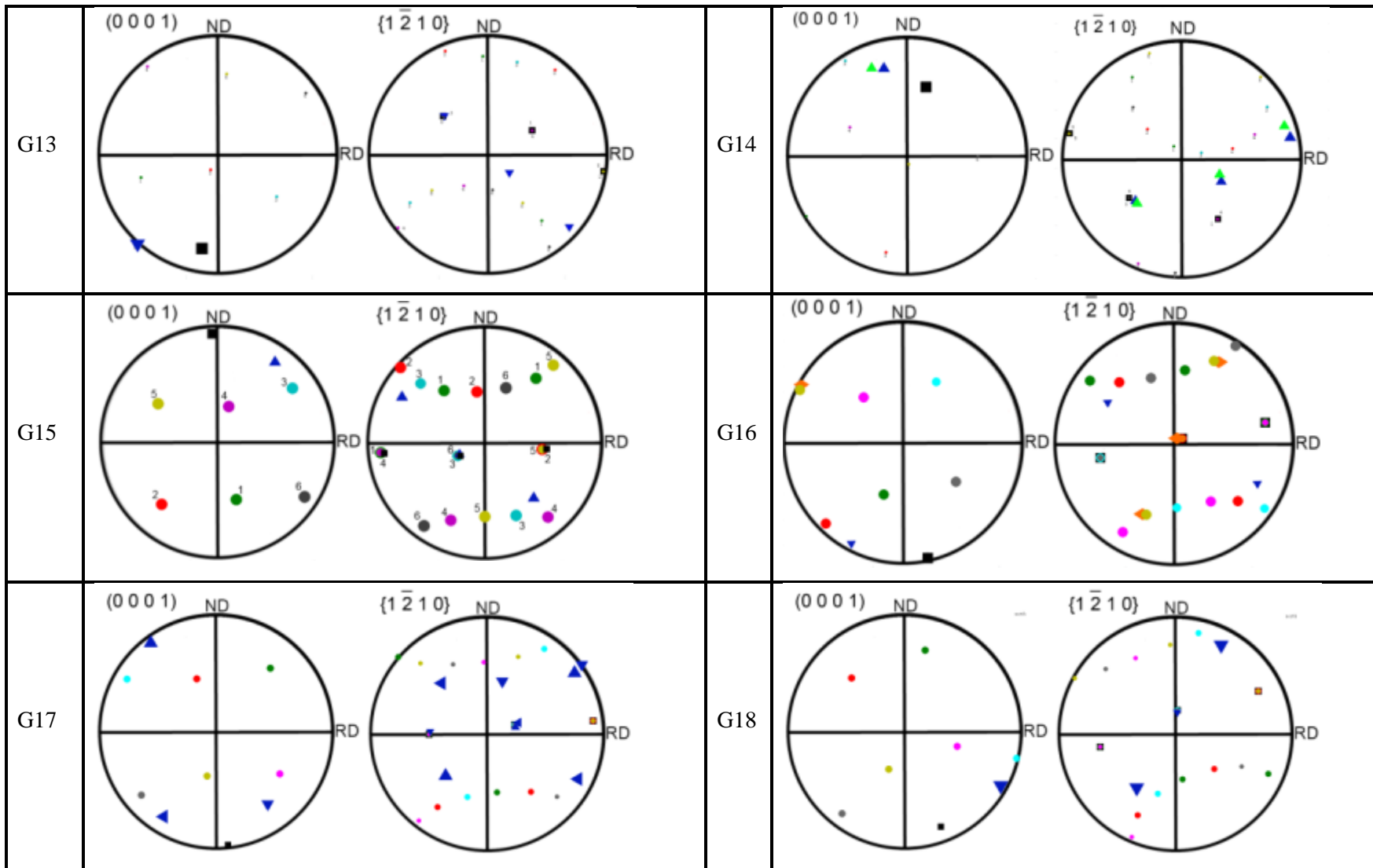


Figure C.3  $(0\ 0\ 0\ 2)$  and  $\{1\ \bar{2}\ 1\ 0\}$  pole-figures for G15 matrix (black square), its six possible  $\{1\ 0\ \bar{1}\ 1\}$  twin variants (circles) and experimentally observed  $\{1\ 0\ \bar{1}\ 1\} - \{1\ 0\ \bar{1}\ 2\}$  double-twin (blue triangle). The value of resolved shear stress for each twin variant is calculated and shown in the table and the variant which was identified in the grain was highlighted by red font

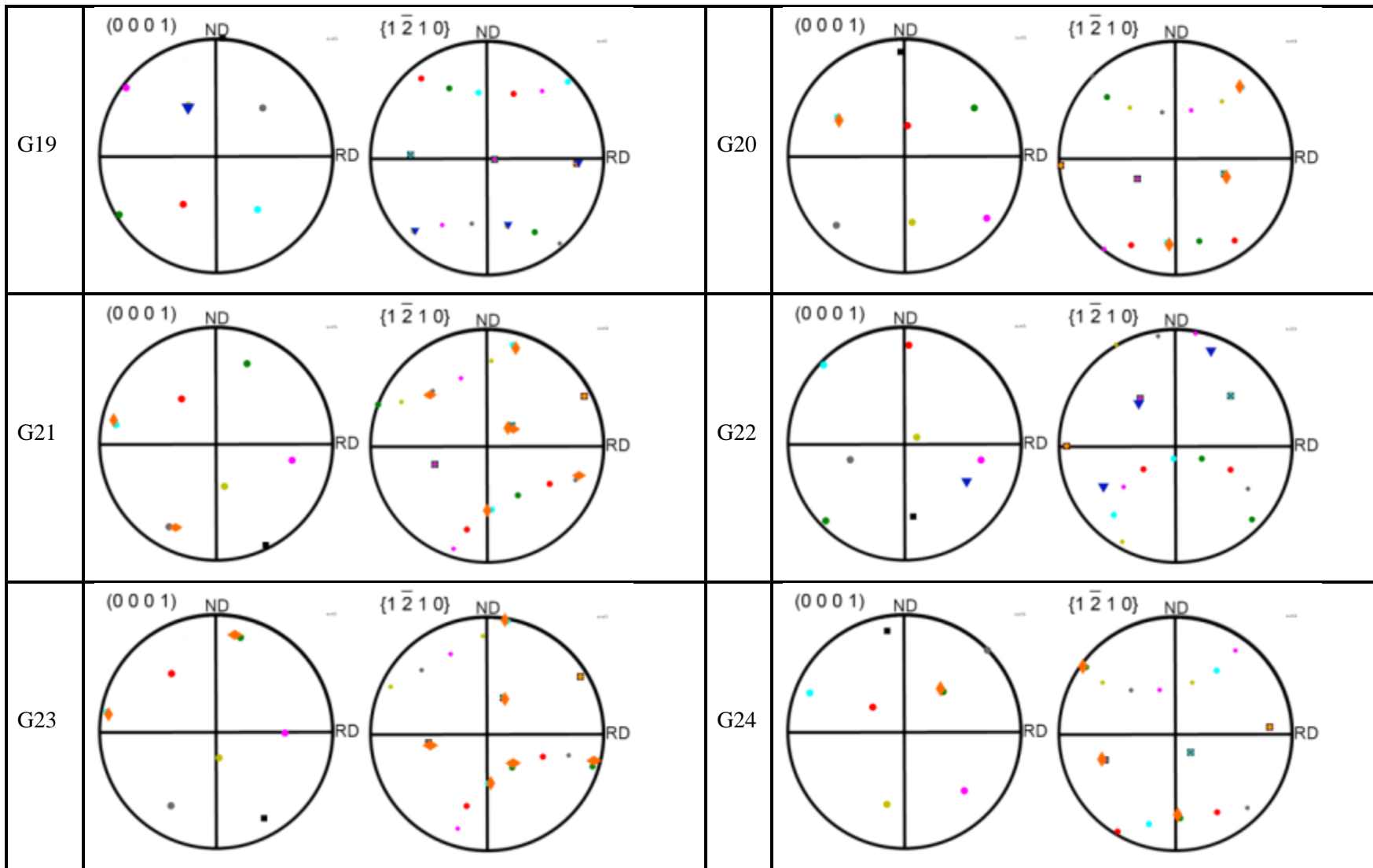
**Table C.4**  $\{0002\}$  and  $\{1\bar{2}10\}$  pole-figures representing the orientation of six possible  $\{10\bar{1}1\}$  twin variants (circles), identified  $\{10\bar{1}1\}$  twin variants (orange rhombic) and  $\{10\bar{1}1\} - \{10\bar{1}2\}$  twin variants (blue and green triangles)

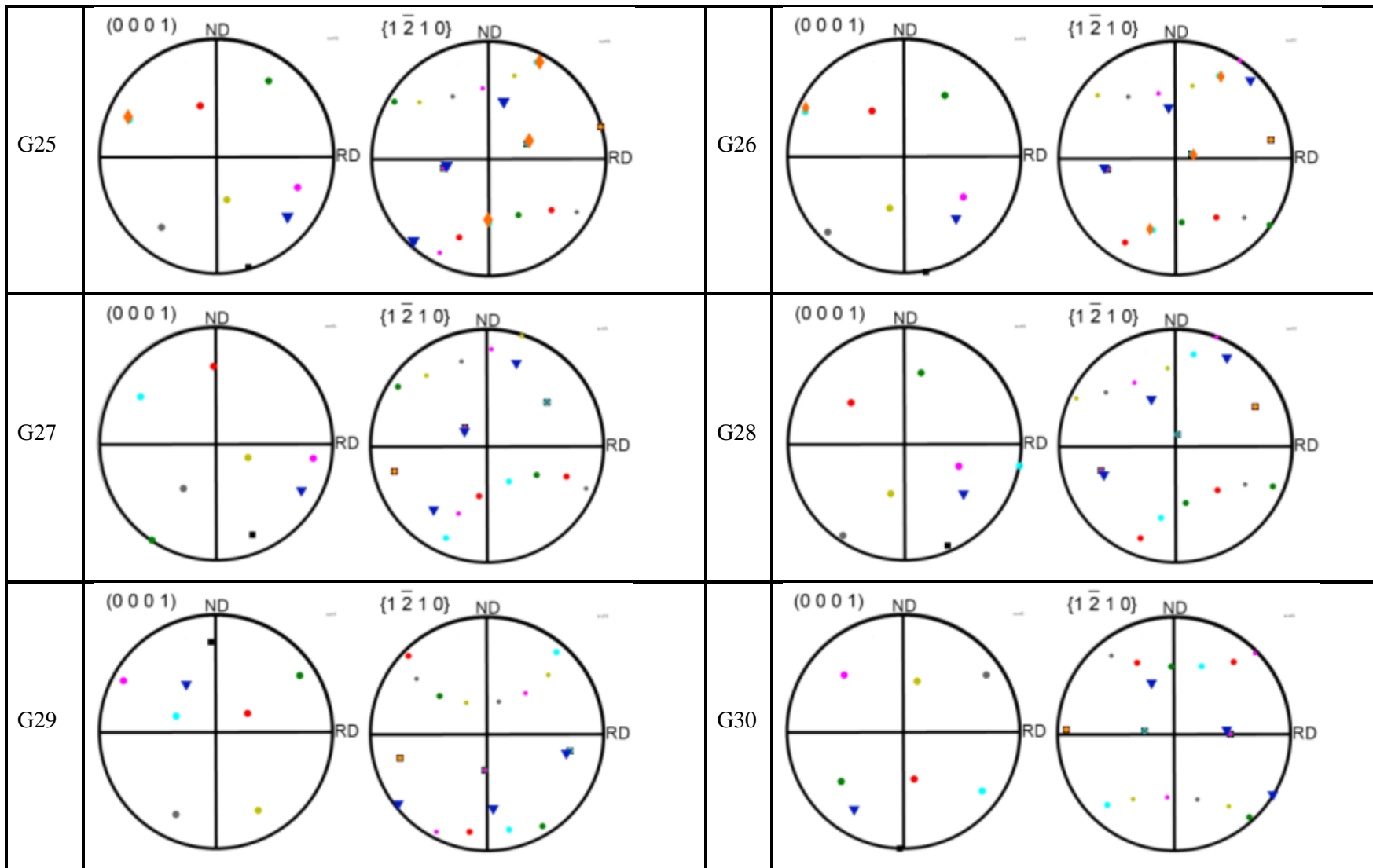


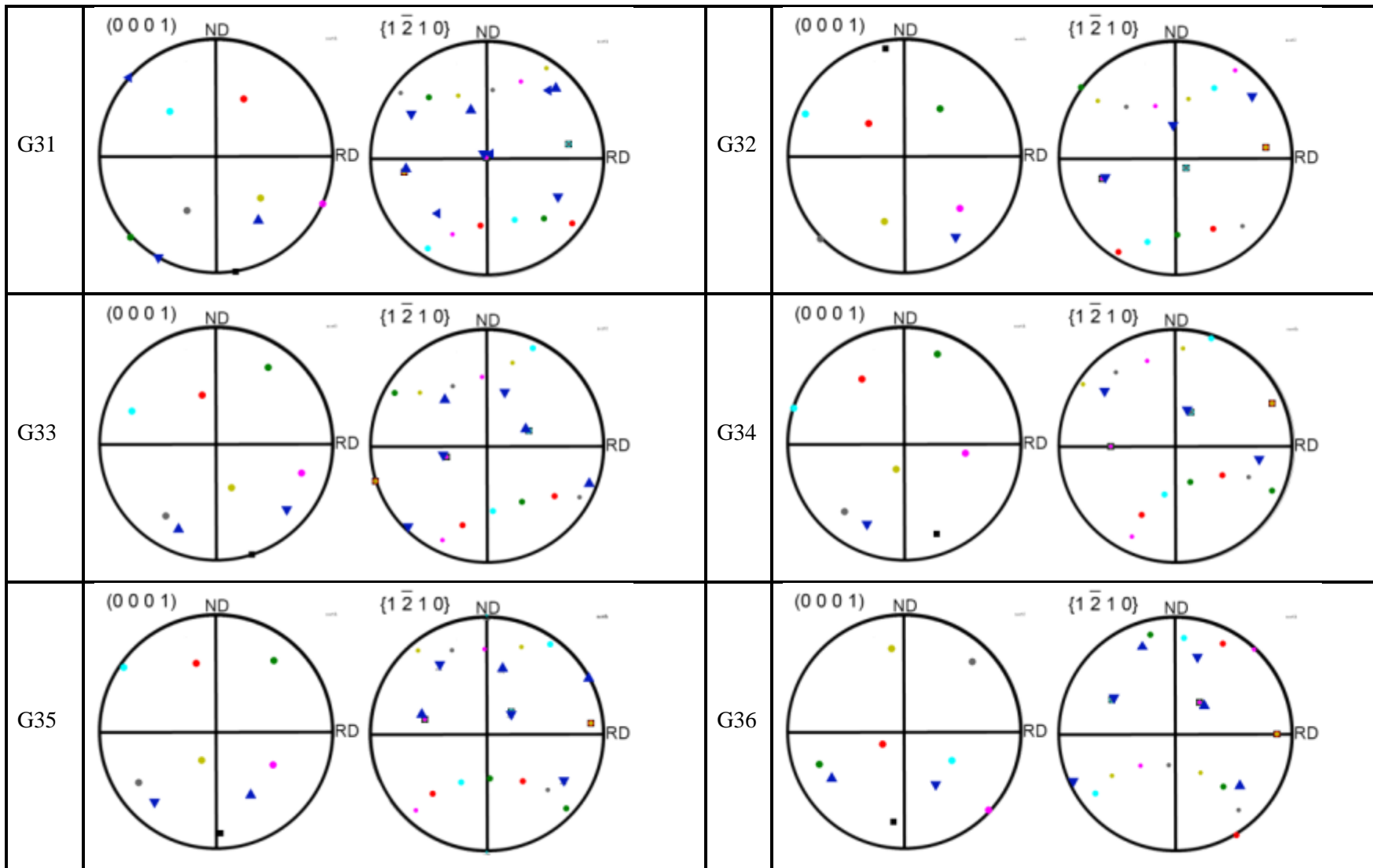


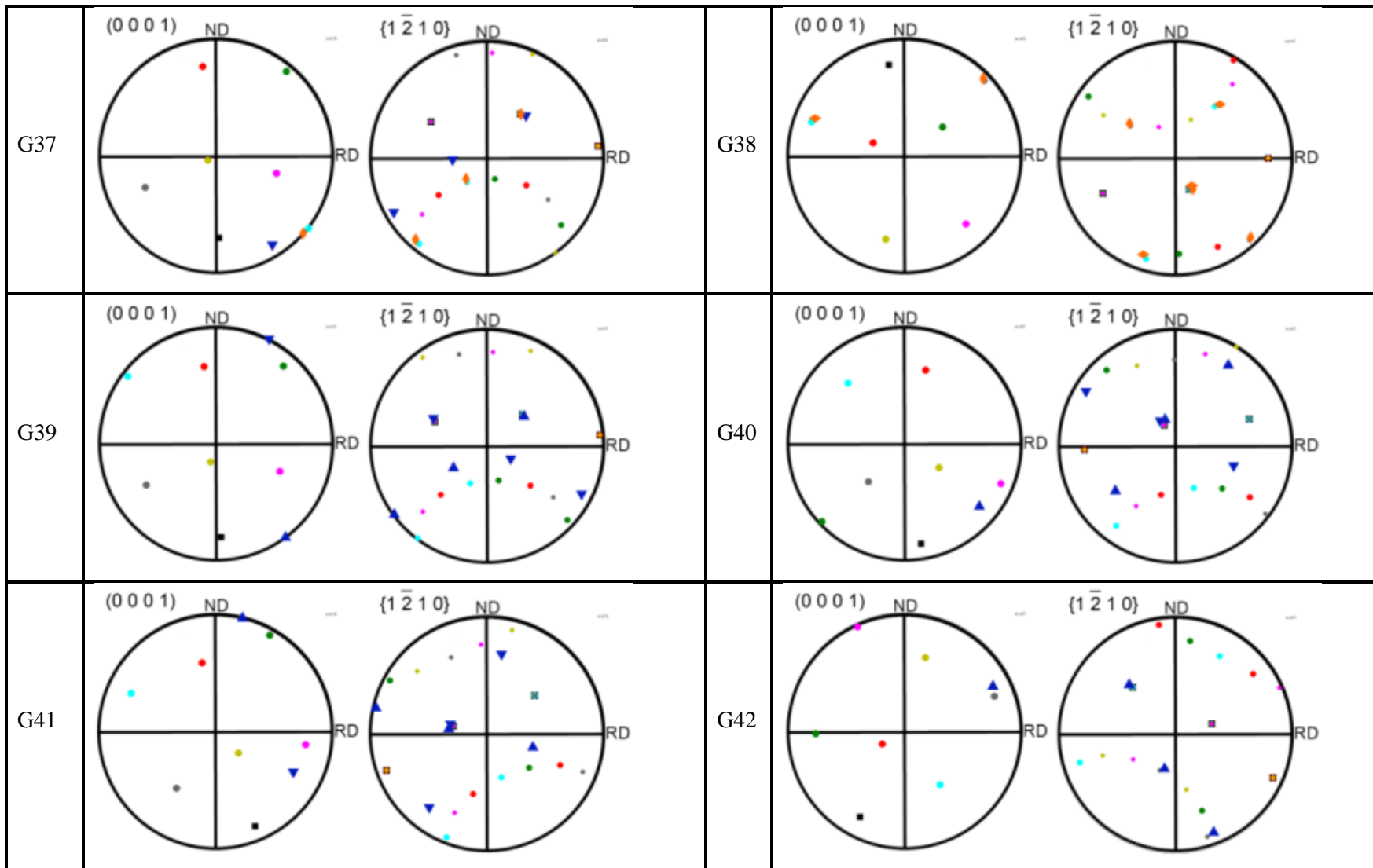


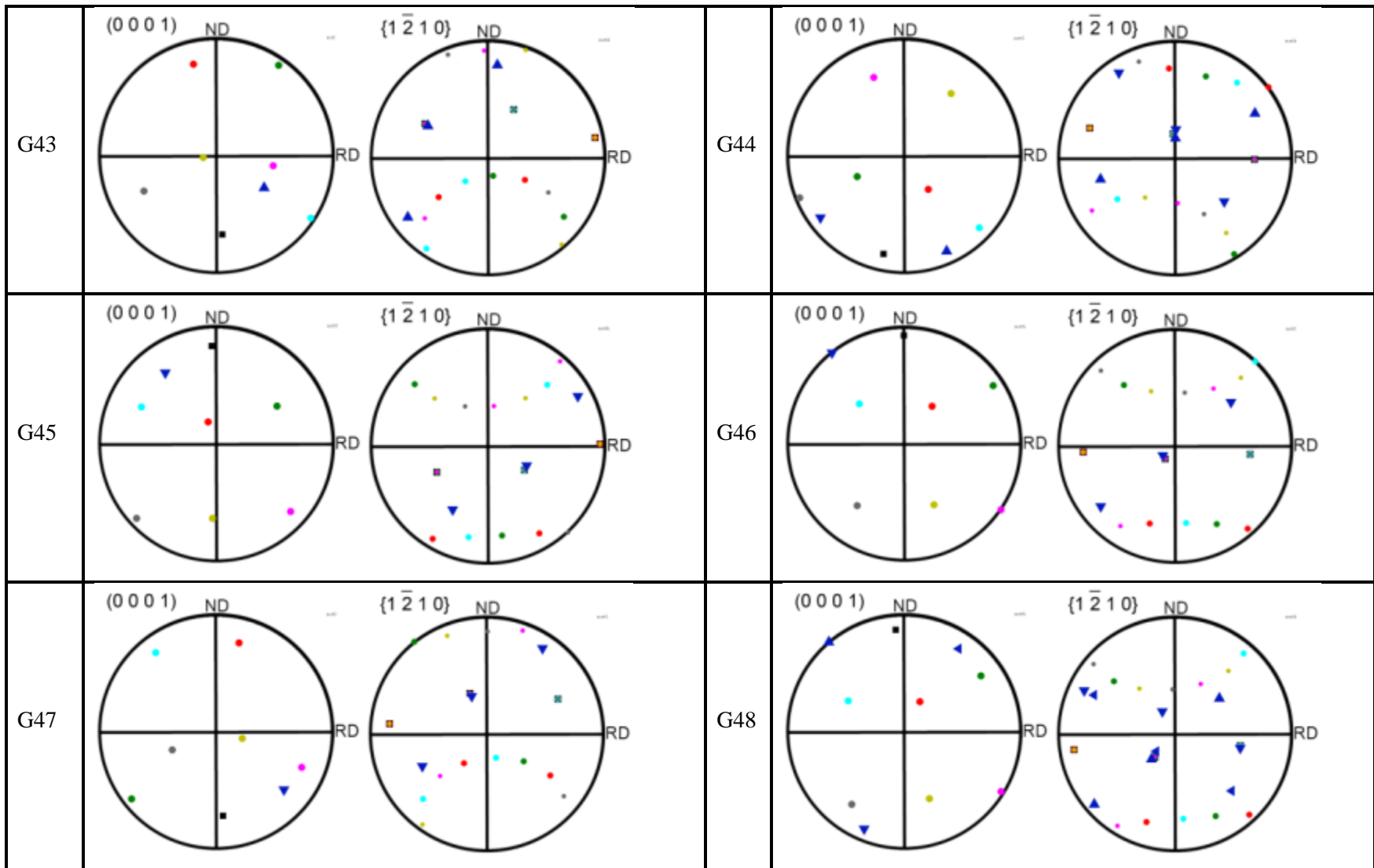


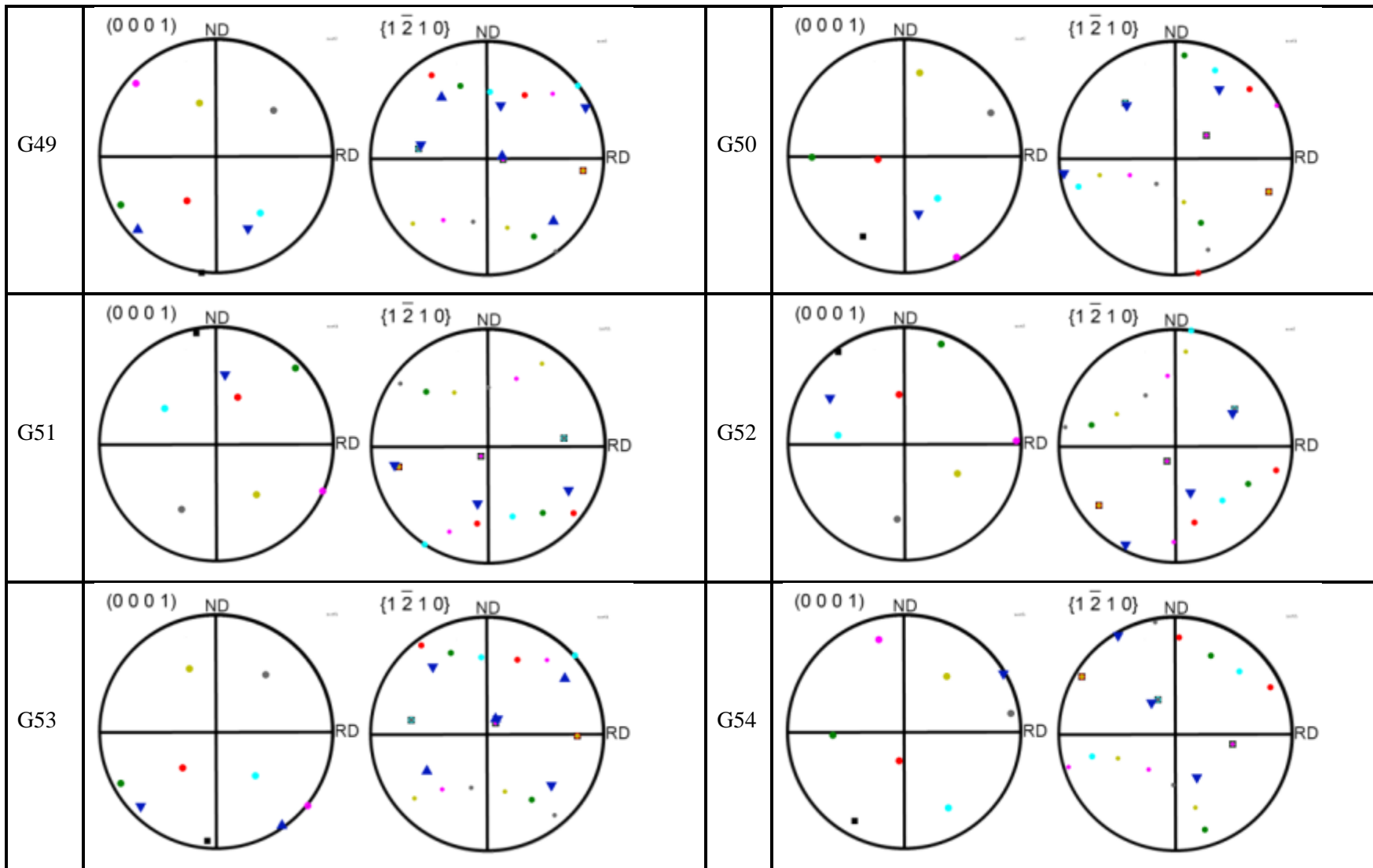


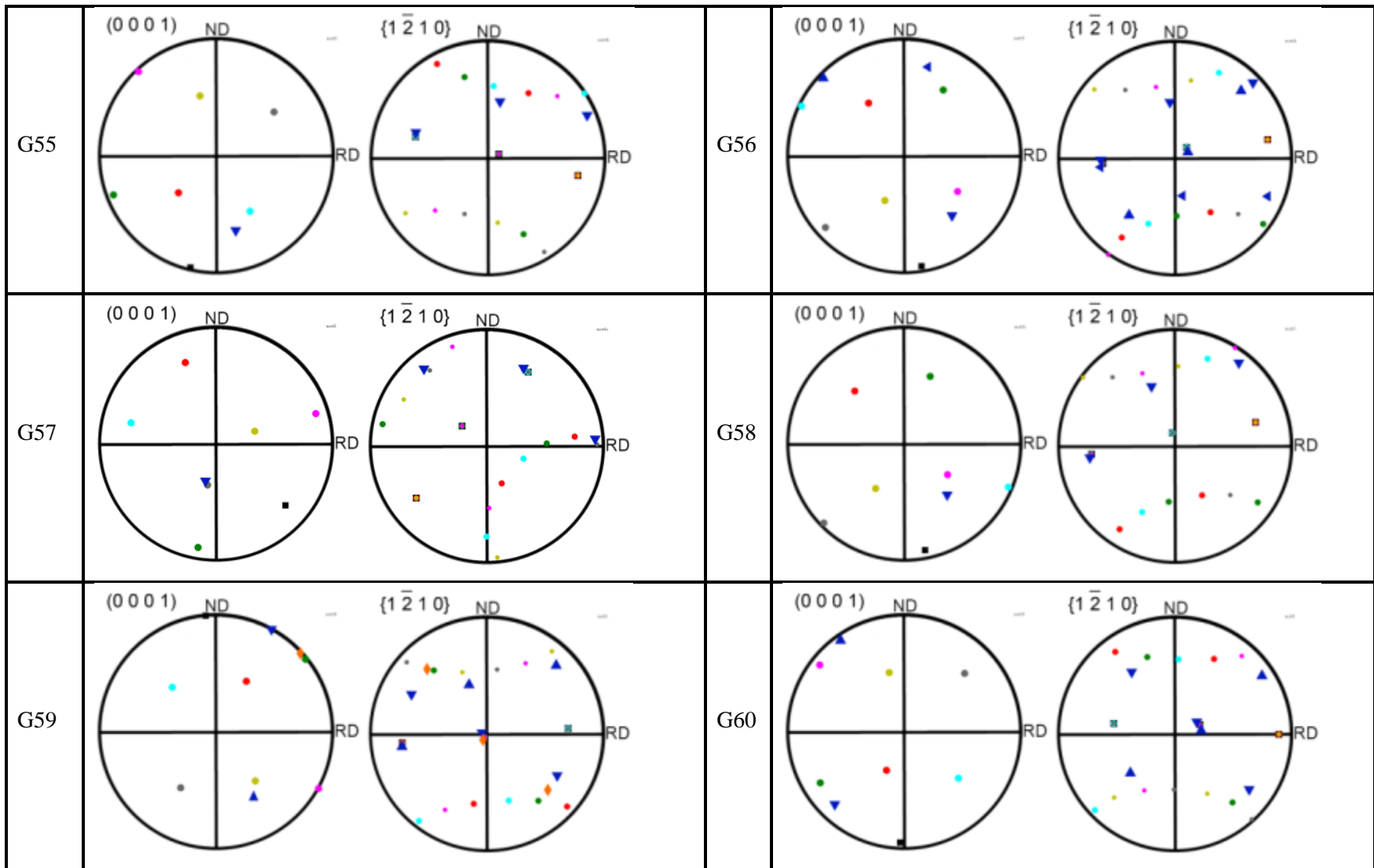


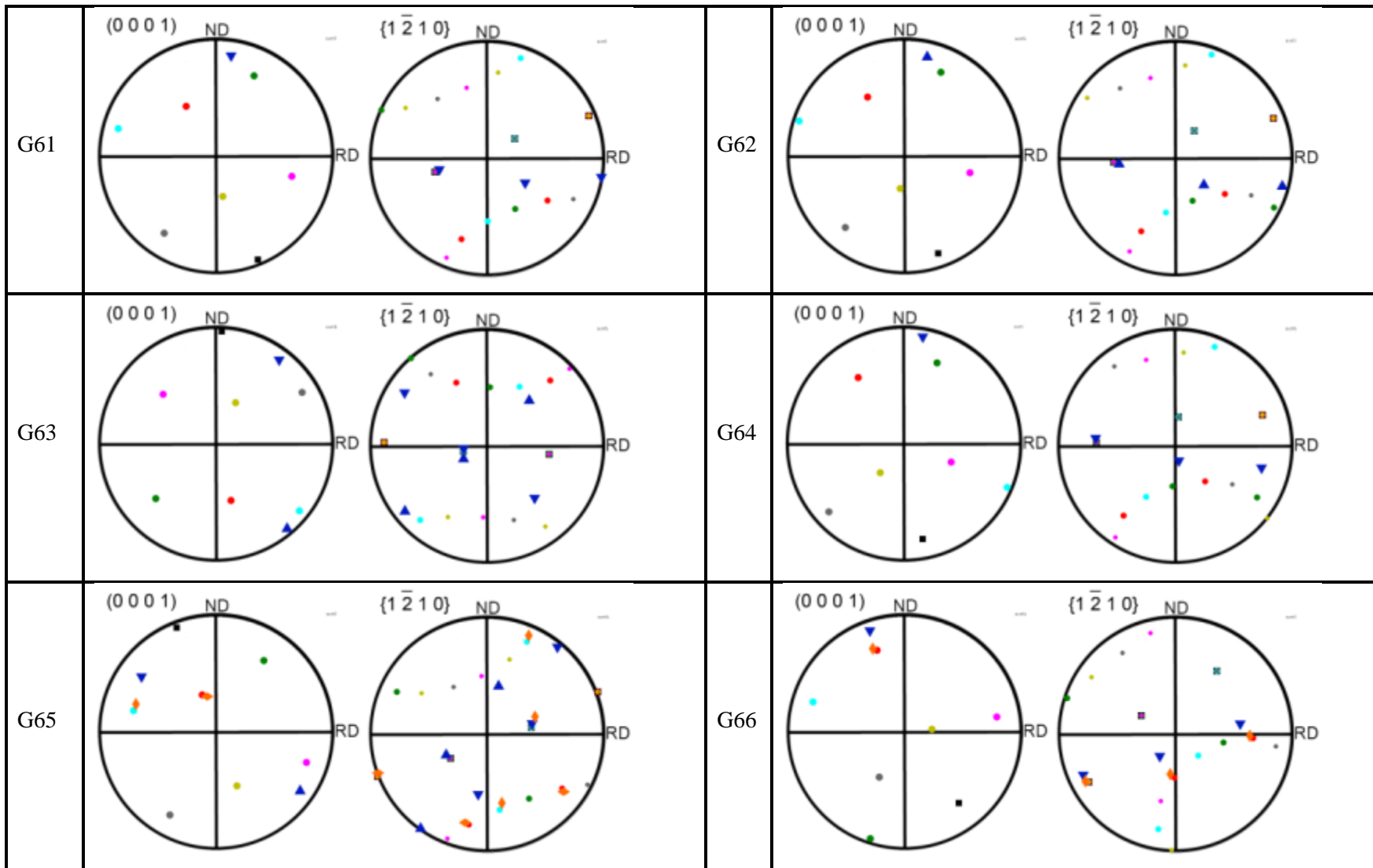




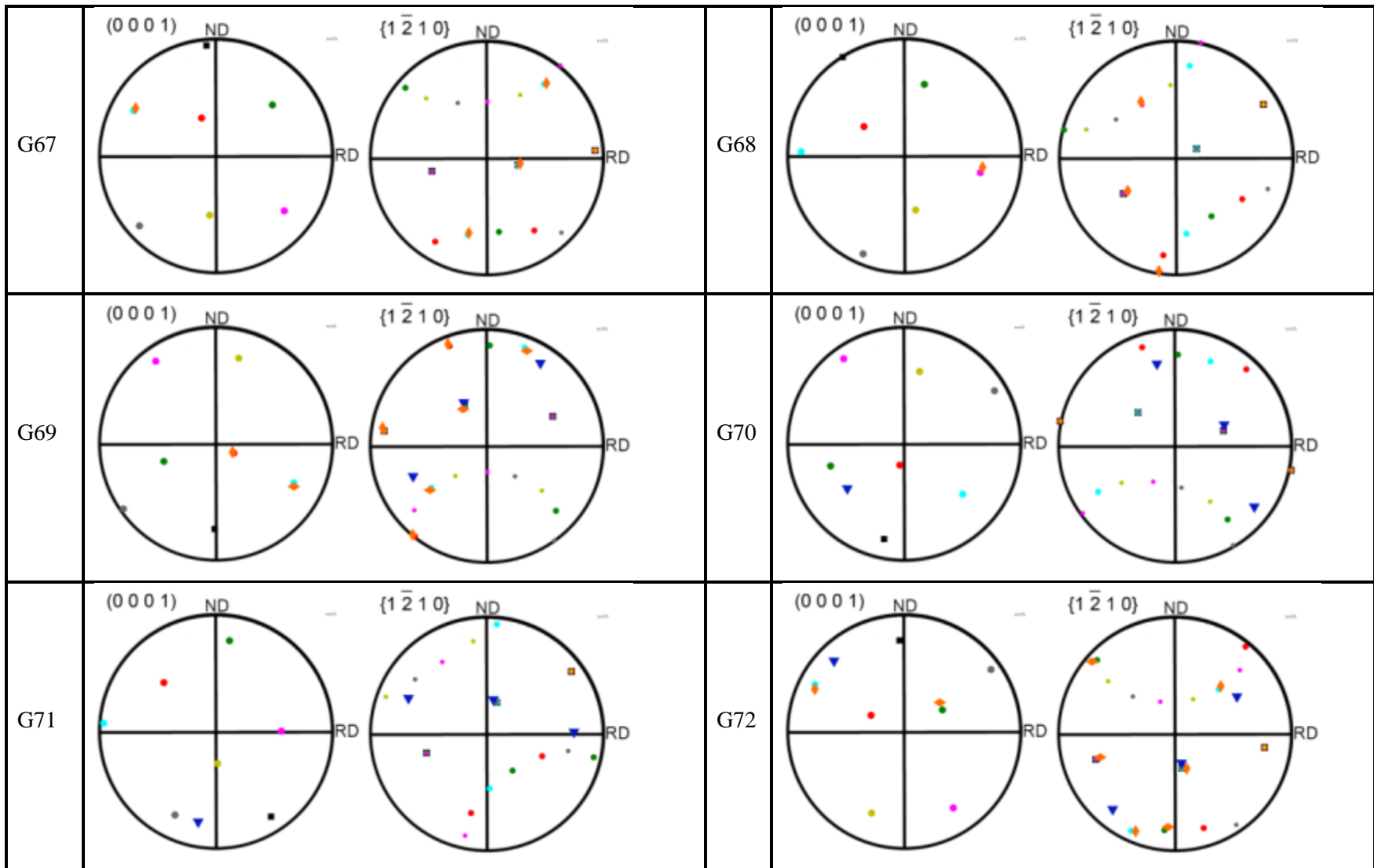












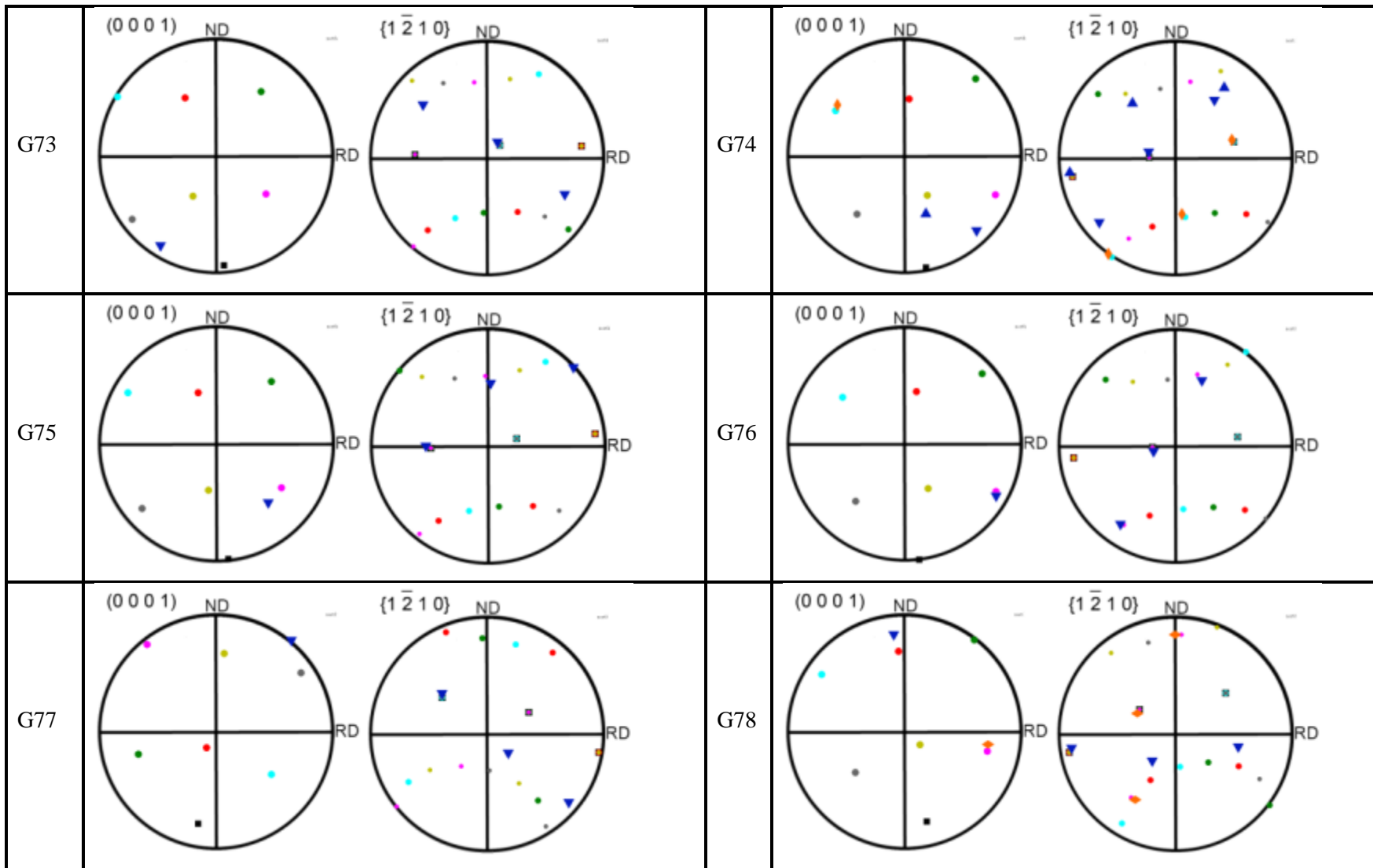


Table C.5 Calculated resolved shear stress on the  $\{1\ 0\ \bar{1}\ 1\}$  twinning variants (1 to 6) for the grains studied in the current work. The values corresponding to the identified twin variants are highlighted by red font

Grain	$\tau_{RSS}$ (MPa)					
	Variant 1	Variant 2	Variant 3	Variant 4	Variant 5	Variant 6
G1	68.6	28.0	57.2	79.0	40.1	58.9
G2	78.2	55.4	85.7	92.8	20.4	50.3
G3	110.8	56.0	35.2	24.6	9.1	74.5
G4	102.4	59.6	70.4	64.5	15.8	64.5
G5	85.4	55.0	74.3	84.7	7.7	48.6
G6	80.2	56.3	83.7	98.6	33.4	42.4
G7	21.2	43.2	95.5	53.3	-28.2	-7.9
G8	98.5	60.6	59.0	95.3	59.0	60.6
G9	32.4	13.0	72.5	60.3	56.4	87.9
G10	89.2	18.5	-27.6	6.0	20.1	57.2
G11	72.5	26.0	60.4	90.7	52.3	68.5
G12	54.4	-9.4	38.1	82.1	43.4	63.3
G13	80.5	50.2	77.0	73.9	15.8	49.3
G14	45.6	-18.1	40.8	64.1	37.5	78.0
G15	40.4	54.7	78.7	52.6	81.9	93.8
G16	41.3	58.9	40.2	57.3	108.5	73.7
G17	65.9	36.7	77.7	66.9	45.2	85.1
G18	16.9	40.7	51.3	66.2	41.5	99.8
G19	101.2	53.0	39.9	60.8	36.6	63.8
G20	85.5	47.4	71.4	58.7	22.1	69.8
G21	21.1	33.1	96.9	81.0	29.9	33.8
G22	73.4	-12.5	28.3	57.7	37.8	63.0
G23	1.0	21.6	93.3	74.0	31.2	29.9
G24	61.3	54.9	89.4	46.5	26.9	76.1
G25	85.8	35.7	87.3	53.6	39.6	59.0
G26	54.9	46.1	90.9	64.3	42.9	78.3
G27	98.5	7.6	59.6	39.8	51.2	44.6
G28	22.0	51.5	103.6	63.7	34.1	44.4
G29	86.6	55.7	56.3	70.4	12.9	29.7
G30	49.8	36.6	60.6	78.3	41.3	93.9
G31	81.4	47.8	53.6	91.6	54.1	49.7

G32	57.5	54.8	91.5	51.9	36.1	78.4
G33	51.6	35.8	88.8	87.3	38.0	52.3
G34	19.5	24.0	92.3	73.7	42.3	56.3
G35	60.2	20.7	64.9	64.5	50.3	90.3
G36	35.5	46.0	48.9	92.9	-1.8	58.5
G37	51.4	-5.9	46.3	65.4	42.2	80.5
G38	59.6	54.6	86.6	34.8	15.5	72.3
G39	60.9	10.1	55.7	69.8	47.4	84.2
G40	77.8	28.2	43.0	88.8	56.3	60.0
G41	33.2	13.0	74.7	95.2	44.9	44.6
G42	69.5	19.6	-2.0	-31.4	-10.4	68.8
G43	39.3	-7.7	54.5	64.1	41.8	79.2
G44	60.5	34.1	33.6	3.2	43.7	100.4
G45	75.7	47.3	74.1	46.3	16.8	78.3
G46	96.9	55.2	53.2	67.3	29.6	57.2
G47	77.2	9.6	20.6	75.2	48.7	61.6
G48	88.0	51.1	66.3	71.8	22.9	54.2
G49	102.1	48.2	34.2	46.2	28.7	70.7
G50	70.9	20.9	4.4	-29.1	-21.9	61.7
G51	79.6	48.9	63.0	91.2	44.2	46.8
G52	-1.4	10.1	61.2	94.2	38.2	-6.2
G53	101.8	56.6	43.5	59.3	24.5	53.9
G54	52.8	7.2	79.1	-35.6	15.8	-17.9
G55	102.6	50.6	23.9	27.2	16.1	64.8
G56	50.7	41.2	82.4	63.9	49.0	87.9
G57	-41.7	-36.3	45.3	65.2	17.7	-7.5
G58	37.7	46.9	92.7	59.5	53.4	77.5
G59	91.0	53.5	52.1	81.9	46.1	53.6
G60	96.2	48.0	53.2	57.8	28.0	71.6
G61	32.1	33.3	94.8	83.5	35.8	45.9
G62	28.5	29.2	93.6	77.3	42.0	57.6
G63	72.4	29.4	56.4	49.3	47.6	97.6
G64	29.4	28.9	87.3	64.3	52.7	76.2
G65	47.5	39.5	89.7	88.2	28.2	37.6

G66	-12.8	-18.6	62.6	80.2	28.8	17.1
G67	74.3	45.4	82.0	59.3	34.1	78.3
G68	11.0	38.6	96.6	72.0	13.4	10.4
G69	67.5	44.4	65.6	17.1	11.1	82.7
G70	11.1	36.5	38.9	82.9	11.4	85.5
G71	-8.9	28.0	94.4	66.2	23.4	14.7
G72	60.4	53.3	72.8	19.0	25.4	86.2
G73	55.8	34.5	76.6	59.1	52.8	91.6
G74	89.6	35.7	68.5	72.7	46.1	62.0
G75	67.3	37.7	77.8	67.2	44.1	84.3
G76	83.4	41.7	63.2	83.1	43.3	65.0
G77	85.6	38.5	42.5	15.2	3.8	78.3
G78	51.7	6.5	58.8	88.1	47.5	63.4

## Bibliography

- [1] M. Gupta and N. M. L. Sharon, *Magnesium, Magnesium Alloys, and Magnesium Composites*. Hoboken, NJ: John Wiley & Sons, 2010.
- [2] H. Shuldiner, “Lower cost key to magnesium’s lightweighting users,” *WardsAuto*, Nov-2013.
- [3] J. M. Amend, “GM claims to crack mystery for making magnesium sheet,” *WardsAuto*, Oct-2012.
- [4] Y. J. Chao, “failure mode of spot welds: interfacial versus pullout,” *Sci. Technol. Weld. Join.*, vol. 8, pp. 133–137, 2003.
- [5] M. K. Kulekci, “Magnesium and its alloys applications in automotive industry,” *Int. J. Adv. Manuf. Technol.*, vol. 39, pp. 851–865, 2008.
- [6] H. Friedrich and S. Schumann, “Research for a new age of magnesium in the automotive industry,” *J. Mater. Process. Technol.*, vol. 117, pp. 276–281, 2001.
- [7] D. Radaj, *Design and analysis of fatigue resistant welded structures*. Abington, Cambridge: Woodhead Publishing Ltd, 1990.
- [8] M. Pouranvari and S. P. H. Marashi, “Failure mode transition in AHSS resistance spot welds. Part I. Controlling factors,” *Mater. Sci. Eng. A*, vol. 528, pp. 8337–8343, Nov. 2011.
- [9] P.-C. Lin, S.-H. Lin, and J. Pan, “Modeling of failure near spot welds in lap-shear specimens based on a plane stress rigid inclusion analysis,” *Eng. Fract. Mech.*, vol. 73, no. 15, pp. 2229–2249, Oct. 2006.
- [10] H. Zhang and B. J. Senkara, *Resistance welding: fundamentals and applications*. Boca Raton, FL: Taylor & Frances, 2006.
- [11] J. Rösler, H. Harders, and M. Bäker, *Mechanical behaviour of engineering materials: metals, ceramics, polymers, and composites*. New York: Springer Berlin Heidelberg, 2007, pp. 120–128.
- [12] J. G. Kaufman, *Fracture Resistance of Aluminum Alloys*. Materials Park, OH: ASM International, 2001.
- [13] I. a. Yakubtsov, B. J. Diak, C. a. Sager, B. Bhattacharya, W. D. MacDonald, and M. Niewczas, “Effects of heat treatment on microstructure and tensile deformation of Mg AZ80 alloy at room temperature,” *Mater. Sci. Eng. A*, vol. 496, no. 1–2, pp. 247–255, Nov. 2008.

- [14] T. Zhu, Z. W. Chen, and W. Gao, "Effect of cooling conditions during casting on fraction of  $\beta$ -Mg<sub>17</sub>Al<sub>12</sub> in Mg–9Al–1Zn cast alloy," *J. Alloys Compd.*, vol. 501, no. 2, pp. 291–296, 2010.
- [15] S. Kleiner, O. Beffort, A. Wahlen, and P. Uggowitzer, "Microstructure and mechanical properties of squeeze cast and semi-solid cast Mg–Al alloys," *J. Light Met.*, vol. 2, no. 4, pp. 277–280, Nov. 2002.
- [16] S. Barbagallo, H. I. Laukli, O. Lohne, and E. Cerri, "Divorced eutectic in a HPDC magnesium–aluminum alloy," *J. Alloys Compd.*, vol. 378, no. 1–2, pp. 226–232, 2004.
- [17] T. Mukai, M. Yamanoi, H. Watanabe, and K. Higashi, "Ductility enhancement in AZ31 magnesium alloy by controlling its grain structure," *Scr. Mater.*, vol. 45, no. 1, pp. 89–94, 2001.
- [18] A. Yamashita, Z. Horita, and T. G. Langdon, "Improving the mechanical properties of magnesium and a magnesium alloy through severe plastic deformation," *Mater. Sci. Eng. A*, vol. 300, no. 1–2, pp. 142–147, Feb. 2001.
- [19] M. R. Barnett, "Twinning and the ductility of magnesium alloys," *Mater. Sci. Eng. A*, vol. 464, no. 1–2, pp. 8–16, Aug. 2007.
- [20] X. Lou, M. Li, R. Boger, S. Agnew, and R. Wagoner, "Hardening evolution of AZ31B Mg sheet," *Int. J. Plast.*, vol. 23, no. 1, pp. 44–86, Jan. 2007.
- [21] G. I. Taylor, "Plastic Strain in Metals," *J. Inst. Met.*, vol. 62, pp. 307–324, 1938.
- [22] R. V. Mises, "Mechanik der plastischen Formänderung von Kristallen," *J. Appl. Math. Mech.*, vol. 8, no. 3, pp. 161–185, 1928.
- [23] M. H. Yoo, J. R. Morris, K. M. Ho, and S. R. Agnew, "Nonbasal Deformation Modes of HCP Metals and Alloys : Role of Dislocation Source and Mobility," *Metall. Mater. Trans. A*, vol. 33, pp. 813–822, 2002.
- [24] G. S. Kim, "Small Volume Investigation of Slip and Twinning in Magnesium Single Crystals," 2011.
- [25] G. W. Groves and A. Kelly, "Independent slip systems in crystals," *Philos. Mag.*, vol. 8, no. 89, pp. 877–887, May 1963.
- [26] P. Bakarian and C. Mathewson, "Strength of Metals and Alloys," *Trans. Met. Soc. AIME*, vol. 152, p. 226, 1943.
- [27] T. Obara, H. Yoshinga, and S. Morozumi, "{11-22}<-1-123> Slip system in Magnesium," *Acta Metall.*, vol. 21, 1973.

- [28] A. Staroselsky and L. Anand, "A constitutive model for hcp materials deforming by slip and twinning," *Int. J. Plast.*, vol. 19, no. 10, pp. 1843–1864, Oct. 2003.
- [29] U. F. Kocks and D. G. Westlake, "The importance of twinning for ductility of polycrystals," *Trans. Met. Soc. AIME*, vol. 239, pp. 1107–1109, 1967.
- [30] S. Mendelson, "Dislocation Dissociations in hcp Metals," *J. Appl. Phys.*, vol. 41, no. 5, p. 1893, 1970.
- [31] P. Cizek and M. R. Barnett, "Characteristics of the contraction twins formed close to the fracture surface in Mg–3Al–1Zn alloy deformed in tension," *Scr. Mater.*, vol. 59, no. 9, pp. 959–962, Nov. 2008.
- [32] M. R. Barnett, Z. Keshavarz, A. G. Beer, and X. Ma, "Non-Schmid behaviour during secondary twinning in a polycrystalline magnesium alloy," *Acta Mater.*, vol. 56, no. 1, pp. 5–15, Jan. 2008.
- [33] J. Koike, N. Fujiyama, D. Ando, and Y. Sutou, "Roles of deformation twinning and dislocation slip in the fatigue failure mechanism of AZ31 Mg alloys," *Scr. Mater.*, vol. 63, no. 7, pp. 747–750, Oct. 2010.
- [34] D. Ando, J. Koike, and Y. Sutou, "Relationship between deformation twinning and surface step formation in AZ31 magnesium alloys," *Acta Mater.*, vol. 58, no. 13, pp. 4316–4324, Aug. 2010.
- [35] E. Schmid, "0 Beitrage zur Physik und Metallographie des Magnesiums," *Z. Elektrochem*, vol. 37, p. 447, 1931.
- [36] P. W. Bakarian and C. H. Mathewson, "Slip and twinning of magnesium single crystals at elevated temperatures," *Trans. AIME*, vol. 152, p. 226, 1943.
- [37] R. E. Reed-Hill and W. D. Robertson, "Additional modes of deformation twinning in magnesium," *Acta Metall.*, vol. 5, no. December, pp. 717–727, 1957.
- [38] E. C. Burke and W. R. Hibbard, "Plastic deformation of magnesium single crystals," *Trans. Met. Soc. AIME*, vol. 194, pp. 295–303, 1952.
- [39] S. S. Hsu and B. D. Cullity, "On the torsional deformation and recovery of single crystals," *Trans. AIME*, vol. 200, p. 305, 1954.
- [40] S. R. Agnew, "Plastic anisotropy of magnesium alloy AZ31B sheet," in *TMS Annual Meeting, Magnesium Technology*, 2002, pp. 169–174.



- [41] D. W. Brown, S. R. Agnew, M. a. M. Bourke, T. M. Holden, S. C. Vogel, and C. N. Tomé, “Internal strain and texture evolution during deformation twinning in magnesium,” *Mater. Sci. Eng. A*, vol. 399, no. 1–2, pp. 1–12, Jun. 2005.
- [42] M. A. Gharghouri, “Study of Mechanical Properties of Mg-8.5wt%Al by in-situ Neutron Diffraction,” Mc Master University, Ont, Canada, 1997.
- [43] G. Dieter and D. Bacon, *Mechanical Metallurgy*. New York, NY: McGraw-Hill, 1988.
- [44] a. Pardo, M. C. Merino, a. E. Coy, R. Arrabal, F. Viejo, and E. Matykina, “Corrosion behaviour of magnesium/aluminium alloys in 3.5 wt.% NaCl,” *Corros. Sci.*, vol. 50, pp. 823–834, 2008.
- [45] P. Villars and L. D. Calvert, *Pearson’s handbook of crystallographic data for intermetallic phases*. Metal Park, OH: ASM, 1991.
- [46] S. Celotto, “TEM study of continuous precipitation in Mg–9 wt%Al–1 wt%Zn alloy,” *Acta Mater.*, vol. 48, no. 8, pp. 1775–1787, May 2000.
- [47] J. T. Wang, D. L. Yin, J. Q. Liu, J. Tao, Y. L. Su, and X. Zhao, “Effect of grain size on mechanical property of Mg–3Al–1Zn alloy,” *Scr. Mater.*, vol. 59, no. 1, pp. 63–66, Jul. 2008.
- [48] I. J. Polmear, *Light alloys, from traditional alloys to nanocrystals*. London: Butterworth-Heinemann, 2006.
- [49] A. F. Crawley and K. S. Milliken, “Precipitate morphology and orientation relationships in an aged Mg-9% Al-1% Zn-0.3% Mn alloy,” *Acta Metall.*, vol. 22, pp. 557–562, 1974.
- [50] A. A. Nayeb-Hashemi and J. B. Clark, “Mg-Al Phase diagram,” *Bull. Alloy Phase Diagrams*, vol. 9, pp. 618–623, 1988.
- [51] H. Liu, J. Liu, L. Ouyang, and C. Luo, “On the multiple orientation relationship of the Mg/ $\gamma$ -Mg 17 Al 12 precipitation system,” *J. Appl. Crystallogr.*, vol. 45, no. 2, pp. 224–233, Feb. 2012.
- [52] C.-T. Chi and C.-G. Chao, “Characterization on electron beam welds and parameters for AZ31B-F extrusive plates,” *J. Mater. Process. Technol.*, vol. 182, no. 1–3, pp. 369–373, Feb. 2007.
- [53] C.-T. Chi, C.-G. Chao, T.-F. Liu, and C.-H. Lee, “Aluminum element effect for electron beam welding of similar and dissimilar magnesium–aluminum–zinc alloys,” *Scr. Mater.*, vol. 56, no. 9, pp. 733–736, May 2007.

- [54] C.-T. Chi, C.-G. Chao, T.-F. Liu, and C.-C. Wang, "A study of weldability and fracture modes in electron beam weldments of AZ series magnesium alloys," *Mater. Sci. Eng. A*, vol. 435–436, pp. 672–680, Nov. 2006.
- [55] Y. C. Guan and W. Zhou, "Calorimetric analysis of AZ91D magnesium alloy," *Mater. Lett.*, vol. 62, no. 30, pp. 4494–4496, Dec. 2008.
- [56] J. Chen, T. Liu, L. Lu, Y. Zhang, and W. Zeng, "Microstructure and mechanical property of rolled-weld magnesium alloy AZ31," *Mater. Des.*, vol. 36, pp. 577–583, Apr. 2012.
- [57] Q. Wang, W. Chen, W. Ding, Y. Zhu, and M. Mabuchi, "Effect of Sb on the Microstructure and Mechanical Properties of AZ91 Magnesium Alloy," vol. 32, no. March, pp. 787–794, 2001.
- [58] B. Kim, J. Do, S. Lee, and I. Park, "In situ fracture observation and fracture toughness analysis of squeeze cast AZ51-xSn magnesium alloys," *Mater. Sci. Eng. A*, vol. 527, no. 24–25, pp. 6745–6757, Sep. 2010.
- [59] G. L. Tuer and A. R. Kaufmann, *The Metal Beryllium*. Cleveland, OH: ASM, 1955, pp. 372–424.
- [60] M. H. Yoo, "Slip, Twinning, and Fracture in Hexagonal Close-Packed Metals," *Metall. Trans. A*, vol. 12, pp. 409–418, 1981.
- [61] H. Somekawa and T. Mukai, "Effect of texture on fracture toughness in extruded AZ31 magnesium alloy," *Scr. Mater.*, vol. 53, no. 5, pp. 541–545, Sep. 2005.
- [62] H. Somekawa, T. Inoue, and T. Mukai, "Deformation mechanism near crack-tip by finite element analysis and microstructure observation in magnesium alloys," *Mater. Sci. Eng. A*, vol. 527, no. 7–8, pp. 1761–1768, Mar. 2010.
- [63] H. Somekawa, A. Singh, and T. Mukai, "High fracture toughness of extruded Mg–Zn–Y alloy by the synergistic effect of grain refinement and dispersion of quasicrystalline phase," *Scr. Mater.*, vol. 56, no. 12, pp. 1091–1094, Jun. 2007.
- [64] H. Somekawa and T. Mukai, "Effect of grain refinement on fracture toughness in extruded pure magnesium," *Scr. Mater.*, vol. 53, no. 9, pp. 1059–1064, Nov. 2005.
- [65] J. Koike, T. Kobayashi, T. Mukai, H. Watanabe, M. Suzuki, K. Maruyama, and K. Higashi, "The activity of non-basal slip systems and dynamic recovery at room temperature in fine-grained AZ31B magnesium alloys," *Acta Mater.*, vol. 51, no. 7, pp. 2055–2065, Apr. 2003.
- [66] J. Koike, R. Ohyama, T. Kobayashi, M. Suzuki, and K. Maruyama, "Grain-Boundary Sliding in AZ31 Magnesium Alloys at Room Temperature to 523 K," vol. 44, no. 4, pp. 445–451, 2003.

- [67] B. J. Senkara and H. Zhang, "Cracking in Spot Welding Aluminum Alloy," no. July, pp. 194–201, 2000.
- [68] H. Search, C. Journals, A. Contact, M. Iopscience, and I. P. Address, "Constriction resistance and the real area of contact," *J. Appl. Phys.*, vol. 17, pp. 1621–1623, 1966.
- [69] H. Luo, C. Hao, and J. Zhang, "Characteristics of Resistance Welding Magnesium Alloys AZ31 and AZ91," *Weld. J.*, vol. 90, pp. 249–257, 2011.
- [70] N. K. Babu, S. Brauser, M. Rethmeier, and C. E. Cross, "Characterization of microstructure and deformation behaviour of resistance spot welded AZ31 magnesium alloy," *Mater. Sci. Eng. A*, vol. 549, pp. 149–156, Jul. 2012.
- [71] L. Liu, S. Q. Zhou, Y. H. Tian, J. C. Feng, J. P. Jung, and Y. N. Zhou, "Effects of surface conditions on resistance spot welding of Mg alloy AZ31," *Sci. Technol. Weld. Join.*, vol. 14, no. 4, pp. 356–361, May 2009.
- [72] E. Feng, D. Cerjanec, and G. A. Grzadzinski, "Energy Consumption in AC and MFDC Resistance Spot Welding," in *Sheet Metal Welding Conference*, 2004, pp. 1–12.
- [73] D. Wang, S. Lin, and J. Pan, "Stress Intensity Factors for Spot Welds and Associated Kinked Cracks in Cup Specimens," *Int. J. Fatigue*, vol. 27, pp. 581–598, 2005.
- [74] T. Satoh, H. Abe, K. Nishikawa, and M. Morita, "On Three-Dimensional Elastic-Plastic Stress Analysis of Spot-Welded Joint under Tensile Shear Load," *Trans. Japan Weld. Soc.*, vol. 22, no. 1, pp. 46–51, 1991.
- [75] L. P. Pook, "Fracture Mechanics Analysis of the Fatigue Behaviour of Spot Welds," *Int. J. Fract.*, vol. 282, no. 2, pp. 173–176, 1975.
- [76] S. B. Behraves, H. Jahed, and S. Lambert, "Characterization of magnesium spot welds under tensile and cyclic loadings," *Mater. Des.*, vol. 32, no. 10, pp. 4890–4900, Dec. 2011.
- [77] S. Zhang, "Approximate Stress Intensity Factors and Notch Stresses for Common Spot-Welded Specimens," *Weld. J.*, pp. 173–179, 1999.
- [78] S. Zhang, "Stress intensities at spot welds," *Int. J. Fract.*, vol. 88, pp. 167–185, 1997.
- [79] D. A. Wang, P. C. Lin, and J. Pan, "Geometric functions of stress intensity factor solutions for spot welds in lap-shear specimens," *Int. J. Solids Struct.*, vol. 42, no. 24–25, pp. 6299–6318, Dec. 2005.
- [80] N. Pan and S. D. Sheppard, "Stress intensity factors in spot welds," vol. 70, pp. 671–684, 2003.

- [81] Y. R. Kan, "Fatigue resistance of spot welds-an analytical study," *Met. Eng. Q.*, vol. 16, pp. 26–36, 1976.
- [82] "Fatigue-life prediction for spotweld using Neuber's rule," in *Design of fatigue and fracture resistant structures*, Abelkis PR: ASTM STP, 1982, pp. 296–309.
- [83] H. Neuber, "Theory of Stress Concentration for Shear-Strained Prismatical Bodies With Arbitrary Nonlinear Stress-Strain Law," *J. Appl. Mech.*, vol. 28, no. 4, pp. 544–550, 1961.
- [84] H. Adib and G. Pluvinaige, "Three-Dimensional Finite Element Analysis of Tensile-Shear Spot-Welded Joints in Tensile and Compressive Loading Conditions," *Strength Mater.*, vol. 36, no. 4, pp. 353–364, 2004.
- [85] X. Deng, W. Chen, and G. Shi, "Three-dimensional finite element analysis of the mechanical behavior of spot welds," *Finite Elem. Anal. Des.*, vol. 35, pp. 17–39, 2000.
- [86] N. Pan, "Spot welds fatigue life prediction with cyclic strain range," *Int. J. Fatigue*, vol. 24, pp. 519–528, 2002.
- [87] L. Xiao, L. Liu, D. L. Chen, S. Esmaili, and Y. Zhou, "Resistance spot weld fatigue behavior and dislocation substructures in two different heats of AZ31 magnesium alloy," *Mater. Sci. Eng. A*, vol. 529, pp. 81–87, Nov. 2011.
- [88] Y. Luo, H. Ye, C. Du, and H. Xu, "Influence of focusing thermal effect upon AZ91D magnesium alloy weld during vacuum electron beam welding," *Vacuum*, vol. 86, no. 9, pp. 1262–1267, Mar. 2012.
- [89] D. X. Sun, D. Q. Sun, and X. Gui, "Hot Cracking of Metal Inert Gas Arc Welded Magnesium Alloy AZ91D," *ISIJ Int.*, vol. 49, pp. 270–274, 2009.
- [90] L. Liu, L. Xiao, J. C. Feng, Y. H. Tian, S. Q. Zhou, and Y. Zhou, "Resistance Spot Welded AZ31 Magnesium Alloys, Part II: Effects of Welding Current on Microstructure and Mechanical Properties," *Metall. Mater. Trans. A*, vol. 41, no. 10, pp. 2642–2650, Jun. 2010.
- [91] L. Xiao, L. Liu, Y. Zhou, and S. Esmaili, "Resistance-Spot-Welded AZ31 Magnesium Alloys: Part I. Dependence of Fusion Zone Microstructures on Second-Phase Particles," *Metall. Mater. Trans. A*, vol. 41, no. 6, pp. 1511–1522, Mar. 2010.
- [92] L. Xiao, L. Liu, S. Esmaili, and Y. Zhou, "Microstructure Refinement After the Addition of Titanium Particles in AZ31 Magnesium Alloy Resistance Spot Welds," *Metall. Mater. Trans. A*, vol. 43, no. 2, pp. 598–609, Sep. 2011.
- [93] S. Chai, D. Zhang, F. Pan, J. Dong, F. Guo, and Y. Dong, "Influence of post-weld hot rolling on the microstructure and mechanical properties of AZ31 magnesium alloy sheet," *Mater. Sci. Eng. A*, vol. 588, pp. 208–213, Dec. 2013.

- [94] L. Commin, M. Dumont, R. Rotinat, F. Pierron, J.-E. Masse, and L. Barrallier, “Texture evolution in Nd:YAG-laser welds of AZ31 magnesium alloy hot rolled sheets and its influence on mechanical properties,” *Mater. Sci. Eng. A*, vol. 528, no. 4–5, pp. 2049–2055, Feb. 2011.
- [95] P. Changizian, a. Zarei-Hanzaki, and H. R. Abedi, “On the recrystallization behavior of homogenized AZ81 magnesium alloy: The effect of mechanical twins and  $\gamma$  precipitates,” *Mater. Sci. Eng. A*, vol. 558, pp. 44–51, Dec. 2012.
- [96] S. M. Fatemi-Varzaneh, a. Zarei-Hanzaki, and H. Beladi, “Dynamic recrystallization in AZ31 magnesium alloy,” *Mater. Sci. Eng. A*, vol. 456, no. 1–2, pp. 52–57, May 2007.
- [97] G. Liang and S. Yuan, “Study on the temperature measurement of AZ31B magnesium alloy in gas tungsten arc welding,” *Mater. Lett.*, vol. 62, no. 15, pp. 2282–2284, May 2008.
- [98] D. A. Porter and K. E. Easterling, *Phase transformation of metals and alloys*. London: Chapman and Hall, 1982.
- [99] R. E. Reed-Hill, *Physical Metallurgy Principals*. Princeton, NJ: van Nostrand, 1964, p. 378.
- [100] Y. Quan, Z. Chen, X. Gong, and Z. Yu, “CO<sub>2</sub> laser beam welding of dissimilar magnesium-based alloys,” vol. 496, pp. 45–51, 2008.
- [101] J. Yang, B. L. Xiao, D. Wang, and Z. Y. Ma, “Effects of heat input on tensile properties and fracture behavior of friction stir welded Mg–3Al–1Zn alloy,” *Mater. Sci. Eng. A*, vol. 527, no. 3, pp. 708–714, Jan. 2010.
- [102] S. Kou, V. Firouzdor, and I. W. Haygood, *Hot Cracking in Welds of Aluminum and Magnesium Alloys*. Berlin, Heidelberg: Springer Berlin Heidelberg, 2011.
- [103] *AWS D17.2 Specification for Resistance Welding for Aerospace Applications*. USA.
- [104] C. W. Bale, E. Bélisle, P. Chartrand, S. a. Deckerov, G. Eriksson, K. Hack, I.-H. Jung, Y.-B. Kang, J. Melançon, a. D. Pelton, C. Robelin, and S. Petersen, “FactSage thermochemical software and databases — recent developments,” *Calphad*, vol. 33, no. 2, pp. 295–311, Jun. 2009.
- [105] Y. Chen, J. Hjelen, and H. J. Roven, “Application of EBSD technique to ultrafine grained and nanostructured materials processed by severe plastic deformation: Sample preparation, parameters optimization and analysis,” *Trans. Nonferrous Met. Soc. China*, vol. 22, no. 8, pp. 1801–1809, Aug. 2012.
- [106] S. Niknejad, L. Liu, M.-Y. Lee, S. Esmaeili, and N. Y. Zhou, “Resistance spot welding of AZ series magnesium alloys: Effects of aluminum content on microstructure and mechanical properties,” *Mater. Sci. Eng. A*, vol. 618, pp. 323–334, Nov. 2014.

- [107] S. T. Niknejad, L. Liu, T. Nguyen, M.-Y. Lee, S. Esmaili, and N. Y. Zhou, "Effects of Heat Treatment on Grain-Boundary  $\beta$ -Mg<sub>17</sub>Al<sub>12</sub> and Fracture Properties of Resistance Spot-Welded AZ80 Mg Alloy," *Metall. Mater. Trans. A*, vol. 44, no. 8, pp. 3747–3756, Apr. 2013.
- [108] E. Scheil, "No Title," *Z. Met.*, pp. 34–70, 1942.
- [109] R. Ohno and Z. Schmid-Fetzer, "Thermodynamic Assessment of Mg-Al-Mn Phase Equilibria, Focusing on Mg-Rich Alloys," *Metallkd*, vol. 96, pp. 857–869, 2005.
- [110] J. Feng and Y. Wang, "Nugget growth characteristic for AZ31B magnesium alloy during resistance spot welding," *Sci. Technol. Weld. Join.*, vol. 11, pp. 154–162, 2006.
- [111] Y. Tamura, Y. Kida, H. Tamehiro, N. Kono, H. Soda, and a. McLean, "The effect of manganese on the precipitation of Mg<sub>17</sub>Al<sub>12</sub> phase in magnesium alloy AZ 91," *J. Mater. Sci.*, vol. 43, no. 4, pp. 1249–1258, Dec. 2007.
- [112] W. Kurz and D. J. Fisher, "Fundamentals of Solidification," *Cryst. Res. Technol.*, vol. 21, pp. 1176–1176, 1986.
- [113] W. C. Winegard and B. Chalmers, "Supercooling and dendritic freezing of alloys," *Trans. Am. Soc. Met.*, vol. 46, pp. 1214–1227, 1954.
- [114] C. Huang and S. Kou, "No Title," *Weld. J.*, vol. 5, pp. 113–120, 2000.
- [115] J. C. Lippold, W. A. Baeslack, and I. Varol, "Heat-affected zone liquation cracking in austenitic and duplex stainless steels," *Weld. Res. Suppl.*, pp. 1–14, 1992.
- [116] S. Kou, *Welding Metallurgy*. Hoboken, NJ: John Wiley & Sons, 2003.
- [117] S. Guldberg and N. Ryum, "Microstructure and crystallographic orientation relationship in directionally solidified Mg – Mg<sub>17</sub>Al<sub>12</sub> -eutectic," *Mater. Sci. Eng. A*, vol. 289, pp. 143–150, 2000.
- [118] G. J. Shiflet and J. H. V. A. N. D. E. R. Merwe, "The Role of Structural Ledges as Misfit-Compensating Defects : fcc-bcc Interphase Boundaries," vol. 25, no. September, pp. 1895–1903, 1994.
- [119] P. M. Kelly and M. Zhang, "Edge-to-Edge Matching — The Fundamentals," *Metall. Mater. Trans. A*, vol. 37, no. March, pp. 833–839, 2006.
- [120] J. . Nie, X. . Xiao, C. . Luo, and B. . Muddle, "Characterisation of precipitate phases in magnesium alloys using electron microdiffraction," *Micron*, vol. 32, no. 8, pp. 857–863, Jan. 2001.

- [121] P. M. Kelly, H.-P. Ren, D. Qiu, and M.-X. Zhang, "Identifying close-packed planes in complex crystal structures," *Acta Mater.*, vol. 58, no. 8, pp. 3091–3095, May 2010.
- [122] T. Hahn, *International Tables for Crystallography Volume A*. Dordrecht: Reidel Publishing Company, 1983.
- [123] D. I. Potter, "The structure, morphology and orientation relationship of V<sub>3</sub>N in Vanadium," *J. Less-Common Met.*, vol. 31, pp. 299–309, 1973.
- [124] M. Zhang, W. Zhang, and F. Ye, "Interpretation of Precipitation Crystallography of Mg 17 Al 12 in a Mg-Al Alloy in Terms of Singular Interfacial Structure," vol. 36, no. July, pp. 20–22, 2005.
- [125] J. Pepe and W. Savage, "The Weld Heat-Affected Zone of 18Ni Maraging Steels," *Weld. J.*, vol. 49, pp. 545–553, 1970.
- [126] J. Pepe and W. Savage, "Effects of Constitutional Liquiation in 18-Ni Maraging Steel Weldment," *Weld. J.*, vol. 46, pp. 411–422, 1967.
- [127] I. Aksay, C. E. Hoge, and J. Pask, "Wetting Under Chemical Equilibrium and Nonequilibrium Conditions," *J. Phys. Chem.*, vol. 78, pp. 1178–1183, 1974.
- [128] B. Radhakrishnan and R. G. Thompson, "Kinetics of Grain Growth in the Weld Heat-Affected Zone of Alloy 718," *Metall. Trans. A*, vol. 24, no. December, pp. 2773–2785, 1993.
- [129] Q. Guo, H. Yan, Z. Chen, and H. Zhang, "Fracture behaviors of AZ80 magnesium alloy during multiple forging processes," *Trans. Nonferrous Met. Soc. China*, vol. 16, no. 4, pp. 922–926, Aug. 2006.
- [130] L. Peng, L. Yajiang, G. Haoran, and W. Juan, "A study of phase constitution near the interface of Mg/Al vacuum diffusion bonding," *Mater. Lett.*, vol. 59, no. 16, pp. 2001–2005, Jul. 2005.
- [131] P. Liu, Y. Li, H. Geng, and J. Wang, "Microstructure characteristics in TIG welded joint of Mg/Al dissimilar materials," *Mater. Lett.*, vol. 61, no. 6, pp. 1288–1291, Mar. 2007.
- [132] M. N. Desmukh, R. K. Pandey, and a. K. Mukhopadhyay, "Effect of aging treatments on the kinetics of fatigue crack growth in 7010 aluminum alloy," *Mater. Sci. Eng. A*, vol. 435–436, pp. 318–326, Nov. 2006.
- [133] J. Chen, L. Zhen, S. Yang, and S. Dai, "Effects of precipitates on fatigue crack growth rate of AA 7055 aluminum alloy," *Trans. Nonferrous Met. Soc. China*, vol. 20, no. 12, pp. 2209–2214, Dec. 2010.
- [134] V. A. Lubarda, M. A. Meyers, and O. Vo, "The Onset of Twinning in Metals : A Constitutive Description," *Acta Mater.*, vol. 49, pp. 4025–4039, 2001.

- [135] S. T. Niknejad, S. Esmaili, and Y. Zhou, “The Role of Double Twinning on Transgranular Fracture in Magnesium AZ61 in a Localized Stress Field,” *to be Submitt. to Acta Mater.*, 2015.
- [136] H. J. Bunge, *Texture analysis in materials science*, English Ed. Berlin: Akademie-Verlag, 1982.
- [137] F. Bachmann, R. Hielscher, and H. Schaeben, “Texture Analysis with MTEX – Free and Open Source Software Toolbox,” *Solid State Phenom.*, vol. 160, pp. 63–68, 2010.
- [138] M. Arminjon, “A Regular Form of Schmid Law Application to the Ambiguity Problem,” *Textures Microstruct.*, vol. 14–18, no. C, pp. 1121–1128, 1991.
- [139] “ANSYS Mechanical APDL Element Reference,” 2014.
- [140] M. Niewczas, “Lattice correspondence during twinning in hexagonal close-packed crystals,” *Acta Mater.*, vol. 58, no. 17, pp. 5848–5857, Oct. 2010.
- [141] J. J. Jonas, S. Mu, T. Al-Samman, G. Gottstein, L. Jiang, and È. Martin, “The role of strain accommodation during the variant selection of primary twins in magnesium,” *Acta Mater.*, vol. 59, no. 5, pp. 2046–2056, Mar. 2011.
- [142] S. R. Agnew, J. a. Horton, and M. H. Yoo, “Transmission electron microscopy investigation of  $\langle c+a \rangle$  dislocations in Mg and  $\alpha$ -solid solution Mg-Li alloys,” *Metall. Mater. Trans. A*, vol. 33, no. March, pp. 851–858, 2002.
- [143] Y. Liu and Y. Wei, “A polycrystal based numerical investigation on the temperature dependence of slip resistance and texture evolution in magnesium alloy AZ31B,” *Int. J. Plast.*, vol. 55, pp. 80–93, Apr. 2014.
- [144] M. R. Barnett, Z. Keshavarz, and X. Ma, “A Semianalytical Sachs Model for the Flow Stress of a Magnesium Alloy,” *Metall. Mater. Trans. A*, vol. 37, no. July, pp. 2283–2293, 2006.
- [145] A. Akhtar and E. Teghtsoonian, “Solid Solution Strengthening of Magnesium Single Crystals-II The Effect of Solute on the Ease of Prismatic Slip,” *Acta Metall.*, vol. 17, pp. 1351–1356, 1969.
- [146] S. Agnew, D. Brown, and C. Tome, “Validating a polycrystal model for the elastoplastic response of magnesium alloy AZ31 using in situ neutron diffraction,” *Acta Mater.*, vol. 54, no. 18, pp. 4841–4852, Oct. 2006.
- [147] O. Muránsky, D. G. Carr, M. R. Barnett, E. C. Oliver, and P. Šittner, “Investigation of deformation mechanisms involved in the plasticity of AZ31 Mg alloy: In situ neutron diffraction and EPSC modelling,” *Mater. Sci. Eng. A*, vol. 496, no. 1–2, pp. 14–24, Nov. 2008.



- [148] S. T. Niknejad, S. Esmaili, and Y. Zhou, "Competitive Fracture Initiation in Resistance Spot Weld of AZ80/ZEK100 Magnesium Alloys: Microstructural Aspects," *to be Submitt. to Mater. Sci. Eng. A*, 2015.
- [149] J. Radakovic and M. Tumuluru, "Predicting Resistance Spot Weld Failure Modes in Shear Tension Tests of Advanced High-Strength Automotive Steels," *Weld. J.*, vol. 87, no. April, pp. 96–105, 2008.
- [150] M. I. Khan, M. L. Kuntz, and Y. Zhou, "Effects of weld microstructure on static and impact performance of resistance spot welded joints in advanced high strength steels," *Sci. Technol. Weld. Join.*, vol. 13, no. 3, pp. 294–304, Apr. 2008.
- [151] J. F. Stohr and J. P. Poirier, "Etude en microscopie electronique du glissement pyramidal {1122} <1123> dans le magnesium," *Philos. Mag.*, vol. 25, no. 6, pp. 1313–1329, Jun. 1972.
- [152] T. Obara, H. Yoshinaga, and S. Morozumi, "{11-22} {-1-123} slip system in magnesium," *Acta Metall.*, vol. 21, pp. 845–853, 1973.
- [153] W. J. Kim, J. B. Lee, W. Y. Kim, H. T. Jeong, and H. G. Jeong, "Microstructure and mechanical properties of Mg–Al–Zn alloy sheets severely deformed by asymmetrical rolling," *Scr. Mater.*, vol. 56, no. 4, pp. 309–312, Feb. 2007.
- [154] X. Gao, S. M. Zhu, B. C. Muddle, and J. F. Nie, "Precipitation-hardened Mg–Ca–Zn alloys with superior creep resistance," *Scr. Mater.*, vol. 53, no. 12, pp. 1321–1326, Dec. 2005.
- [155] L. Guo, Z. Chen, and L. Gao, "Effects of grain size, texture and twinning on mechanical properties and work-hardening behavior of AZ31 magnesium alloys," *Mater. Sci. Eng. A*, vol. 528, no. 29–30, pp. 8537–8545, Nov. 2011.
- [156] A. Ince and G. Glinka, "A numerical method for elasto-plastic notch-root stress-strain analysis," *J. Strain Anal. Eng. Des.*, vol. 48, no. 4, pp. 229–244, Apr. 2013.
- [157] K. M. Flores and R. H. Dauskardt, "Enhanced toughness due to stable crack tip damage zones in bulk metallic glass," *Scr. Mater.*, vol. 41, no. 9, pp. 937–943, Oct. 1999.
- [158] K. M. Flores and R. H. Dauskardt, "Mean Stress Effects on Flow Localization and Failure in a Bulk Metallic Glass," *Acta Mater.*, vol. 49, pp. 2527–2537, 2001.
- [159] G. Glinka, "Energy Density Approach to Calculation of Inelastic Strain-Stress near Notches and Cracks," *Eng. Fract. Mech.*, vol. 22, no. 3, pp. 485–508, 1985.
- [160] R. T. Qu, M. Calin, J. Eckert, and Z. F. Zhang, "Metallic glasses: Notch-insensitive materials," *Scr. Mater.*, vol. 66, no. 10, pp. 733–736, May 2012.

- [161] X. L. Zheng, H. Wang, and M. S. Zheng, *Notch strength and notch sensitivity of materials*. Beijing: Science Press, 2008.
- [162] H. J. Zhou and M. Z. Huang, *Strength of metallic materials*. Beijing: Science Press, 1989.
- [163] Z. Zeng and a Fatemi, “Elasto-plastic stress and strain behaviour at notch roots under monotonic and cyclic loadings,” *J. Strain Anal. Eng. Des.*, vol. 36, no. 3, pp. 287–300, Jan. 2001.
- [164] S. T. Niknejad, S. Esmaeili, and Y. Zhou, “Notch Strength and Notch Sensitivity of Magnesium Alloys: Effects of Microstructure,” *to be Submitt. to Mater. Sci. Eng. A*, 2015.
- [165] R. Qu, P. Zhang, and Z. Zhang, “Notch Effect of Materials: Strengthening or Weakening?,” *J. Mater. Sci. Technol.*, vol. 30, no. 6, pp. 599–608, Jun. 2014.